Novel Power Electronic Device Structures for Power Conditioning Applications

By

Ajith Balachandran

A thesis submitted for the degree of PhD.

Department of Electronic & Electrical Engineering,

The University of Sheffield, UK

OCTOBER 2014

ABSTRACT

Silicon MOS controlled bipolar devices are considered to be the most preferred device technology for most low and medium voltage power applications. The economic and environmental benefits achievable by moving to more energy efficient power semiconductor and power conversion systems are well documented. A major factor that limits the performance of the MOS controlled bipolar structures is the current distribution within the device. An inhomogeneous current distribution within the device is a well known cause current filamnetation leading to device failure. Therefore it was logical to evaluate the key manufacturing parameters that might impact the current distribution in the device, other than ones already discussed in available literature. The work presented in this thesis evaluates the variation in resistivity caused due to the growth of the silicon wafer on the device performance. It was concluded that the variation of resistivity might not impact device performance substantially. However, the variation can cause a drift in the device characteristics across the wafer which can then impact the power module if the devices are not chosen properly.

The focus then moves to the design optimisation of a CIGBT structure and shows methods of optimising the anode side of the device so as to give better performance trade off without compromising the other characteristics of the device. The proposed anode design shows how an existing structure can further optimise the device performance by reducing the turn off losses of the device by about 50% while maintaining the on-state voltage. It is then shown how the CIGBT concept can provide a short circuit withstand capability of more than 100µs, which is higher than any MOS controller bipolar device ever reported.

The thesis also looks at various methods of optimising the cathode end of the device by the use of a segmented P-base structure. This structure is also experimentally evaluated and the

results show that the device can improve the turn-off performance while maintaining or improving the on-state voltage.

The final focus of the work then looks at a converter optimisation method using low voltage silicon devices and commercially available GaN devices. The results clearly show the dominance of GaN technology which, in the years to come, can become one of the most favourable technologies as compared to that of their silicon counterparts. However, this technology requires to be developed upon further with the aspect of thermal management requiring special attention.

ACKNOWLEDGEMENTS

LIST OF PUBLICATIONS

1. ISPSD Conference Publication "Enhanced Short-circuit performance of 3.3kV Clustered Insulated Gate Bipolar Transistor (CIGBT) in NPT technology with RTA Anode." A.Balachandran, L.Ngwendson, E.M.Sankara Narayanan, Shona Ray, Henrique Quaresma, John Bruce.

2. IEEE – Electron Device "Performance Evaluation of 3.3-kV Planar CIGBT in NPT Technology With RTA Anode", A. Balachandran, M.R. Sweet, N. Luther-King and E.M. Sankara Narayanan, Senior Member, IEEE, Shona Ray, Henrique Quaresma. John Bruce

3. ISPS Conference Publication "Evaluation of 1.2kV segmented cathode cell design for Trench Clustered Insulated Gate Bipolar Transistor (TCIGBT)", A. Balachandran, L. Ngwendson and E.M. Sankara Narayanan, Senior Member, IEEE.

4. ISPSD Conference Publication "2.4kV GaN Polarization Superjunction Schottky Barrier Diodes on Semi-Insulating 6H-SiC Substrate", Vineet Unni, Ajith Balachandran, Hong Long, Mark Sweet and E. M. Sankara Narayanan, Senior Member, IEEE

5. IEEE – Electron Devices - "Evaluation of 1.2kV segmented cathode cell design for Trench Clustered Insulated Gate Bipolar Transistor (TCIGBT)", A. Balachandran, L. Ngwendson and E.M. Sankara Narayanan, Senior Member, IEEE. (Working on reviewers comments)

LIST OF FIGURES

LIST OF TABLES

TABLE OF CONTENTS

CHAPTER ONE

1.1.   INTRODUCTION

The major motivation behind the power electronics industry is to facilitate cost reduction in the power generated, transmitted and distributed while maintaining stability of the power system for various different applications. It is observed that the efficiency for most power plants is less than 50% as shown in Figure 1-1 [1.1] [1.2].

Figure 1-1: Efficiency of Power Plants [1.1]

This inefficiencies is due to the process of converting energy from fuel stock (such as coal, gas, uranium etc...) into mechanical energy and finally into electrical energy via the generators. Once converted into electrical energy this needs to be transmitted and distributed to various users. In most cases the losses in transmission and distribution of electrical energy

account for 6% to 8% of the overall losses [1.3]. If this trend continues, along with an increase in the power demand as predicted by [1.4] [1.5], the net result will be an increase in associated costs.

In addition to the above, as the power demand and losses keep increasing, more natural resources will get consumed resulting in an increase in the carbon footprint. The carbon footprint provides a direct relation to the amount of greenhouse gases emitted from our day to day activities. This is usually composed of two parts [1.1] .

1. The primary footprint: A measure of the direct emission of CO2 from burning fossil fuels including domestic energy consumption and transportation.

2. The secondary footprint: It is a measure of the indirect CO2 emission caused due to the lifecycle of the products we use (manufacturing to disposal), and forms a direct relation to supply and demand.

The long term effect of the increase of greenhouse gases has been well documented and their effects are observed in our day to day lives (i.e., change in ocean salinity, wind patterns, increased precipitation and intense tropical cyclones, tsunamis etc...). Although there is a great deal of effort being directed towards developing and discovering renewable sources of energy with an aim to reduce an impact on the environment [1.5], these efforts would be undermined if a solution to minimise the losses in the rest of the system is not arrived at. It would be therefore quite logical to conclude that it is imperative that we move to newer methods of power production/distribution and conversion based on the development and use of more energy efficient and, consequently, cost effective devices

1.2. POWER ELECTRONICS

The field of power electronics involves the control, conversion and conditioning of electrical power. Hence, the application range of power electronics is from a few milliwatts (mobile phones) to hundreds of megawatts (Transmission systems). Power electronics is based on

providing an average equivalent power to the system while operating the devices in their switching state. Control and conditioning methods are then adopted to ensure that the efficiency and reliability of system is not compromised at different operating points.

1.2.1.   POWER CONVERTERS

Industrial applications always demand power conversion from one form to the other. Power electronic converters have been proven to process electrical power in a controlled manner as required by the load or the specific industrial process. In their most basic form, power electronic converters can be divided into the following categories: AC to DC (Rectifiers), DC to DC (Choppers), DC to AC (Inverters) and AC to AC (AC controllers/ Frequency changers). AC to AC power conversion normally requires a DC interlink with the exception of Matrix / Cyclo converters. During the 1940's, power conversion usually necessitated the use of expensive rotating machines. Hence these were rarely employed. With the development of the Silicon Control Rectifiers (SCR) technology in the late 1950's, power conversion can been more controlled. The development of semiconductor devices over the past decade has further made power electronic converters more economical, reliable, flexible and completely controllable. Hence their applications are myriad. In a variable speed drive, the power and speed rating are now no longer governed by semiconductor devices but by the performance of the electric motor [1.6]. Power electronic converters have now become an integral part of the electric drive system.

1.2.2.   POWER SEMICONDUCTORS DEVICES

One of the most important elements of a power electronic system is the power semiconductor device where the term semiconductor applies to all solid state materials which, due to their band structure, have a small or large number of electrons which are freely available for conduction. Over the past decade silicon based semiconductor device technology has matured

at an exponential rate. This follows from the increased reliability and performance benefits expected by the power electronic conversion stages in aerospace, automotive and various other applications. Insulated gate bipolar transistors (IGBT) are currently the most widely favoured silicon based power devices used in the industry; this is due to their MOS gate control, low on state and switching losses. In addition to this, the IGBTs also offer a relatively easy parallel connection with preferable temperature coefficients and a large safe operating area. A lot of attention has been focused on improving the performance of these IGBTs in terms of their on-state performance and switching speeds to improve the gravimetric power density of the power converters. Currently, in high power applications, Trench IGBTs are more favoured over the planar counterparts as they have the ability to boost the carrier density in the device through an increase in the active cell density per unit area. This is particularly helpful in improving the on-state performance of the device. However, they tend to lack the dynamic response required during the short circuit phase as compared to planar devices. The various advantages and disadvantages of the planar and trench technologies have been highlighted in [1.7] [1.8] [1.9].

In addition to the trench gate structures, various other methods have been discussed in available literature to improve the performance of IGBTs. One method actively employed by semiconductor manufacturers to improve on-state performance of IGBTs, is to boost the hole concentration at the cathode side of the device. The improvement in the hole concentration demands more electrons to be injected into the active silicon area, thus allowing for a higher conductivity modulation in the device. This method is commonly referred to as the hole pile up effect or the electron injection enhancement. Technologies such as the Injection-Enhanced Gate Transistor (IEGT) [1.10] [1.11] are reported to enhance the injection of electrons using a hole pile-up effect, but they result in instabilities as a result of charge imbalance at the gate [1.10]. Carrier Stored Trench-Gate Bipolar Transistor (CSTBT) and

High-Conductivity IGBT (HiGT) devices use an n-type barrier layer to achieve lower on-state voltages with similar saturation characteristics to that of conventional IGBTs [1.12] [1.13]. However, the concentration of n-type barrier layer needs to be carefully controlled in terms of the implant and drive condition so that the expansion of depletion region does not increase the turn-off losses of the device or degrade the forward blocking performance.

The other method to improve the on-state performance of the MOS controlled bipolar power devices is to have a thyristor mode of operation. MOS Controlled Thyristor (MCT) [1.14], Emitter Switched Thyristor (EST) and Clustered Insulated Gate Bipolar Transistor (CIGBTs) [1.15] are devices that show a thyristor mode of operation in their on-state. However, of these, the planar gate CIGBT and trench gate CIGBT structures are the only MOS controlled thyristor devices which have been experimentally proven to show excellent current saturation characteristics even at high gate voltages due to their inherent self-clamping capability [1.15]. Hence further development of the CIGBT technology has been discussed as part of this thesis.

Wide bang gap devices have also made remarkable progress in the last few years and these devices are now challenging the Silicon market due to their improved material properties. As these device technologies improve by reducing losses, the cost of device fabrication and operation needs to be simultaneously reduced.

1.3.   THESIS STRUCTURE

The work presented in this thesis contains an investigation into the methods by which the semiconductor device performance can be improved with an aim to reduce the overall losses in the power conversion system. The types of device technologies discussed and evaluated in this thesis include Silicon MOSFETs, IGBT, CIGBT and GaN HEMT devices. The performance improvement methods suggested in literature usually involve a trade-off of device characteristics with one another. Therefore an investigation into new device

technologies and structures is deemed necessary such that the performance trade-off can be avoided or be improved.

The work presented in this thesis initially looks at the drift engineering of the device with a focus on IGBT structures. The variation of substrate resistivity is investigated using a SENTARUS DEVICE simulator and the results clearly show the variation will not cause any significant impact on device on-state and turn-off performance of the IGBT.

The thesis then covers the development and optimisation of the 3.3kV CIGBT devices. The anode and cathode optimisation of the structure is done using commercially available simulation packages such as MEDICI and TSUPREM IV. The devices are then designed in TCAD SENTARUS–IC and fabricated in Semifab, once the fabrication process was baselined. The fabricated devices were then packaged via a third party supplier in TO-247 package and experimentally evaluated using industrial standard techniques at The University Of Sheffield. These devices are then compared with other commercially available IGBTs in order to evaluate the performance benefits. The work presented here also builds on the work done by Dr.Mark Sweet and Dr. Luther-King Ngwendson [1.16]. The results presented show the CIGBT with RTA anode reduces the turn-off losses of the device by more than 50% as compared to the previous technology demonstrated [1.16]. It is further shows that the devices provide a short circuit capability of more than 100µs which is 10 times higher than commercially available devices.

The thesis work then focuses on the cathode optimisation of CIGBT structures using a segmented P-base concept for a 1.2kV CIGBT device. All segmented P-base devices structures were simulated using MEDICI and TSUPREM IV and the preferred device structures were designed in TCAD SENTARUS-IC. These devices were then fabricated in collaboration with in industrial partner. Finally the devices were then assembled in The

Sheffield of University on a metallised substrate for further experimental evaluation. The results presented for this work clearly show that the turn-off losses of the device can be reduced by 23% while maintaining its on-state performance. In addition to this the structure also enhances the short circuit performance of the device due to the reduction of active cells per unit area. Although the work presented here is based on a 1.2kV device. The work can be applied to any voltage rating.

The remaining part of the thesis looks at a converter design from a device point of view. The device selection is discussed with aim to reduce the overall losses. A number of prototypes are then built to evaluate the 1st generation GaN device. Various challenges were encountered during this process. This included the assembly of the dies, the reduction of the stray inductance in the circuit and technology issues such as current collapse in order to switch the device within the safe operating area. These devices were experimentally evaluated in a chopper circuit and an H-Bridge arrangement. The gate drive circuit and the switching algorithms were developed during the process of testing the devices. The experimental and simulation results presented for this work clearly show that although GaN devices can provide a far better performance as compared to Silicon devices. However, the technological advancement needed to make this device feasible for high power converter applications are far too many.

The work outlined above in structured into the thesis in the following manner.

Chapter 1:   Introduction.

Chapter 2:   Reviewing the challenges encountered in the fabrication of solid state semiconductor devices such as IGBTs and evaluating its impacts on the device performance.

Novelty- The chapter provides simulation results to justify the amount of substrate variability that can be allowed for device fabrication without compromising device performance.

Chapter 3: Performance evaluation of the CIGBT with planar gates in Non Punch Through Technology (NPT) with Rapid thermal annealing (RTA) of anode.

Novelty- The chapter provides simulation and experimental results to support the use of RTA process in CIGBT structures and shows how the device performance can be further improved. The results for this work are published in ISPSD and IEEE Electron devices (Publication 1 and 2).

Chapter 4: Novel TCIGBT structures to improve the short circuit capability of device while maintaining the on-state and switching performance.

Novelty- This chapter provides simulation and experimental results to support the use of Segmented P-base structures in TCIGBT and shows how the device performance can be improved while maintaining the Vce-Eoff trade-off. The results from this work are published in ISPS and are being submitted for IEEE Electron devices also (Publication 3 and 5).

Chapter 5, 6: Investigating and evaluating the use of wide bang gap devices (WBG) and low voltage silicon devices in a converter application.

Novelty- The chapter provides simulation and experimental results investigating the use of low voltage devices and GaN devices for a converter application as compared to traditional high voltage silicon devices.

Chapter 7: Concluding remarks and future work

Appendix A: This contains the MEDICI and ISE Sentarus files used for the IGBT / CIGBT structures.

Appendix B: This contains the device characterisation files for the IGBT/CIGBT strcutrues.

Appendix C: Contains the Simulink and Spice model for the converter simulations.

Appendix D: Contains the Layout and schematic files used to develop the H-Bridge circuits in order to evaluate the GaN devices.

1.4.   REFERENCES

[1.1]   E. U. S.-G. Livio HONORIO, "Efficiency in Electricity Generation," July 2003.

[1.2]   D. S. Henderson, "Variable speed electric drives-characteristics and applications," in *Energy Efficient Environmentally Friendly Drive Systems Principles, Problems Application (Digest No: 1996/144), IEE Colloquium on*, 1996, pp. 2/1-2/8.

[1.3]   A. Inc. (2007, 19/07/2015). Energy Efficiency in the Power Grid. 1-8. Available: https://www.nema.org/Products/Documents/TDEnergyEff.pdf

[1.4]   E. W. Sabena Khan, "Energy Consumption in the UK (2014)," 31st July 2014 2014.

[1.5]   F. M. a. E. O. Christine Pout, "The impact of changing energy use patterns in buildings on peak electricity demand in the UK," 31st October 2008 2008.

[1.6]   J. T. Bialasiewicz, E. Muljadi, and R. G. Nix, "RPM-Sim-based analysis of power converter applications in renewable energy systems," in *IECON Proceedings (Industrial Electronics Conference)*, Denver, CO, 2001, pp. 1988-1993.

[1.7]   M. Harada, T. Minato, H. Takahashi, H. Nishihara, K. Inoue, and I. Takata, "600V trench IGBT in comparison with planar IGBT - an evaluation of the limit of IGBT performance," *IEEE International Symposium on Power Semiconductor Devices & ICs*, pp. 411-416, 1994.

[1.8]   R. Hotz, F. Bauer, and W. Fichtner, "On-state and short circuit behaviour of high voltage trench gate IGBTs in comparison with planar IGBTs," in *Power Semiconductor Devices and ICs, 1995. ISPSD '95. Proceedings of the 7th International Symposium on*, 1995, pp. 224-229.

[1.9]   H. Iwamoto, H. Kondo, S. Mori, J. E. Donlon, and A. Kawakami, "An investigation of turn-off performance of planar and trench gate IGBTs under soft and hard switching," in *Industry Applications Conference, 2000. Conference Record of the 2000 IEEE*, 2000, pp. 2890-2895 vol.5.

[1.10] I. Omura, T. Demon, T. Miyanagi, T. Ogura, and H. Ohashi, "IEGT design concept against operation instability and its impact to application," in *Power Semiconductor Devices and ICs, 2000. Proceedings. The 12th International Symposium on*, 2000, pp. 25-28.

[1.11] T. Takeda, M. Kuwahara, S. Kamata, T. Tsunoda, K. Imamura, and S. Nakao, "1200 V trench gate NPT-IGBT (IEGT) with excellent low on-state voltage," in *Power Semiconductor Devices and ICs, 1998. ISPSD 98. Proceedings of the 10th International Symposium on*, 1998, pp. 75-79.

[1.12] H. Takahashi, H. Haruguchi, H. Hagino, and T. Yamada, "Carrier stored trench-gate bipolar transistor (CSTBT)-a novel power device for high voltage application," in *Power Semiconductor Devices and ICs, 1996. ISPSD '96 Proceedings., 8th International Symposium on*, 1996, pp. 349-352.

[1.13] M. Mori, Y. Uchino, J. Sakano, and H. Kobayashi, "A novel high-conductivity IGBT (HiGT) with a short circuit capability," in *Power Semiconductor Devices and ICs, 1998. ISPSD 98. Proceedings of the 10th International Symposium on*, 1998, pp. 429-432.

[1.14] D. Quek and S. Yuvarajan, "A novel gate drive for the MCT incorporating overcurrent protection," in *Industry Applications Society Annual Meeting, 1994., Conference Record of the 1994 IEEE*, 1994, pp. 1297-1302 vol.2.

[1.15] N. Luther-King, E. M. S. Narayanan, L. Coulbeck, A. Crane, and R. Dudley, "Comparison of Trench Gate IGBT and CIGBT Devices for Increasing the Power Density From High Power Modules," *Power Electronics, IEEE Transactions on*, vol. 25, pp. 583-591.

[1.16] M. Sweet, N. Luther-King, S. T. Kong, E. M. S. Narayanan, J. Bruce, and S. Ray, "Experimental Demonstration of 3.3kV Planar CIGBT In NPT Technology," in *Power*

Semiconductor Devices and IC's, 2008. ISPSD '08. 20th International Symposium on, 2008, pp. 48-51.

CHAPTER TWO

IMPACT OF SUBSTRATE RESISTIVITY VARIATION ON IGBT DEVICE PERFORMANCE

2.1   INTRODUCTION

The growth of Silicon wafers which provide the required functionality for processing semiconductor devices is an extremely complex process in which the wafer quality directly impacts on the device performance. Silicon in its raw state is a very brittle element which is abundant in nature. Key electrical, mechanical and thermal properties of Silicon are summarised in Table 2-1.

Table 2-1: Material properties of Silicon [2.1] [2.2]

Property	Value
Band Structure Properties	
Dielectric Constant	11.9(@1MHz)
Energy Gap E_g	1.12 eV
Intrinsic Carrier Concentration	1×10^{10} cm^{-3}
Auger Recombination co-efficient C_n	1.1×10^{-30} cm^6/s
Auger Recombination co-efficient C_p	3×10^{-31} cm^6/s
Mechanical Properties	
Density	2.33 gm/cc
Hardness	1150 knoop
Tensile Strength	113 MPa
Modulus of Elasticity	112 GPa
Flexural Strength	~300 MPa
Possion's Ratio	0.28
Fractural Toughness	3-6 MPa m1/2
Electrical properties	
Mobility electrons	≈ 1400 cm^2 / (V x s)
Mobility holes	≈ 450 cm^2 / (V x s)
Diffusion Co-efficient electrons	≈ 36 cm^2/s
Diffusion Co-efficient Holes	≈ 12 cm^2/s
Electron Thermal Velocity	2.3×10^5 m/s
Hole Thermal Velocity	1.65×10^5 m/s
Work Function	4.15 eV
Electronegativity	1.8 Paulings
Volume Resistivity	10^{-3} ohm-cm
Thermal properties	
Co-efficient of Thermal Expansion	2.6×10^{-6} / ° C
Thermal Conductivity	156 W/mK
Specific Heat	0.15 cal/g° C

Maximum Working Temperature	1350 ° C
Boiling Point	2628 K
Melting Point	1687 K
Specific heat	0.7 J / (g x ℃)

Monocrystalline undoped Silicon is usually not a good conductor of electricity. The conductivity of such material can be controlled by the amount of impurities or dopants introduced into its crystal structure. Doping is the process by which impurities are intentionally introduced in into a pure (Intrinsic) semiconductor to modulate its electrical characteristics. Doping can be achieved in practice either by diffusion or during the wafer processing stage as described below.

The processing of Silicon wafers involves growing monocrystalline Silicon Ingots with a uniform controlled dopant and oxygen content. These ingots are then taken through further processing stages which involve grinding, slicing and polishing to attain a number of defect free wafers, of various thickness and diameters. Such a wafer forms the basic building block of power semiconductor devices. Silicon ingots are usually grown from polysilicon chips which are purified using Trichlorosilane and Hydrogen [2.3]. Further processing allows these polysilicon chips to be loaded into a pulling furnace in granular form. The Silicon ingots are usually grown using one of the following methods.

1. CZ method (Czochralski method)

2. FZ method (Floating Zone method)

In the Czochralski method, the Polysilicon chips are melted at a process temperature of 1400℃ in a high purity Argon gas ambient. Once the proper "melt" is achieved a "seed" of single crystal Silicon is dipped into the melt. The temperature of the melt is then adjusted and the seed is rotated as it is slowly pulled out of the molten Silicon. The surface tension between the seed and the molten Silicon causes a small amount to rise with the seed, as it is pulled and cooled into a perfect monocrystalline ingot. This Czochralski method is the most

widely used method in the industry today. Figure 2-1 (a) shows a cross section of the crystal pulling furnaces used for manufacturing of Silicon Ingot and Figure 2-1 (b) shows a silicon ingot.

(a)   (b)
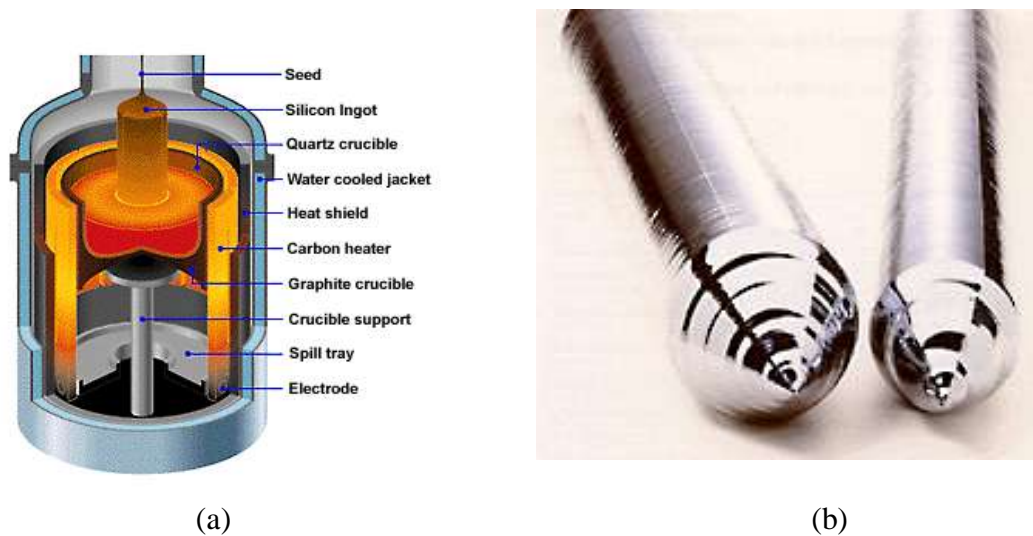
Figure 2-1 (a) Czochralski crystal pulling furnace, (b) Silicon Ingot [2.3]

In the float zone method, the Silicon is melted using an induction heater without using a quartz crucible. The melted silicon is then retained by the surface tension. The advantage of this method is that it is possible to obtain a very high quality silicon ingot. However, the drawback of this method is the cost associated to grow large Silicon wafers. Another method used today is the MCZ method which is an extension of the Czochralski method where a magnetic field is applied in a controlled manner to improve the quality of the crystal [2.4].

Having grown a high quality ingot, the next stage of wafer processing involves grinding the ingot to a nominal diameter. The ingots are also notched along their length to indicate the orientation of the crystal. These are then sliced into thin wafers using a diamond saw and then lapped to produce a high quality surface finish. The surface roughness for an acceptable silicon wafer is given in SEMI standards [2.5]. After lapping, the wafers are sent through a cleaning and etching process using sodium hydroxide or acetic and nitric acids to remove

microscopic cracks and surface damage caused by the lapping process. The wafer is then rinsed with deionized water. The final process involves polishing and sorting of the wafers. Wafer sorting is a long process which involves checking the wafer for various defects such as, 1) Thickness variation in the wafer, 2) Flatness of the wafer, 3) Bow and Warp, 4) Electrical resistivity, 5) Mechanical defects and 6) contamination (Scratches, copper precipitates, etc.).

Among these, the variation of electrical resistivity throughout the wafer is considered to be an important feature for power semiconductor devices. In this regard it is worth noting that, unlike large scale integration devices such as Microprocessors, power devices are also reliant on the wafer properties in the vertical direction. Therefore, a variation in resistivity can lead to inhomogeneous current distribution and non-uniform oxide growth, in turn adversely affecting device performance. The maximum variation of resistivity across the ingots has been reported to be some 15% [2.6]. Wafers with the least number of defects are usually categorised as 'prime wafers'. This chapter investigates the influence of the variation in the substrate resistivity on IGBT power device performance.

2.2   INSULATED GATE BIPOLAR JUNCTION TRANSISTORS

The concept of an IGBT was initially proposed by Baliga [2.7] in 1980 following which, IGBT has been extensively developed to obtain high performance for switching applications. Modern IGBTs exhibit extremely low switching losses and low on-voltage drop. With the performance of the IGBTs reaching their theoretical limits, manufacturers work on a trade-off between the on-state losses and switching losses of the device to provide the most efficient solution for a given application. The use of IGBTs in hard-switching applications requires them to accommodate simultaneous high current and voltages and, hence, these devices must be robust and reliable especially for safety critical applications. To optimize the performance

of IGBTs it is essential to understand the internal device dynamics. IGBTs are a functional integration of MOS and bipolar technologies and it combines the best attributes of both these technologies. IGBTs are bipolar devices having high input impedance and commercially available IGBTs are designed to support high voltages of up to 6.5kV.

The cross section of a Trench-IGBT is shown in Figure 2-2. IGBT modules contain an array of many such cells arranged in a topological layout, providing extremely high current carrying capability at module level. IGBT in their most basic form can be classified as punch through devices (PT) or non-punch through devices (NPT). The advantages and disadvantages of these structures have been widely discussed in [2.8] [2.9] [2.10].
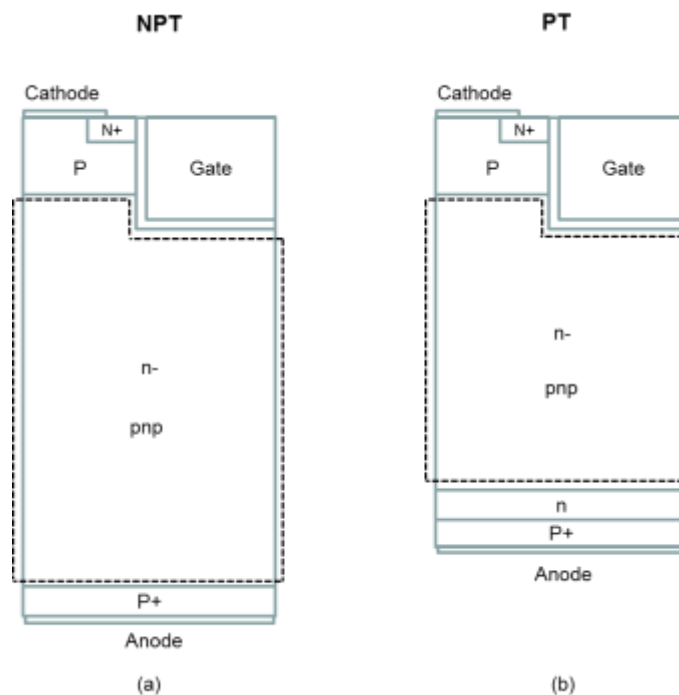
Figure 2-2: Generic IGBT Trench-Structures (a) NPT-IGBT (b) PT-IGBT

2.2.1   DEVICE OPERATION

When a positive voltage is applied to the gate with respect to the cathode, electrons from n+ region are attracted to the surface of the gate. At the threshold voltage these electrons invert the silicon contact between the P-base and the gate to form an inversion layer grounding the N-drift region. This allows current flow between N-drift region and n+ region. The flow of

electrons into the N-drift region lowers the potential of the N-drift region where the P$^+$ Anode / N-drift diode becomes forward biased. This allows a high density of minority carriers to be injected into the N-drift by the P+ Anode. The minority carrier injected into the N- drift travels vertically upward and some of these holes are repelled by the positively charged accumulation layer below the gate. These holes then transverse through the P-base and reach Cathode contact. At high forward voltages a high density of holes builds up in the N-drift. These holes attract electrons from the cathode contact to maintain charge neutrality which drastically enhance the conductivity of N-drift. The increased conductivity modulation of the N-drift allows flow of electrons through this region with very less resistance. Figure 2-3 shows a graphical interpretation of the flow of charge in an IGBT.

To regain blocking state the gate voltage applied to the devices must be removed and the charges injected into the bulk region must be extracted. Most of this charge is extracted as the depletion region moves towards the P+ Anode. However, the decay of excess carriers happens through the process of recombination and no external circuit can be used to speed up the process. In punch-through devices a lifetime killing technique can be employed to decrease the turn-off time and losses.
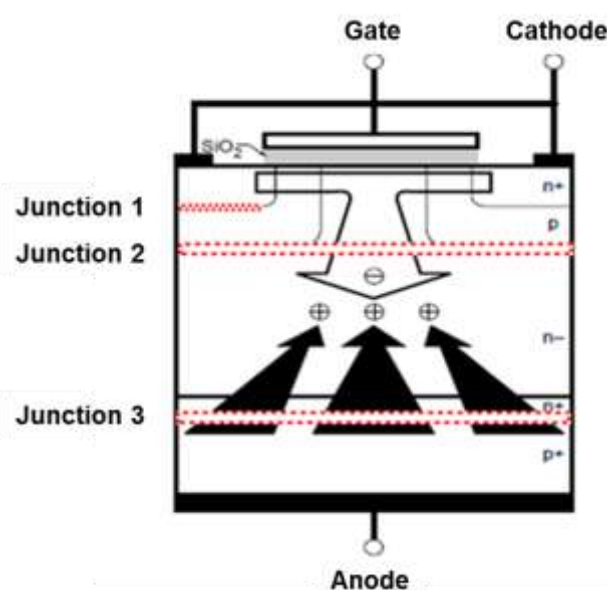
Figure 2-3: Graphical interpretation of the flow of charge in an IGBT during its on-state [2.11]

2.2.2 DRIFT ENGINEERING

The design of the drift region is driven primarily by the ability of the device to support voltage, when operated in its forward blocking state. During the on-state, the drift region is flooded with charge which contributes to its on-state voltage. During turn-off, this charge needs to be extracted from the drift region as otherwise they contribute to increased turn-off losses of the device. Therefore, enhancing the conductivity modulation of the device can potentially give rise to an increase in the turn-off losses of the device. In a NPT (Non-punch through) IGBT, the drift region is uniformly doped and the length of the drift region must be sufficient to support the electric field. In a PT (punch through) device, the length of the drift region is reduced by introducing a heavily doped buffer region. The thickness of the buffer region is adjusted to support the expansion of depletion region avoiding premature breakdown due to punch through. However, there are many disadvantages to the punch through structure which are highlighted in [2.12], a brief summary of this is shown below.

- The epitaxial growth of PT IGBT more than 100μm thick is difficult and expensive.

- As the epitaxial layer is grown on heavily doped regions, it inserts a large concentration of minority carriers increasing the turn-off time of the device.

- Limits high frequency switching due to higher turn-off losses.

- The PT IGBT has a negative temperature co-efficient of the forward voltage drop. This essentially means the devices are difficult to parallel. Therefore requires further optimisation of the buffer region.

These drawbacks led to the development of the field stop structure which uses a transparent anode (such as that in an NPT IGBT) and buffer region which is less doped in comparison to the punch-through structure. This combination achieves low on-state voltage during the on-state and also supports the DC-link voltage in forward blocking mode. The field stop structure has a positive temperature co-efficient in comparison to a punch-through structure,

which is very important for the paralleling of devices. The electric field distributions of three structures are shown in Figure 2-4 [2.12].
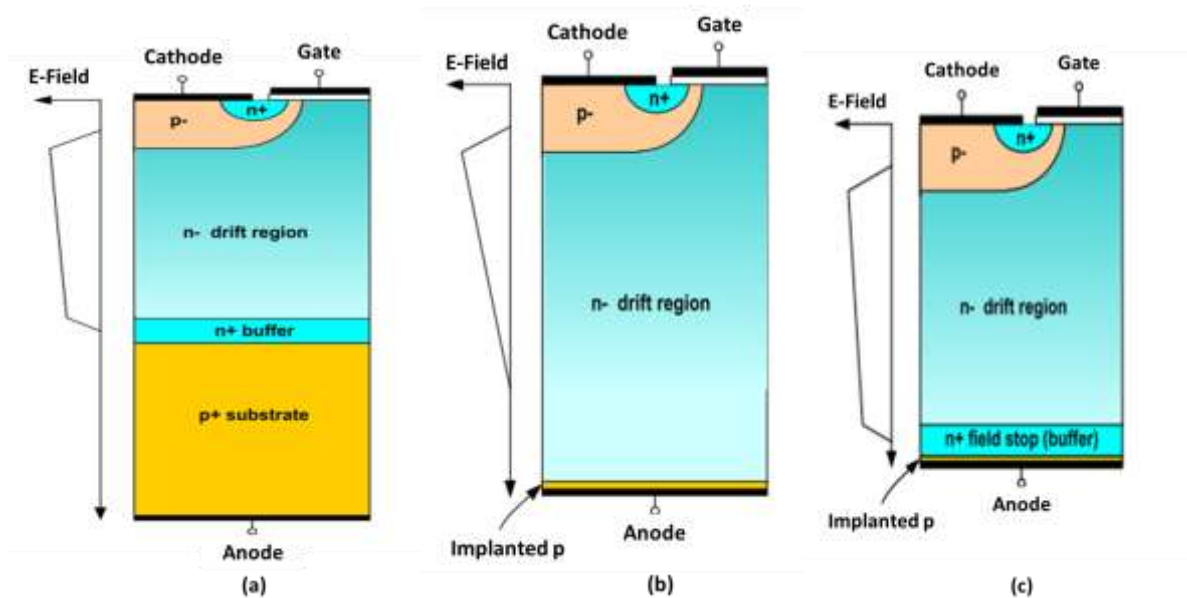
Figure 2-4: Electric field distribution of the a) PT (punch through) b) Non-punch through c) field stop structure [2.12]

2.3 IMPACT OF VARIATION OF DOPING CONCENTRATION

In previous studies it has been suggested that the difference in the hole injection density across the P+ anode can result in an inhomogeneous distribution across the IGBT as the electric field across the structure varies significantly [2.13]. Therefore this chapter investigates the influence of process variations, particularly the variation of resistivity across the drift region, on the performance of the IGBT.

2.3.1 HALF CELL DEVICE STRUCTURE

In order to investigate the variation of the substrate bulk resistivity on the performance of an IGBT, a representative device was simulated in the Sentaurus TCAD simulation package. A cross-section view of the IGBT along with its leading dimensions is shown in Figure 2-5. The drift doping concentration of the structure was varied in three steps (8.0×10^{13} cm^{-3}, 7.2×10^{13} cm^{-3} and 8.8×10^{13} cm^{-3}) which corresponds to the 10% variation in the resistivity as

discussed in section 2.1. The breakdown voltage of the structure was designed to be 1.2kV, (by appropriate setting of the thickness of the drift region) and the cell dimensions of the IGBT are in line with sub-micro device technologies.
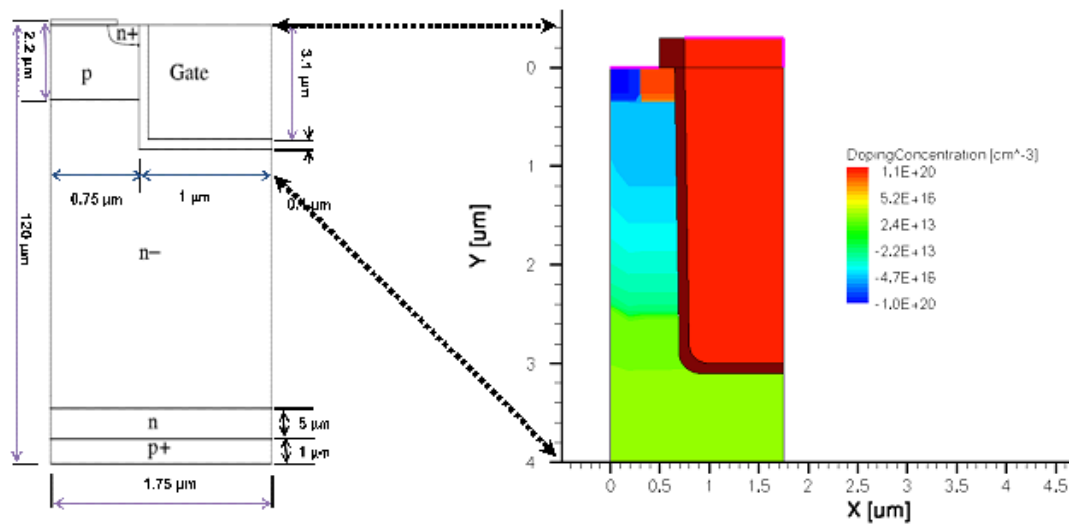
Figure 2-5: Cross section view of the IGBT along with its leading dimensions

2.3.1.1 SIMULATION RESULTS

A series of predicted static characteristics for the device with the different drift doping concentrations considered are summarised in Table 2-2. The inductive switching performance of the trench IGBT structure for the various drift doping concentrations is shown in Figure 2-7. The test setup used for simulation is shown in Figure 2-6.

Table 2-2: Simulated static characteristics of 1.2kV Trench-IGBT

1. Structure	Drift Concentration	Oxide Thickness	Temperature (°C)	Threshold voltage (Volts)	Breakdown Voltage (Volts)	Vce(sat) (Volts)
IGBT	7.2×10^{13} cm^{-3}	0.0979µm	25	5.02	1424	1.61
			125	4.06	1684	1.99
	8.0×10^{13} cm^{-3}	0.0979µm	25	5.02	1385	1.61
			125	4.05	1654	1.99
	8.8×10^{13} cm^{-3}	0.0979µm	25	4.99	1364	1.61
			125	4.07	1630	1.99

As will be evident from Table 2-2 and Figure 2-7, the variation of the drift doping concentration has a minimal impact in the on-state performance and the turn-off performance of the device, while the variation of resistivity has a 5% impact on the breakdown voltage of the device. This can be explained by reference to the relationships that govern the breakdown voltage of the device [2.14]. Equation 2.1 shows the impact of doping concentration (N_D) on the critical electric field of silicon devices ($E_c(Si)$).
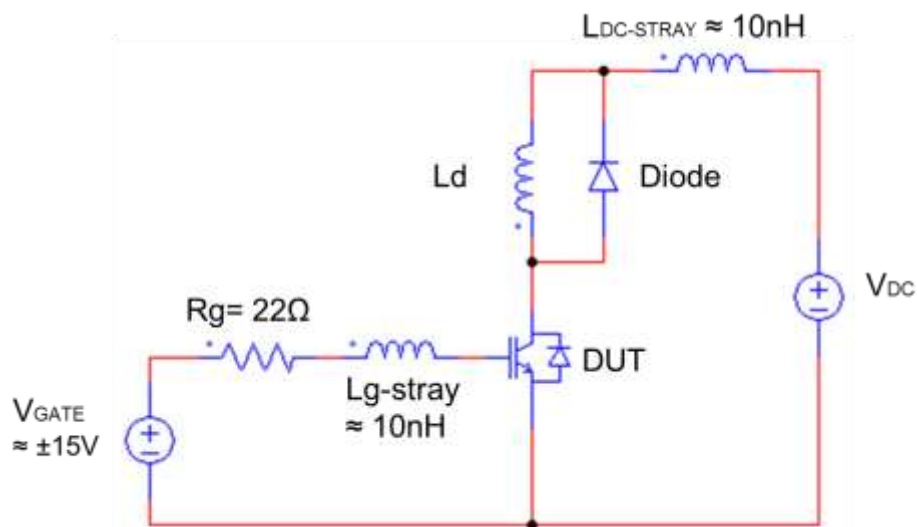
Figure 2-6: Typical chopper circuit used for simulation.

As the doping concentration of the device is inversely proportional to the resistivity of the material, the resistivity of the material has a direct impact on the breakdown voltage of the device.

$$E_c(Si) = 4010 \, N_D^{1/8} \quad \text{....} (2.1) \, [2.14]$$

These simulations highlight the fact that the current distribution across a multi-cell structure should not vary significantly as a result of any resistivity variations across the starting wafer.
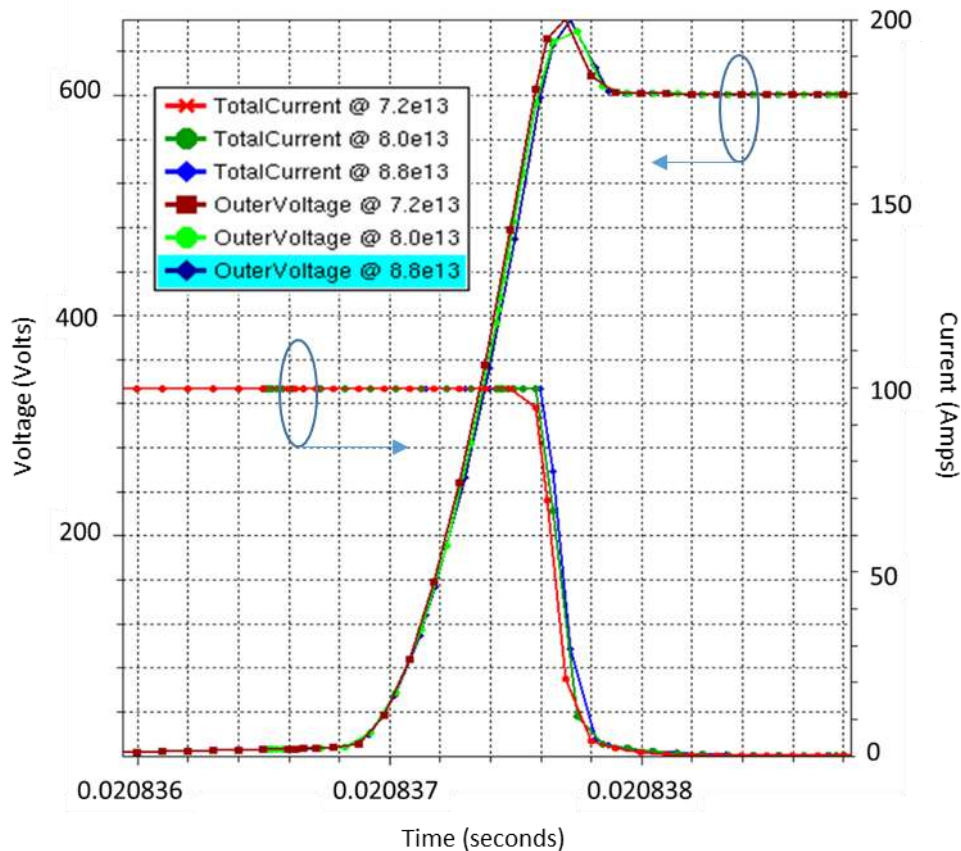
Figure 2-7: Simulated inductive turn-off switching performance of 1.2kV IGBT. VDC=600V,

I=100Amps, τ=10μs, T=25°C

2.3.2   MULTI-CELL DEVICE STRUCTURE

A practical IGBT structure will consist of a number of cells connected in parallel to form the main device (typically several thousand depending on the cell dimension, the current rating of the device and the design constraints imposed by the fabrication process). Hence, a multi-cell structure was simulated with the same variation in the drift doping concentration, to confirm results shown previously in section 2.1. The cross section view of the multicell structure along with the variation of resistivity considered is shown in Figure 2-8 and Figure 2-9.
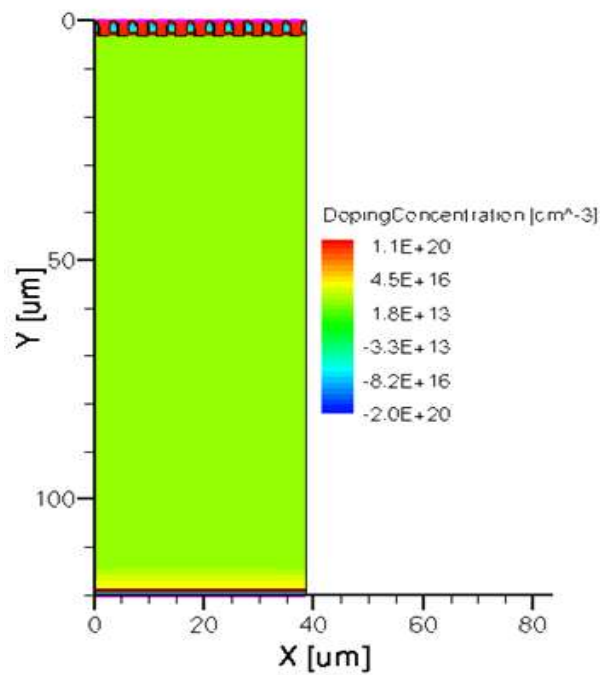
Figure 2-8: Cross section of the multi-cell structure of the IGBT along with the variation of the drift doping concentration in the X direction
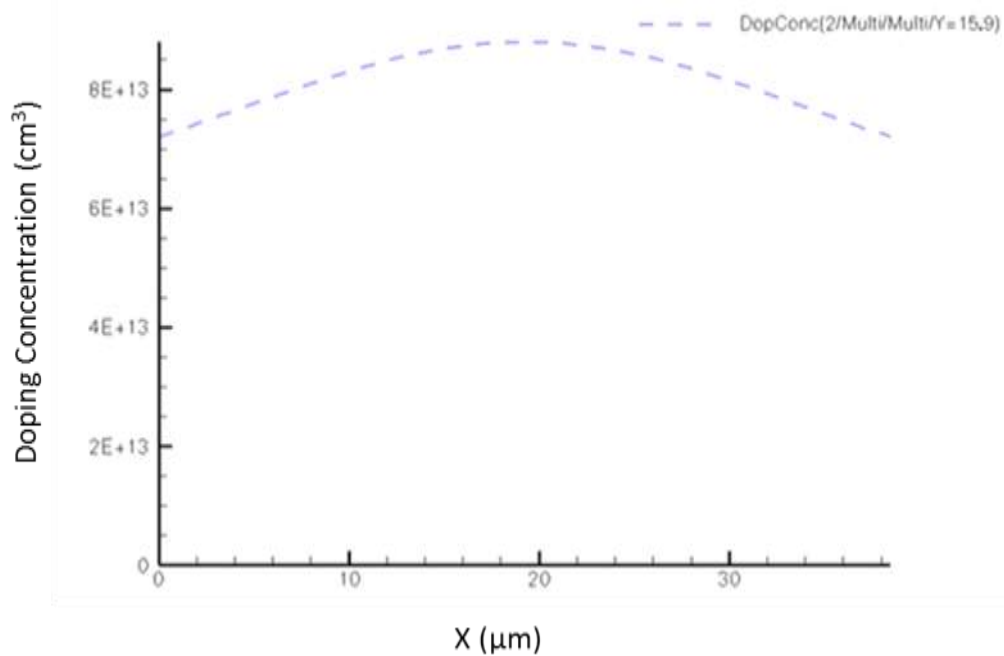
Figure 2-9: Variation of doping concentration along X axis for the IGBT structure shown in Figure 2-8

2.3.2.1 SIMULATION RESULTS

Figure 2-10 shows the turn-off characteristics of the multi-cell structure, where t1 and t2 refer to different points in the switching cycle. Figure 2-11shows the predicted current distribution in the multi-cell structure for a variation in the substrate doping concentration at the various points in the switching cycle. It can be seen from Figure 2-11 that there is no discernible variation in current distribution between the cells during the on-state operation. This behaviour in the on-state is a consequence of the drift region being flooded with charge carriers, and so the charge concentration is an order of magnitude higher than the background doping concentration. The effect of the variation in resistivity across the device rendered is of secondary importance. During the turn-off period there is small inhomogeneous distribution. However, this is not significant enough to cause current filamentation or device failure.
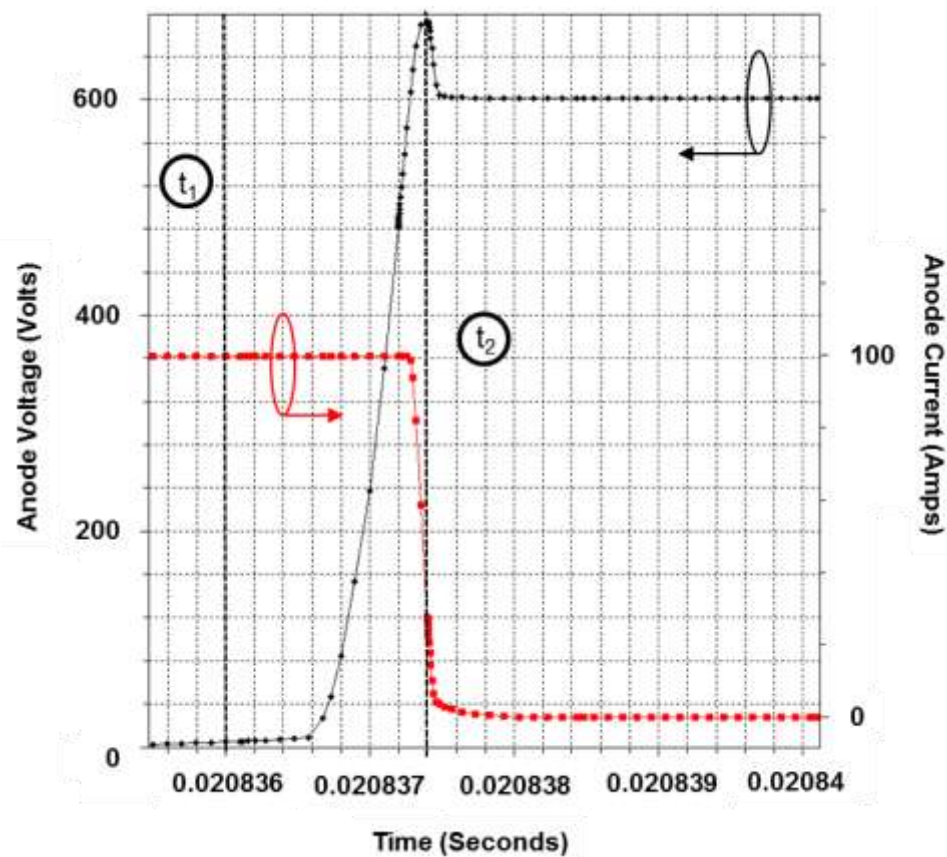
Figure 2-10: Simulated Inductive switching performance of the 11-cell structure. V$_{DC}$=600V, I=100Amps, Carrier lifetime (τ) =10us, T=25°C
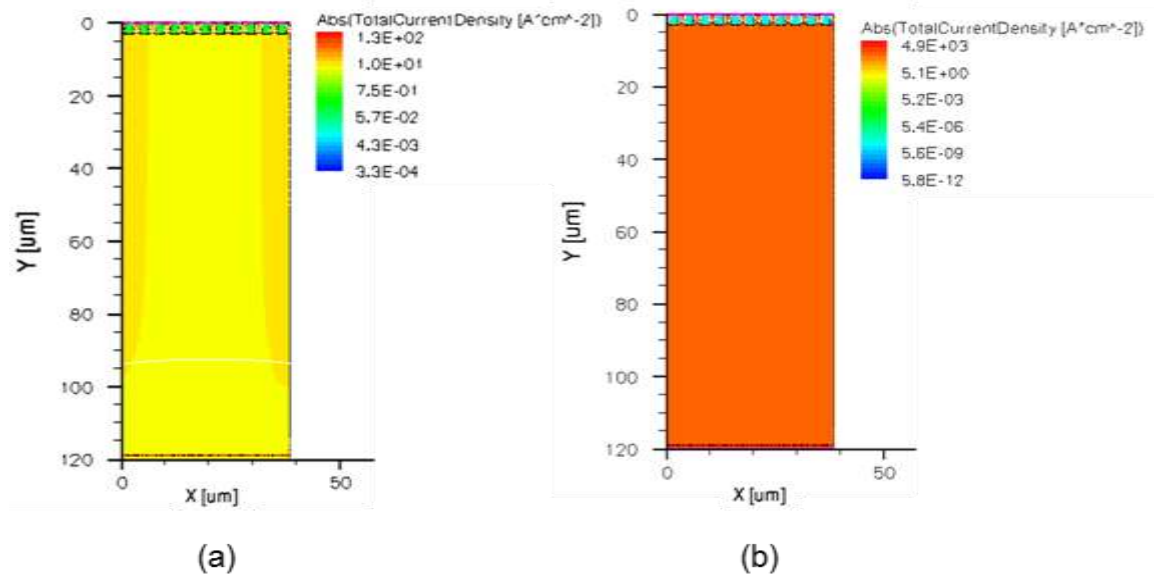
Figure 2-11: Current distributions across the 11-Cell structure during (a) turn-off condition (b) the on- state condition

As demonstrated by Figure 2-11 a 10% variation of doping concentration specified above does not affect device performance to a meaningful extent. The next part of the study is focused on establishing the maximum variation that can be tolerated without affecting the device characteristics.

2.3.3   MAXIMUM ACCEPTABLE VARIATION

The unit cell structure shown in Figure 2-5 was considered with homogenous base concentration in order to establish whether there was any substantial effect on the static performance of the device. Figure 2-12 shows the effect of variation of resistivity on the threshold and saturation characteristics of the device with the baseline drift doping concentration of around $1 \times 10^{14}\, cm^{-3}$ identified by the green marker. It can be seen that there is a minimal variation in both of the properties and therefore the short-circuit performance of the devices should also not be influenced by the variation of the drift resistivity. Figure 2-13 shows the influence of variation in resistivity (resistivity of the material is inversely

proportional to the doping concentration), on the on-state voltage of the device. It is seen that there is an insignificant change in on-state voltage.
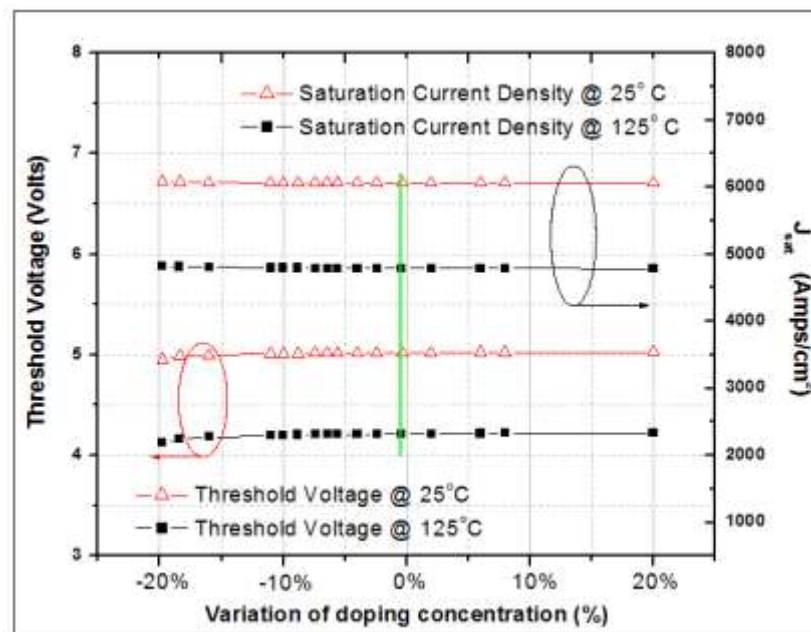
Figure 2-12: Variation of threshold voltage and saturation current density of the device with substrate resistivity, Drift depth = 120µm, baseline for variation = 1×10^{14} cm^{-3}, Carrier lifetime (τ) =10us
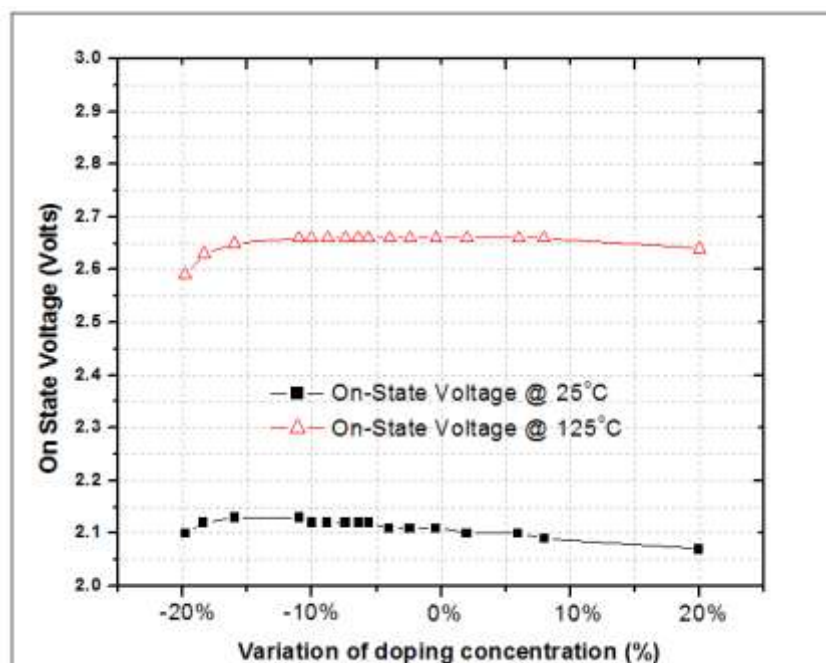
Figure 2-13: Variation of resistivity on the on-state voltage, Drift depth = 120µm, 0% variation = 1e14 cm^{-3}, Carrier lifetime (τ) =10us

Figure 2-14 and Figure 2-15 shows the effect of the resistivity variation on the breakdown voltage and the turn-off losses of the device, respectively. It can be observed from Figure 2-14 that if the variation of resistivity is positive, i.e. the doping concentration of the material increases, the breakdown voltage of the device reduces. This is a consequence of the avalanche breakdown voltage of the device decreasing with increasing doping concentration. Hence, the device would breakdown before the depletion region impacts on the buffer.

In contrast, if the doping concentration is decreased by a large degree, breakdown occurs as a result of the punch-through phenomenon of the device. In this case, the depletion region punches-through the buffer region. This can be avoided by increasing the buffer thickness or doping concentration. However, the remedial actions increase the turn-off losses of the devices as more charge now needs to be extracted through recombination as described in [2.13] [2.15].
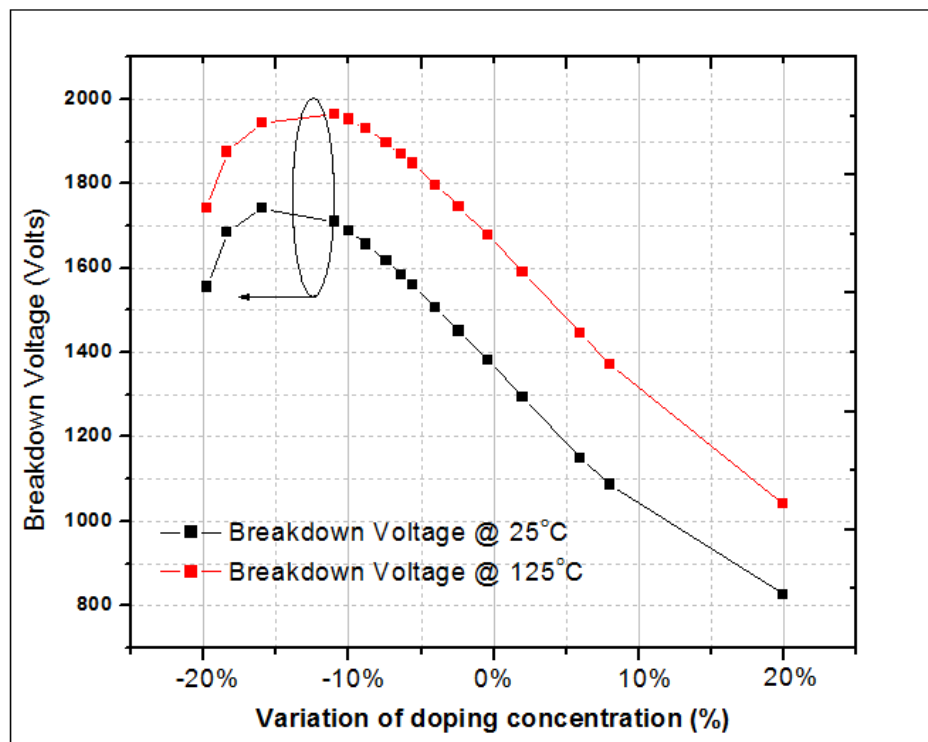
Figure 2-14: Variation of resistivity on the breakdown voltage of the device, Drift depth = 120µm, 0% variation = 1x10^{14} cm^{-3}, Carrier lifetime (τ) =10us

Figure 2-15: Variation of resistivity on the turn-off losses on the device, Drift depth = 120µm, 0% variation=1x10^{14} cm^{-3}, Carrier lifetime (τ) =10us

2.4   CONCLUSION

The results presented in this chapter demonstrate that a variation in substrate resistivity (at least within reasonable bounds expected within a controlled production environment) will not impact the device performance to any meaningful degree in terms of on-state voltage and switching performance. However a significant variation in substrate resistivity can lead to changes in the device properties across the cell, such as the breakdown voltage and turn-off losses as presented above.

This means that when devices are paralleled to form a power module, the mismatch in device properties can lead to premature failure of the power module. To avoid such behaviour, it would be prudent to conclude that the variation of resistivity should be as low as possible. Device manufacturers currently consider a substrate resistivity variation of less than 5% across the wafer. The results presented above justify this choice such that any variation in

device characteristics does impact the operation of the power module and the converter thereof.

2.5   REFERENCES

[2.1]   J. Hudgins, "Wide and narrow bandgap semiconductors for power electronics: A new valuation," *Journal of Electronic Materials,* vol. 32, pp. 471-477, 2003/06/01 2003.

[2.2]   C.P.Table, "Silicon Semiconductor Material," 3/26/2011.

[2.3]   P.S.Inc. (1996). *Silicon, Process Speciaities Inc.* . Available: http://www.processspecialties.com/siliconp.htm

[2.4]   S. Takasu, K. Homma, E. Toji, K. Kashima, M. Ohwa, and S. Takahashi, "Neutron transmuted magnetic Czochralski grown silicon wafer for power device," in *Power Electronics Specialists Conference, 1988. PESC '88 Record., 19th Annual IEEE*, 1988, pp. 1339-1345 vol.2.

[2.5]   S. I. Standard, "SEMI MF523-1107 (Reapproved 1012) - Practice for Unaided Visual Inspection of Polished Silicon Wafer Surfaces," ed, 2012.

[2.6]   P. S. Inc. (1996, 10/11/2010). Silicon. Available: http://www.processspecialties.com/siliconp.htm

[2.7]   B.J.Baliga, "Gate Enhanced Rectifier.," U.S. Patent Patent 4,969,028, November 6th 1990, 1980.

[2.8]   M. Harada, T. Minato, H. Takahashi, H. Nishihara, K. Inoue, and I. Takata, "600V trench IGBT in comparison with planar IGBT - an evaluation of the limit of IGBT performance," *IEEE International Symposium on Power Semiconductor Devices & ICs,* pp. 411-416, 1994.

[2.9]   R. Hotz, F. Bauer, and W. Fichtner, "On-state and short circuit behaviour of high voltage trench gate IGBTs in comparison with planar IGBTs," in *Power Semiconductor Devices and ICs, 1995. ISPSD '95. Proceedings of the 7th International Symposium on*, 1995, pp. 224-229.

[2.10] H. Iwamoto, H. Kondo, S. Mori, J. E. Donlon, and A. Kawakami, "An investigation of turn-off performance of planar and trench gate IGBTs under soft and hard switching," in *Industry Applications Conference, 2000. Conference Record of the 2000 IEEE*, 2000, pp. 2890-2895 vol.5.

[2.11] M.S.Power, "Using IGBT Modules," 1998.

[2.12] P. E. Jonathan Dodge, "Technology to the Next Power," in *IGBT Technical Overview, Distinguishing Featuresm, Application Tips*, ed, 2004.

[2.13] Y. Mizuno, R. Tagami, and K. Nishiwaki, "Investigations of inhomogeneous operation of IGB under Unclamped Inductive Switching condition," in *Power Semiconductor Devices & IC's (ISPSD), 2010 22nd International Symposium on*, 2010, pp. 137-140.

[2.14] B. J. Baliga, *Fundamentals of Power Semiconductor Devices*: Springer, 2010.

[2.15] A. R. Hefner and D. L. Blackburn, "A Performance Trade-Off for the Insulated Gate Bipolar Transistor: Buffer Layer Versus Base Lifetime Reduction," *Power Electronics, IEEE Transactions on,* vol. PE-2, pp. 194-207, 1987.

CHAPTER THREE

EVALUATION OF 3.3kV PLANAR CIGBT IN NON-PUNCH THROUGH TECHNOLOGY

3.1   INTRODUCTION

MOS controlled bipolar devices such as IGBTs are commercially available for a blocking voltage range of up to 6.5kV [3.1]. Beyond 3.3kV, IGBTs begin to compete with Gate turn-off thyristor (GTOs) and it becomes increasingly important to optimise their performance, both in terms of their on-state and switching losses.

In this chapter, a 3.3kV rated CIGBT (Clustered Insulated Gate Bipolar Transistor) with planar gates in Non Punch Through technology (NPT) with Rapid Thermal Annealing (RTA) anode, is evaluated. The benefits of using an RTA anode structure as compared to a diffused anode structure in an NPT technology are discussed. Previously it has been shown [3.2], that for identical turn-off losses, the on-state voltage of a 3.3kV NPT-CIGBT was 2.3Volts which is less than 0.7 Volts as compared to that of a commercially available Field Stop(FS) IGBT. In this chapter, the optimisation of the switching performance of the device is addressed by using a RTA anode structure. This approach maintains a similar on-state voltage as that of a diffused anode structure. This chapter also evaluates the various structural parameters of the MOS clusters located within the P-WELL region and the variation of the N-WELL implant dose.

3.2   TRANSPARENT ANODE DESIGN

The turn-off and on-state conduction losses of Silicon based MOS controlled bipolar structures can be optimised by using various methods. The traditional approach to reducing the switching losses in the device is based on reducing the lifetime of the carriers in the drift region to accelerate the recombination of the stored charge. This method has been widely

adopted by industry. However, this increases the on-state voltage of the device considerably, as less stored charge is now available for forward conduction. The second method used by semiconductor manufactures to reduce switching losses is to employ a thinner and lightly doped anode/collector region. This method is commonly referred to as the Transparent Anode Structure or a Transparent Emitter Structure since the anode or the collector region behaves as an emitter, to inject minority carriers into the drift region. To aid this discussion, a schematic cross section of a representative CIGBT structure along with its equivalent circuit is shown in Figure 3-1.
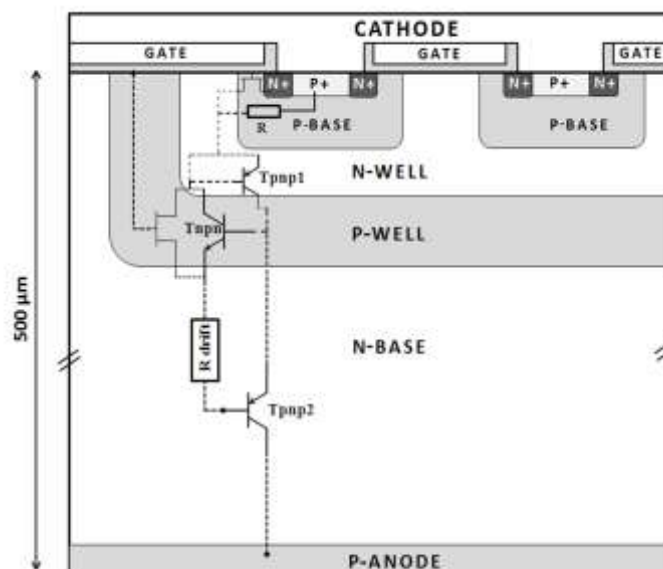
Figure 3-1: A schematic of the NPT-CIGBT cell along with its equivalent circuit.

In the on-state, the P-ANODE region and N-BASE junction is forward biased and the electrons flowing from the cathode side are injected into the P-ANODE region where they recombine. In a transparent anode structure, the electrons injected into the P-ANODE region diffuse to the collector contact without significant recombination within the P-ANODE region. Since the thickness of this region is set to be much shorter than the diffusion length the electron concentration at the contact can be assumed to be zero as the recombination rate would be significantly higher due to an ohmic contact. The use of such a transparent anode

does not reduce the on-state voltage of the device considerably as a high-level lifetime is maintained in the drift region. However, the turn-off losses of the device are reduced considerably as there is less stored charge in the drift region during the turn-off phase.

3.3 DEVICE STRUCTURE AND OPERATION

CIGBT is a three terminal MOS controlled thyristor which has been experimentally demonstrated at 1200V 1700V, 3300V ratings [3.2] [3.3] [3.4]. A schematic cross section of a typical CIGBT structure was shown previously in Figure 3-1 The CIGBT consists of a number of closely packed MOS cells enclosed within floating N-WELL and P-WELL layers to form clusters. Within each cluster, the P-bases can be arranged as squares, stripes or circles. A number of these clusters form the overall device active area. The influence of the number of clusters on the on-state and turn-off performance of the device is discussed in [3.5].

The operating mechanism of a CIGBT has been discussed in literature many times [3.6] [3.7] and has been summarised here for clarity. The MOS gate which extends over the P-WELL region acts as a turn-on gate and the rest of the MOS gates act as control gates. All the gates are electrically connected together to form a three terminal structure. When a positive voltage is applied to the gate with respect to the cathode terminal an inversion layer is created underlying the gate region. The threshold voltage of the structure is adjusted based on the concentration of the P-base, and is designed similar to the IGBT cells for comparison. The creation of the inversion layer grounds the N-WELL and N-BASE region via the inversion and accumulation regions. The P-WELL region is floating under this condition and is capacitively coupled to anode. Therefore, the potential of the P-WELL region increases with the anode potential. When the potential drop across the P-WELL / N-WELL junction rises above the built in potential, the thyristor formed by the P-ANODE/N-BASE/ P-WELL/ N-

WELL regions is triggered without a snapback. In the conduction mode of operation, the P-BASE/N-WELL junction is reverse biased and as the anode voltage increases, the depletion region of this junction extends towards the N-WELL region resulting in punch through at a predefined voltage. Once punch though has occurred the potential of this region does not increase anymore and any further increase in the anode potential is dropped across the P-WELL and N-BASE regions. This prevents high electric field from reaching the cathode region. The anode voltage at which the punch through occurs is known the Self-clamping voltage (Vscl). Self-clamping also helps to limit the saturation current density (Jsat) [3.7] and realise fast switching. CIGBT therefore provides a complete MOS gate control over thyristor conduction mode.

3.4   EXPERIMENTAL RESULTS

For this study, research dies rated at 50A and 6A with dimensions of 12.5x12.5 mm^2 and 7x7 mm^2 respectively were fabricated in 4", 300 Ω cm, 500μm thick Silicon wafers as shown in Figure 3-2. The active areas for the 6A and 50A devices are 10.8mm^2 and 94.2mm^2 respectively.
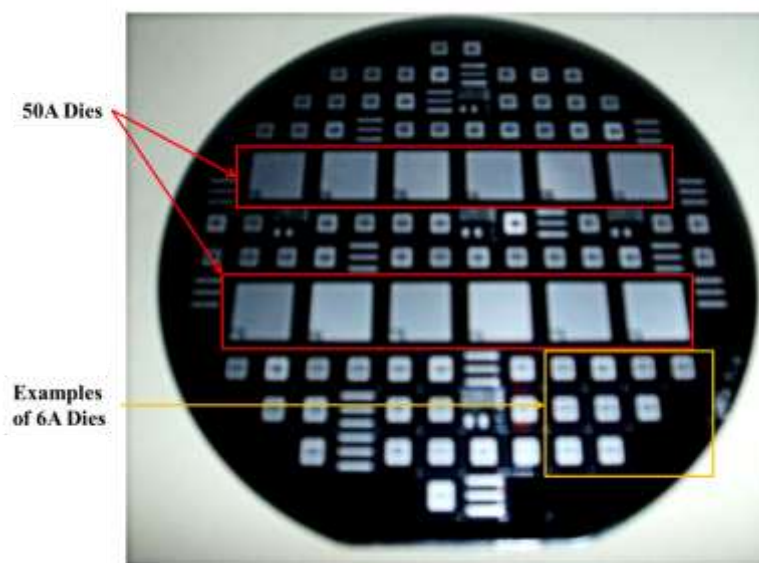
Figure 3-2: A fabricated wafer showing devices rated 50A and 6A. The layout contains several CIGBT and IGBT designs for comparison

The 6A devices were packaged in a TO-247 package for further experimental evaluation. The results presented below refer to the 6A samples only. The series of 6A packaged devices contain a progressive variation of the N-WELL doping concentrations, and all devices have an RTA anode structure. Figure 3-3 show the doping profile obtained by Spreading Resistance Profiling plots for the 3.3kV NPT CIGBT structure. The anode implant dose is 1×10^{12} at 40keV.
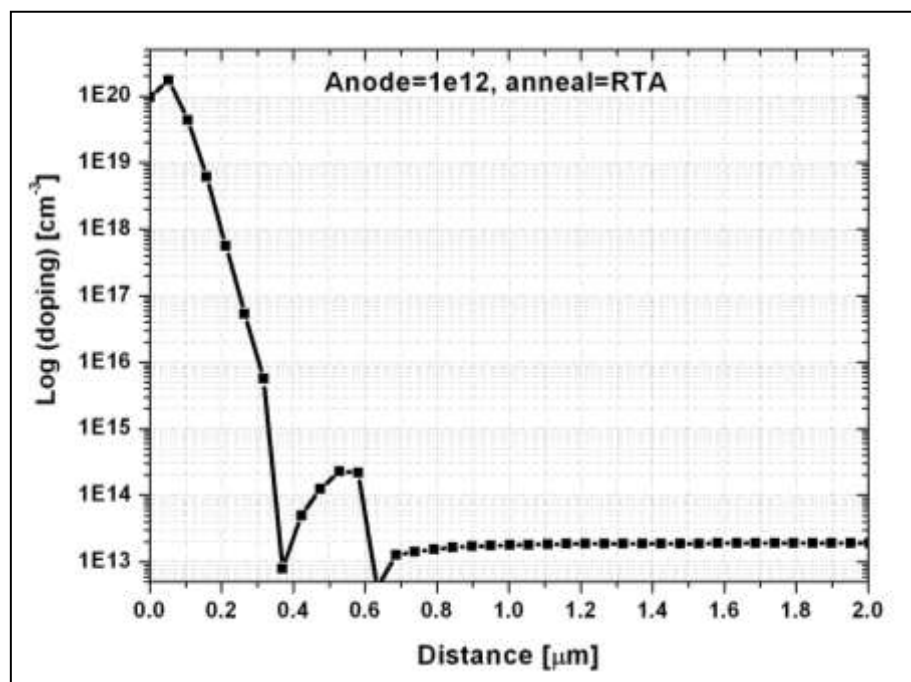
Figure 3-3: SRP plots for the 3.3kV NPT anode structure of 1×10^{12} @ 40keV

3.4.1   FORWARD BLOCKING VOLTAGE

The devices were simulated using a two dimensional numerical simulator TSUPREM^{TM} and MEDICI^{TM}. The device parameters used for simulation are provided in Appendix A2. The breakdown voltage for the devices have been optimised by carefully optimizing the implant energy dose and diffusion time of the P-WELL, N-WELL, P-base and the termination region. Figure 3-4 shows the simulated electric field profile across the CIGBT in the off state at 3.3kV, with the peak electric field supported across the P-WELL N-drift junction. The

simulation results show that for a blocking voltage of 3.3kV, the depletion region does not reach the anode nor penetrate through the P-WELL. The N-WELL region under the P-base is depleted at low anode voltages (≈13-15V), and remains in this "self-clamping" mode until the device turns-on again. Hence, it is the P-WELL/N-drift junction that is used to support high anode voltages. The polyamide passivation edge termination used in the devices is a novel guard ring structure made of a combination of deep P-WELL and P-base implants, as in the CIGBT main structure [3.8]. The guard ring structure is optimised, such that the peak surface electric field not exceed the critical field strength at any point in time. The maximum breakdown voltage for the fabricated structures (BV) was measured to be greater than 3.6kV at room temperature for all the devices.
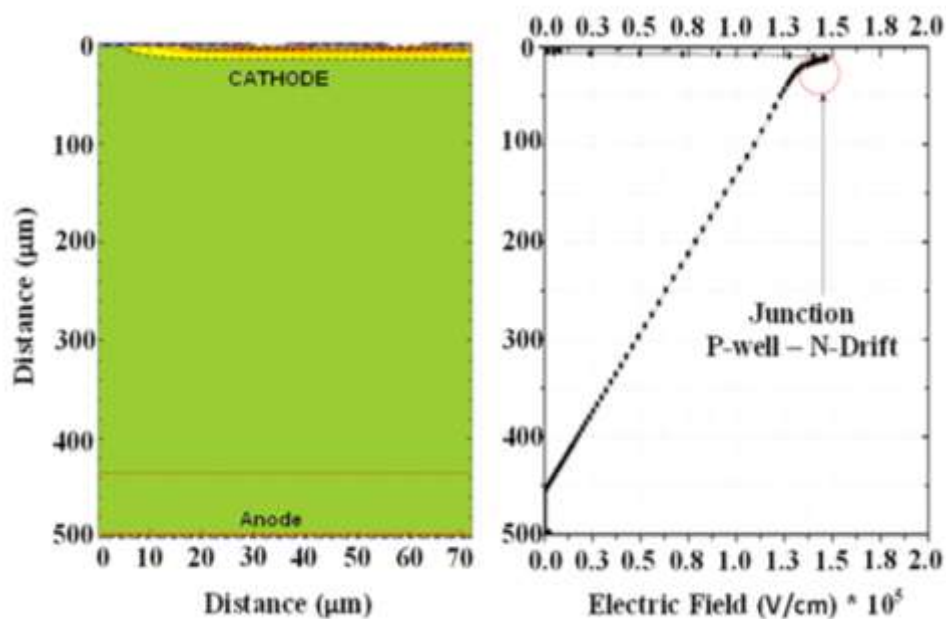
Figure 3-4 : Simulated electric field profile across the 3.3kV NPT-CIGBT, Anode Voltage=3.3kV, Drift depth=500μm

3.4.2   ON-STATE PERFORMANCE

Figure 3-5 shows the variation in current density with anode voltage for a typical sample that was measured using a Tektronix 371B curve tracer. This illustrates that the CIGBT exhibits a

snap-back free turn-on and its Vce(sat) has a positive temperature coefficient. The temperature co-efficient of on-state voltage at 125°C is some 1.39 times the value at 25°C. Figure 3-5 further shows that the saturation current density of the CIGBT can be controlled to 4 times its rated current at 125°C. This is necessary to enhance the short circuit performance of the device.
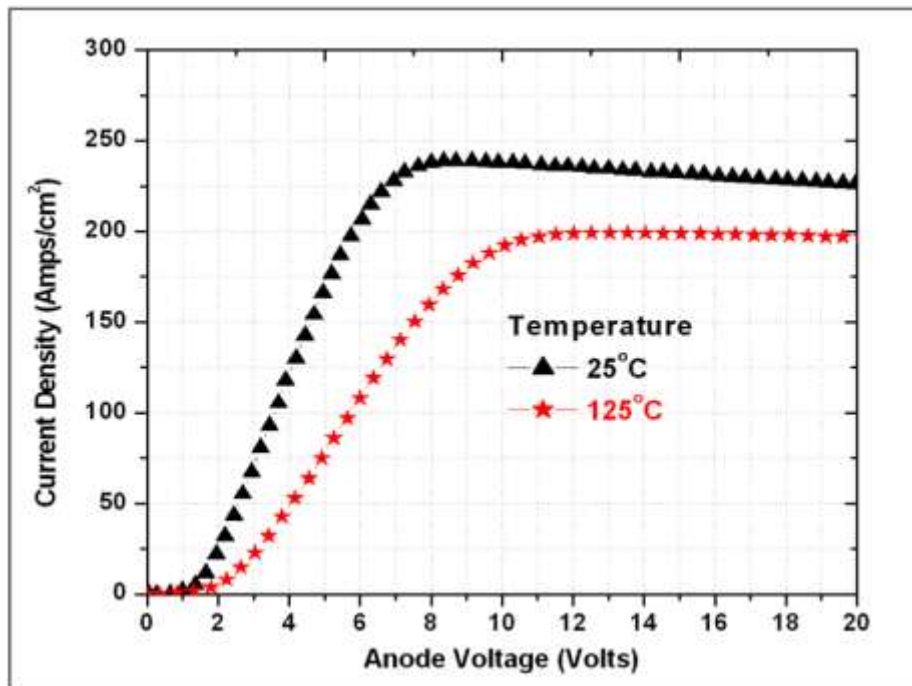
Figure 3-5: Typical experimental CIGBT on-state I (V) at 25°C and 125°C, Vg=+15V

Figure 3-6 shows the variation in current saturation at high gate voltages, measured using Tektronix 371B curve tracer. The enhanced current saturation capability of the CIGBT as compared to any other known MOS controlled thyristor, is due to its 'self-clamping' feature which limits the potential within the MOS clusters and prevents premature breakdown of the N-channel MOSFETs [3.6] [3.9]. The lower Vce(sat) of a CIGBT is because its on-state conduction is via a controlled thyristor action rather than the pnp transistor in the IGBT [3.6]. The thyristor action allows more charge to be injected into the drift region, in turn allowing a higher conductivity modulation within the drift region. Figure 3-7 shows that the thyristor conduction in CIGBT results in excellent conductivity modulation within the cathode area of

the device, which is more than twice that of an equivalent rated IGBT. Apart from exhibiting a low Vce(sat), another very important feature of CIGBTs is that the current saturation level can be controlled to only few multiples of the rated current.
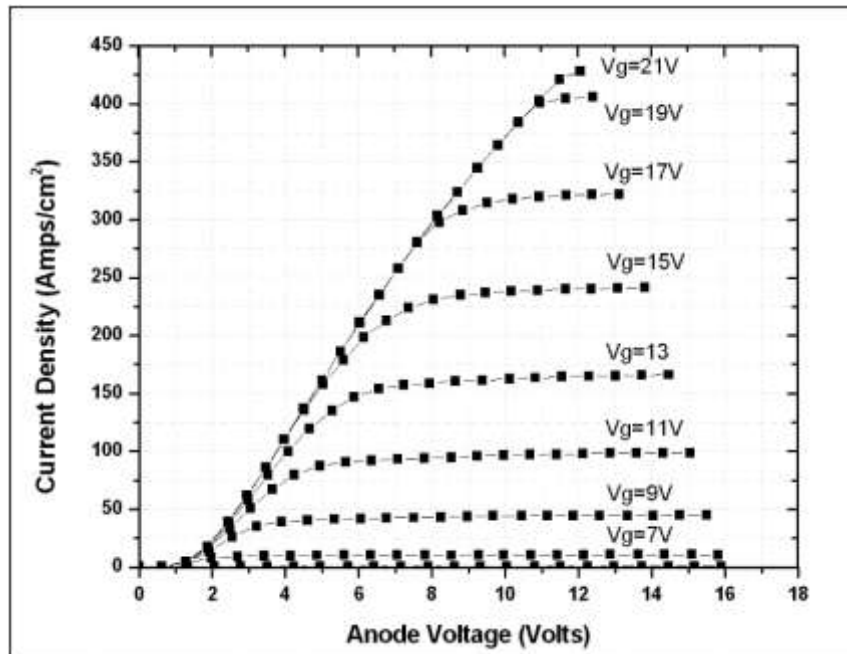
Figure 3-6: Experimentally measured CIGBT current saturation characteristics Vth = 5.5V, Tj= 25°C
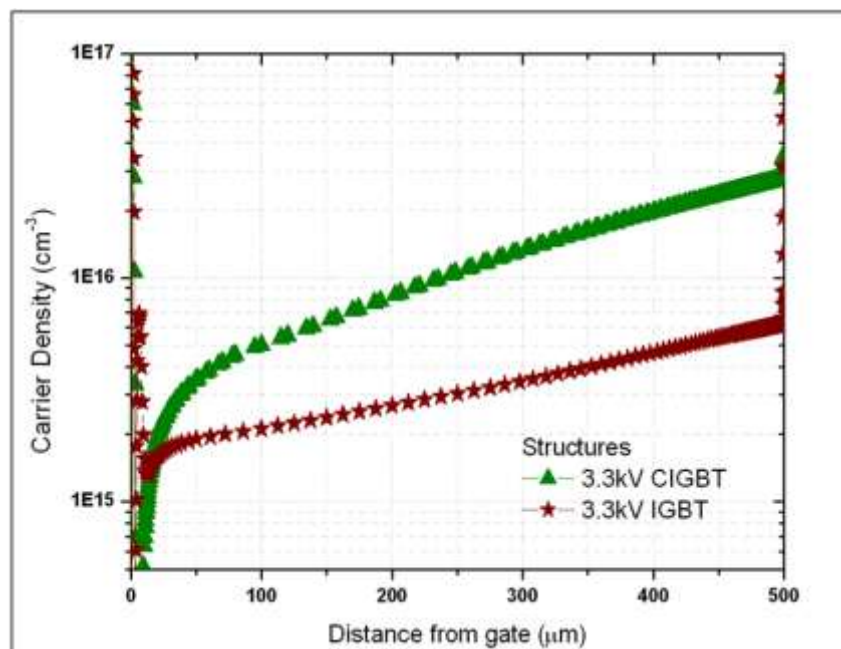
Figure 3-7: Simulated carrier density profile within the CIGBT compared with IGBT at $J_A = 50Acm^{-2}$

3.4.2.1 INFLUENCE OF CATHODE CELL GEOMETRY

It has been previously shown in [3.4] that the P-base spacing in the NPT-CIGBT has a minor influence on its V_{ce}(sat) because its N-WELL doping is in the region of 10^{16} cm^{-3}[3.4]. It has also been shown in [3.2], that the circular geometric cell design leads to be slightly lower V_{ce}(sat) than that of a rectangular cathode cell geometry. The lower V_{ce}(sat) and higher J_{sat} for the circular cathode cell design can be explained in terms of area (A), and perimeter (P) (of the MOS channels). Figure 3-8 shows the layout of the circular and square designs. From equation 3.1 and 3.2 it can be said that the square cell design is 1.27 times larger as compared to the circular design.

$$\frac{A_{square}}{A_{Circle}} = \frac{4\,r^2}{\pi r^2} = 1.27 \qquad \text{.... (3.1)}$$

$$\frac{P_{square}}{P_{Circle}} = \frac{8r}{2\pi r} = 1.27 \qquad \text{.... (3.2)}$$
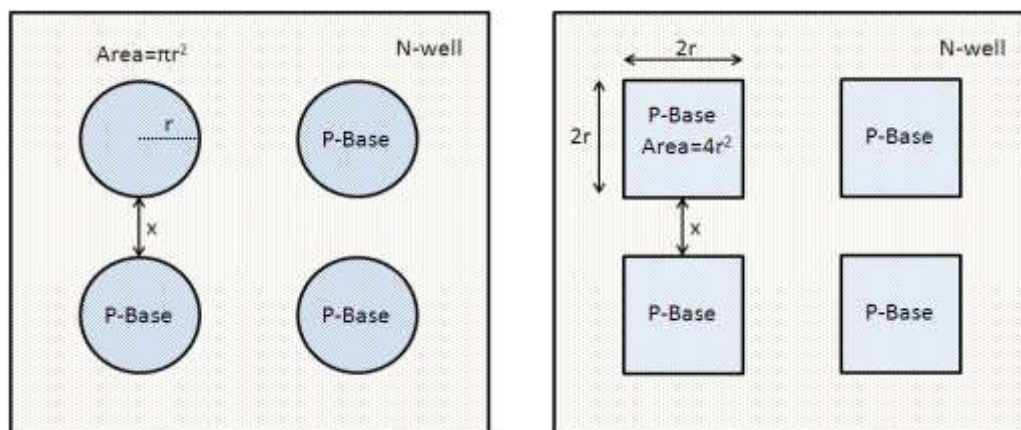
Figure 3-8: Schematic of the cathode cells showing the N-WELL and P-base circular and square designs in CIGBT

The smaller area of the circular design means that less N-WELL area is counter doped by the P-base, and its slightly shorter channel length ensures that there is more electron current than is the case with the square design. This results in an improved conductivity modulation, but at the expense of a higher J_{sat}.

3.4.2.2 INFLUENCE OF N-WELL IMPLANT DOSE

The N-WELL implant dose influences both, the on-state voltage and saturation characteristics of the devices as shown by the experimental measurement on the 6 A samples in Figure 3-9. These experimental results show that an improvement in the on-state performance can be achieved by using a higher N-WELL implant dose, as better conductivity modulation can be achieved by increasing the NPN (N-WELL/P-WELL/N-drift) gain of the thyristor. However, Increasing the N-WELL dose also increases the saturation current density of the device, which in turn will impact its short circuit capability and reduce its safe operating area (SOA).
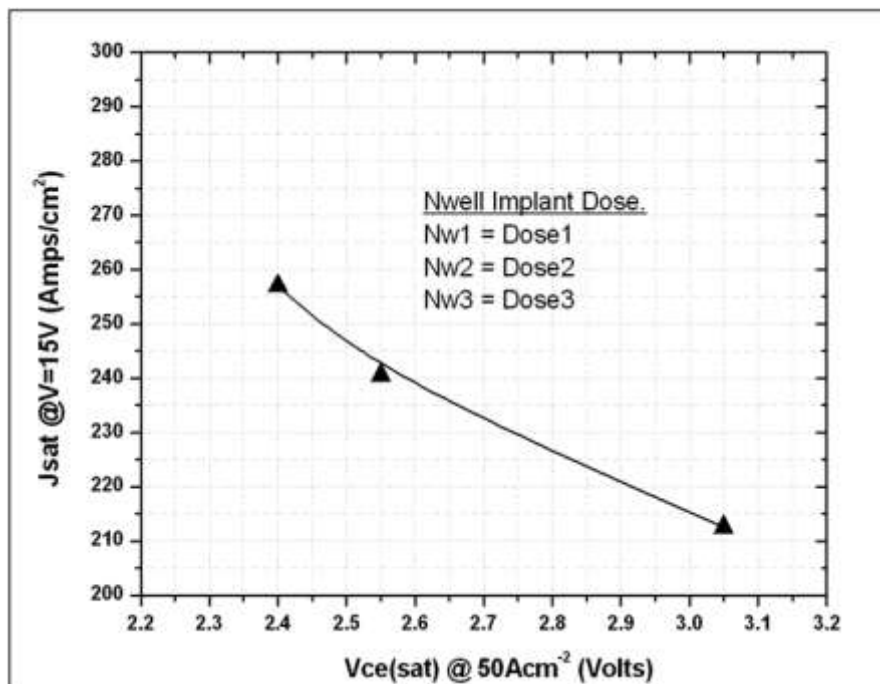
Figure 3-9: Experimental results on the influence of N-WELL dose (Nw1 (6.9e13) > Nw2 (6.7e13) > Nw3 (6.5e13)) on the on-state voltage Vce(sat) and saturation current density of CIGBT at 25°C

This behaviour arises because higher N-WELL dose increases the quantity of charge to be depleted, thereby increasing the self-clamping voltage. In addition, increasing the N-WELL concentration counter-dopes the P-base which can result in a reduction of the V_{th} (threshold voltage) of the device. Hence, careful consideration must be given to the level of N-WELL

implant dose. The amount of charge in the N-WELL is related to the self-clamping voltage

and is shown in equation 3.3 [3.10].

$$V_{scl} = \frac{(W_{n-well} - L_P)^2 q N_b}{2\varepsilon\varepsilon_0} \quad \dots (3.3)$$

Where Vscl is the punch through voltage, N_b is the N-WELL doping concentration, $W_{N\text{-WELL}}$

is the depth of N-WELL, L_p is diffusion length, q is the electronic charge, ε_o= permittivity of

free space and ε = permittivity of silicon, q= electron elementary charge.
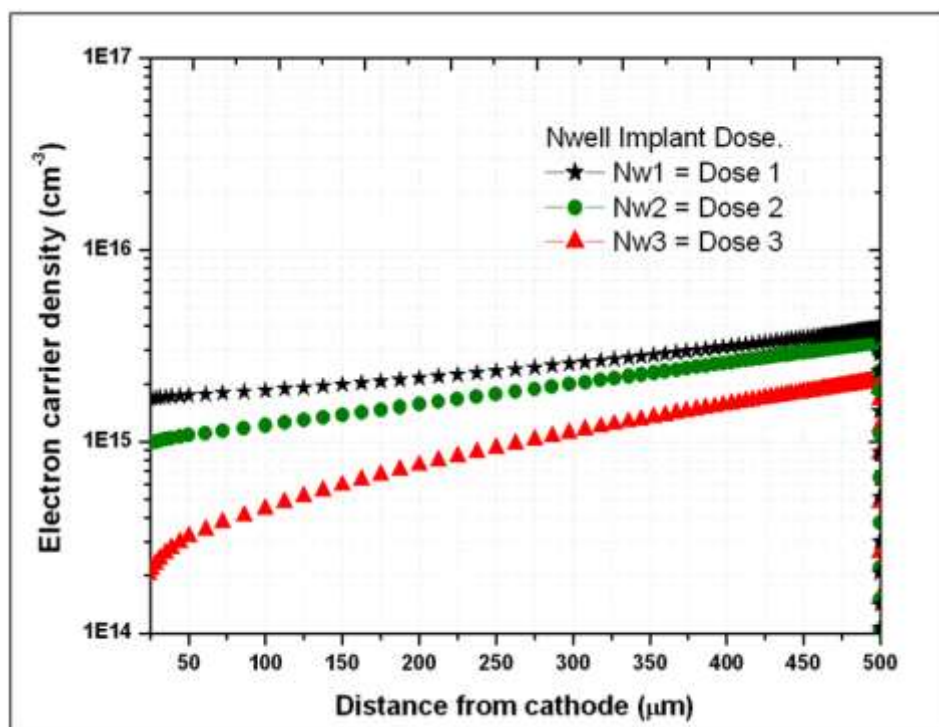
Figure 3-10: Simulated carrier density comparison of the 3.3kV CIGBT structure with variation of the N-WELL implant dose (Nw1 (6.9e13) > Nw2 (6.7e13) > Nw3 (6.5e13))

Figure 3-10 shows the simulated influence of the N-WELL implant dose on the carrier

density profile within CIGBT. The results clearly show that the thyristor conduction in

CIGBT can be improved as the N-WELL concentration is improved. Nw1 exhibits an order

of magnitude improvement in carrier concentration compared to Nw3. Figure 3-11 shows the

simulated influence of the N-WELL doping on the self-clamping voltage of the device. As

the N-WELL dose is increased, more voltage is required to deplete the N-WELL regions

between the P-base and P-WELL leading to higher self-clamping voltage and J_{sat} as discussed earlier in this section previously.
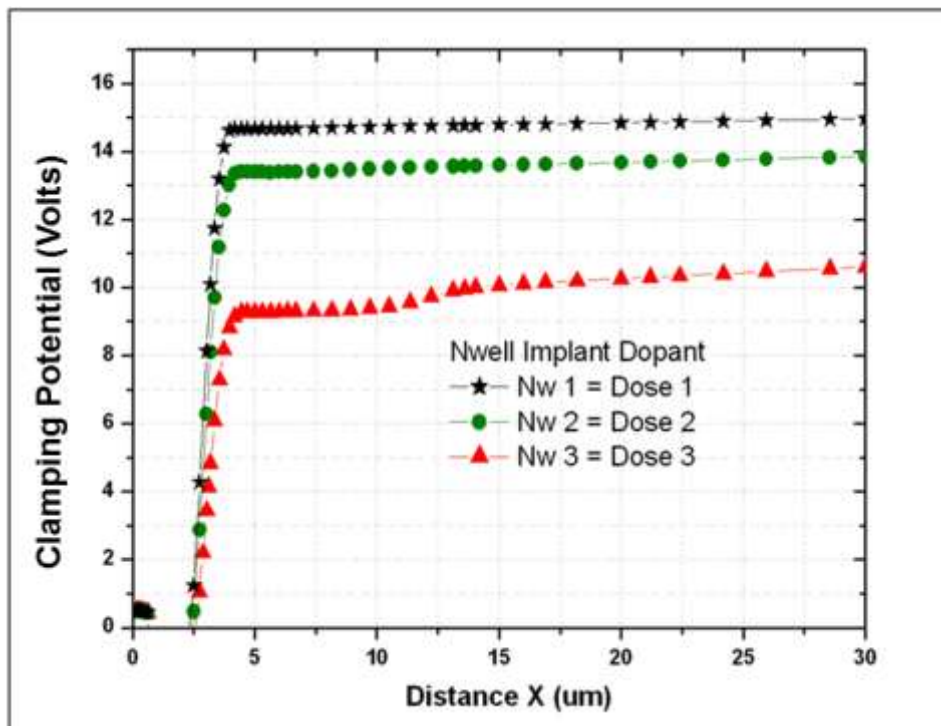
Figure 3-11: Simulated results showing the Influence of N-WELL dose (Nw1 (6.9e13) > Nw2 (6.7e13) > Nw3 (6.5e13)) on the self-clamping voltage of the CIGBT at 25°C

3.5   CLAMPED INDUCTIVE SWITCHING PERFORMANCE

Experimental snubberless inductive turn-off measurements were carried for in a typical chopper circuit arrangement. The typical chopper circuit used for testing is shown in Figure 3-12 and Figure 3-13 shows typical experimental CIGBT current and voltage waveforms at 25°C. The long current tails can be attributed to the thick (500um) drift region of the NPT devices. Furthermore, the lack of overshoot in the voltage waveform is an indication that the drift region is heavily flooded with carriers, which suggest that the anode implant can be optimized further. Figure 3-14 shows the benchmark results of the 3.3kV CIGBT using RTA anode against a commercially available FS-IGBT, the previous generation CIGBTs and NPT IGBT structures.
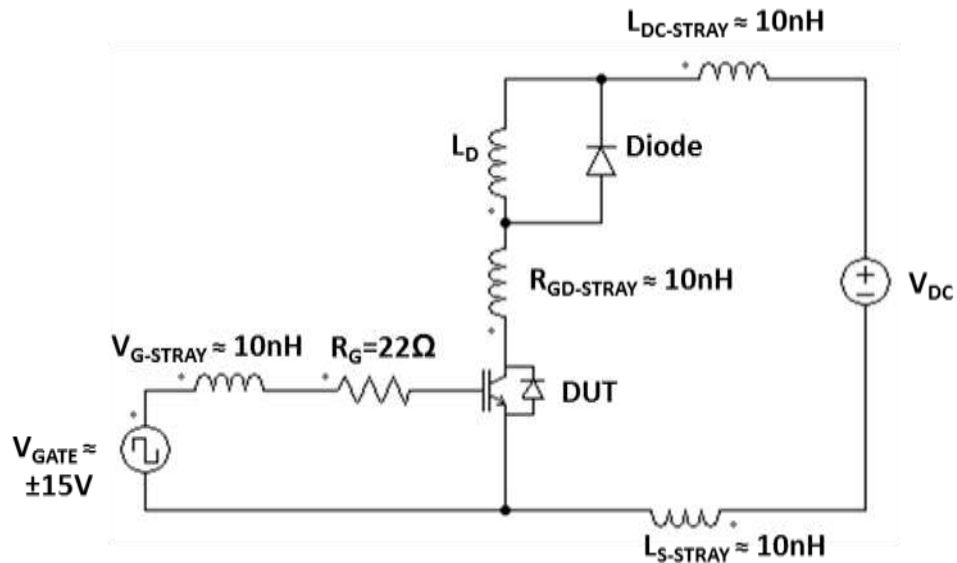
Figure 3-12: Typical chopper circuit used for testing
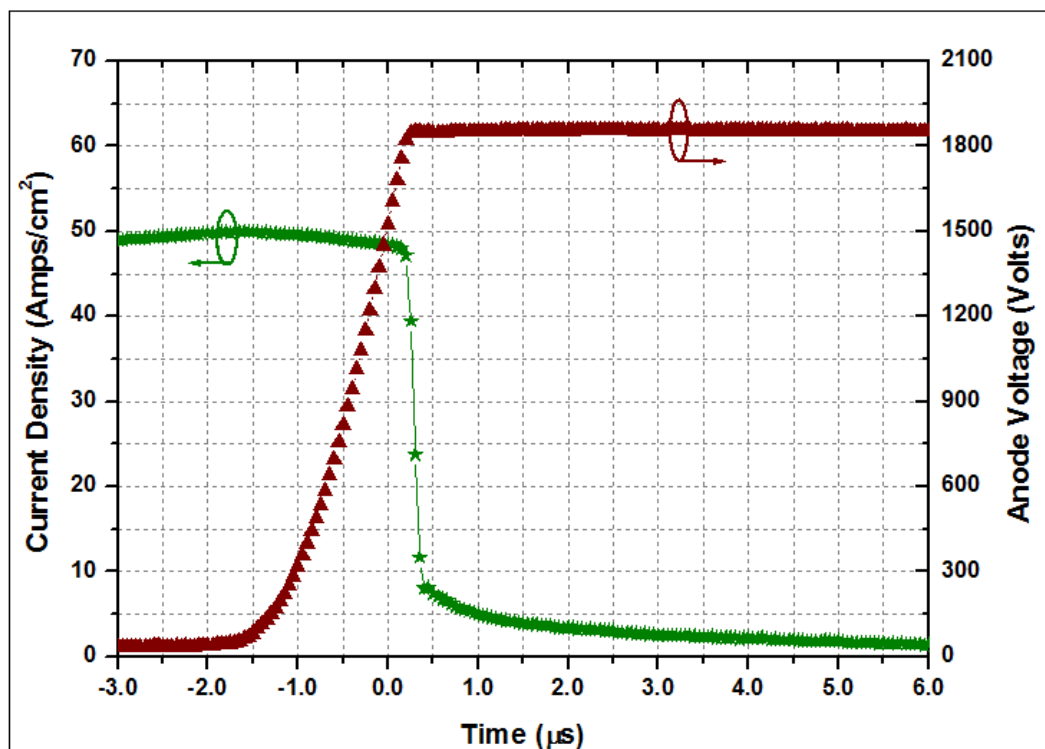
Figure 3-13: Typical measured CIGBT turn-off curves at 25°C (Rg = 22ohm, Vdd=1800V)

The Vce(sat)/Eoff trade-off curves show that the CIGBT with diffused anode technology can provide comparable turn-off energy loss to that of a corresponding IGBT, even though it's Vce(sat) is lower. However the energy dissipated on turn-off, Eoff, can be lowered by more

than 50% with RTA anode compared to diffused anode technology. Such levels are better than commercially available Field Stop-IGBT structures. The reduction in turn-off losses can be attributed to the reduced current tail due to a more transparent anode structure as discussed in section 3.2 of this chapter. The device provided by Company-A uses Field Stop technology and is thinner than the NPT devices. Therefore the use of Field stop technology in the RTA anode structure can boost the performance even more.
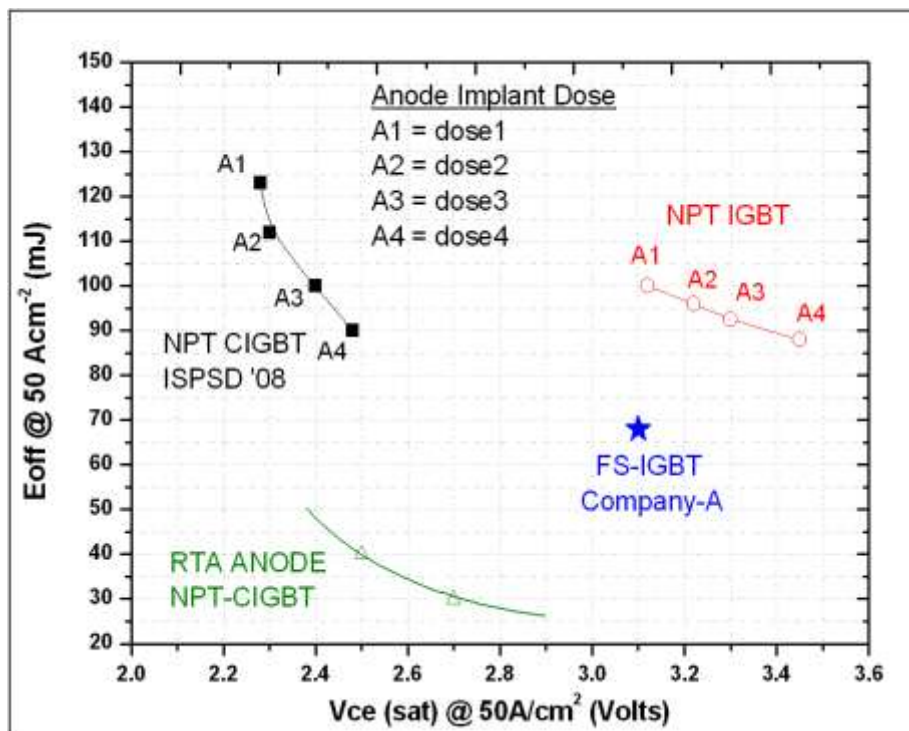
Figure 3-14: Comparison of experimental NPT-CIGBT and IGBT trade-off curves at 25°C.

A1>A2>A3>A4, Rg = 22Ω, Vdd = 1800V

The low turn-off loss in a CIGBT design can be explained as follows:-

The 'self-clamping' phenomenon which occurs when the anode potential is <20V is maintained throughout the turn-off process, and only disappears when the device turns on again. Hence, during turn-off, the holes which are collected within the P-WELL region flow to the cathode contact at the saturation velocity through the high electric field depleted N-WELL regions as shown in Figure 3-15. This mechanism is very efficient, and results in fast

turn-off speed and low turn-off loss (Eoff). Figure 3-16 show that the CIGBT with RTA anode can readily turn-off more than 3 times the rated current at 25℃. This indicates that the CIGBT can be used in rugged applications.
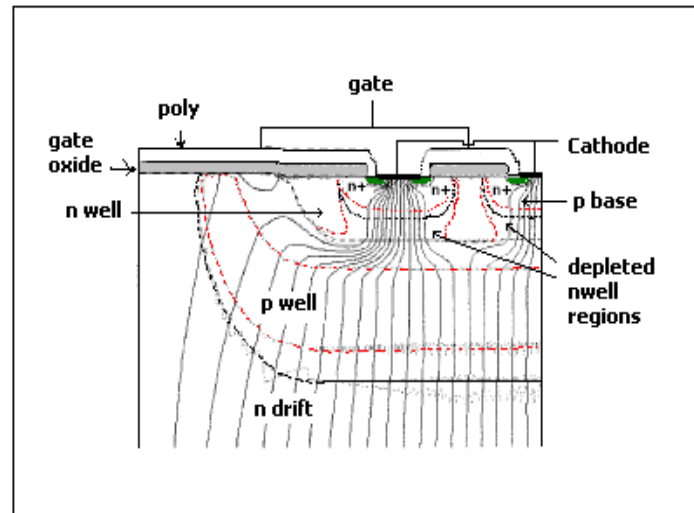
Figure 3-15: Simulated CIGBT current flow during turn-off showing holes flowing through the depleted N-WELL regions
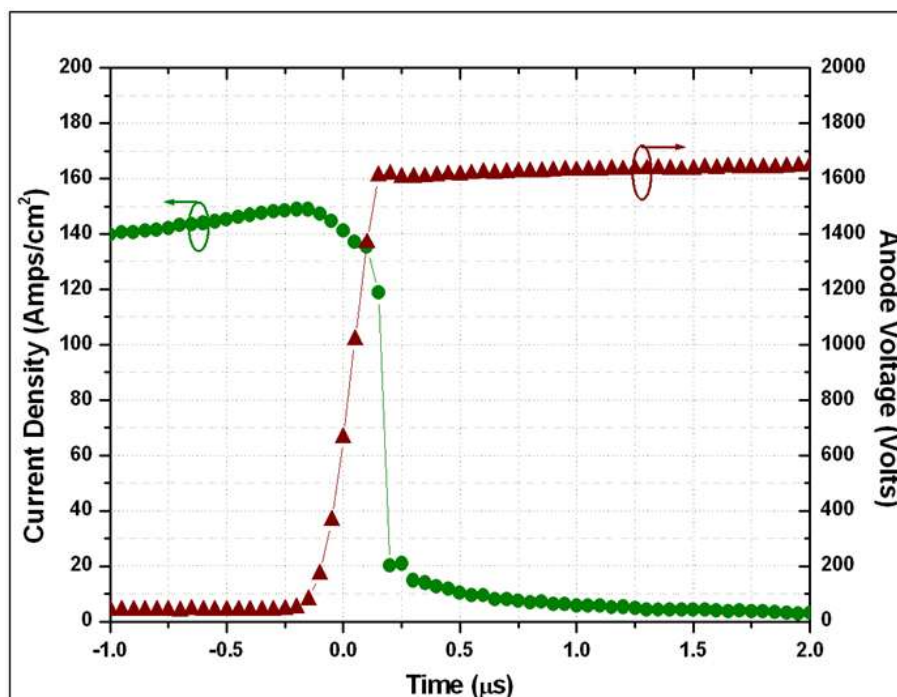
Figure 3-16: Typically measured CIGBT turn-off at 25°C (Rg = 100ohm, Vdd=1650V) for Vg=+15V

3.6   UNCLAMPED INDUCTIVE SWITCHING PERFORMANCE

The unclamped inductive switching (UIS) conditions are high stress switching conditions where the devices are subjected to high current and high voltage simultaneously, when the freewheeling diode in parallel with the load fails. The experimental test circuit for the UIS operating mode is shown in Figure 3-17. The load inductor is unclamped as there is no freewheeling diode to discharge the inductor energy when the device turns off.

Figure 3-18 shows the general waveforms that would be expected when a device is operated under UIS. The pulse on the gate of the device is applied over the interval t1 to t2. During this interval, the current will ramp up through the device and the inductor, reaching a peak value I_p. At time t_2, the device is turned off by reducing the gate voltage to 0V s. At this time, the energy stored in the inductor must be dissipated. However, the absence of the freewheeling diode means that the energy stored will be dissipated thought the device. This forces the device into its avalanche breakdown mode until the inductor is effectively fully discharged.
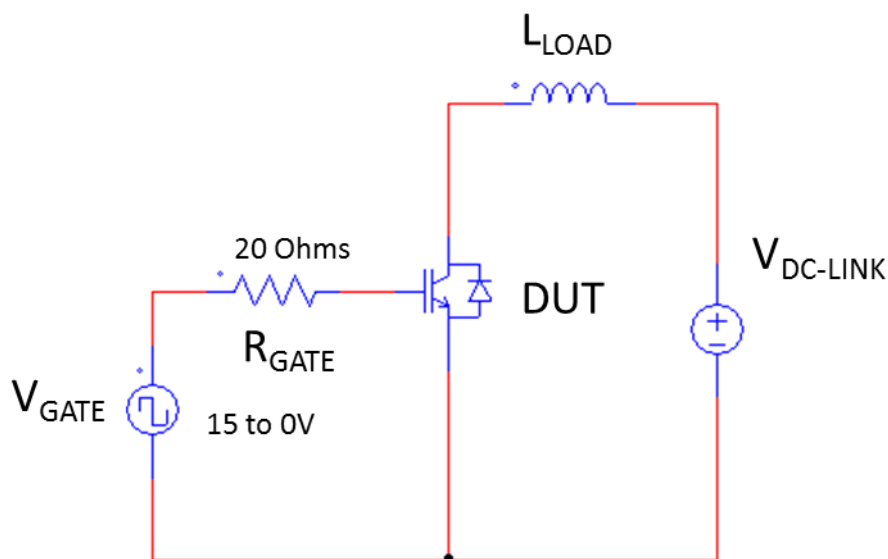
Figure 3-17: Test Circuit used to study the CIGBT behaviour under UIS
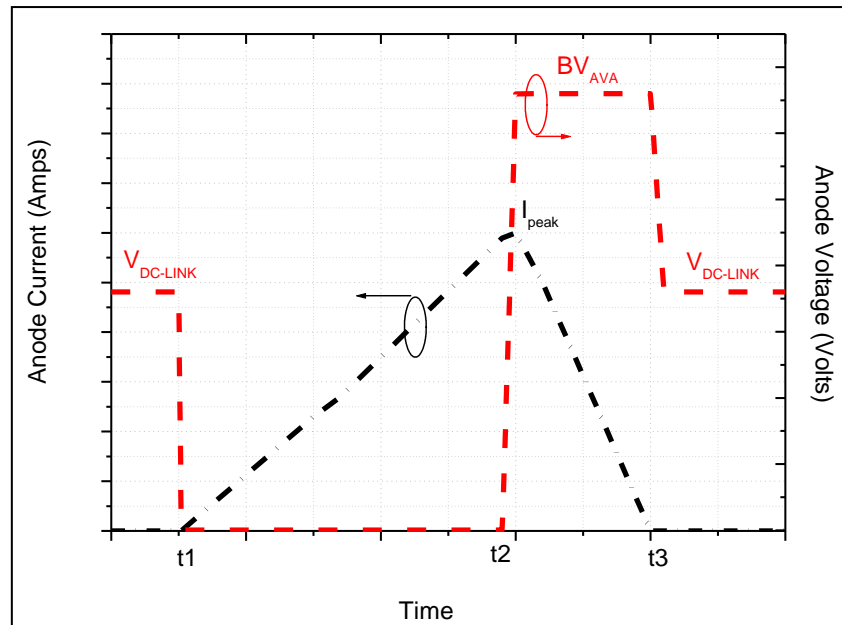
Figure 3-18: Anode current and voltage expected waveforms under UIS
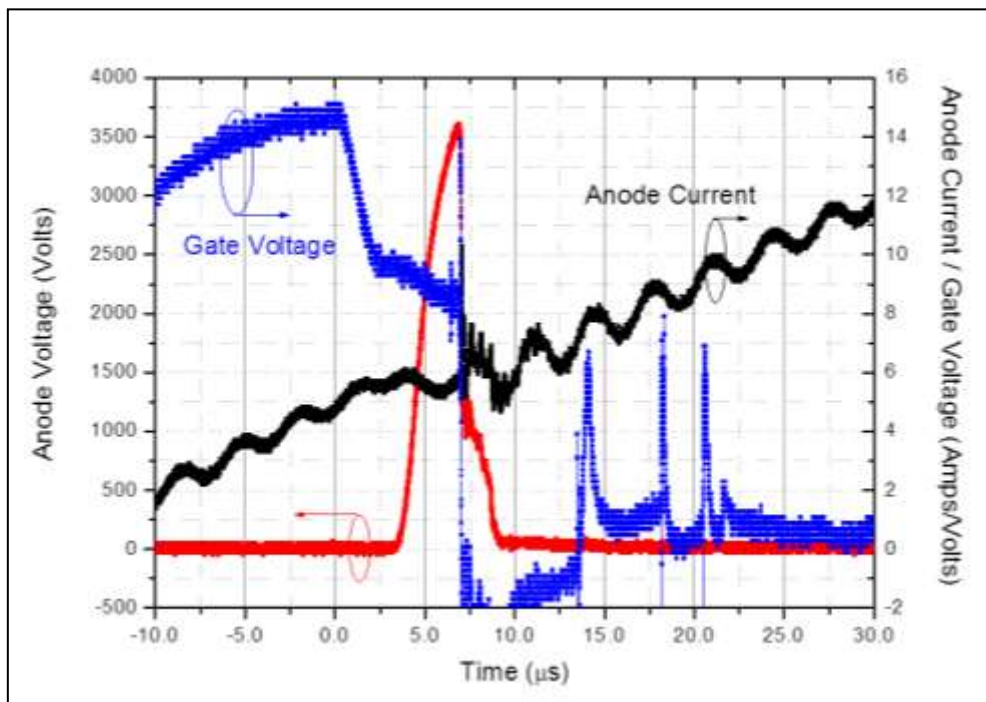
Figure 3-19: Typically measured UIS waveforms for CIGBT at 25°C (Rg = 100ohm, Vg=+15 to 0)

The values of the energy dissipated within the device can be calculated as shown in equation 3.4. Where, L = load inductor, Ip= Peak current, BV_{AVA} is the avalance breakdown voltage of the device, $V_{DC-LINK}$ is the DC-link voltage applied across the device.

$$E_D = \frac{1}{2}LI_p^2 * \left(\frac{BV_{AVA}}{BV_{AVA} - V_{DC-LINK}}\right) \quad \dots (3.4)$$

Figure 3-19 shows that the CIGBT under test is unable to withstand the UIS condition at full rated current. It can be seen that the anode current continues to ramp up as the device enters into avalanche mode. Various IGBT failure methods been reported in literature [3.11]. However, the main reason for the CIGBT failure under UIS is due to the variation of the poly-sheet resistance. This essentially means that the cells at the periphery of the device are not able to turn-off as quickly as those closer to the gate. This causes inhomogeneous current distribution within the device leading to device failure under UIS condition. Figure 3-20 shows the measured UIS waveforms when the anode voltage and peak current flowing through the device is reduced. Under this condition, the CIGBT is able to withstand the stress condition for a short period of time as the device enters into avalanche mode, allowing the cells in the periphery to turn-off quickly.
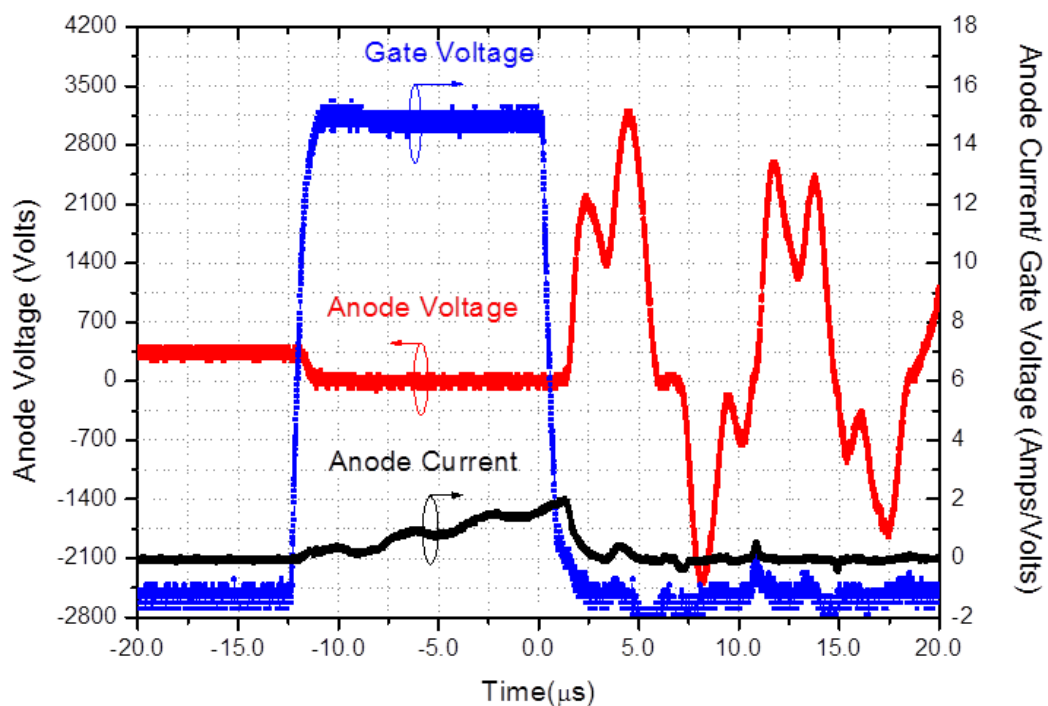
Figure 3-20: Measured UIS waveforms for CIGBT at 25°C (Vanode=400V, Rg = 100ohm, Vg=+15 to 0)

3.7   SHORT CIRCUIT PERFORMANCE

Figure 3-21 shows the typical circuit used to evaluate the short circuit performance of the device. Failure of a MOS controlled device under short circuit can occur under the following conditions:-

a) Destruction of the device during the application of the gate pulse (peak current failure)

b) Destruction of the device following the application of the gate pulse (steady state failure)

c) Destruction of the device at the end of the gate pulse (turn-off failure/Thermal runaway).

The most commonly observed failure for a well-designed device is after the application of the gate pulse and, conventionally, a minimum short circuit time of 10us is required for the system to recover from such an event. As it takes a finite time for the shoot through protection of the device to be triggered. The ability of CIGBT to internally clamp the N-WELL potential to a predetermined value allows it to achieve lower saturation current as compared to IGBT structures.
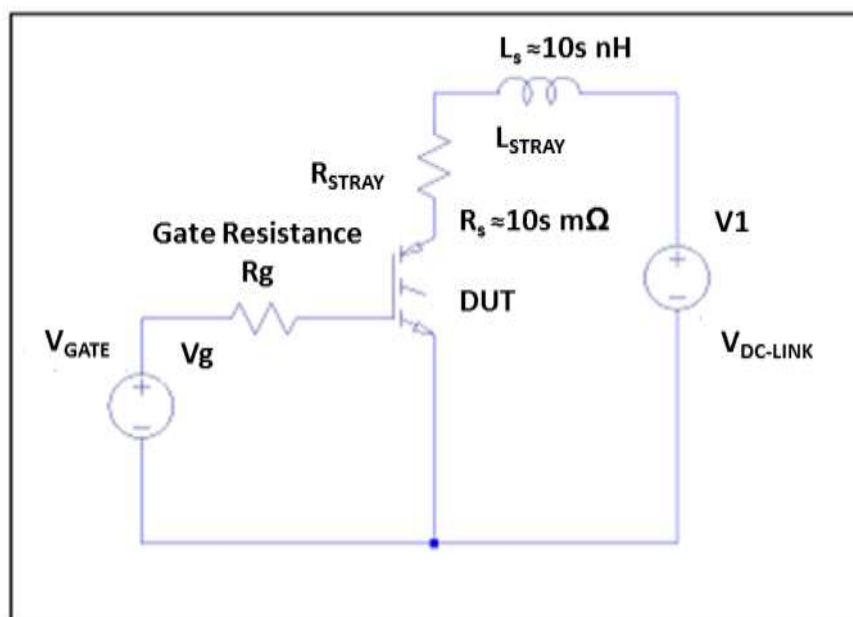
Figure 3-21: Experimental setup used to evaluate the short-circuit performance of the device

As the CIGBT has a low saturation current density, this ensures that the rate of heat generation and consequent temperature rise in the device is lower under short circuit condition than in an IGBT. Therefore, one could reasonably content that a CIGBT would be able to withstand higher short circuit durations.

The typical measured short circuit capability of the 3.3kV CIGBT at gate voltage of 15V at 25°C and 125°C is shown in Figure 3-22. The results show that the 3.3kV CIGBT can readily exceed the desired 10μs short circuit time. More importantly, it also shows that the CIGBT technology can successfully turn-off 4 times the rated current even at 125°C.
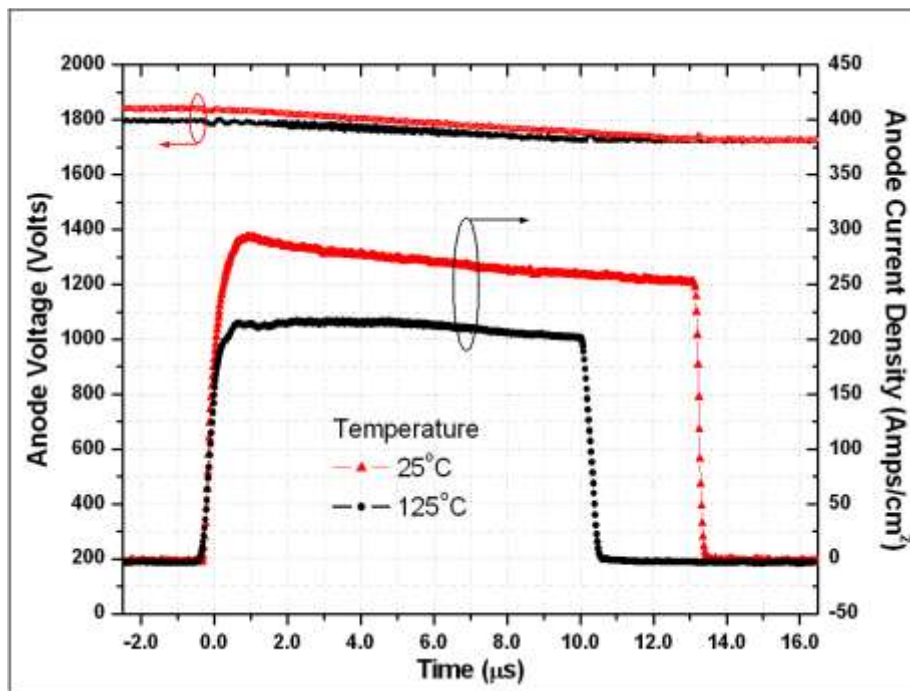
Figure 3-22: Typically measured CIGBT Short-circuit waveforms at 25°C and 125°C (Rg = 22ohm, Vdd=1800V) for a 6A rated device Vg=+15V

Figure 3-23 shows that the maximum short circuit duration for the 3.3kV CIGBT can exceed 100μs at 25°C, which is much higher than any MOS controlled bipolar device ever reported. This means that the otherwise expensive short circuit detection circuits required with other device types can be eliminated, leading to less complexity and increased reliability. However,

measured results also show that the anode voltage drops with time as the DC-link capacitors in the system are not able to maintain the voltage during the entire event. The maximum power dissipated in one cycle is calculated to be 3.36 Watts. Therefore, if the anode voltage is held at a constant value, the simulated short-circuit period for similar power dissipation is calculated to be over 80µs and is verified via simulations.
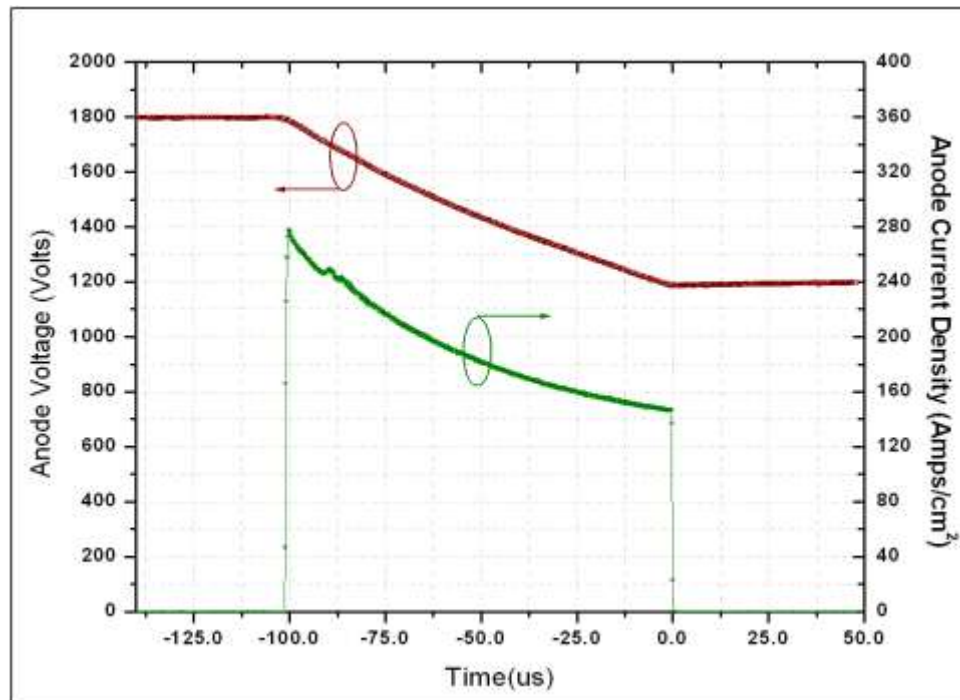
Figure 3-23: Maximum measured CIGBT Short-circuit waveforms at 25°C (Rg = 22ohm, Vdd=1800V) Vg=+15V

3.7.1 INFLUENCE OF GATE RESISTANCE

Figure 3-24 shows the influence of the gate resistance on the short circuit performance of the device more specifically that as the gate resistance is reduced, the current overshoot during the turn-on phase of the device is eliminated for all practical purposes. The overshoot appearing during the turn-on phase of the device when the gate voltage exceeds the threshold voltage is a consequence of the accumulation layer created underneath the planar gates,

which attracts holes. For a higher value of gate resistance, this causes a feedback effect into the gate leading to gate voltage amplification which in turn causes the anode current to rise.
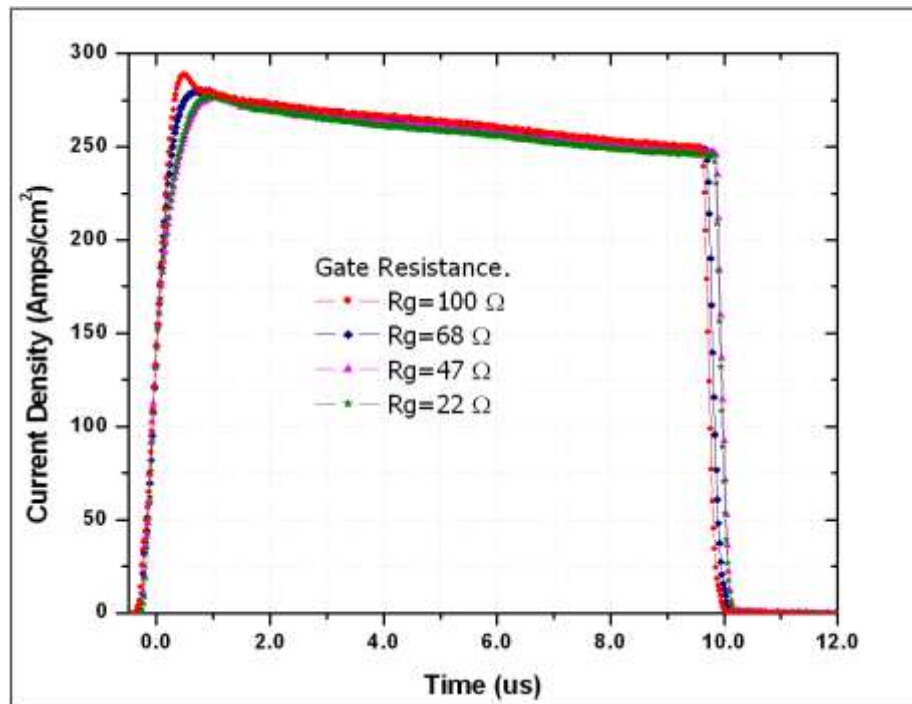
Figure 3-24: Typically measured CIGBT Short-circuit waveforms with variation of gate resistance at 25°C (Vdd=1800V)

3.8   CONCLUSION

In this chapter the work done towards the 3.3kV rated CIGBT is presented. The device fabrication, functionality and the experimental and simulation results are discussed in detail. The experimental and simulation results presented in this chapter clearly show how the optimisations of the CATHODE GEOMETRY, the N-WELL and ANODE doping concentrations have been performed. The experimental results also demonstrate that the 3.3kV rated CIGBT has many aspects of improved performance compared to an equivalent rated 3.3kV IGBT not only in terms of Vce(sat)/turn-off loss trade-off but also in terms of its short circuits performance. In addition, it has been shown that the use of RTA anode technology reduces the turn-off losses of the device by more 50% compared to diffused

anode technology. The experimental short-circuit evaluation of the device shows that the CIGBT can withstand a short circuit time of more than 10µs even at 125°C and has a maximum short circuit withstand capability of more than 100µs, a value which is much higher that any MOS controlled bipolar device even reported.

3.9   REFERENCES

[3.1]   M. E. Corporation, "CM750HG-130R - High Power Switching use Insulated Type," M. E. Corporation, Ed., ed: Mitsubishi Electric Corporation, 2013.

[3.2]   M. Sweet, N. Luther-King, S. T. Kong, E. M. S. Narayanan, J. Bruce, and S. Ray, "Experimental Demonstration of 3.3kV Planar CIGBT In NPT Technology," in *Power Semiconductor Devices and IC's, 2008. ISPSD '08. 20th International Symposium on*, 2008, pp. 48-51.

[3.3]   K. Vershinin, M. Sweet, L. Ngwendson, J. Thomson, P. Waind, J. Bruce, *et al.*, "Experimental Demonstration of a 1.2kV Trench Clustered Insulated Gate Bipolar Transistor in Non Punch Through Technology," in *Power Semiconductor Devices and IC's, 2006. ISPSD 2006. IEEE International Symposium on*, 2006, pp. 1-4.

[3.4]   K. Vershinin, M. Sweet, O. Spulber, S. Hardikar, N. Luther-King, M. M. De Souza, *et al.*, "Influence of the design parameters on the performance of 1.7 kV, NPT, planar clustered insulated gate bipolar transistor (CIGBT)," in *Power Semiconductor Devices and ICs, 2004. Proceedings. ISPSD '04. The 16th International Symposium on*, 2004, pp. 269-272.

[3.5]   K. Vershinin, M. Sweet, L. Ngwendson, and E. M. S. Narayanan, "Influence of the device layout on the performance of 20A 1.2kV clustered insulated gate bipolar transistor (CIGBT) in PT technology," in *Power Electronics, Electrical Drives, Automation and Motion, 2006. SPEEDAM 2006. International Symposium on*, 2006, pp. 275-278.

[3.6]   M. S. S. E. M. Sankara Narayanan, J. V. Subhas Chandra Base and M. M. De Souza, "Clustered insulated gate bipolar transistor (CIGBT) - a new power semiconductor device," presented at the IWPSD, 1999.

[3.7]   E. M. Sankara Narayanan, M. R. Sweet, N. Luther-King, K. Vershinin, O. Spulber, M. M. De Souza, *et al.*, "A novel, clustered insulated gate bipolar transistor for high power applications," in *Semiconductor Conference, 2000. CAS 2000 Proceedings. International*, 2000, pp. 173-181 vol.1.

[3.8]   J. V. S. C. B. M.M. De So-, E.M.S Narayanan, T.J. Pease, G. Ensell and J. Humphreys "A novel area efficient floating field limiting edge termination technique," *Solid State Electronics,* vol. 44, pp. 1381-1386 2000.

[3.9]   M. S. K.V. Vershinin, J.V. S.C Base, 0. Spulber, N. Luther-King, M. M. De Souza, S. Sverdlof E.M. Sankara Narayanan, D. Hinchley, I. Leslie, J. Bruce, "A novel. ultra-high performance 2.4kV clustered insulated gate bipolar transistor," *Power System World* 2001.

[3.10] V. K. Khanna, *The Insulated Gate Biploar Transistor (IGBT) Theory and Design.*: Wiley Inter-Science, 2003.

[3.11] G. Breglio, A. Irace, E. Napoli, M. Riccio, and P. Spirito, "Experimental Detection and Numerical Validation of Different Failure Mechanisms in IGBTs During Unclamped Inductive Switching," *Electron Devices, IEEE Transactions on,* vol. 60, pp. 563-570, 2013.

CHAPTER FOUR

SEGMENTED P-BASE CLUSTERED INSULATED GATE BIPOLAR JUNCTION TRANSISTOR

4.1. INTRODUCTION

This chapter evaluates the merits of incorporating a segmented P-base into a trench CIGBT structure to further improve the carrier concentration at the cathode side without degrading the short circuit capability and Eoff-Vce(sat) trade-off. The influence of the structural parameters of the segmented P-base device is investigated in detail using the two-dimensional numerical device simulator, MEDICI^{TM}. In addition, the functionality of the PMOS (turn-off gates) gate is also reviewed and discussed in detail.

4.2.   ELECTRON INJECTION EFFICIENCY

This section highlights the importance of carrier profile engineering in order to improve the performance of MOS control bipolar devices. To simplify the discussion, the p-i-n diode structure shown in Figure 4-1 provides a useful starting point. For this discussion, the intrinsic semiconductor region can be assumed to be the N-drift region of an IGBT while the P-type/N-type regions can be considered to be the anode and cathode ends respectively. The electron injection efficiency (γ_k), can be defined as the ratio of the electron current (J_e) to the total current density (J) at junction of the N-type emitter and the intrinsic semiconductor region. The total current density is a function of the eletron (J_e) and the hole current densities (J_h).

$$\gamma_k = \frac{J_e}{J} = \frac{J_e}{J_e + J_h} \qquad \dots (4.1)$$
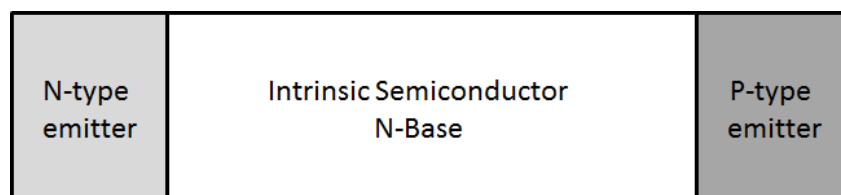
Figure 4-1: Schematic structure of a p-i-n diode

The cathode side carrier storage is controlled by the electrons injected from the cathode end of the device. Therefore higher the electron injected at the cathode side, higher is the stored carriers at the cathode end of the device. This property can be explained by a series of straightforward equations that govern the conductivity modulation of the device:

If we assume that the ambipolar condition is satisfied in the intrinsic layer in the conduction state, i.e. the hole and the electron density are the same in the intrinsic layer (h=e), the Einstein relationship shows that for a given concentration gradient, the diffusion coefficient for electrons and holes can be expressed as.

$$D_e = \frac{kT\mu_e}{q} \qquad \dots (4.2)\ [4.1]$$

$$D_h = \frac{kT\mu_h}{q} \qquad \dots (4.3)\ [4.1]$$

Where, k=boltzman constant, T=temperature, μ_e and μ_h is the mobility of electrons and holes

The electron and hole current densities are hence given by:

$$J_h = -q\mu_h n\frac{d\varphi}{dx} - kT\mu_h\frac{dn}{dx} \quad \dots (4.4)$$

$$J_e = -q\mu_e n\frac{d\varphi}{dx} + kT\mu_e\frac{dn}{dx} \quad \dots (4.5)$$

Combining the two equations and by eliminating $\frac{d\varphi}{dx}$ we get

$$\mu_h J_e - \mu_e J_h = 2\mu_e\mu_h kT\frac{dn}{dx} \quad ....(4.6)$$

By simplifying the equation further:

$$J\left(\gamma_k - \frac{\mu_e}{\mu_e + \mu_h}\right) = 2\frac{\mu_e\mu_h}{\mu_e + \mu_h} kT\frac{dn}{dx} \quad ....(4.7)$$

$$\gamma_k = \frac{J_e}{J_e + J_h} > \frac{\mu_e}{\mu_e + \mu_h} \quad ....(4.8)$$

This equation clearly shows that a high electron injection efficiency enhances the cathode side carriers with an increase of carrier profile slope $\frac{dn}{dx}$ in the N-type emitter base. The stored carriers at the cathode side are enhanced with an increase of the electron injection efficiency. Hence, by a combination of segmenting the P-base and reducing the width of the P-base with the inclusion of the PMOS gates, the total hole current extracted from the cathode end is reduced. This enhances the cathode side carrier storage, as the reduced hole current which is extracted automatically results in a higher electron injection efficiency [4.2].
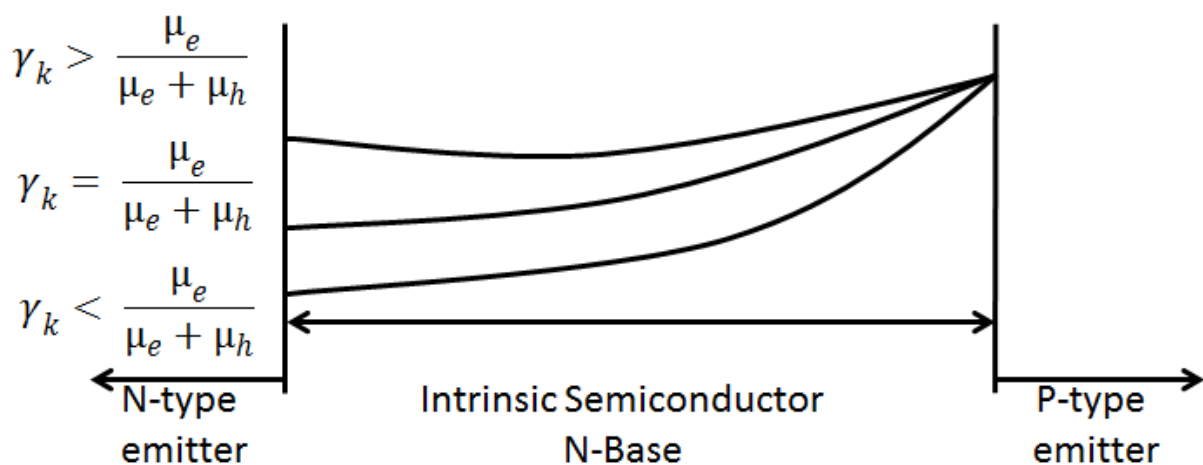
Figure 4-2: Change of stored carrier profile with electron injection efficiency

4.3. DEVICE STRUCTURE AND OPERATION

The schematic cross section of a conventional TCIGBT structure along with its equivalent circuit is shown in Figure 4-3. This structure is taken as the baseline for this study. The working of CIGBT, both in its planar and trench form, has been discussed in chapter 2 and widely in literature [4.3]. The operation of the structure has been also explained in section 3.3. Figure 4-4 shows the various implementations of the Segmented P-base structures that have been explored in this chapter. In this chapter, as illustrated in Figure 4-4, the segmented P-base structure will be referred to as - Type A, the segmented P-base structure with PMOS gates will be referred to as - Type B and the segmented P-base structure with deep PMOS and NMOS gates will be referred to as - Type C.
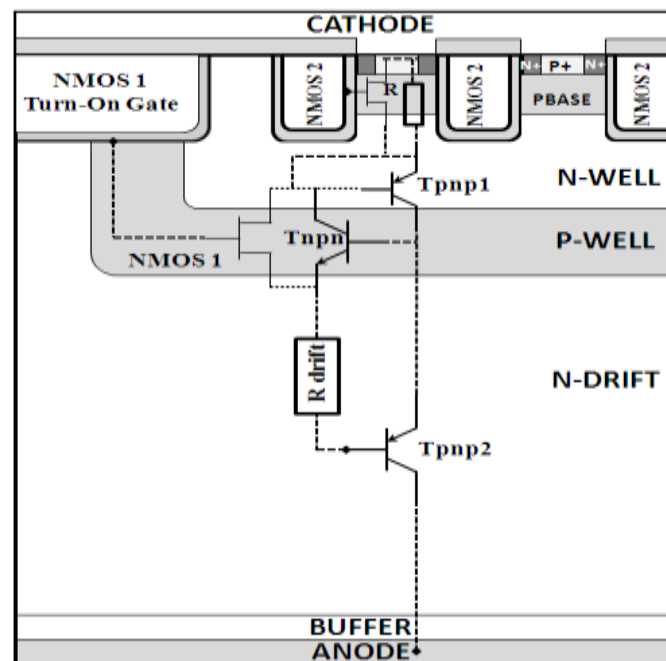
Figure 4-3 Schematic cross section of a conventional TCIGBT with its equivalent circuit

All the TCIGBT structures have the same channel length of 3µm and all gates electrically connected to each other. The structures described have a 120µm thick substrate with a doping density 8×10^{13} cm^{-3}. The trench pitch, which is the distance between adjacent NMOS2 trench gates, is 5µm and the NMOS 2 trench width is 2µm. The buffer depth is 5 µm with a peak

doping density of 1×10^{16} cm^{-3}. The doping profile across the various implementations of the TCIGBT structures has been shown in Figure 4-5.
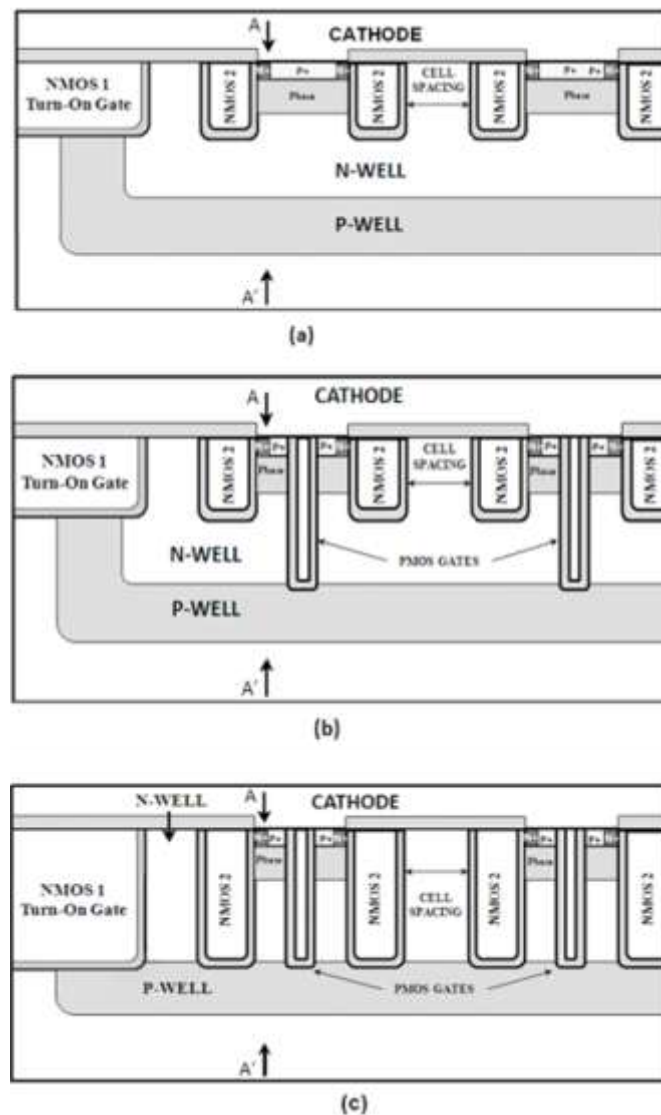
Figure 4-4: The various implementation of the TCIGBT structure with cell spacing (CS) (a) Type A: Segmented P-Base (b) Type B: Segmented P-Base with PMOS Gates, (c) Type C: Segmented P-Base with deep PMOS and deep NMOS gates

The mask layout of the fabricated device is shown in Figure 4-24. This structure can also be fabricated by using a hexagonal pattern to reduce the size of the NMOS1 turn-on gate, leading to an improvement in the packing factor of the device [4.4].

In the proposed structures, the cell spacing between the trench gates will form a part of the N-WELL. The NMOS 1 gate acts as a turn-on gate and has no control on the device once the main thyristor is turned on. The NMOS 2 gates acts as control gate and determines the threshold voltage of the device. The doping concentration of the P-base is adjusted to obtain the required threshold voltage. The PMOS gates in Type B and Type C structures are used to improve the on-state performance of the device by achieving carrier constriction and they turn-on only during the turn-off cycle of the device by providing a path for hole extraction from the n-drift region.
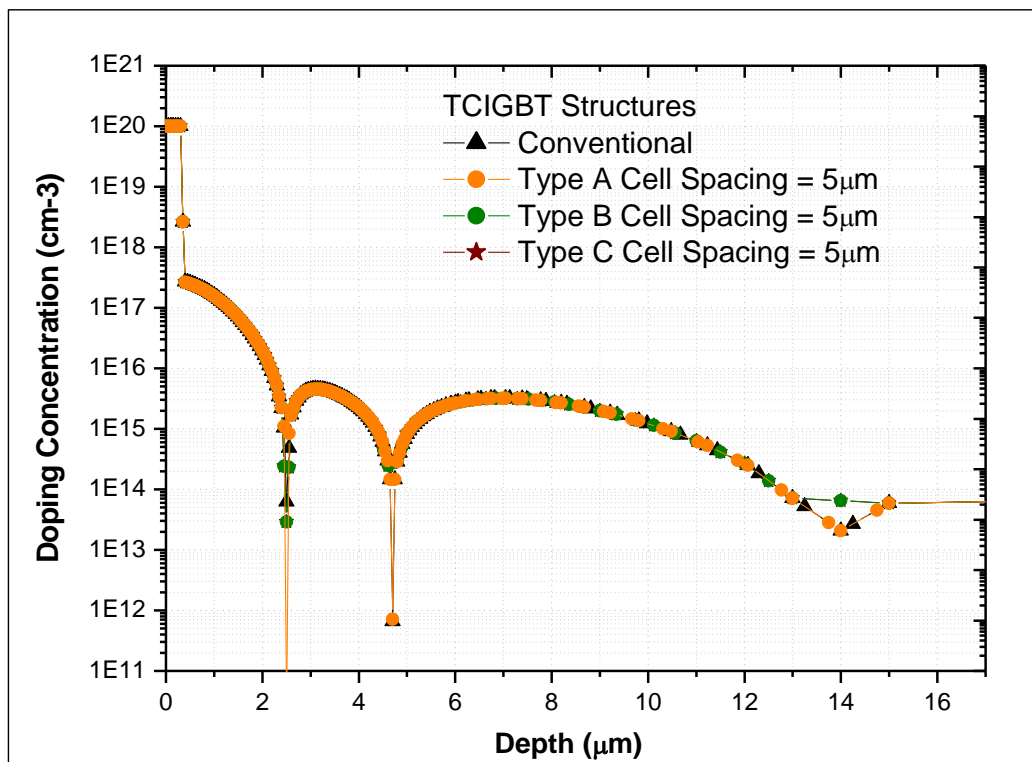
Figure 4-5: The doping concentration across the CIGBT structures (cutline taken along A-A')

The electrical characteristics of the structures have been simulated at 25°C and 125°C using MEDICI™. As shown in Figure 4-6, the breakdown voltage of all the TCIGBT structures is greater than 1.2kV.
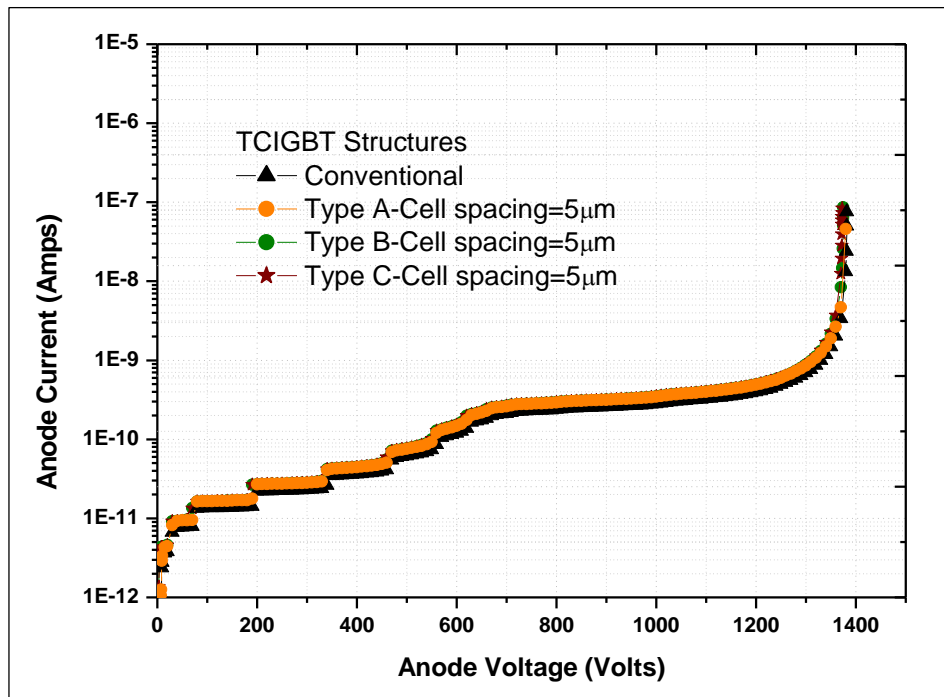
Figure 4-6: Typical Breakdown characteristics of the TCIGBT structures
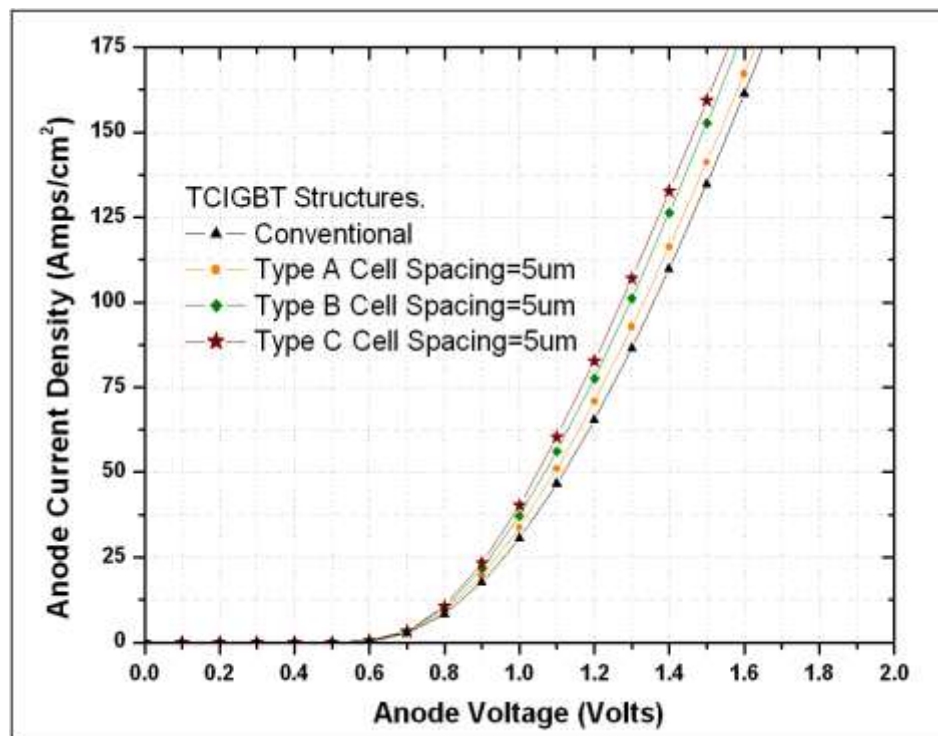
Figure 4-7: Typical I-V characteristics for 1.2kV TCIGBT Structures Tj=25ºC

The breakdown voltage is not affected by the electric field spreading around the trench gates

(behaviour which is usually observed in TIGBTs), as the peak electric field in this region is

well below the critical field strength. Figure 4-7 shows the typical simulated on-state characteristics of the three TCIGBT structures along with the conventional baseline device. It can be clearly seen that the Type-C structure can lead to an improved on-state performance of the device, without influencing the breakdown voltage of the device in any way. The improvement obtained in the on-state performance along with the reduction in the saturation current density of the device is the major focus of this chapter.

4.4.   INFLUENCE OF CELL SPACING ON SEGMENTED P-BASE TCIGBT

Figure 4-8 shows the simulated influence of cell spacing on the on-state and inductive turn-off energy loss of the device. "▲/Δ" show the on state voltage of the devices at 25°C and 125°C respectively and "★/☆" shows the turn-off losses of the device at 25°C and 125°C respectively. In addition to this the results at 175A/cm^2 and 100A/cm^2 has been shown for comparison. As the cell spacing of the device is increased, a modest improvement in the on-state performance of the device is observed. This is the result of improved carrier concentration at the cathode side of the device due to improvement in the accumulation region by redundant gates. However improvements in the on-state performance are gained at diminishing returns as the cell spacing is increased beyond 5μm, as the positive effects of redundant gates are reduced due to the decrease in the active channel density per unit area. Figure 4-9 shows the simulated influence of the cell spacing on the saturation current density of the device. As the cell spacing of the Type-A structure is increased, the saturation current density of the device decreases due to the decrease in the active trench gate density per unit area.
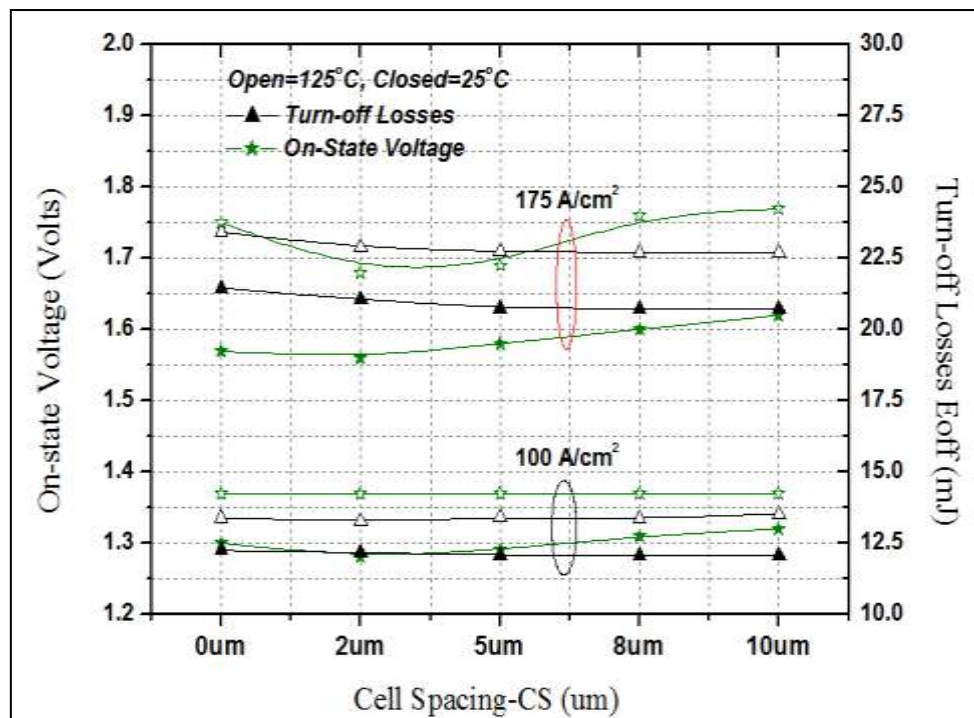
Figure 4-8: Variation of on-state voltage and turn-off losses with cell-spacing (CS) in TCIGBT with

Segmented P-base
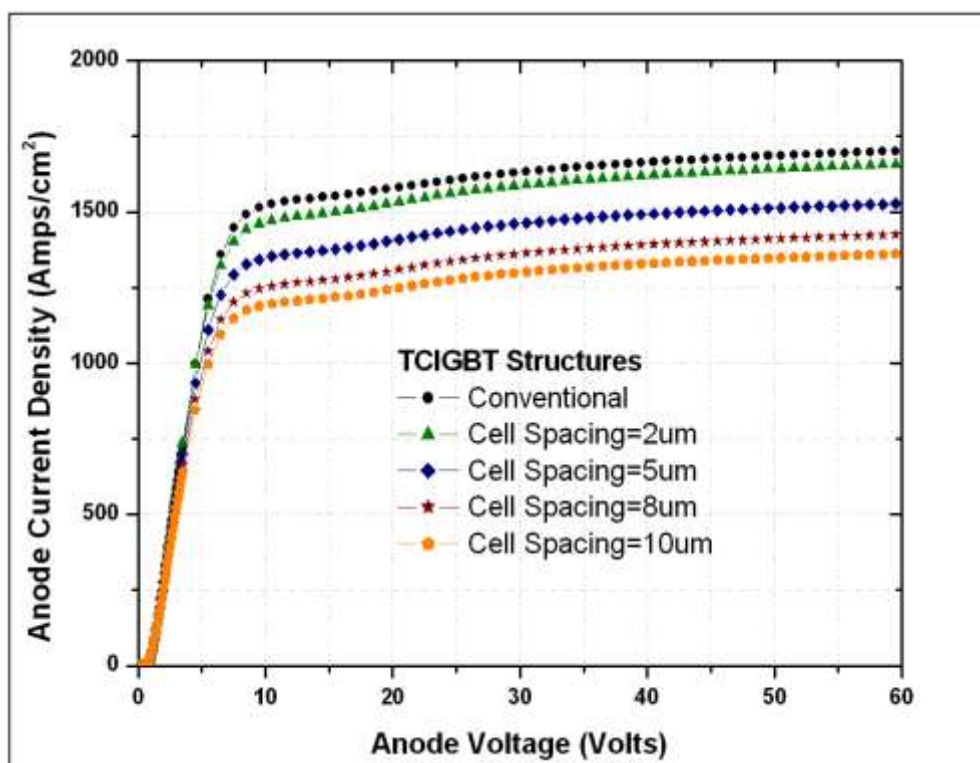
Figure 4-9: Simulated I-V Characteristics showing current saturation with variation of cell-spacing

(CS) for TCIGBT with Segmented P-base

These results clearly illustrate that by increasing the cell spacing between the active NMOS trenches, the saturation properties of the device can be substantially reduced without influencing the on-state or the switching performance of the device to a meaningful degree.

4.5. INFLUENCE OF PMOS TRENCH GATE

4.5.1. ON-STATE PERFORMANCE

Figure 4-10 shows the influence of the PMOS trench width on the on-state performance of the device as predicted by simulations. It can be observed that as the width of the PMOS trench gates are increased, the on-state voltage performance of the device is improved. This improvement in the on-state voltage is a result of the enhanced electron injection efficiency due to the carrier constriction achieved by PMOS gates at the cathode end of the device as discussed in section 4.2.
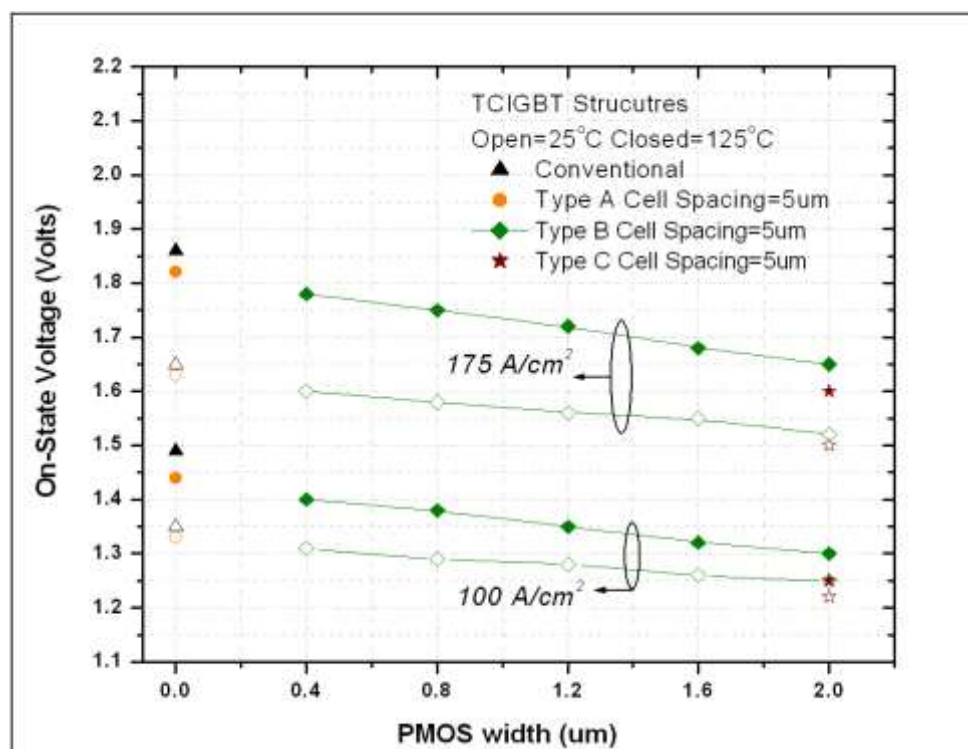
Figure 4-10: Simulated variation of on-state voltage with PMOS trench width for TCIGBT structures with cell spacing (CS) =5μm

The cell width has been kept constant at 5µm for the Type B structure while the width of the PMOS gates was varied. Figure 4-11 shows the improvement in the carrier concentration of the segmented P-base structures in their on-state, as a result of the introduction of PMOS gates. It can be clearly seen that as the width of PMOS gates is increased, the carrier density at the cathode side of the device also increases so as to allow higher conductivity modulation within the device, in turn leading to a lower on-state voltage drop across the device.
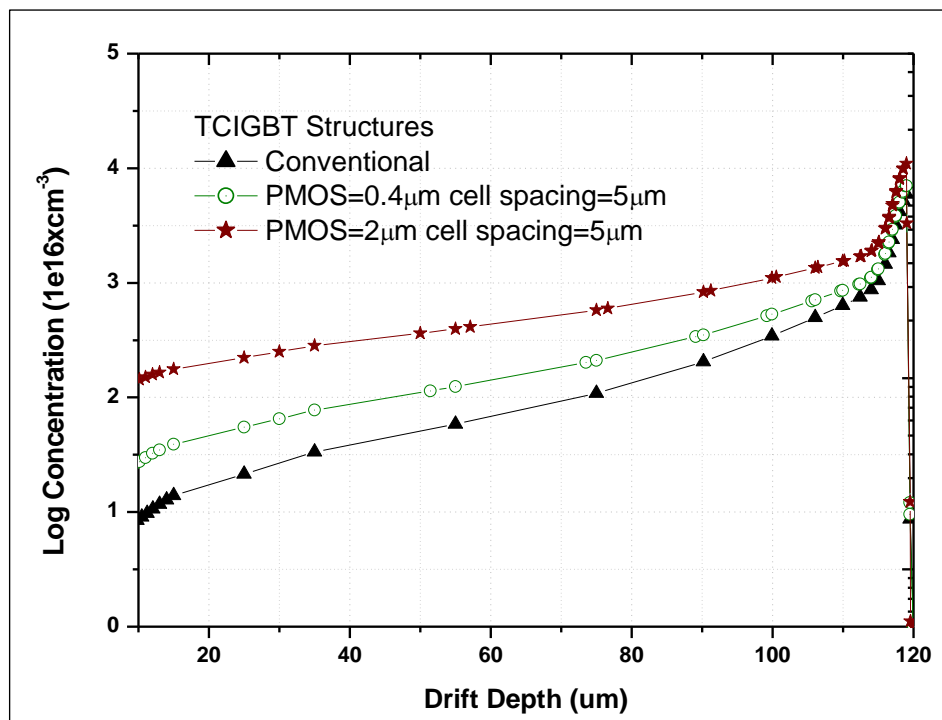
Figure 4-11: Simulated electron carrier density comparison of the TCIGBT structures in their on-state with variation of the PMOS trench gates

4.5.2. INDUCTIVE SWITCHING PERFORMANCE

In most cases as more charge is introduced into the device to reduce the on-state voltage, the turn-off losses increases as this charge now needs to be extracted. However, an increase in charge due to the carrier concentration does not seem to significantly affect the turn-off losses of the proposed structure as the PMOS gates are also responsible for hole extraction during the turn-off phase of the device. Figure 4-12 shows the influence of the PMOS trench width

on the turn-off performance of the device. The effect of the PMOS gates on the turn-off loss of the devices has been previously explored in [4.4] [4.5]. The PMOS channels provide a path for hole extraction from the n-drift region. This allows the device to have greater conductivity modulation in the on-state and does not impact the turn-off losses during the switching transitions.
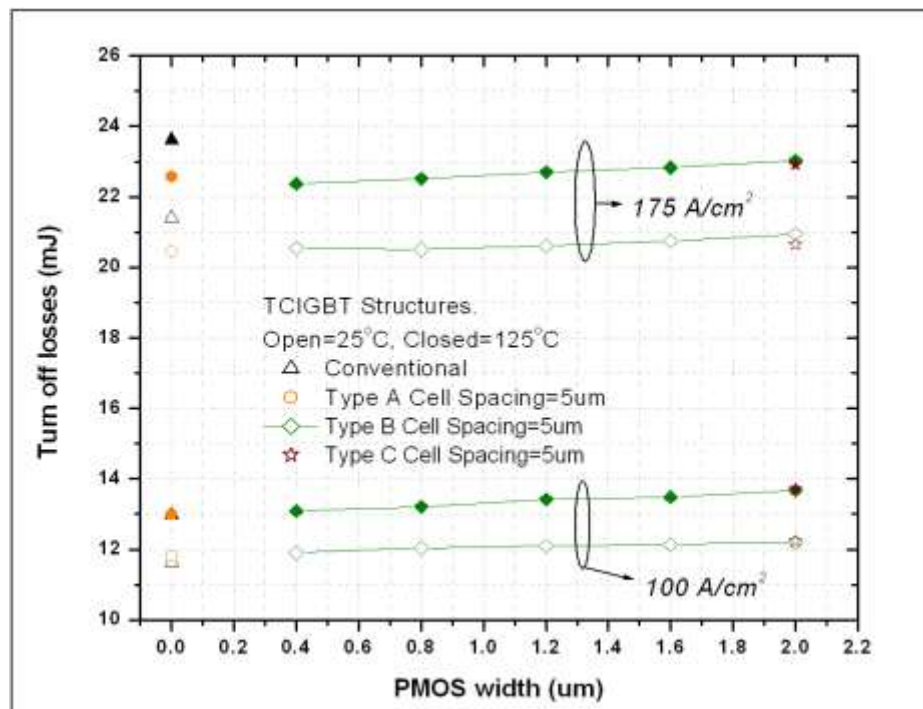
Figure 4-12: Variation of turn-off losses with PMOS trench width for TCIGBT structures with cell spacing (CS) =5μm

4.5.3. ELECTROTHERMAL SHORT CIRCUIT PERFORMANCE

Figure 4-14 shows the influence of the PMOS trench width on the short circuit performance of the device. It can be observed that as the width of the PMOS trench is increased, the short circuit performance of the device degrades. This is because the holes now have a tighter path to travel to the cathode, thus increasing the possibility of a latch up occurring which leads to a degradation of the dynamic performance of the device. However, this can be avoided by the formation of ladder structure at the cathode side of the device thereby allowing the reduction

in the width of the n+ electron emitters in the MOS channel regions as shown in figure Figure

4-13
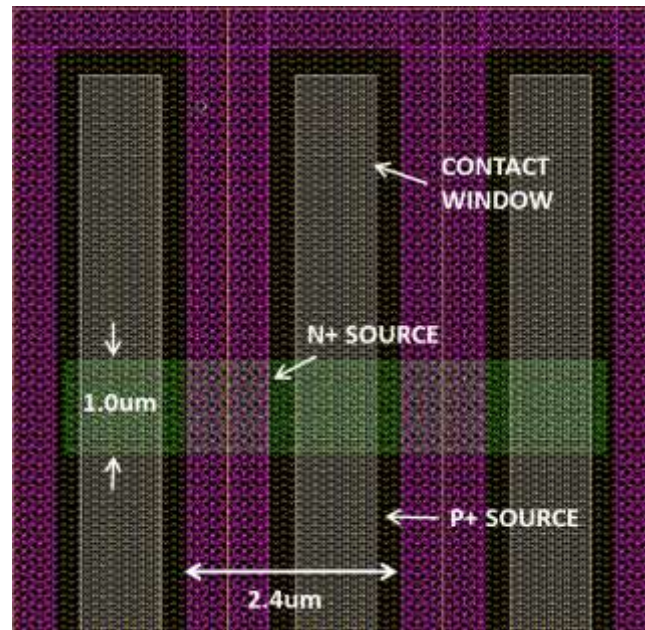
Figure 4-13: Mask Layout of the TCIGBT structure showing the ladder layout of the cathode side
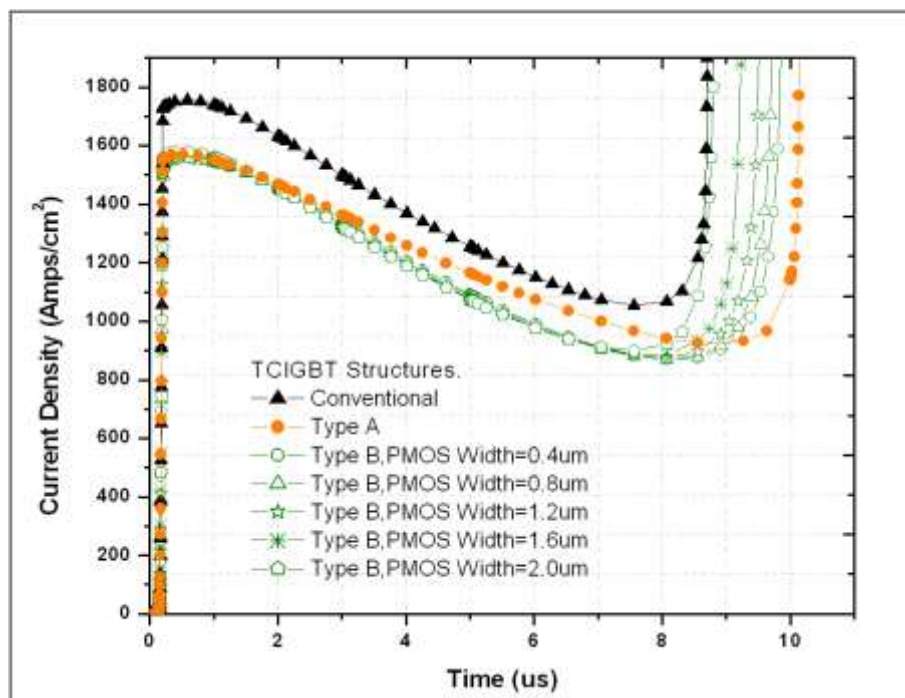
Figure 4-14: Influence of variation of the PMOS trench width on the electro thermal short-circuit

performance of the device, cell spacing=5µm, V=600V, Vg=±15V and τ =20µs

4.6.   INFLUENCE OF CELL SPACING ON TCIGBT WITH PMOS GATES

4.6.1.   ON-STATE PERFORMANCE

Figure 4-15 shows the influence of cell spacing on the on-state and inductive turn-off energy loss of the Type B structure. "★/☆" show the on state voltage of the devices at 25°C and 125°C respectively and "▲/Δ" shows the turn-off losses of the device at 25°C and 125°C respectively. In addition to this the results at 175A/cm^2 and 100A/cm^2 has been shown for comparison. An improvement in the on-state voltage is observed when the cell spacing of the device is progressively increased from 0μm to 5μm. This is due to the improvement in the carrier concentration at the cathode side of the device as a result of an effect similar to that discussed in section 4.2 and 4.4.
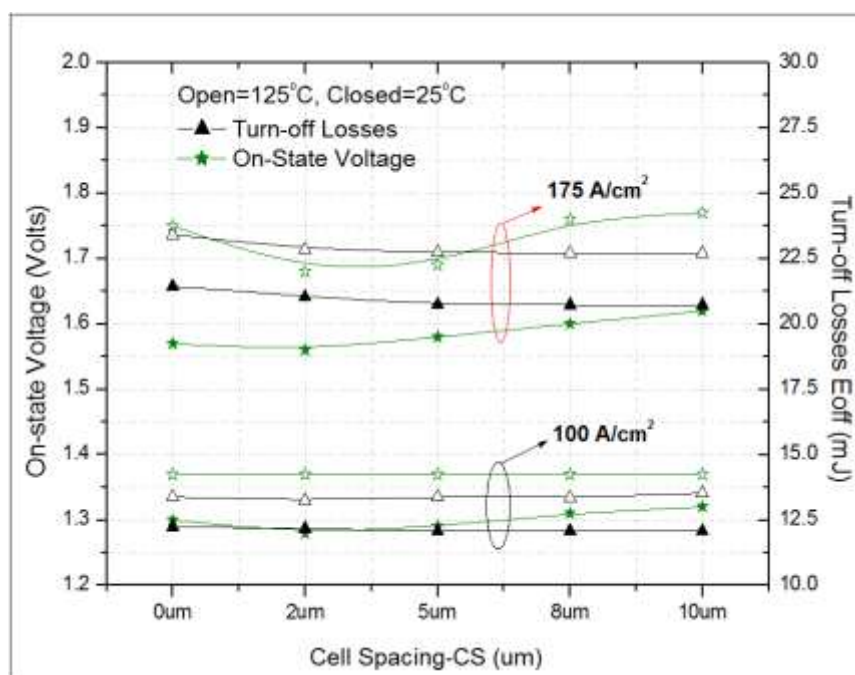
Figure 4-15: Variation of on-state voltage and turn-off losses with cell-spacing (CS) for the Type B structure

4.6.2.   ELECTROTHERMAL SHORT CIRCUIT PERFORMANCE

This section considers the influence of the cell-spacing on the short circuit performance of the segmented P-base TCIGBT structure. The circuit used for short circuit evaluation is shown in

Figure 4-16. During the short circuit phase, the current in the device under test (DUT) is limited by the saturation properties of the device. The power dissipated (P_D) by the device can thus be established from:

$$P_D = J_{SAT} * V_A \quad ..... (4.9)$$
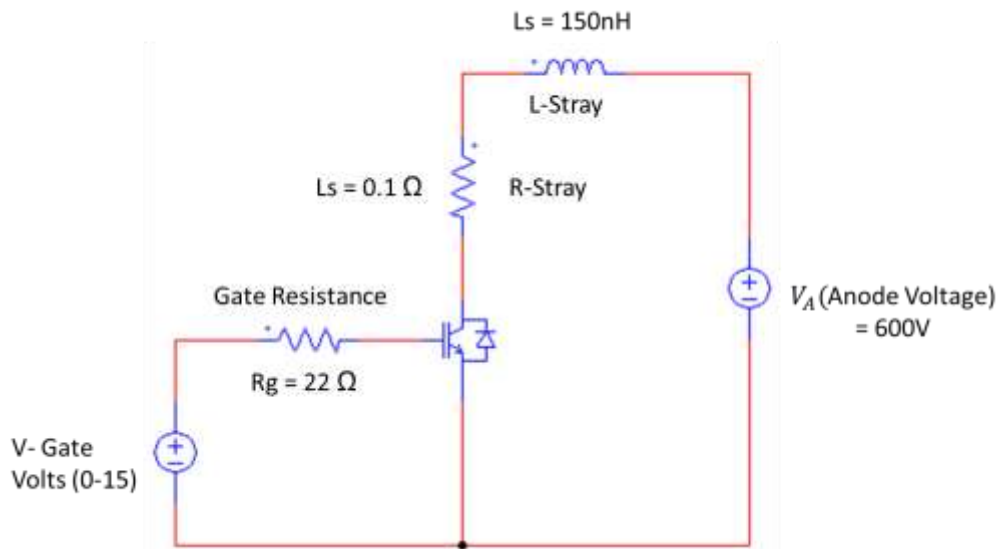
Figure 4-16: Typical circuit used to evaluate the short-circuit performance of the TCIGBT

This constant power dissipated into the device will result in heating of the device. When the temperature rise within the device reaches a critical value, the device would fail destructively, at which point in-built potential becomes zero [4.6]. The time duration for the device to withstand short circuit is thus found to be.

$$t_{sc} = \frac{((T_{CR} - T_{HS}) * W_{Si} * C_V)}{(J_{SAT} * V_A)} \quad ..... (4.10)$$

Where, T_{CR}=Critical value of temperature, T_{HS}=Heat sink temperature, W_{Si}= Thickness of wafer, C_V=Volumetric specific heat, J_{SAT} = Saturation current density, V_A=Anode DC Supply. Figure 4-17 shows a comparison of the short circuit durations of the structures with variation of cell-spacing. It is observed that the TCIGBT with the segmented P-base has

improved short circuit performance without degradation in its Eoff-Vce(sat) Trade-off. This is a consequence of its saturation current level being some 23% lower than that of a conventional TCIGBT which means that the rate of heat generation and temperature rise would be markedly slower than a conventional TCIGBT structure.
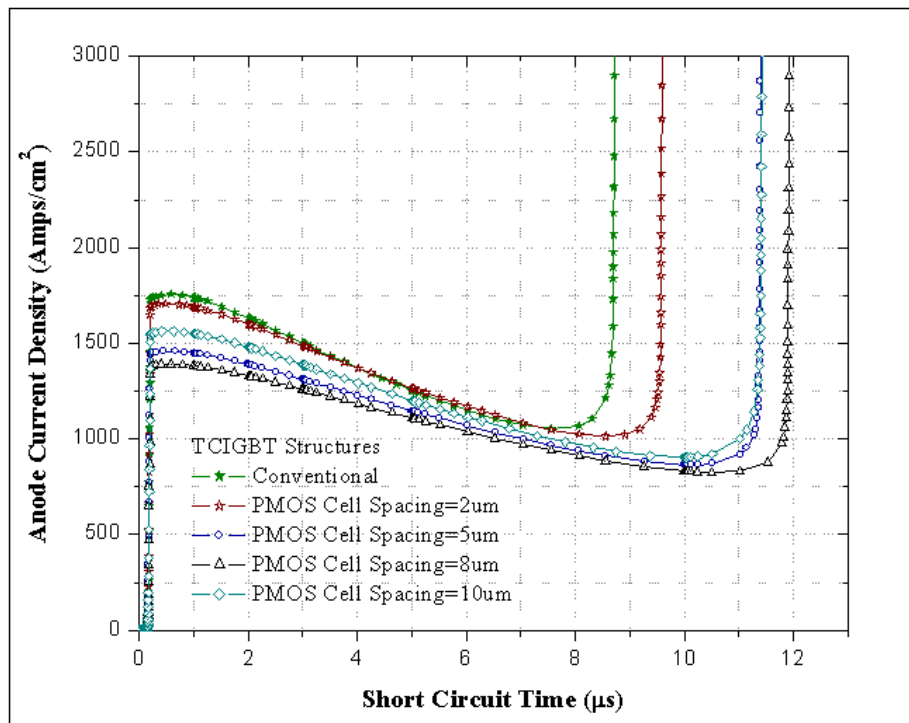
Figure 4-17: Influence of cell spacing (CS) on the electro thermal short circuit performance of the segmented P-Base TCIGBT structure, V=600V, Vg=±15V and τ =20µs

4.7. INFLUENCE OF DEEP NMOS AND PMOS TRENCH GATES

The influence of the deep NMOS and PMOS trench gates on the on-state performance is seen in Figure 4-7 previously. The segmented P-base structure with deep NMOS trenches tends to exhibit a lower on-state voltage as compared to the shallow NMOS trench devices. This is because more electrons are injected during the turn-on phase. Figure 4-18 and Figure 4-19 shows the current flow lines in the Type B and Type C structures. Figure 4-20 shows the electron concentration in the various TCIGBT structures when they are operated in their on-

state. It can be clearly observed that the Type C structure facilitates the improvement in the carrier density at the cathode side of the device, leading to an improved on-state performance.
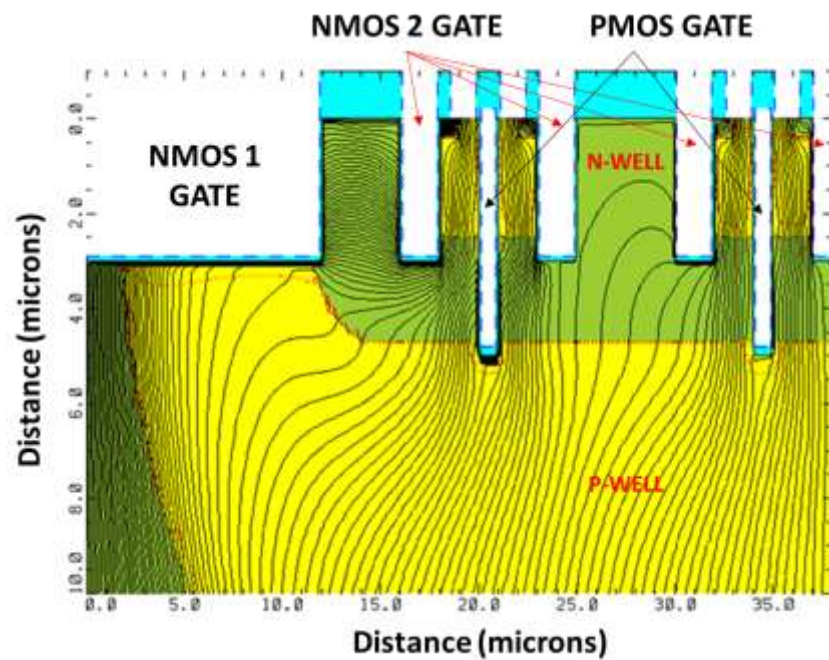
Figure 4-18: Predicted current flow lines in the segmented P-Base TCIGBT structure with PMOS trench gates
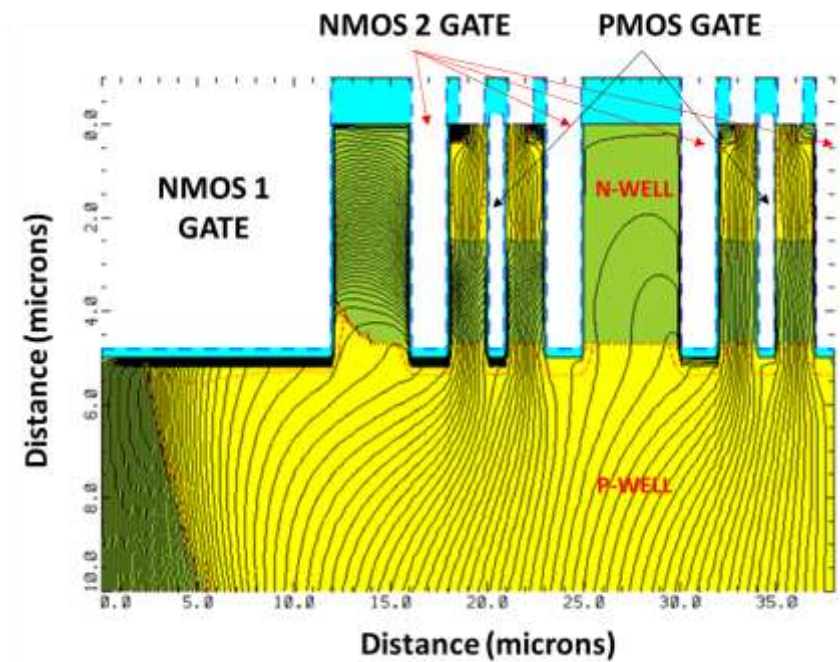
Figure 4-19: Predicted current flow lines in the segmented P-Base TCIGBT structures with deep NMOS and PMOS trench gates
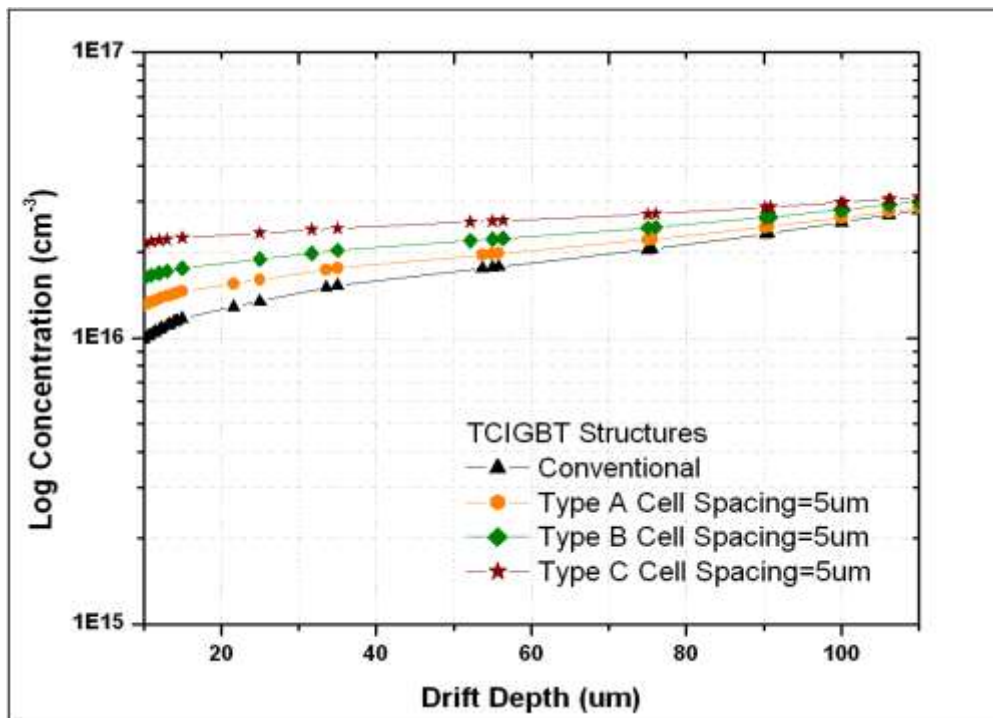
Figure 4-20: Electron carrier density of the various TCIGBT structures in their on-state along A-A'

4.7.1. PERFORMANCE TRADE OFF

A model of a standard chopper circuit was used to calculate switching losses of the TCIGBT structures. Figure 4-21 and Figure 4-22 shows the simulated Vce(sat)-Eoff trade-off curves at 25°C and 125°C respectively. The segmented P-base Structure with deep NMOS trenches reduces the turn-off losses of the device by 23% and 25% for $100A/cm^2$ and $175A/cm^2$ respectively. The results shown below clearly show that the Type B and Type C structure offer a better performance trade off as compare to the Conventional structure. This is due to the result of an increased conductivity modulation at the cathode end of the device while using the PMOS gates for turn-off. In addition to this it is also observed that the use of segmented P-base can also help in reducing the saturation current density of the device as the active cell per unit area decreases. This happen without having an adverse impact on the on-state voltage of the device. It is also observed that the Type C structure might simply the

fabrication process as all trench gates have similar depth. Hence an optimisation and fabrication of this device has been further considered.
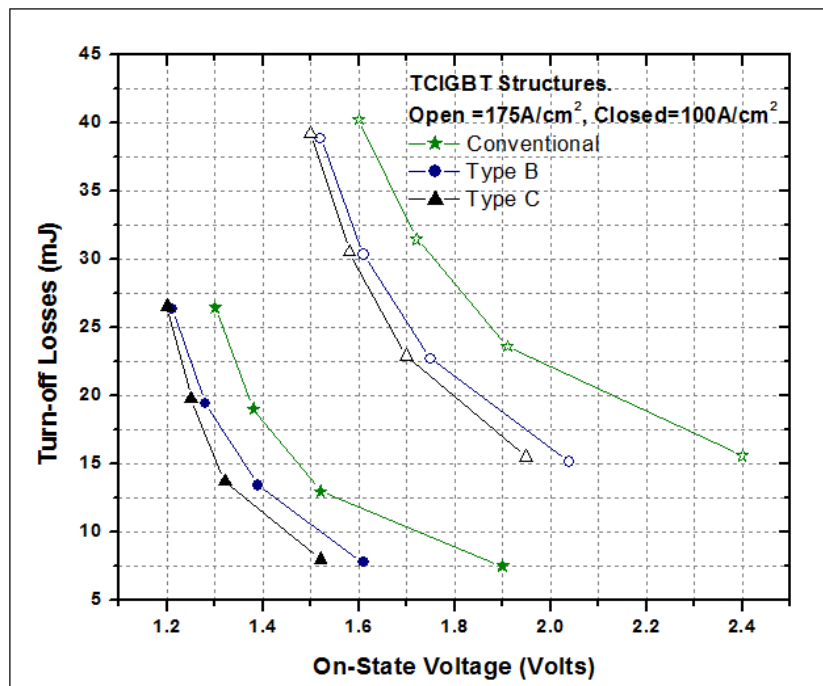
Figure 4-21: Comparison of Eoff-Vce(sat) trade-off for conventional and Segmented P-base

Structures at Tj=125ºC , V=600V, Rg=22Ω, Vg=±15V and τ =20µs, Lstray=100nH
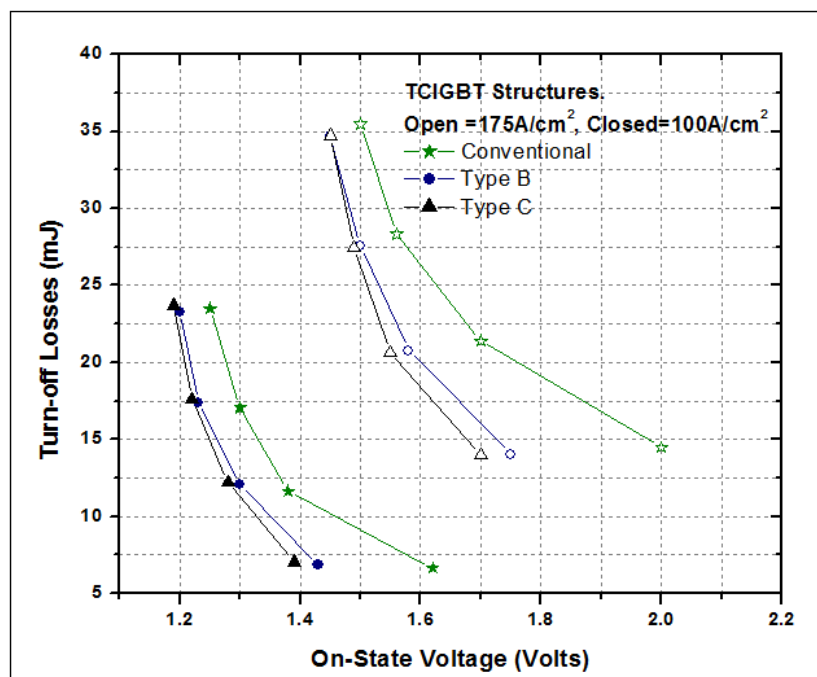
Figure 4-22: Comparison of Eoff-Vce(sat) trade-off for conventional and the Segmented P-base

Structures at Tj=25ºC , V=600V, Rg=22Ω, Vg=±15V and τ =20µs, Lstray=100nH

4.8. DEVICE FABRICATION

Having explored many aspects of performance of various devices by simulation, this section describes the fabrication of a segmented P-base TCIGBT structure with deep NMOS and PMOS gates. The typical process fabrication steps for TCIGBT structures are listed in Table 4-1. The first few steps involve the formation of the floating deep P-WELL/N-WELL regions.

Table 4-1: Proposed process for the 1.2kV segmented P-base TCIGBT structures

Starting material N+ Substrate
P-WELL and N-WELL regions are selectively implanted and annealed to form the clusters.
P-base regions are formed at the same time as the field rings, which are to support breakdown voltage in the termination area
N+ region is selectively implanted
The trench gate regions are etched
Gate oxides and polysilicon layers are grown
P+ is selectively implanted and annealed at high temperatures.
Contact windows are etched and metal is deposited.
Backside of the wafer is thinned by grinding and is chemically etched.
N+ and P+ are implanted as required to form the buffer and collector regions respectively.
Anode Metal is deposited by evaporation.
Annealed at a relatively low temperature.

The P-base regions are then implanted inside and outside the MOS clusters to form the P-base and termination regions, respectively. The floating P-base regions outside the TCIGBT clusters act as field termination rings for the TCIGBT structures and prevent the surface electric field from exceeding the critical field strength. The n+ regions are then selectively implanted. The trench gates are formed by etching into the silicon area followed by the

growth of poly-silicon to form the control and turn-on trench gates, respectively. The gates which operate as turn-on gate are formed by the same trenches that act as control gates and this is illustrated in Figure 4-23. The p+ regions are then selectively implanted and the contact windows are etched and metallised to form the cathode side of the TCIGBT structure.
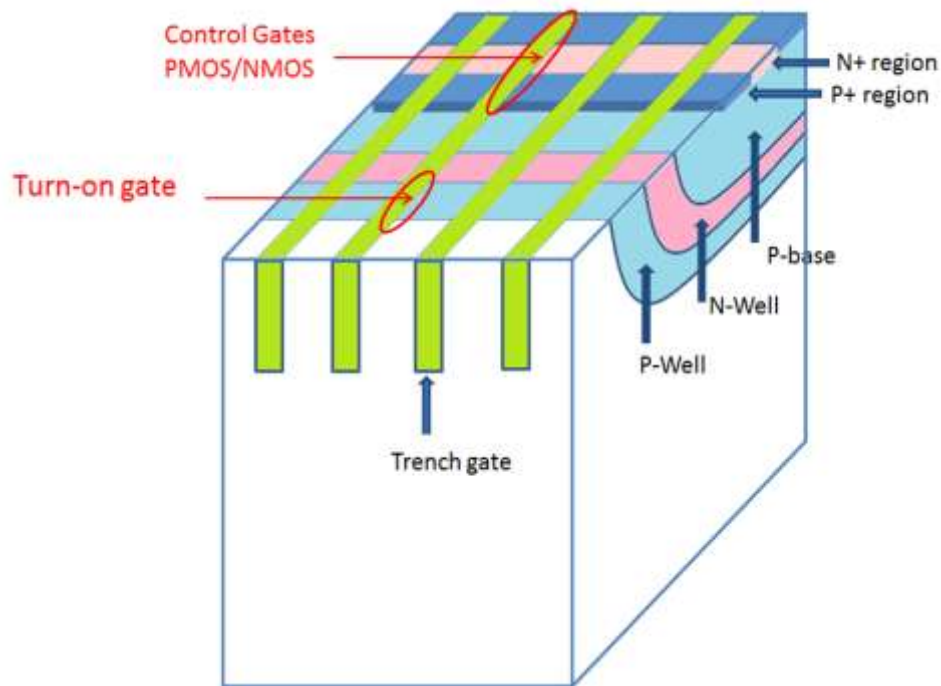
Figure 4-23: The cross section schematic of the TCIGBT structure

The formation of the anode region is achieved by first grinding the wafer (thinning) followed by boron and phosphorus implantation to form the buffer and the P+ regions, respectively. The last step involves the deposition of the anode metal by evaporation. The mask layout for the segmented TCIGBT structure is shown in Figure 4-24. The cell spacing is adjusted to form the segmented PBASE structure. The n+ and p+ implants are controlled, based on the minimum design rules. The MOS cells are designed to meet the minimum cell dimensions that ensure that the channel density is not compromised substantially.
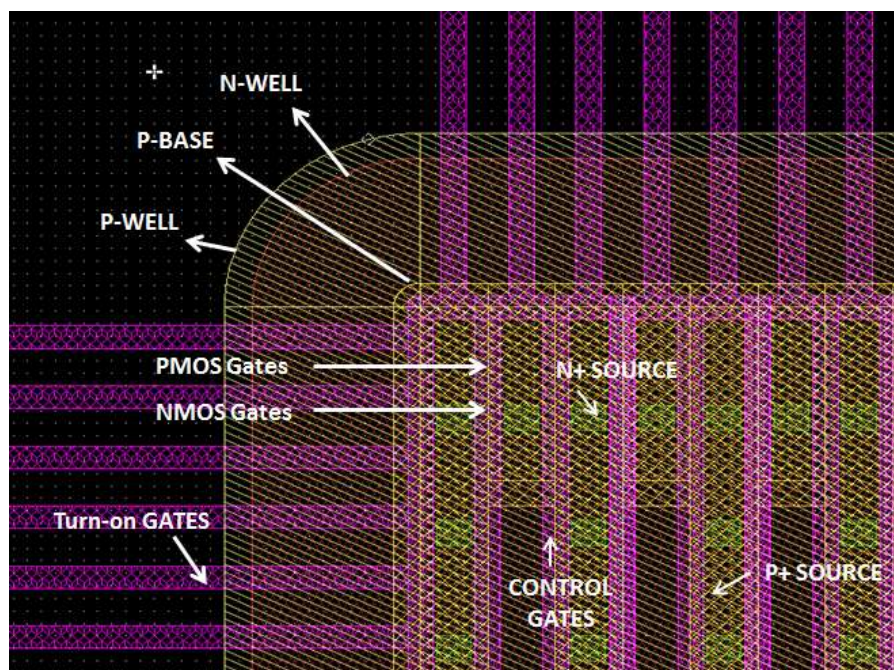
Figure 4-24: Mask Layout of a TCIGBT with Segmented P-Base and PMOS Gates

4.9. EXPERIMENTAL RESULTS

Three different structures were designed for this work using MENTOR GRAPHICS IC, and were fabricated by an industrial partner, in order to evaluate the segmented P-base concept in TCIGBT. These structures are derivations of the Type C structure described in section 4.7. Henceforth in this chapter, the structure with deep NMOS and PMOS gates is referred to as Type C1; the structure with deep NMOS and PMOS gates with a cell spacing equal to the minimum cell dimension is referred to as Type C2 and the structure with deep NMOS and PMOS gates with an equivalent cell spacing equal to 3 times the minimum cell dimension is referred to as Type C3.

The devices were rated at 10A with a dimension of 4.2 x 4.5 mm^2. The active area for the 10Amp devices including the gate pad area is 9.6mm^2 , and the TCIGBT structures were rated at a current density of 125Acm^2. These devices were assembled on a ceramic substrate as shown in Figure 4-25, for further experimental evaluation. The trench depth for the deep

NMOS and PMOS gates is designed to penetrate the Pwell-Nwell junction and is therefore ~6μm deep.
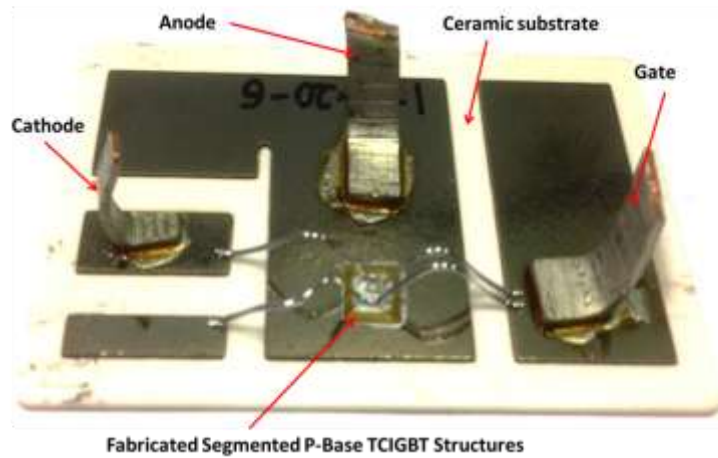
Figure 4-25: TCIGBT devices assembled on a ceramic substrate

4.9.1. MEASURED ON-STATE PERFORMANCE

Figure 4-26 and Figure 4-27 show that the TCIGBT structures have a snap-back free turn-on, and its on-state behaviour exhibits a positive temperature coefficient at higher temperatures.
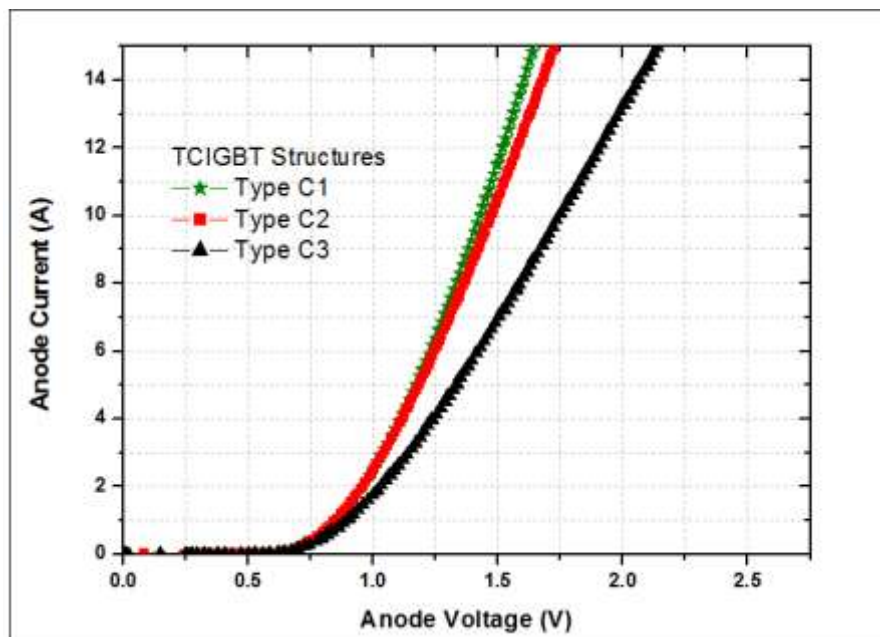
Figure 4-26: Typical experimental CIGBT on-state I(V) at 25ºC Vg=15V
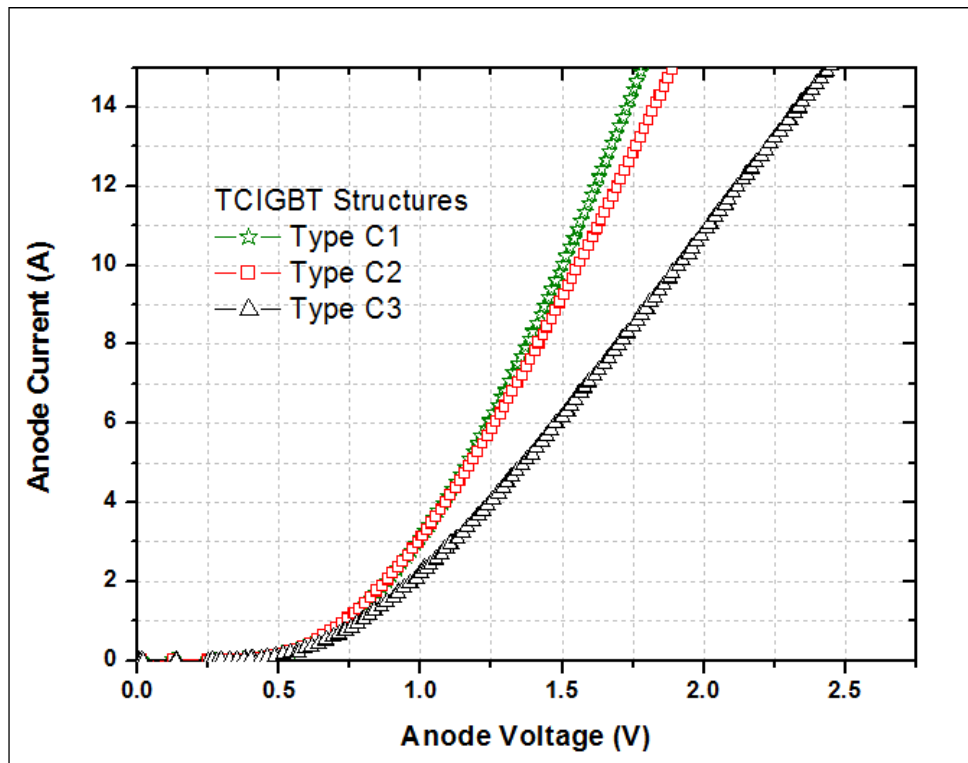
Figure 4-27: Typical experimental TCIGBT on-state I(V) at 125ºC Vg=15V

The on-state performance of the TCIGBT structures follows a similar trend described in the previous sections. As the cell spacing is increased, the number of MOS channels used for forward conduction is reduced leading to an inferior on-state performance in the Type C3 structures. However, the Type C1 and Type C2 structures show similar on-state performance to each other as the MOS channels are not significantly compromised. The on-state voltage at 125°C was measured to be 105% of that at 25°C. The saturation current of the various TCIGBT structures is shown in Figure 4-28. The saturation current densities of the TCIGBT structures with cell spacing follow the same trend described in section 4.4 and section 4.6. The saturation current level for the TCIGBT with segmented PBASE structures is less than half of the conventional TCIGBT structure. Hence, the TCIGBT structures with segmented PBASE should be capable of sustaining longer short circuit duration, as the rate of heat generation within the device will be reduced.
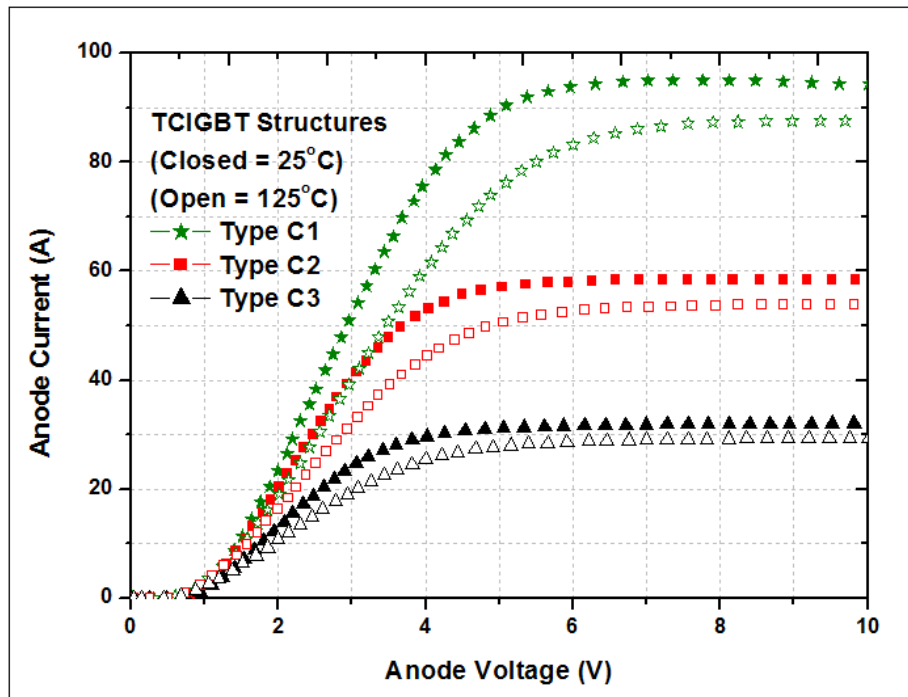
Figure 4-28: Typically measured current saturation characteristics for TCIGBT structures Tj= 25°C and 125°C

4.9.2. CAPACITANCE MEASUREMENT

The switching behaviour of an MOS controlled bipolar device is determined by its internal structure, internal capacitance (charges), and the internal and external resistance of the device. These parasitic components are inherent parts of the die and a schematic showing the equivalent capacitance of the die is shown in Figure 4-29.
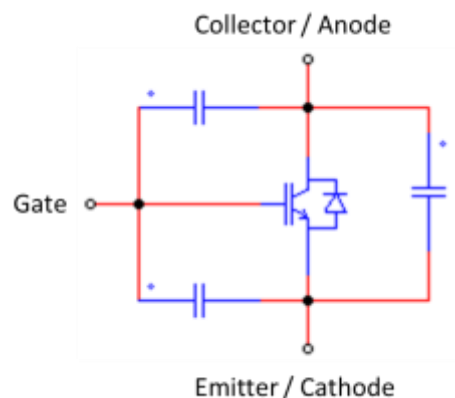
Figure 4-29: A schematic diagram showing the equivalent capacitance of the device

When calculating the output power requirements of the drive circuit, the key parameters of interest is the gate charge. This gate charge is characterised by the equivalent internal capacitance (C_{GC} and C_{GE}). The relationship between the internal capacitance of the device and the input capacitance (Cies) is given in equation 4.11.

Therefore, for the device to turn on and turn off, the input capacitance must be charged to the threshold level and discharged to the plateau voltage respectively. This indicates that the impedance of the drive circuit and Cies, has a direct relationship to the turn-on and turn-off performance of the device.

$$C_{ies} = C_{GE} + C_{GC} \quad .... (4.11)$$

Figure 4-30 compares the measured input capacitance C_{ies} for the Trench CIGBT structures.
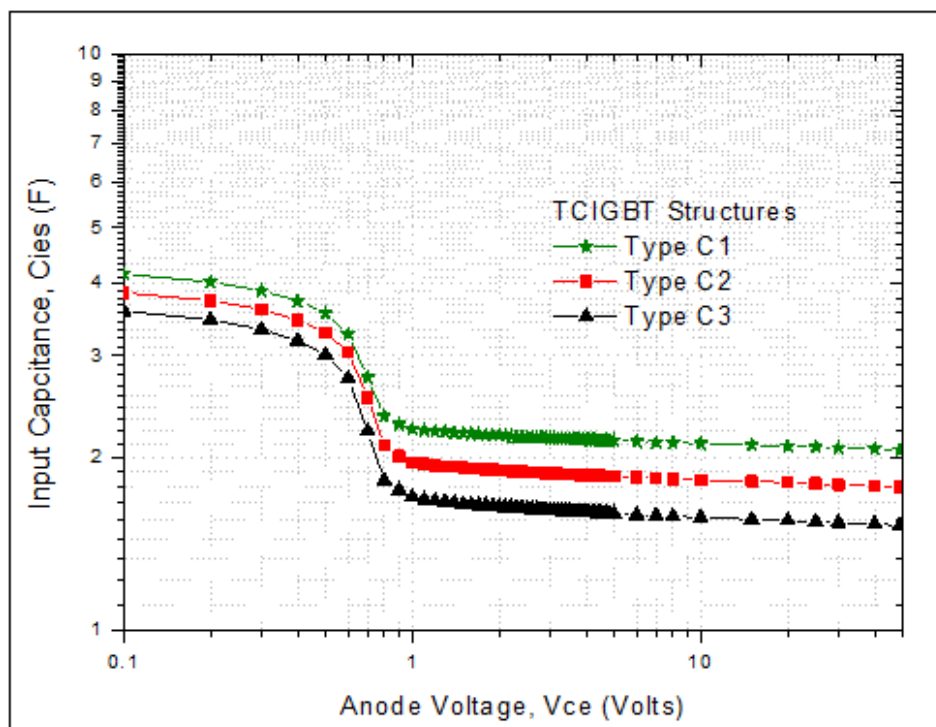
Figure 4-30: Input capacitance measurement for the TCIGBT structures

The segmented P-Base structures (Type C2 and Type C3 structures) show a lower value of C_{ies} as compared to the Type C1 structures. Hence, the segmented P-Base structures will be easier to drive, which should in turn manifest itself in shorter switching times and reduced switching losses as compared to the Type C1 structures.
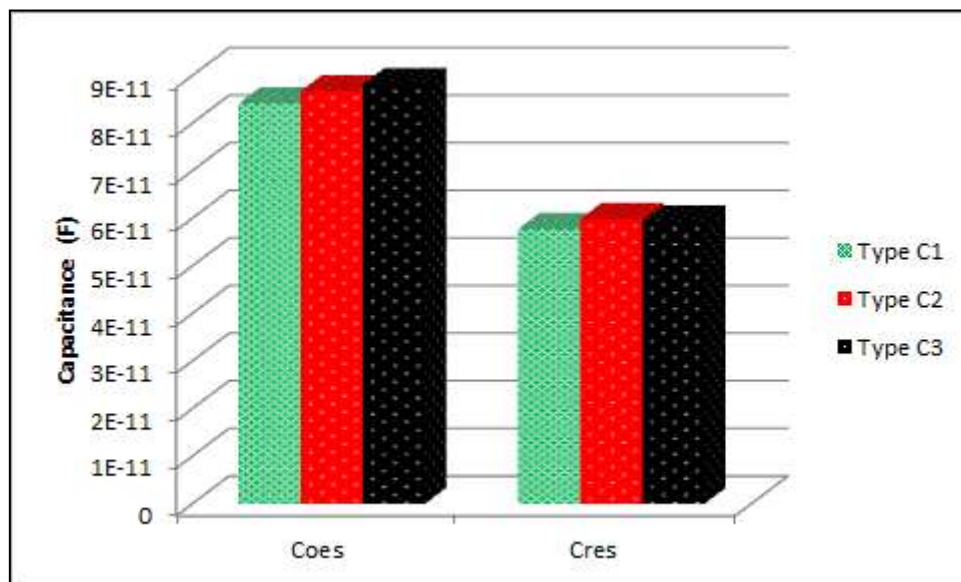
Figure 4-31: Measured Output and Transfer capacitance for the TCIGBT structures

The use of segmented P-base structure has very little impact on the reverse transfer capacitance and the output capacitance as shown in Figure 4-31. Hence, these capacitances do not affect the switching performance between the TCIGBT structures to any significant degree.

4.9.3. PERFORMANCE TRADE OFF

The $V_{ce(sat)}/E_{off}$ trade-off shows that the segmented P-base structures with deep NMOS and PMOS gates (Type C2 and Type C3) exhibit an improved trade-off performance as compared to the TCIGBT structure with deep NMOS and PMOS gates (Type C1). This can be attributed to the fact that the segmented PBASE structures have a lower input capacitance. In addition to this, as the number of MOS channels per unit area is higher for the Type C1

structure as compared to the Type C2 and Type C3 structures, the amount of charge to be extracted from the drift region would be lower resulting in lower turn-off losses. The trade performance of the TCIGBT structures is shown in Figure 4-32.
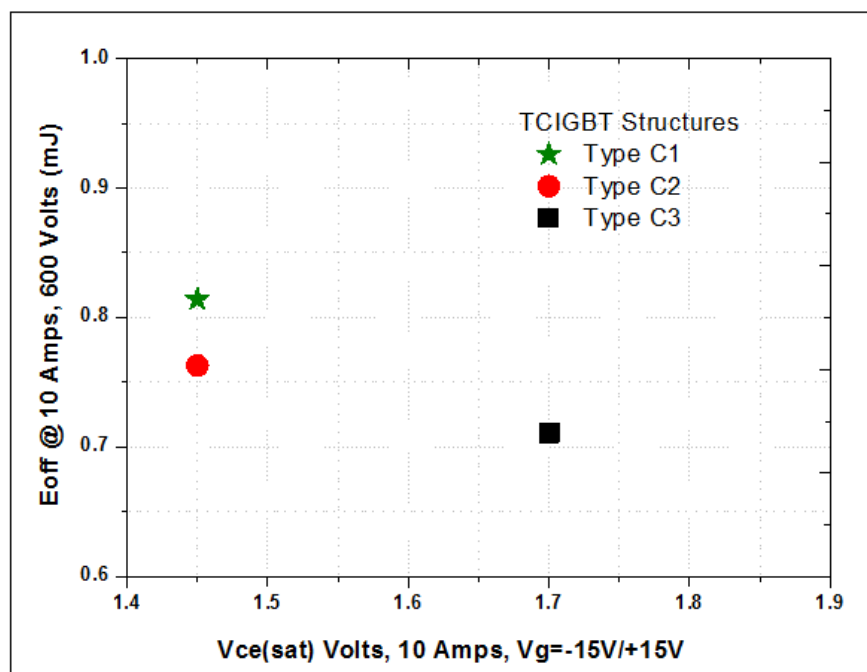
Figure 4-32: Comparison of performance trade-off for the TCIGBT structures Vce=600V, Ic= 10Amps, Vge=+15V/-15V, Tj=25ºC

4.10. CONCLUSIONS

Detailed simulations have been performed on the various TCIGBT structure. The simulated structures include the segmented P-base structure, the segmented P-base structure with PMOS gates and the segmented P-base structures with deep PMOS and NMOS gates. The structures have been compared to the baseline device which otherwise defined as the conventional TCIGBT structure. The simulations results show that the segmented P-base structure help in the reduction of the current saturation levels which leads to an improvement in the short circuit performance of the device. This decrease in the current saturation levels is due to the reduction of active cell per unit area. The use of the PMOS gates further shows to improve the on-state performance of the device without compromising the turn-off

performance. This is because the PMOS gates help in charge extraction during the turn-off phase. Lastly it has been observed that the Deep NMOS and PMOS trench gates along with the segmented P-base structures give rise to improved performance trade-off without compromising the on-state voltage, the switching performance or the short-circuit performance of the device. This is due to the optimised use of the N-well concentration. It is also noted that as the trench gates are of equal depth, this structure simplifies the fabrication process and leads to a reduction in the fabrication cost.

Following the simulation results a few variations of the TCIGBT structure with deep NMOS and PMOS gates were fabricated and experimentally evaluated. The results obtained verify the simulation results shown in this chapter. This work was done in collaboration with device manufacturer. Hence a number of design rules were pre-defined in order to reduce the cost of fabrication. However, the results clearly show the influence of the segmented P-base on the fabricated structures. The reduction of the current saturation levels is observed and its impact on the on-state voltage also follows the trend discussed in the simulations.

4.11. REFERENCES

[4.1]   B. J. Baliga, *Fundamentals of Power Semiconductor Devices*: Springer, 2010.

[4.2]   M. Kitagawa, I. Omura, S. Hasegawa, T. Inoue, and A. Nakagawa, "A 4500 V sinjection enhanced insulated gate bipolar transistor (IEGT) operating in a mode similar to a thyristor," in *Electron Devices Meeting, 1993. IEDM '93. Technical Digest., International*, 1993, pp. 679-682.

[4.3]   E. M. Sankara Narayanan, M. R. Sweet, N. Luther-King, K. Vershinin, O. Spulber, M. M. De Souza, *et al.*, "A novel, clustered insulated gate bipolar transistor for high power applications," in *Semiconductor Conference, 2000. CAS 2000 Proceedings. International*, 2000, pp. 173-181 vol.1.

[4.4]   N. Luther-King, E. M. S. Narayanan, L. Coulbeck, A. Crane, and R. Dudley, "Comparison of Trench Gate IGBT and CIGBT Devices for Increasing the Power Density From High Power Modules," *Power Electronics, IEEE Transactions on,* vol. 25, pp. 583-591.

[4.5]   L. Ngwendson and E. M. Sankara Narayanan, "Evaluation of 1.2kV Super Junction Trench-Gate Clustered Insulated Gate Bipolar Transistor (SJ-TCIGBT) " presented at the ISPSD'11, 2011.

[4.6]   H. Hagino, J. Yamashita, A. Uenishi, and H. Haruguchi, "An experimental and numerical study on the forward biased SOA of IGBTs," *Electron Devices, IEEE Transactions on,* vol. 43, pp. 490-500, 1996.

CHAPTER FIVE

EVALUATION OF POWER DEVICES FOR A MULTILEVEL POWER CONVERTER APPLICATION

5.1.   INTRODUCTION

All power conversion applications use power semiconductor devices to convert, control and manage electrical power. The need of efficient, reliable, high power and high temperature conversions stages has increased the design challenges of developing high power converters. The weight, size and cost of the power converters form some of the key criteria used to determine the feasibility of using power conversion stages in aerospace and automotive application. Figure 5-1 shows the expected development trend for power conversion stages for a number of different applications [5.1]. Most aerospace and automotive applications tend to target reductions in cost, weight and volume of the power conversion system while maintaining or improving on the reliability and efficiency of the system.
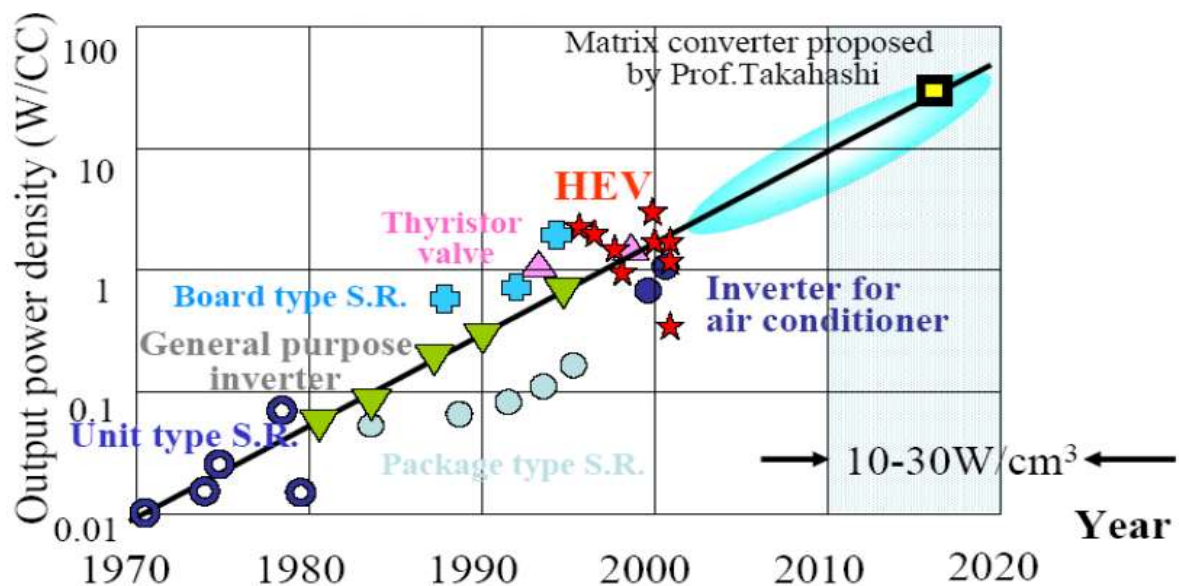
Figure 5-1: Expected development trends for power converters [5.2]

As will be apparent from Figure 5-1, although there is marked upward trend with time, at any given point there remains large variations in the power density achieved by the converter depending on the type of power conversion stage and the application. In terms of the influence of the application, a converter for a motor drive tends to be subject to very different constraints vis-à-vis the requirements placed on a power converter for power bus/grid provision. Power converters which are responsible for bus provision usually require large and bulky filters to meet stringent power quality requirements, which tend to result in a reduction in the power density of the converter as compared to power converters that are used for motor drive applications. Even this limited example demonstrates that a comparison of power converters solely on power density is potentially misleading without some context in terms of the application requirements, the operating environment and the nature of the cooling employed. In addition to this limitation, the power density figures quoted for high performance converters often do not include allowance for the mass or volume of ancillary systems that are required for the normal operation of the power converter, e.g. heat exchangers, EMI filters, the DC-Link capacitors, external housing and the terminal connectors. Very often, power density values are quoted solely in terms of the gross weight of the bare minimum of components required to operate the power converter. Considering power density values with such limited scope is not sufficient to fully understand or evaluate the technology barriers to high power dense converter systems. Therefore one must consider all the elements that form the converter system, viz: -

1. Power semiconductor module

2. Control circuits and Auxiliary systems (Protection circuits, Power supply units etc...)

3. Power level passive components (largely filter components)

4. Heat exchangers

5. Interconnections and packaging

A useful measure of gravimetric (ρ_m) or volumetric (ρ_v) power density of the converter is the total output power divided by the weight or the volume of the entire system. In the case of a system comprising n component/subsystems, these measures of power density can be evaluated as: -

$$\rho_m = \frac{P_{Output}}{\sum_{i=1}^{n} M_i} \qquad \dots (5.1)$$

$$\rho_v = \frac{P_{Output}}{\sum_{i=1}^{n} V_i} \qquad \dots (5.2)$$

Where, P_{Output} = Total power output of the converter, M_i = Mass of the component in kilograms, V_i = Volume of the components in litres and n=is the number of components that make up the converter. In order to optimise the gravimetric power density of the power converter, one needs to concentrate on the elements beyond the power module and its immediate heat sink, which tend to dominate the remainder of the volume and weight of the system. It has been suggested in literature that the heat exchanger, the passive filters/ EMI filters and the dc-link capacitor are the components usually responsible for compromising the power density of the converter [5.3]. The key methods that can be employed to reduce the size of these components are listed in Table 5-1. As seen in the table below, the use of -lower loss switching devices either capable of switching at high frequencies and/or operating in a different converter topology as compared to the standard 6 switch inverter offers scope to reduce the size of the heat exchanger and passive components.

The focus of this chapter is to evaluate the merits of using GaN power devices within the context of a power converter application in order to establish whether the potential of these devices translates into corresponding benefits in the power density of converters, with particular emphasis on using commercially available devices.

Table 5-1: Key methods used to allow reduction in power converter weight and size

Key Converter Components	Mass and Volume Reduction Methods
Heat exchanger size	1. Use of low loss semiconductor devices. 2. Use of advanced thermal management techniques. 3. High temperature operation of devices. 4. Use of other coolant & Heat exchanger technologies
Passive/EMI filters	2. High switching frequency operation via the use of low loss semiconductor devices. 3. Use of multilevel converters 4. Improvements in material properties and manufacturing methods.

5.2.   CANDIDATE SEMICONDUCTOR DEVICE TECHNOLOGY

The selection of the semiconductor device technology for a given converter is usually influenced by factors such as the nature of the application of the power converter, the operating voltage and current, environmental and coolant constraints, and the reliability and maturity of technology, which might for example include deployment in safety critical applications.

5.2.1.   SILICON BASED DEVICE TECHNOLOGY

Silicon based power devices are preferred in an overwhelming majority of power converters as they offer a more mature device technology and a well understood and proven reliability behaviour. In addition, in many cases, the use of Silicon power devices allows the risk associated to the power converter development to be reduced. The range of Silicon devices for power conversion include Diodes, Thyristors, Triac, Gate turn-off Thyristors (GTO), Integrated Gate Commutated Thyristor (IGCT), Metal-Oxide Semiconductor Field Effect

Transistors (MOSFET), Insulated Gate Bipolar Transistors (IGBT), Bipolar Junction Transistors (BJT). Table 5-2 shows representative characteristics of these device types, while Figure 5-2 shows the application scope of these technologies in terms of power levels and operational frequency. As illustrated by both, Table 5-2 and Figure 5-2, there is no single device technology that is capable of operating over the full range of current and voltage rating while offering the best performance match.

Table 5-2: Typical Power device characteristics [5.4]

Property	Thyristor (SCR)	Triac	GTO	IGCT	MOSFET	IGBT
Self-commutation ability	No	No	Yes	Yes	Yes	Yes
Maximum rms current ratings (A)	5000	400	2000	1700	300	2400
Maximum Voltage ratings (V)	12000	1200	6000	5500	1500	6500
Maximum Switching VA ratings	30MVA	240kVA	30MVA	12MVA	30kVA	4MVA
Maximum operation junction temperature	125^0C	125^0C	125^0C	115^0C	175^0C	175^0C
On-state losses	Low	Low	Medium	Low	High*	Medium
Switching Losses	Very High	High	Very High	Medium	Very Low	Low
Turn-on ability	Medium (di/dt limit)	Medium (di/dt limit)	Medium (di/dt limit)	Medium (di/dt limit)	Very good	Very good
Turn-off ability	None via gate	Medium	Poor – slow and lossy	Good	Very good	Very good
Minimum on or off time	$10-100$µs	$10-50$µs	$10-50$µs	10µs	<100ns	<1µs
Maximum switching frequency	A few 100 Hz	A few 100 Hz	A few 100 Hz	A few 100 Hz	>50kHz	<25kHz
Control of switching time	No	No	No	No	Yes	Yes
Drive circuit power	Low	Medium	High	High	Low	Low
Drive circuit complexity	Low	Medium	High	High	Low	Low
Series and parallel operation	Yes	Yes	Difficult to series or parallel	Easy to series, difficult to parallel	Yes	Depending on type of IGBT technology.

* Voltage and current dependent.
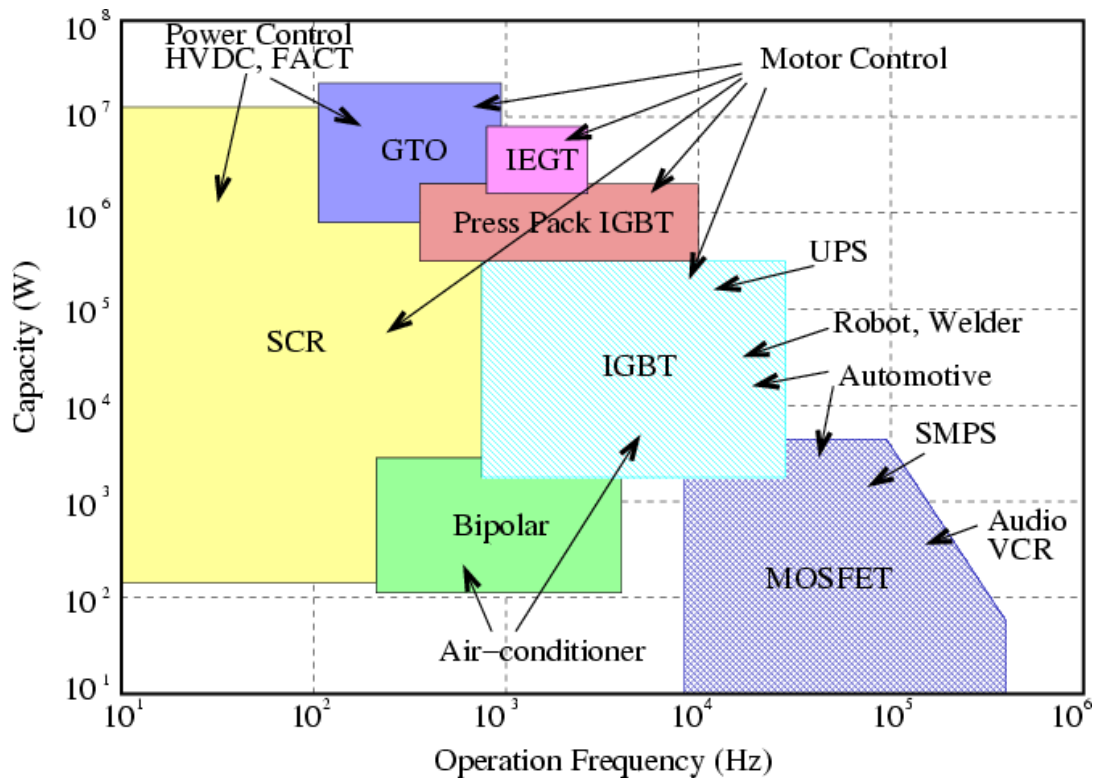
Figure 5-2: Application range of discrete power semiconductor device technologies in Silicon [5.5]

Power MOSFETs allow very high switching frequencies due to their method of conduction (Majority Carriers only), and commercially available MOSFETS have limited blocking voltage capability and high losses in the forward conduction mode for all but modest voltage & current ratings.

5.2.1.1. SILICON POWER MOSFETS

As described in the above section, Silicon power MOSFETs are more preferred for a low to medium power and high frequency operation. This section discusses the operation of a power MOSFET and its main limitation. The basic structure of a power MOSFET is shown in cross-section in Figure 5-3. Power MOSFETs have a drift region which is used to support the breakdown characteristics of the device and a buffer region that can be used to reduce the forward voltage drop of the device during the forward conduction mode.

The buffer region prevents the depletion region from reaching either the metallisation or the drain, which allows a reduction in the thickness N-drift region and thereby the on-state resistance. The on-state resistance of the Power MOSFETS is usually dependent on thickness and the doping concentration of the drift region. For high voltage and high current applications, the on-resistance of MOSFETs is usually higher than IGBT [5.6].
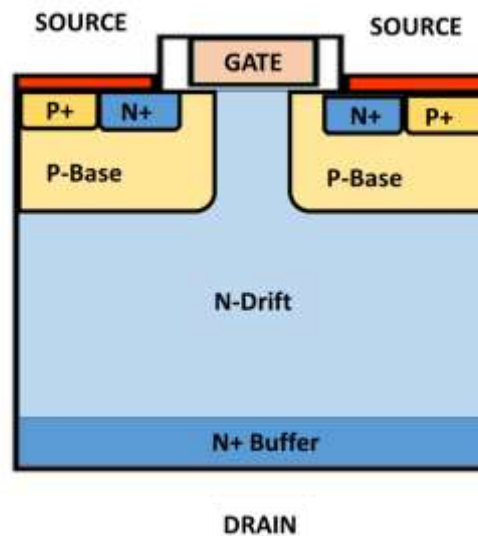
Figure 5-3: Structure of a Vertical MOSFET/ Power MOSFET

Figure 5-4 shows a cross-section through the structure of a Power MOSFET with the contributing factors toward the on-state resistance identified schematically, as a series connected set of discrete resistors. The total on-resistance (R_{DSON}) of this power MOSFET is the sum of all the effective resistances observed between the source and drain terminal:-

$$R_{DSON} = R_S + R_{CH} + R_a + R_{JFET} + R_n + R_D \quad ....(5.3)$$

Where R_S= Source resistance, R_{CH}= Channel resistance, Ra=Accumulation charge resistance, R_{JFET}= Intrinsic JFET resistance, Rn=Resistance of the epitaxial layer, R_D= Drain resistance.

The on-state resistance of a Vertical MOSFET is a function of the channel-length, channel doping concentration, depth of drift layer and its doping concentration. Therefore as the

breakdown voltage of the device is increased, the R_{DSON} and the on-state losses of the device also increase. The relationship between MOSFET breakdown voltage and the on-state resistance is broadly governed by equation 5.4. :-

$$\frac{V_{BR}^2}{R_{ON}} = \frac{\varepsilon\mu E_c^2(Si)}{4} \qquad \dots. (5.4)$$

Where V_{BR} = Breakdown voltage of the device, R_{ON}= On-state resistance of the device, μ=mobility of charge electrons, ε= permittivity, and E_C= Critical electric field [5.7]. As a useful guideline, the R_{DSON} of power MOSFETs is often considered to increase in proportion to the breakdown voltage to the power of 2.5 [5.8]. The R_{DSON} of power MOSFETs is also dependent on the charge carriers in the drift region during the conduction period. Due to its unipolar nature, the quantity of charge during forward conduction mode is greatly reduced, increasing the R_{DSON} of the devices rated substantially beyond 1.2kV. Various other structures and design features have been explored by manufactures to boost the carrier profile in the drift region [5.9] [5.10] [5.11]. However these structures tend to give rise to an increase in the switching losses, thereby limiting the switching frequency of MOSFETs.
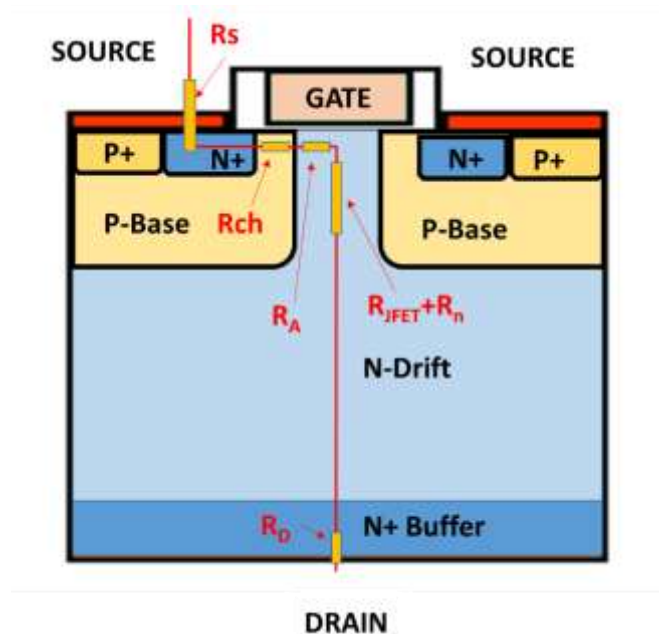
Figure 5-4: Components of Rds(on) in a Vertical MOSFET

Figure 5-5 shows the variation of specific on-resistance of commercially available Silicon MOSFETs with the breakdown voltage. As the required breakdown voltage ratings of Power MOSFETs are reduced, the lateral MOS structures become more favourable since they allow the removal of the drift and the buffer regions leading to a decrease in on-state resistance (R_{DSON}). The on-state resistance for these MOSFETs now depend only on the channel dimension (length and width) and its doping concentration. The channel resistance becomes the limiting factor on the on-resistance of the device performance. However as the breakdown voltages of these devices are much lower as compared to vertical structures (typically limited to <200V) , it may be necessary to consider alternative converter topologies, most notably the series connection of a number of devices so as to cater for a similar voltage application as compared to standard vertical power MOSFETs. The basic structure of a lateral MOSFET is shown in Figure 5-6.
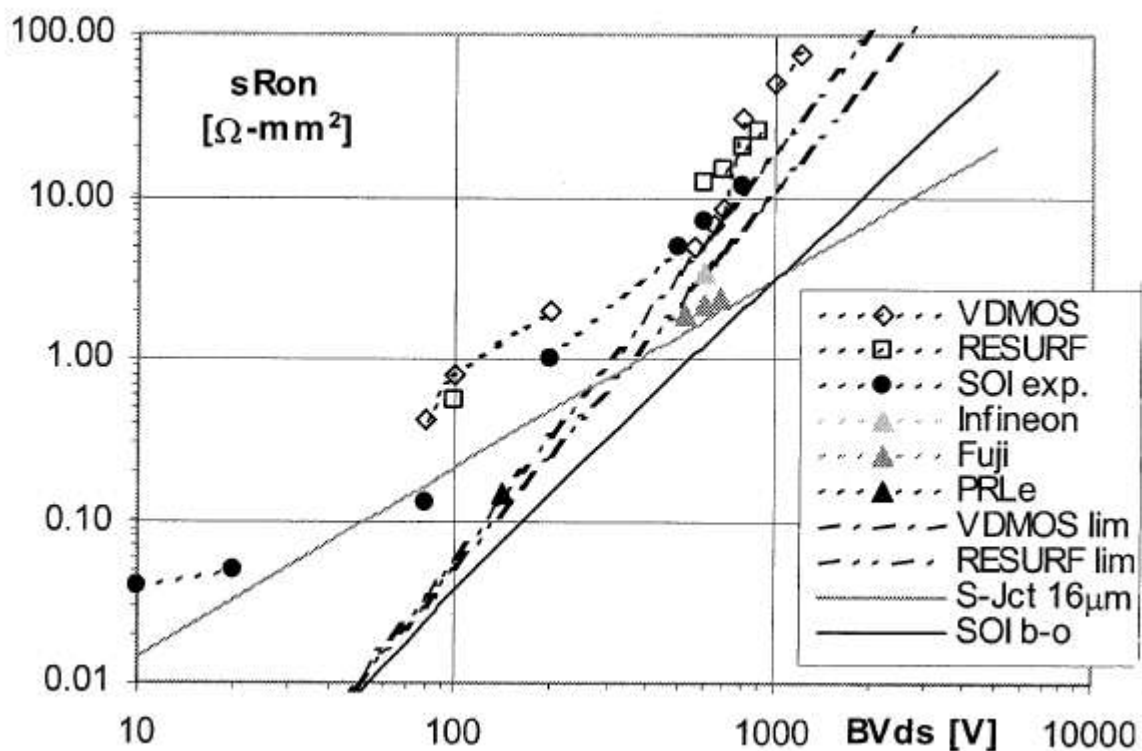
Figure 5-5: The specific on resistance ($R_{DS(ON-SP)}$) of MOSFETs with increase in their voltage ratings [5.2]
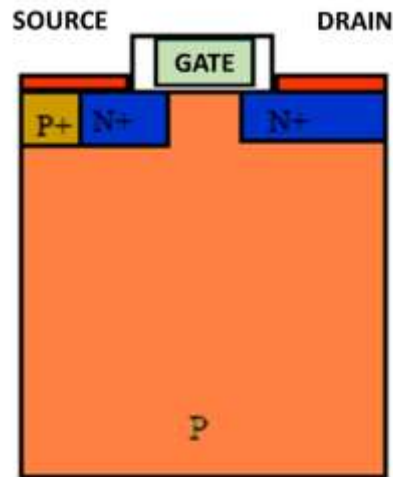
Figure 5-6: Basic Structure of a Lateral MOSFET

The main disadvantage of lateral structures as compared to vertical structures is that they have lower current density as the effective area of silicon is underutilised. The vertical region of Silicon is only used to support the breakdown voltage and does not take part in current conduction. However they can still be switched at very high frequencies, allowing the size of the passive elements to be reduced while improving the power density.

5.2.2. GALLIUM NITRIDE (GAN) BASED DEVICE TECHNOLOGY

Figure 5-7 shows the specific on-resistance as a function of the breakdown voltage for a number of different materials and technologies. This data was collected from [5.8]. It can be clearly seen that for a similar voltage rating, GaN material offers a much lower specific $R_{DS(ON-SP)}$ as compared to Silicon or Silicon Carbide. This offers scope for fabricated GaN devices to be smaller as compared to their Silicon or Silicon Carbide counterparts for a given breakdown voltage.

GaN based power devices are usually available in a HEMT structure (High Electron Mobility Transistor), a structure first described by T.Mimura et.al in 1975. This structure, a cross-section of which is shown in Figure 5-8, demonstrates an unusually high electron mobility

which is often referred to as a 2-D electron gas (2DEG). The presence of a 2DEG gas near the interface of the GaN and AlGaN heterostructure interface is responsible for the low on-state performance of the device. The GaN based HEMT structures are normally on-structures due to the large polarisation-induced charge carried in the AlGaN/GaN interface.

Similar to the Silicon MOSFET structure, the HEMT structure in its basic form has three terminals, viz. source, drain and gate. The source and drain terminals pierce through the top AlGaN layer to from an ohmic contact with the 2DEG- electron gas layer. This creates a short between the drain and source terminal, resulting in a normally-on device. In order to turn-off the device, a gate electrode is place on the top of the AlGaN layer such that a Schottky contact is formed in the top surface. When a negative voltage is applied to this contact, the Schottky barrier becomes reverse biased and the electrons underneath the gate region are depleted which in turn allows the device to turn-off.
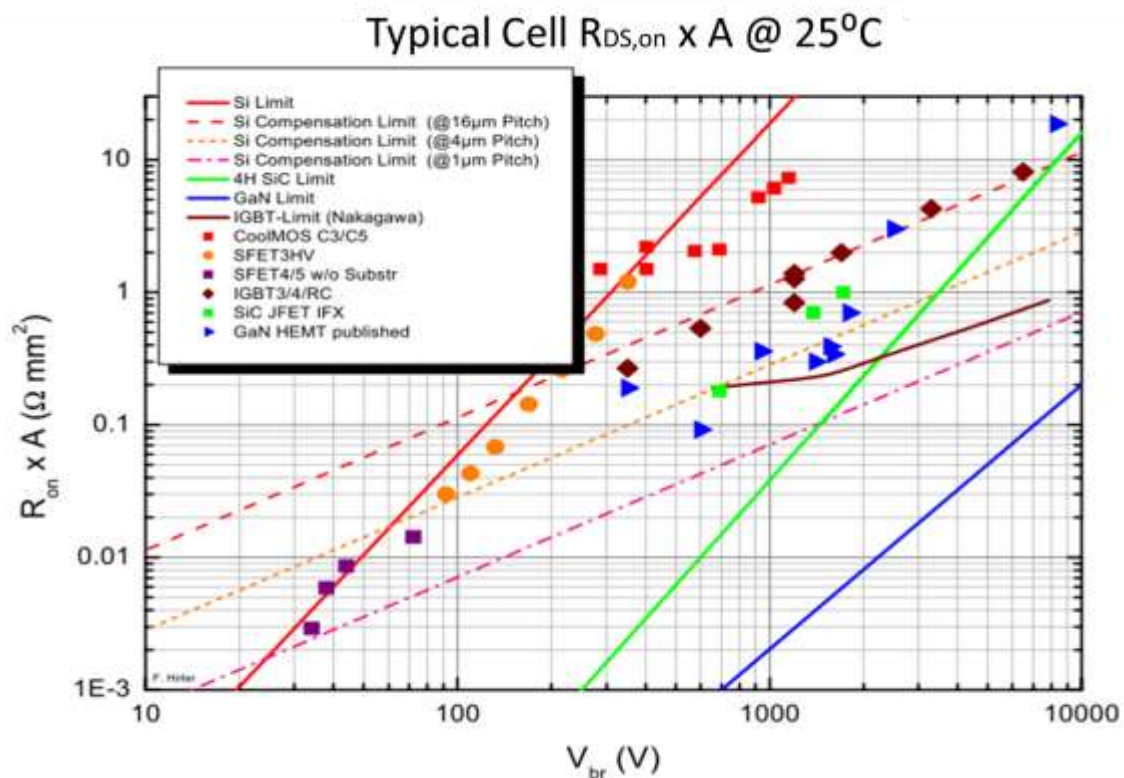
Figure 5-7: Ron*A relation with designed blocking voltage of Si, SiC and GaN-Mosfet and JFET devices as well as for bipolar IGBT devices [5.8]
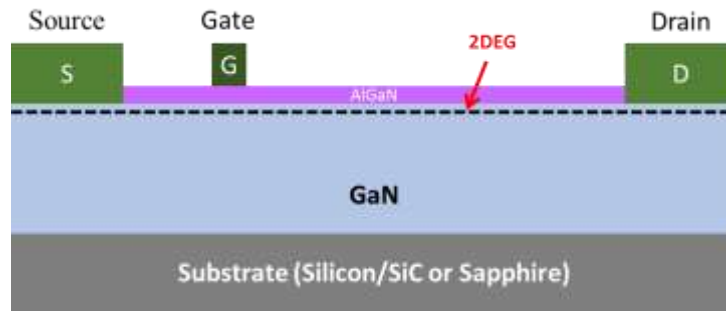
Figure 5-8: A typical AlGaN/GaN HEMT structure with three metal-semiconductor contacts

This type of device is usually referred to as a depletion mode HEMT structure. In most applications, a normally-off or enhancement mode device with a positive threshold voltage (V_{th}) is preferred over a depletion mode structure. This is to ensure the safe operation of the power converter during start up and during any failure of the control electronics or other componets. Various methods have been proposed in literature to develop an enhancement mode HEMT structure. The most common methods described in the literature are given below [5.12] .

1. Cascode configuration.

2. Fluorine Plasma Implantation. [5.13]

3. Recessed Gate Structure.[5.14]

4. Gate Injection Transistor Configuration. [5.15]

5. PN Junction Gates[5.16]

In early 2009, a few companies offered enhancement mode GaN devices with a view to catering to the power conversion market. A cross section of this structure is shown in Figure 5-9. Unlike Silicon devices, these devices are made by depositing a highly resistive layer of gallium nitride (GaN) over silicon (Si). A thin layer of Aluminium Nitride is used for Isolation between the GaN and Silicon Layers. An electron generating material is then applied to the GaN layer producing an abundance of electrons near the top of the underlying

GaN. The further processing of GaN layers assists in the formation of a depletion region under the gate.
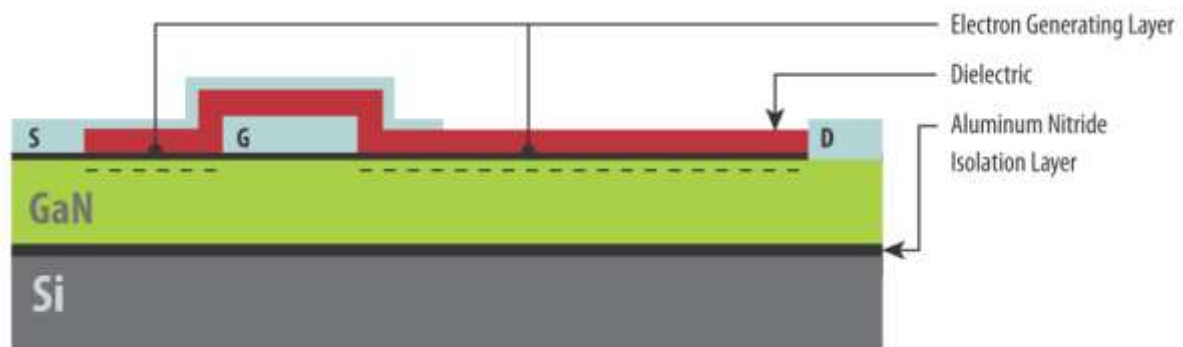
Figure 5-9: Structure of an enhancement mode GaN Power transistor [5.17]

Under normal conditions, theses device are in a normally off-state. However when a positive voltage is applied to the gate relative to the source, a field effect is created which attracts electrons to form a bidirectional channel between drain and source. The maximum ratings of these commercially available GaN devices are 200V/12A). Hence although they offer a potentially attractive device for power conversion, their limited voltage capability dictates that different topologies of power converters would need to be considered in order to cater to higher voltage applications. The breakdown voltage of GaN devices is usually increased by increasing the distance between the gate and the drain contacts and, since the resistivity of the GaN electron pool is very low, the impact of increasing the breakdown voltage of the on-resistance is also very low. The relationship between breakdown voltage to Ron for these devices is given in equation 5.5 [5.18].

$$V_{BR}^2 = R_{ON} * qn_s\mu \left(E_C^2\, E_p^2 \right) \qquad ....(5.5)$$

Where V_{BR}= Device breakdown voltage, R_{ON}= On-state resistance, q = electron elementary charge, n_s= 2DEG density of channel, μ= Mobility of carriers, E_C= Critical Electric Field GaN (Volts/cm), E_P= Polarisation Field. Therefore as the distance between the source and drain terminals are increased, the effect on on-state resistance is minimal. The breakdown

voltage of the GaN devices is usually increased by increasing the gate to drain distance. However in the absence of a field plate structure, the electric field is concentrated at the edge of the gate due to the positive polarisation charges at the AlGaN/GaN interface. Therefore, a field plate structure is essential to supress this electric field crowding and to ensure that the critical field strength across the device is effectively managed such that the surface electric field is maintained well below its critical point [5.19]. The structure of a GaN device with a field plate is shown in Figure 5-9.

5.2.3. SILICON CARBIDE BASED DEVICE TECHNOLOGY

During the initial stages of this study, Silicon Carbide devices (MOSFETs & BJTs) were not available commercially. However, more recent advancement of the fabrication process has made the performance of this technology increasingly more favourable than Silicon technology. This is specifically because these devices are available in higher current ratings and are capable of switching at much higher speeds as compared to Silicon based power devices. The reliability concerns surrounding SiC technology have been highlighted many times [5.20] [5.21]. The key properties of various material technologies are shown in Table 5-3.

Table 5-3: Material properties of GaN, SiC and Silicon [5.22]

Properties	Si	SiC	GaN	Diamond
Dielectric constant e	12	10	9.0	5.5
Mobility m [cm^2/Vs]	1450	1000	2000	3800
Field strength Ec [MV/cm]	0.25	2.5	3.5	5
Thermal conductivity sth [W/cmK]	1.5	4.5	1.3	21
$M^*_{RonA} = \varepsilon\mu E_C$	1	560	2100	9300
$M^*_{Loss} = \sqrt{\mu E_C}$	1	8.2	14	32
$M^*_{Area} = \varepsilon\sqrt{\mu E_C^2}$	1	68	150	290

* M_{RonA}, M_{Loss}, M_{Area} are figures of merits [5.22]

It can be clearly seen that GaN will offer much better performance in comparison to SiC, and is likely to ultimately offer a better performance/cost ratio when both technologies achieve some comparable level of maturity.

5.3.   POWER CONVERTER TOPOLOGIES

The general functionality required of any power conversion system is to convert electrical power from one voltage and/or frequency to another in a controlled manner as efficiently as possible. Many different power conversion topologies exist, and depending on the application and the requirement, a preferred topology is identified. Some topologies are specifically well suited to different motor types and some topologies are more general in that they can be used as a motor drive as well as for bus provision. Two-level power converters are the most commonly used for three phase converter topologies. Indeed they are the dominant topology in low to medium power applications (i.e. <100kW). The basic circuit arrangement of a 2-level converter is shown in Figure 5-10.
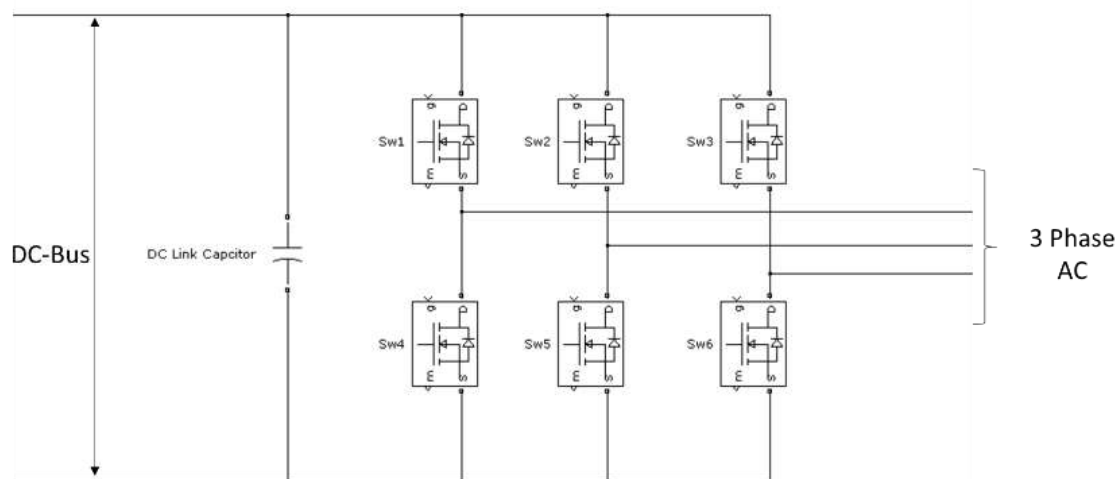
Figure 5-10: General arrangement of 3-Phase 2-Level voltage source converter

This arrangement can be considered as comprising of three single phase half bridge legs connected across a common DC voltage bus with each leg consisting of two series-connected

semiconductors switching devices equipped with accompanying freewheeling diodes. The rating and nature of the duty of diodes in the freewheeling path depends on the mode of operation. The 2-level power converter can generally be operated in two distinct modes:-

1. To function as an inverter providing a variable or fixed frequency ac voltage waveform. In this mode, the power converter could, for example, drive a multiphase AC electrical machine or provide a multiphase controllable AC supply from a DC bus.

2. To function as an active or passive rectifier to provide power from the AC side to the DC-bus.

The two-level, six-switch inverter of the type shown in Figure 5-10 is often used with some form of pulse width modulation (PWM) controller to control the switching devices, to synthesise the desired output at its output terminals. The switching frequency used is a trade-off between acceptable switching losses and suitable device technology and output filtering requirements. Most Silicon based power devices can be used in this configuration with DC bus voltages in the low kV range, as they are available at the different voltage and current ratings. However, commercially available GaN devices are at present only rated at modest voltage and current levels meaning that this topology would not be viable for power applications with bus voltages of a few hundred volts and above, e.g. 270V DC and 540V DC aerospace networks. In such cases, a multilevel converter arrangement needs to be adopted.

Indeed, multi-level converters are likely to provide a means for the outstanding performance of low voltage Silicon MOSFETs and high performance GaN enhanced mode devices to be exploited at representative aerospace power bus voltages.

5.3.1. MULTILEVEL CONVERTERS

In comparison to traditional two-level converters, multi-level converters can offer benefits in terms of improved power quality by switching a greater number of lower voltage levels. This improvement in the fidelity of the voltage waveform is achieved without increasing the switching frequency of the devices. Moreover, they offer scope to use lower voltage rated devices. The various other advantages and disadvantages of the multilevel converter as compared to a two level converter as discussed in detail in [5.23] [5.24]. A summary of the advantages and disadvantages are given below.

Key Advantages:-

- o **Reduced stress on semiconductor devices:** One of the key motivations for adopting multilevel converters is to reduce the voltage stress seen by the power devices to improve reliability.

- o **Improved power quality:** Increasing the number of levels allows the synthesis of the output waveform with a reduced harmonic content and, in turn, an improvement in the power quality of the converter.

- o **Reduction in the common mode voltage:** A number of mechanical failures in rotating machinery, principally as a result of bearing currents, have been linked to the common mode voltage and electromagnetic interference on two-level converters. The use of multilevel converters can result in the reduction of the common mode voltage and EMI filtering.

Key Disadvantages:-

- o **Increase in complexity of the system:** Since the number of individually controlled switches increase with the number of levels, the number of gate drive and isolated

power supplies required to power the gate drive also increases. In addition to this the complexity in the controller also increases markedly

o **Voltage balancing across levels:** As the number of levels increases the voltage levels across the capacitors need to be balanced to provide a sinusoidal output.

In the early days of solid-state power converter, many devices were interconnected in very high power and/or high voltage applications where a single power device was not able to cope with the application requirements. In such cases, several power devices were arranged in series and parallel combinations to improve the voltage and current handling capabilities. However, many problems were encountered in such converters as the devices did not have identical switching properties and hence additional circuitry was required to ensure that the current sharing issues were resolved and to ensure that the devices were not overly stressed. In order to accommodate such issues, in 1975 R.H.Baker and L.H.Bannister explored a new family of power converters mainly for high power applications [5.25]. The basic idea was to obtain the desired sinusoidal voltage by synthesising the waveform from various levels of DC voltage applied at the input stage of the converter. These converters are commonly known as multilevel converters. In their most elementary form there are three types of multi-level converters:-

- Cascaded multilevel converters.

- Diode clamped converters.

- Flying capacitor converters.

A comparison between the basic multilevel converter topologies is presented in [5.26] [5.27] [5.28]. A brief summary of these comparisons has been captured in the Table 5-4 below. The comparison is predominantly within the context of medium and high voltage power applications, where the converters were initially targeted. A detailed review of more recent

emerging topologies such as the mixed-level hybrid and asymmetric hybrid multilevel cells is contained in [5.28].

In order to explore the benefits of using a low voltage rated Silicon devices or GaN devices within a multi-level power converter application, a cascaded H-bridge arrangement was considered as a starting point. This topology has fewer number of power devices as compared to a diode clamped arrangement which, in turn, has a significant bearing on the complexity and power loss within the power converter particularly when the number of levels is increased. In addition, the cascaded H-bridge arrangement also allows the relatively straightforward evaluation of power loss. General arrangements of the basic multilevel converter topologies are shown in Figure 5-11, Figure 5-12 and Figure 5-13. The operation of such multilevel converter is described in detail in [5.24] [5.27] [5.28] [5.29].

Table 5-4: A high level comparison of the basic multi-level converter arrangements

Cascaded H-Bridge	Diode Clamped	Flying Capacitor
Advantages		
• Intrinsic voltage sharing. • Redundancy incorporated. • Circuit is modular.	• Can operate from a single DC-bus.	• Can operate from a single DC-bus • No diode required to clamp the input voltage.
Disadvantages		
• Each H-Bridge needs an isolated power supply which leads to complex transformer arrangement.	• Voltage balancing issues • Not modular. • Switching pattern is constrained. • Difficult to build in redundancy. • As number of levels increases the capacitor size increases • Increased component count as compared to the other arrangements	• Capacitors needs to be pre-charged to required voltage. • Switching pattern is constrained. • As number of levels increases the capacitor size increases.
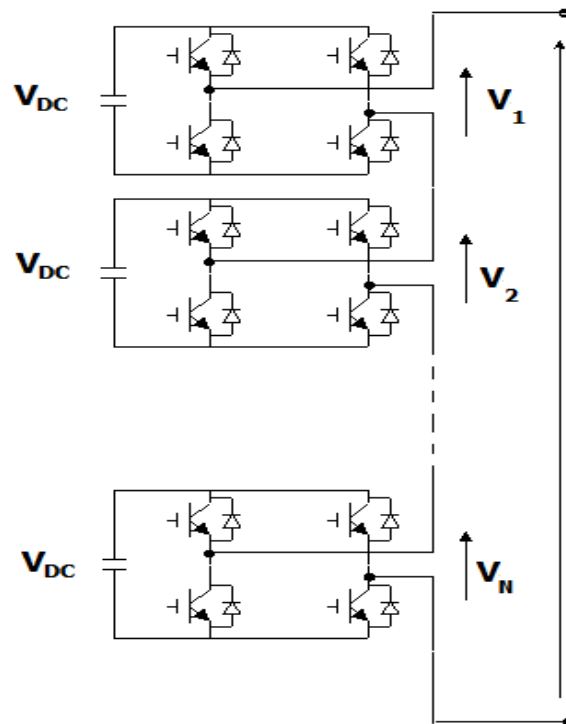
Figure 5-11: Cascaded H-Bridge Multilevel Topology (Single phase output) [5.27]
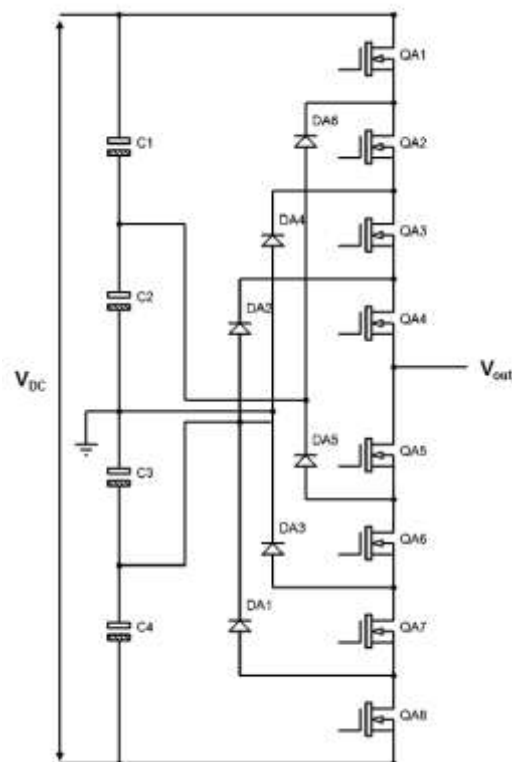
Figure 5-12: General arrangement of a diode clamped multilevel converter (Single phase output) [5.27]
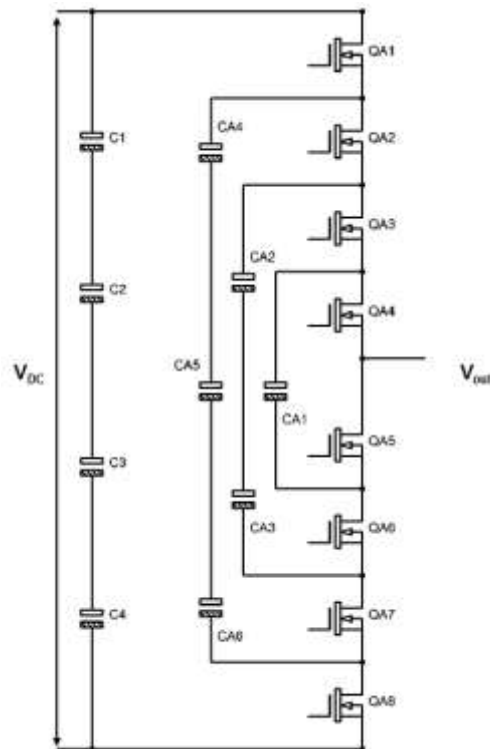
Figure 5-13: General arrangement of a flying capacitor multilevel converter (Single phase output)
[5.27]

5.4.   LOSS ANALYSIS OF LOW VOLTAGE SILICON DEVICES

In order to quantify typical performance benefits in terms of losses, a multilevel converter using low voltage silicon devices is compared to a 2-level converter using a single high voltage device. The investigation was carried out within the context of a 300V/50A single phase output converter as this was stated as a reasonable power level for the converters.

Table 5-5 shows all the commercially available devices that were considered for this study along with their basic characteristics.   It is important to note that the power devices listed in Table 5-5 are of different technology types and in order to compare then on common grounds, a figure of merit (FOM) needs to be defined. A FOM that has been commonly used by manufacturers to show both, improvement in power devices performance is the product of gate charge Q_G as well as $R_{DS(ON)}$ of the device. This is a useful method of comparison as it

is independent of the size of the die, the generation of device or technology. There are two distinct FOM defined - one which is used for transistors which operate more on the conduction period where Q_{GD} plays a less important role and, the other for hard switching applications where Q_{GD} is highly influential. A detailed analysis on the FOM is discussed in [5.30]. The second FOM is of greater importance for a hard switching application and Figure 5-14 shows the FOM of commercially available devices at different breakdown voltages for a hard switching application.

Table 5-5: Devices considered as a part of this study

Device	Rated Voltage (Volts)	Rated Current (Amps)	Rds (mΩ)	Gate Charge Q_{GD}
IXFN64N60P	600	50	96	68
FQL50N40	400	50	75	78
IXFV52N30P	300	52	66	53
IRFP260N	200	50	40	110
IRL3215PbF	150	12	166	21
HUF75542P3	80	75	14	33
FDD13AN06A0	60	50	13.5	6.4
IRLH7134PbF	40	50	2.8	16
IRLR3717	20	50	2.3	7.6
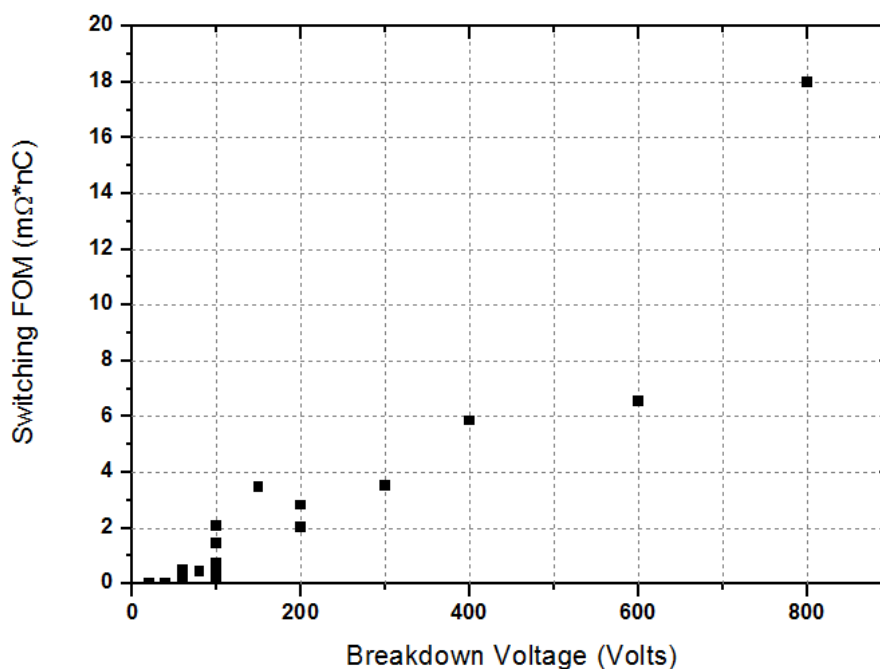
Figure 5-14: Switching figure of merit of Silicon MOSFETs for different voltage ratings

It can be clearly seen, from Figure 5-14 that the lower rated voltage devices can perform much better as compared to high voltage devices in terms of this FOM. Table 5-6 shows the total R_{on} of devices based on the number of levels (or H-Bridges) in the power converter. Although the R_{on} of individual devices is lower for low voltage rated devices, it is important to recognise that the effective Ron must account for the increased number of series connected devices. Notwithstanding the need for more devices, as the device rating is reduced to 40V the total Ron drops significantly as the drift region now contributes lesser to the on-state performance. As will be apparent from Table 5-6, for this selection of commercial devices, a minimum effective R_{on} is achieved with 40V rated devices.

Table 5-6: Ron comparison of series connected devices with number of levels

Device	Rated Voltage (Volts)	No of H-Bridges	No-of output levels	Effective Ron of devices (mΩ)
IXFN64N60P	600	1	3	190
IXFV52N30P	300	2	5	260
IRFP260N	200	3	7	240
IRL3215PbF	150	4	9	332
FDD13AN06A0	60	10	21	270
IRLH7134PbF	40	15	31	84
IRLR3717	20	30	61	138

The power losses within a converter tend to be dominated by the losses in the power semiconductor devices. The losses within the semiconductor devices are influenced by a number of factors. These include the conduction losses, the switching losses, forward blocking losses, diode losses (antiparallel diode/body diode) and gate drive losses. However, the conduction losses and the switching losses usually tend to dominate the power losses within a MOS controlled device and hence it is reasonable to disregard the leakage losses and other losses. The total losses in a power device can be expressed as a summation of the conduction and switching losses as shown in equation 5.6.

$$P_{Losses} \cong P_{Conduction} + P_{Switching} \qquad \text{.... (5.6)}$$

5.4.1. EVALUATION OF CONDUCTION LOSSES

The total on-resistance for a power converter application based on the number of levels is shown in Table 5-6. The average conduction loss within a power MOSFET in an H-Bridge configuration for a duty cycle D can be determined by:

$$P_{Conduction} = (R_{DSON-LS}+R_{DSON-HS}) \times I^2_{out(rms)} \times D \quad \dots \, (5.7)$$

Where, $P_{Conduction}$ = Conduction losses, $R_{DSON-LS}$ = On-resistance of the low side switch, $R_{DSON-HS}$ = On-resistance of the high side switch, $I_{out(rms)}$= RMS output current and D = Duty cycle. The total calculated conduction losses of the converter vs the number of levels in shown in Figure 5-15 for an rms output current of 50Amps. The total conduction losses of the low voltage devices, especially the 31 level converters, are ~43% lower as compared to the two-level converter thus illustrating the benefits of moving to low voltage silicon devices in terms of conduction losses.
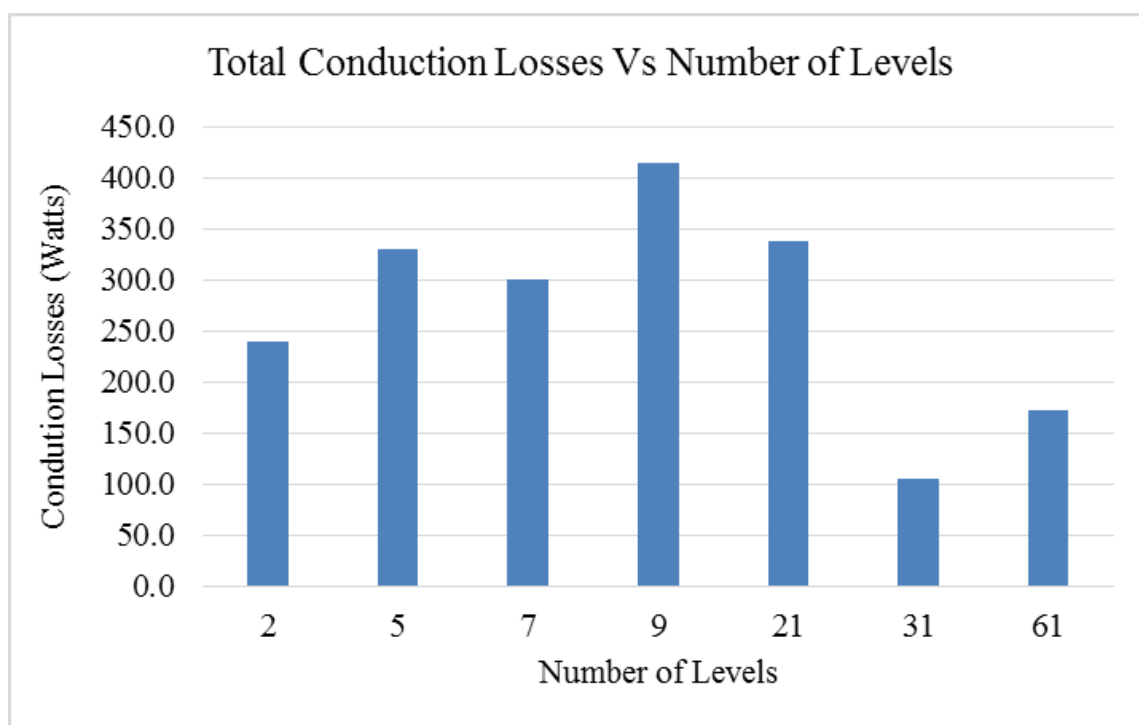
Figure 5-15: Variation of conduction losses in a single phase with number of levels (Silicon)

5.4.2. EVALUATION OF SWITCHING LOSSES

The time required to establish the voltage changes across the internal parasitic capacitance, determines the switching performance of the MOSFET. This dictates that the switching losses for similar voltage and current rated devices might vary significantly. This also means that as the drift depth is increased, the drain to source capacitance also increases the power dissipated during switching. The switching loss for the power devices is usually determined by the non-zero product of the drain current and the drain source voltage as shown in equation 5.8. The key factors that influence the switching loss of the device are:-

1. Rise and fall times of the output voltage and current,

2. Supply Voltage.

3. Output Current.

4. Frequency of operation.

Hence, the switching loss not only depends on the intrinsic properties of the switching device but also the nature of the application. However in order to support this comparison, the switching losses of the multilevel converter and the reference two-level converter are varied in order to understand the impact of the application. The switching losses of the MOSFET are usually expressed as:-

$$P_{Switching} = \frac{1}{2} * I_D * V_D * (t_{on} + t_{off}) * f + \frac{1}{2} * C_{OSS} * V_D^2 * f \quad \dots (5.8)$$

Where, $P_{Switching}$ = Switching losses, I_D = Drain current, V_D = Drain voltage, t_{on} = turn on time (as per datasheet), t_{off} = turn off time (as per datasheet), f = frequency of operation and C_{OSS} = device output capacitance. The first term represents the switching loss as the area under the I_D, V_D curve, while the second term accounts for the output capacitance loss. This energy stored within the intrinsic capacitance is usually dissipated within the MOSFET

during the turn-off phase of the device and this is not usually accounted for in the first part of the equation. However, it has been suggested [5.31] that this term can lead to an erroneous increase in the switching loss of the device. The operating voltage for the devices has been de-rated by 50% to ensure the devices are operated within their safe operating area. This de-rating factor is consistent with current design practices.
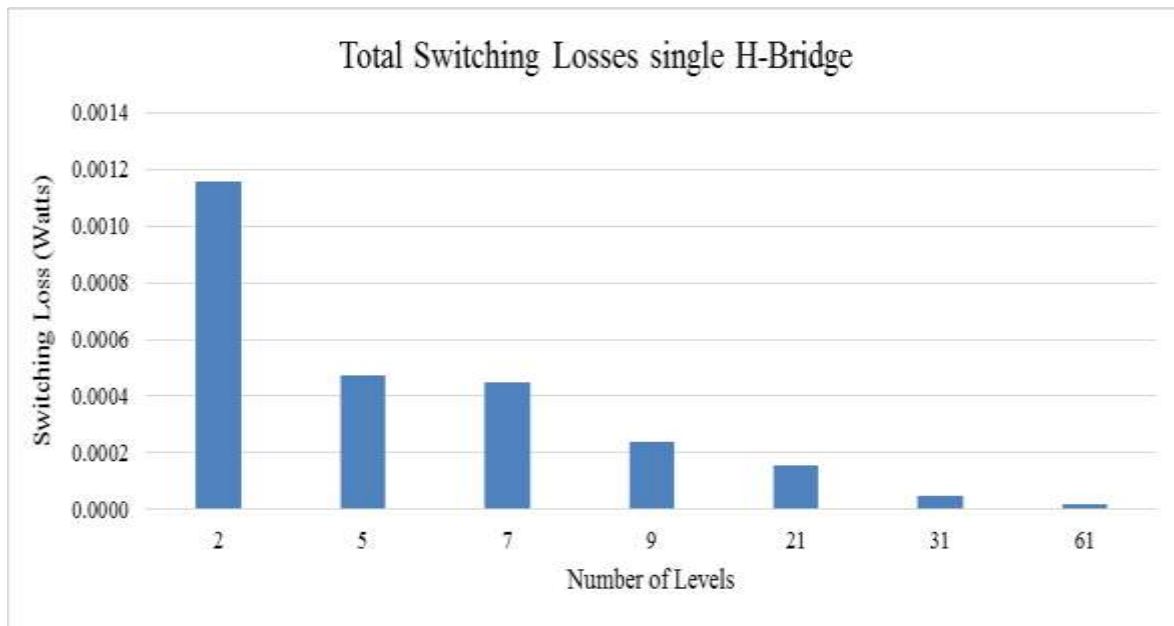
Figure 5-16: Switching loss of a single H-Bridge
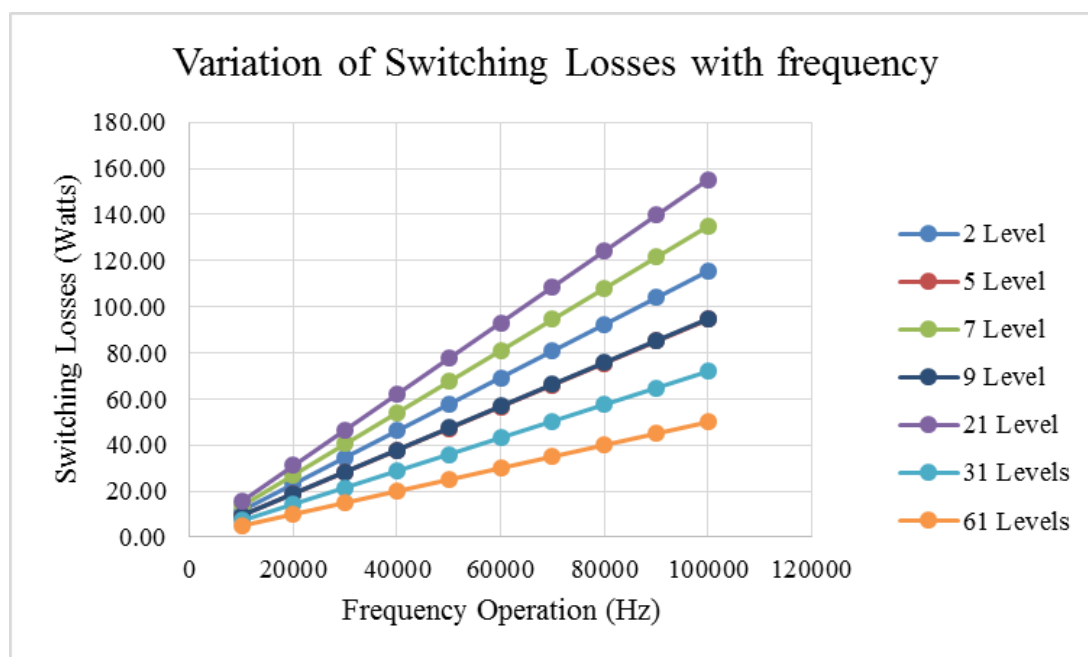
Figure 5-17: Total switching loss of the converter with number of levels

It is to be noted that for a similar quality of output the multilevel converter can be switched at a lower frequency. However, this has been ignored for time being to make a comparison in terms of the losses for similar switching frequency.

Figure 5-17 shows the resulting variation in switching losses of the power converter with the number of levels and variation of switching frequency. It can be observed that as the switching losses of the two-level converter seem to be more favourable as compared to a 7-level and 21 level multilevel converters. However, it is less favourable for the other options. This is solely due to the choice of device and its technology. The devices in the 9-level converter have same current rating as the GaN device hence these devices need to be paralleled and this has been accounted in the overall calculation. It has been assumed that the on-state resistance does not increase when these devices are paralleled. Figure 5-16 shows the switching loss comparison for a single H-Bridge configuration. Although the switching losses for the low voltage devices are far lower as compared to the high voltage devices, the number of levels has a major impact overall losses.

5.4.3.   TOTAL LOSSES OF LOW VOLTAGE SILICON DEVICES

This section shows the total loss of the converters with the use of low voltage silicon devices. Figure 5-18 shows the total loss of the power converter depending on the number of levels and with variation of switching frequency. It can be clearly seen that at a particular switching frequency, at least for the more practical options of 5 level and 7 level, the two level Silicon solution is more favourable in terms of losses as compared to a multilevel converter with low voltage silicon devices. However, the 2-level converter seems to be less favourable in terms of losses as compared to the 31-level and 61-level converters. This is due to use of fast switching low voltage silicon devices.
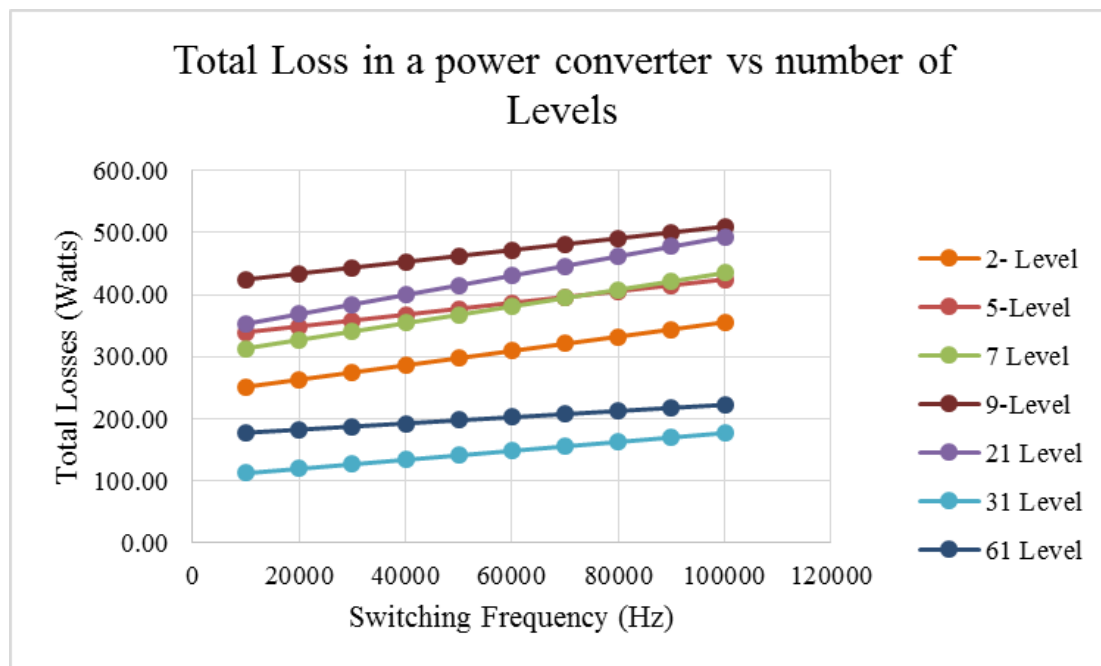
Figure 5-18: Total losses in the power converter with number of levels

5.5.   LOSS ANALYSIS OF GAN DEVICES

In order to compare the GaN based devices with their Silicon counterparts, a loss analysis was performed for commercially available GaN devices. Table 5-7 shows the commercially available GaN devices used for comparison along with their basic characteristics.

Table 5-7: Commercially available GaN devices used for comparison

Device	Rated Voltage (Volts)	Rated Current (Amps)	Rds (Ω)	Gate Charge Qgd
EPC1010	200	12	2.50E-02	3.50E-09
EPC1011	150	12	2.50E-02	2.80E-09
EPC1001	100	25	7.00E-03	3.30E-09
EPC1005	60	25	7.00E-03	2.50E-09
EPC1015	40	33	4.00E-03	2.20E-09

In comparison to Silicon devices, the GaN devices have a much lower on-state resistance and gate charge. This essentially means that the GaN based devices should produce lower losses in a multilevel converter application when compared to corresponding Silicon devices. Table 5-8 shows the variation of the on-state resistance with the number of levels.

Table 5-8: Ron comparison for series connected devices with number of levels

Device	Devices Voltage (Volts)	No of H-Bridges	Number of output Levels	Total number of devices	Rds(on) mΩ
EPC1010	200	3	7	12	0.15
EPC1011	150	4	9	16	0.2
EPC1001	100	6	13	24	0.084
EPC1005	60	10	21	40	0.14
EPC1015	40	15	31	60	0.12

Similar to the silicon devices it has been assumed that the on-state resistance does not increase when these devices are paralleled. In addition to this it has also been assumed that these devices can be switched at the speed suggested by the manufacture and the effects of parasitic components have been neglected.

5.5.1. EVALUATION OF CONDUCTION LOSSES

Although the operation of the GaN devices is different to those of Silicon devices, the conduction losses of the device are still largely determined by on-resistance seen across the device. Figure 5-19 shows the variation of conduction losses with the number of levels.
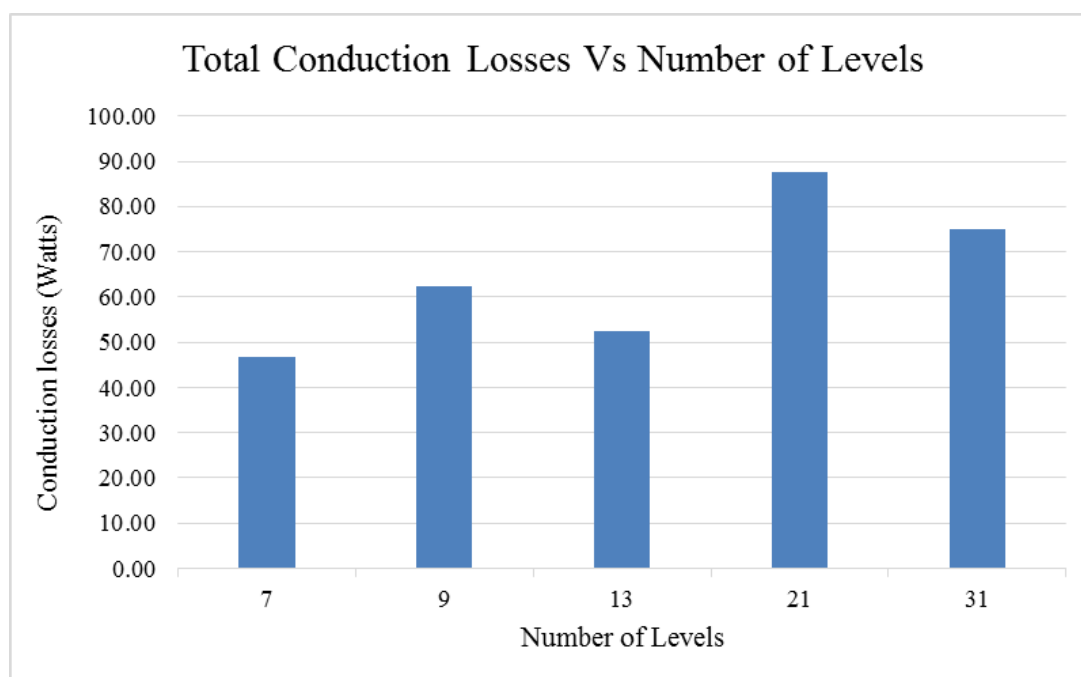
Figure 5-19: Variation of conduction losses with number of levels

The increase in the conduction losses for the 9 and 21 level converters is due to the increased number of series connected devices while employing devices with similar on-state resistance of the 7 level and the 13 level converters, respectively. The increase in losses of the 31 level converter can be attributed to the number of devices connected in series to derive the same output power.

5.5.2. EVALUATION OF SWITCHING LOSSES

The switching loss of GaN devices can also calculated in a similar manner to the Silicon devices for the same rated converter current of 50A. The switching losses of the GaN device as a function of switching frequency are shown in Figure 5-20.
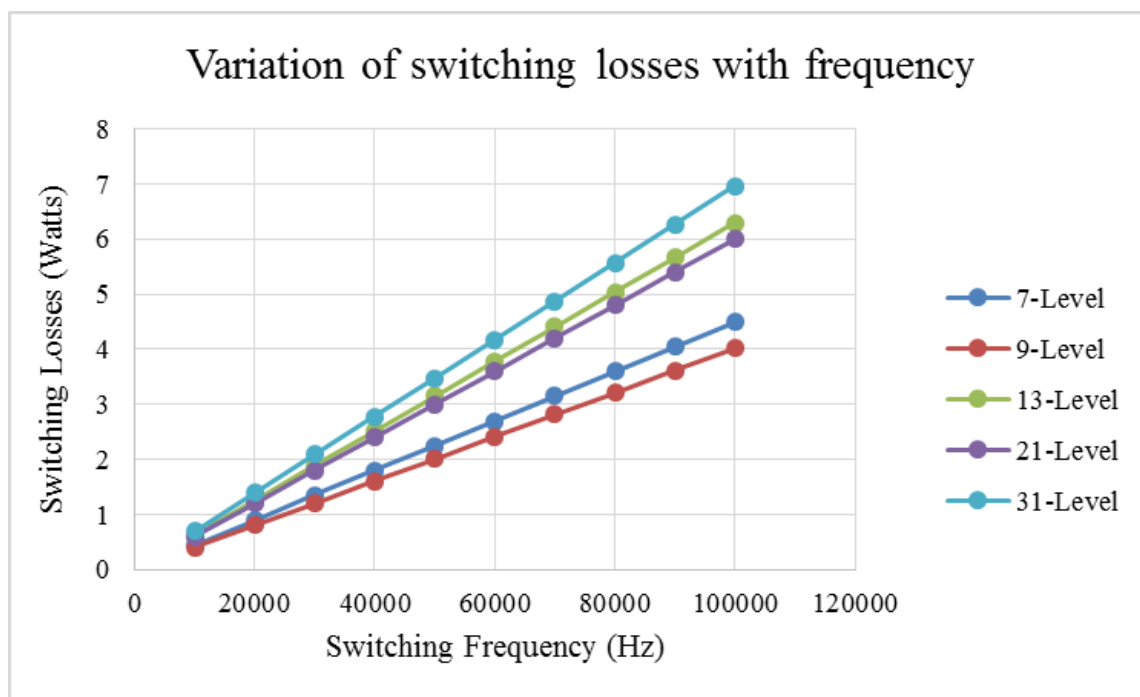
Figure 5-20: Variation of GaN converter switching loss with frequency

The switching losses of the GaN devices are far lower than the corresponding Silicon based devices. This is due to the superior critical field strength offered by the material as compared to Silicon devices. Therefore in principle, one should be able to operate the GaN devices at much higher switching frequency while also reducing the losses of the device substantially.

5.5.3. TOTAL LOSSES OF THE GAN DEVICES

The variation in the total losses of the GaN devices with switching frequency is shown in Figure 5-21. It can be observed that the losses of GaN devices seem to be reasonably independent of the switching frequency. This is because the losses in the GaN device are dominated by the on-state losses. Figure 5-22 shows the breakdown of conduction losses and switching losses for a 7-Level converter operated at a switching frequency of 100 kHz.
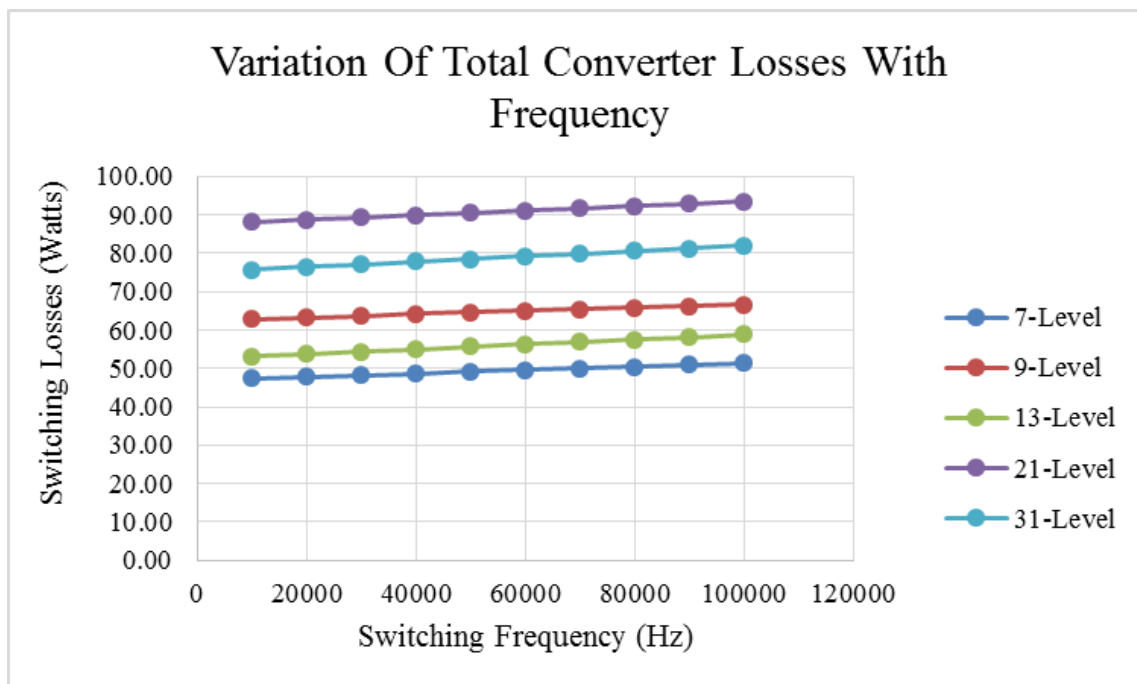
Figure 5-21: Total losses converter with variation of switching frequency
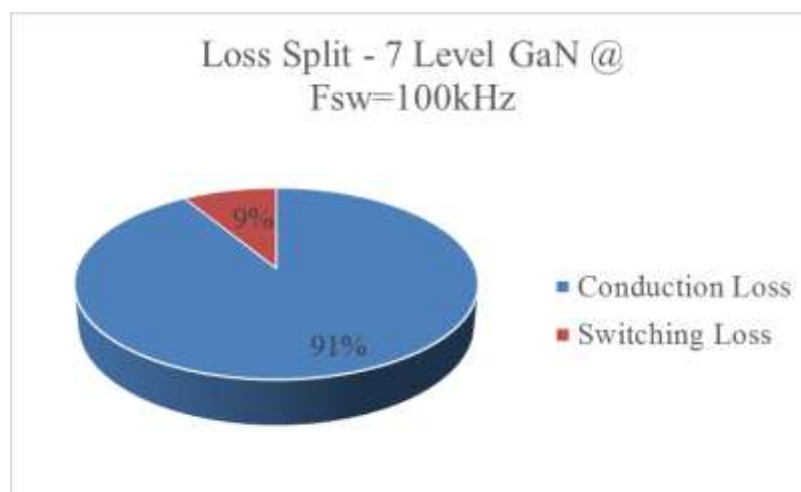
Figure 5-22: Comparison of switching losses and conduction losses

It can be clearly seen that the losses of the GaN transistor is mainly due to its operation in conduction mode, and in this case it is close to 91% of the overall losses. Therefore optimising the devices for the on-state operation would be very useful.

5.5.4. COMPARISON OF GAN AND SILICON DEVICES

Figure 5-23 shows the loss comparison of silicon devices in two-level and 31-level converters with respect to the losses of a seven-level converter equipped with GaN devices. It can be clearly seen that the GaN based device can offer a far superior performance in terms of losses as compared to the Silicon based device, particularly when switching at very high frequencies.
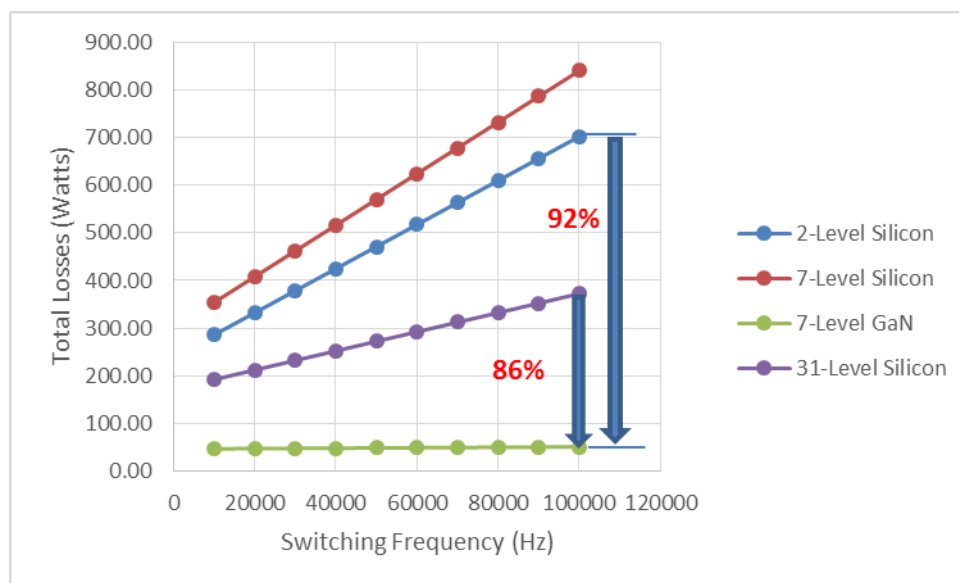
Figure 5-23: Comparison of GaN and Silicon devices in a multilevel converter

The total losses in a 7-Level GaN converter is 92% lower than an equivalent 2-level silicon converter operating at 100 kHz, and 86% lower than an equivalent 31-level silicon converter operating at 100kHz. As the GaN devices show much lower losses as compared to Silicon devices. A multilevel converter with low voltage GaN devices is proposed. The remaining

part of this chapter experimentally compares the commercially available GaN device with an equivalent Silicon.

5.6. EXPERIMENTAL EVALUATION OF Si AND GAN DEVICES

As demonstrated by the theoretical considerations above, a GaN device appears as a favourable device option when compared to a Silicon MOSFET in the power range considered. This section experimentally evaluates the performance of commercially available GaN devices as compared to Silicon devices, so as to establish the extent to which these theoretical properties can be achieved in a practical circuit arrangement. The GaN devices listed previously in Table 5-8 usually come in a flip-chip package design [5.32]. The flip-chip concept was initially developed by IBM for solid state computing systems. The implementation of the flip-chip design in power devices is to reduce the signal inductance and to improve the device reliability and performance.
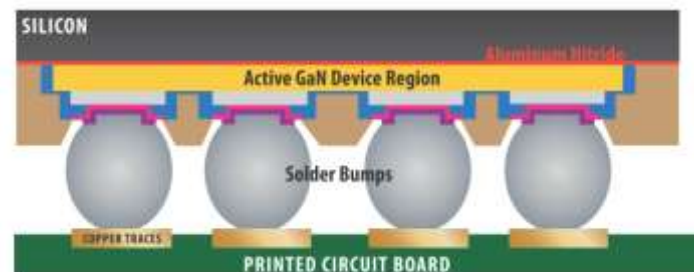
Figure 5-24: The flip chip design used for the GaN devices

The basic principle which underpins the flip chip, is to introduce a solder bump which replaces the solder wires used traditionally to contact the die surface. The chip is then flipped face down onto the package carrier using a reflow process. Bump sizes ranges from 10-100 microns. Figure 5-24 shows the flip chip design for commercially available GaN devices and Figure 5-25 shows the pad layout for the same [5.32].
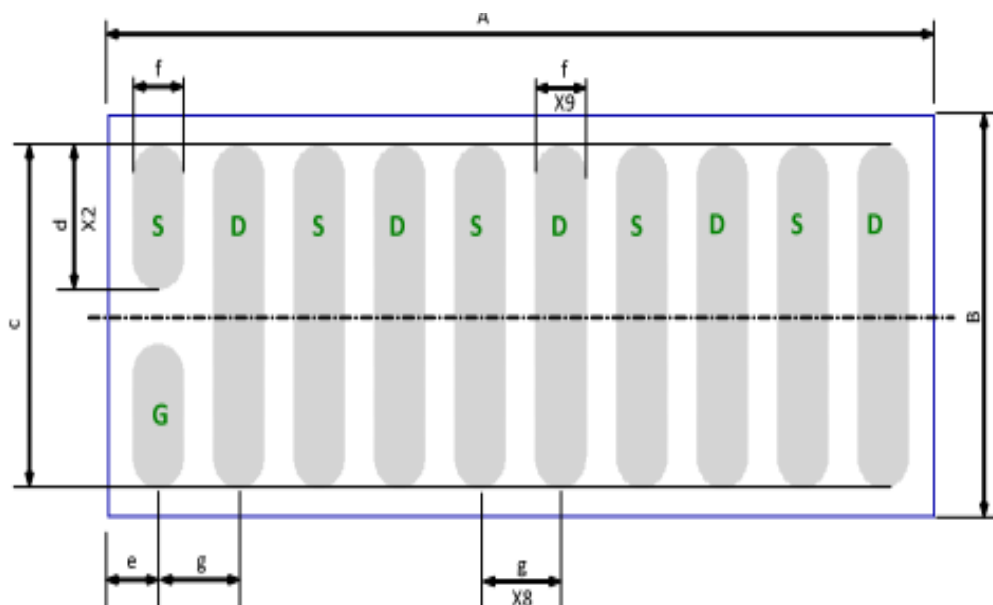
Figure 5-25: The general pad layout for the EPC devices

In order to test the device performance, a PCB was developed to form the basic building block of the power converter. The design of the PCB block is as shown in Figure 5-26.
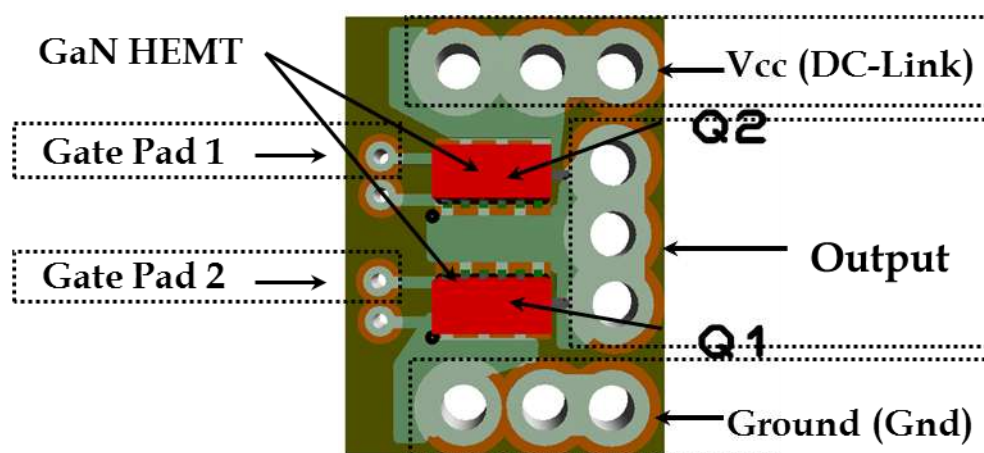
Figure 5-26: PCB Layout for the initial testing of GaN devices

The goal was to develop a half bridge module in order to test the basic performance and the functionality of the GaN device, and then use this as a building block to implement a complete power converter. Q1 and Q2 form the top and bottom half devices of the phase leg respectively. The circuit diagram for the plug-in module is contained in Appendix D.

5.6.1.   STATIC CHARACTERISTICS

The static characteristics of the devices were evaluated using a Tektronix 310B curve tracer.

Figure 5-27 shows a typical I-V characterises of the GaN device in comparison to Silicon. It

can be observed that the GaN device saturates at much higher current. Therefore, the GaN

device will be subjected to a higher current during the short circuit phase.
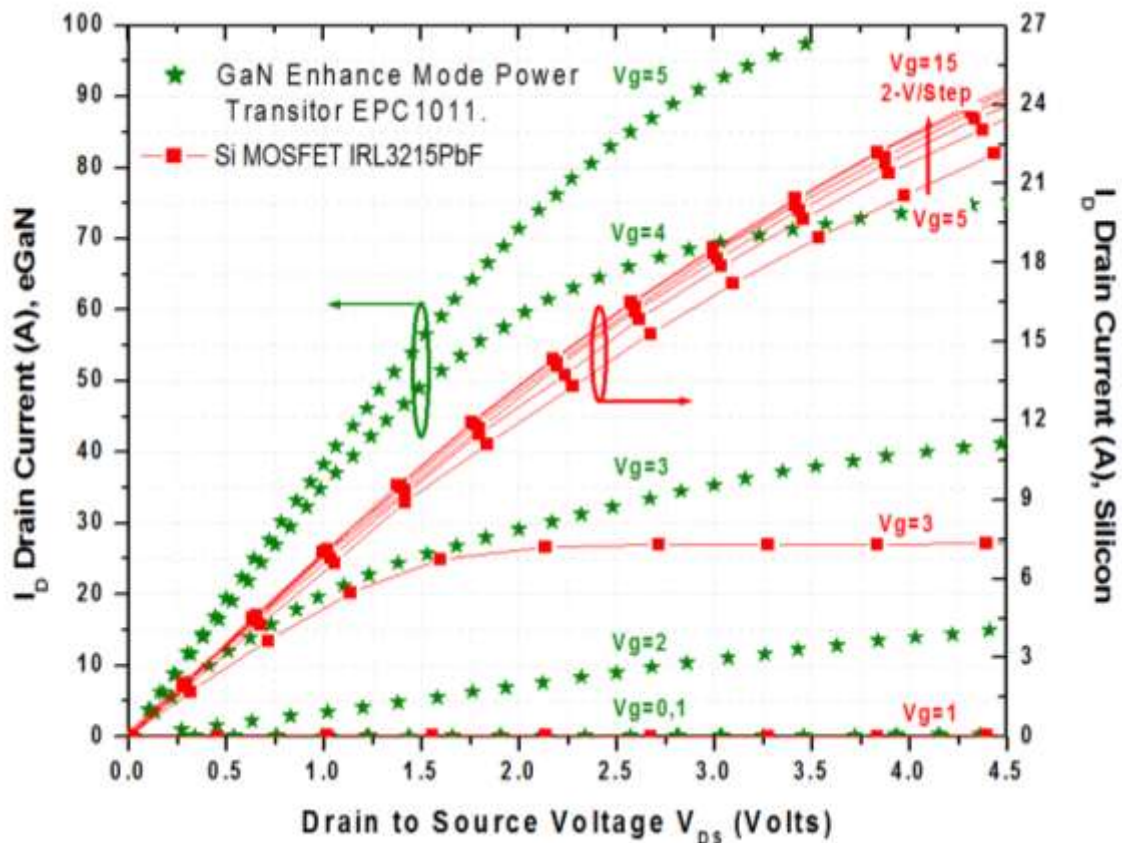
Figure 5-27: Measured I-V characteristics of GaN and Silicon Devices

Figure 5-28 clearly shows the improvement in the on-state performance of the GaN devices

compared to the Silicon devices. The specific R_{on} was found to be some 10 times lower than

that of an equivalently rated Silicon device. The temperature co-efficient of R_{on} was found to

be similar to those of silicon devices (1.45 in GaN devices and 1.7 in Silicon). This positive

coefficient allows the GaN device to be paralleled in order to cater to higher current

applications.
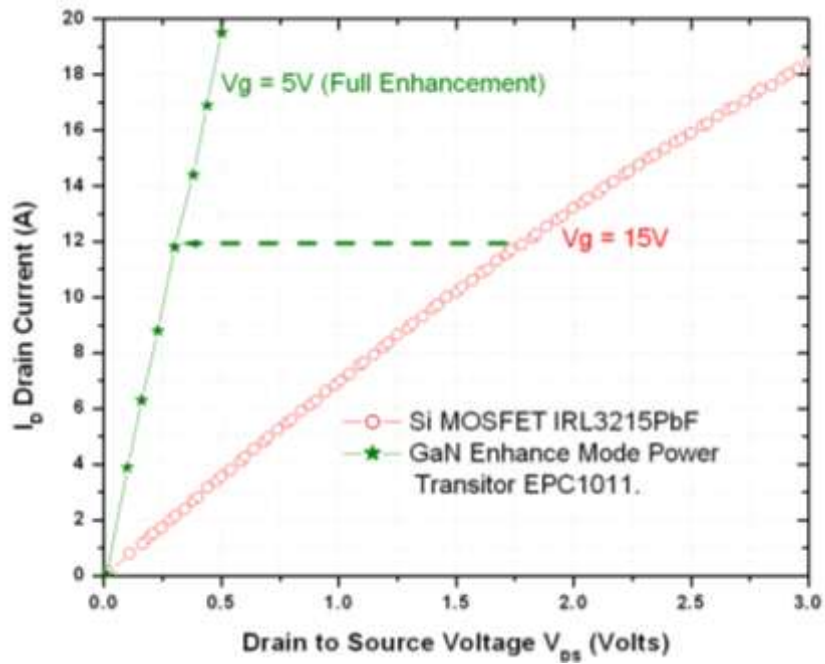
Figure 5-28: Measured on-state comparison at full enhancement of the channel

The measured threshold voltage of GaN devices is slightly lower to that of the Silicon devices, as shown in Figure 5-29. However they cannot be treated as simple replacement plug-in devices for Silicon, as the gate drive considerations are very different.
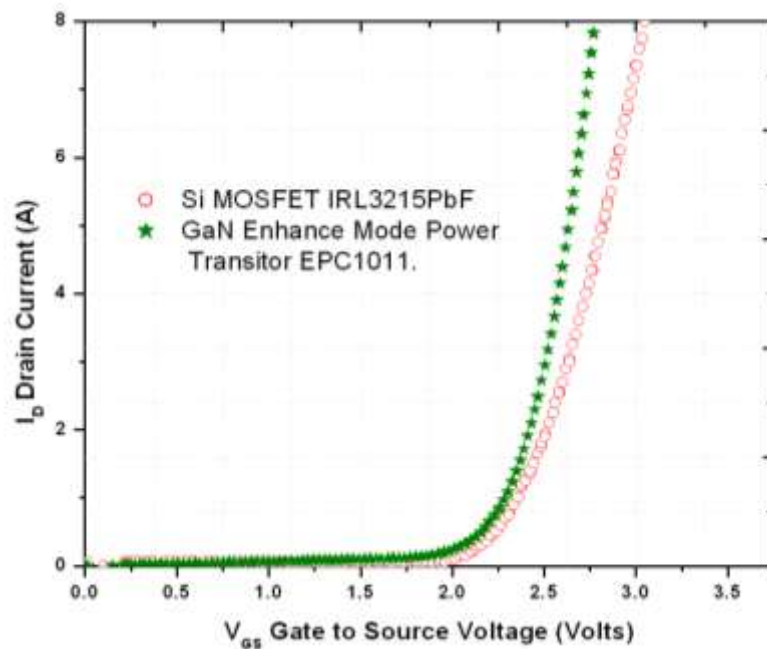
Figure 5-29: Measured threshold voltage comparison of GaN and Silicon Devices

It has been suggested by the GaN device manufacturer that a low inductance path should be provided from the gate driver to the device gate pads in order to avoid undesirable turn-on of the device during switching conditions. It is recommended that the maximum inductance at the gate terminal be less than 2nH.

5.6.2. DYNAMIC CHARACTERISATION

The dynamic performance of the devices was measured using a clamped inductive switching circuit similar to the one it will encounter in a hard switching application. During the initial phase of testing, it was observed that the stray inductance associated with the setup was prohibitive, leading to excessing oscillation in the anode output waveforms. Therefore a snubber circuit was introduced to decouple the stray inductance associated with the test rig. The switching results for the GaN and the Silicon devices are shown in Figure 5-30.
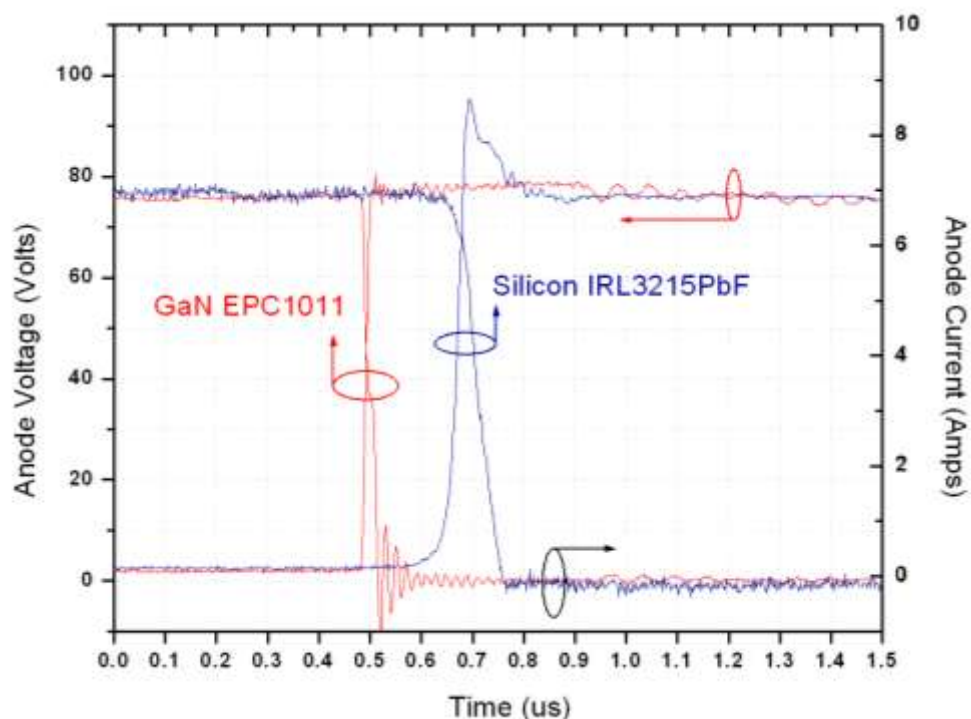
Figure 5-30: Experimental Turn-off switching waveforms of GaN EPC1011 and Silicon Devices (IRL3215PbF)

It can be clearly seen that the GaN devices outperform the Silicon devices and, more specifically, that he measured turn-off losses of the GaN devices are 26% lower than an equivalent silicon devices. Figure 5-31 shows the variation in Vce with Eoff, of both Silicon and GaN devices. It can be clearly seen that the GaN devices outperform the Silicon devices both in terms of switching and turn off performance.
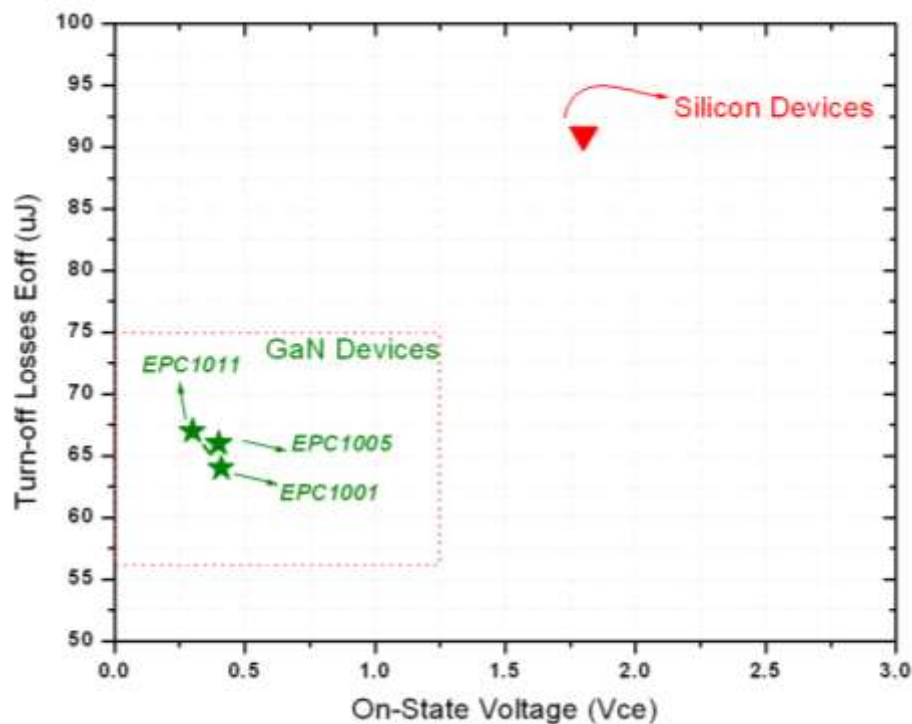
Figure 5-31: Comparison of Turn-off losses and on-state voltage of the devices at V=1/2BV, Rg=22Ω, Vg=5(GaN) and ±15 V(Silicon)

5.6.3. SHORT CIRCUIT PERFORMANCE TEST

The short circuit ruggedness of a device is another key metric for high power applications. The circuit used for testing the short circuit performance of the device is similar to the one shown in section 3.7. The aim of this test is to verify if the device would be able to withstand the required short circuit period of 10µs without failure. A drain voltage $60V_{DC}$ is applied across the device while the load is disconnected. During this period the current is limited by the saturation properties of the devices as discussed previously in section 3.7. Figure 5-32

and Figure 5-33 shows the measured short circuit performance of GaN and Silicon devices, respectively.
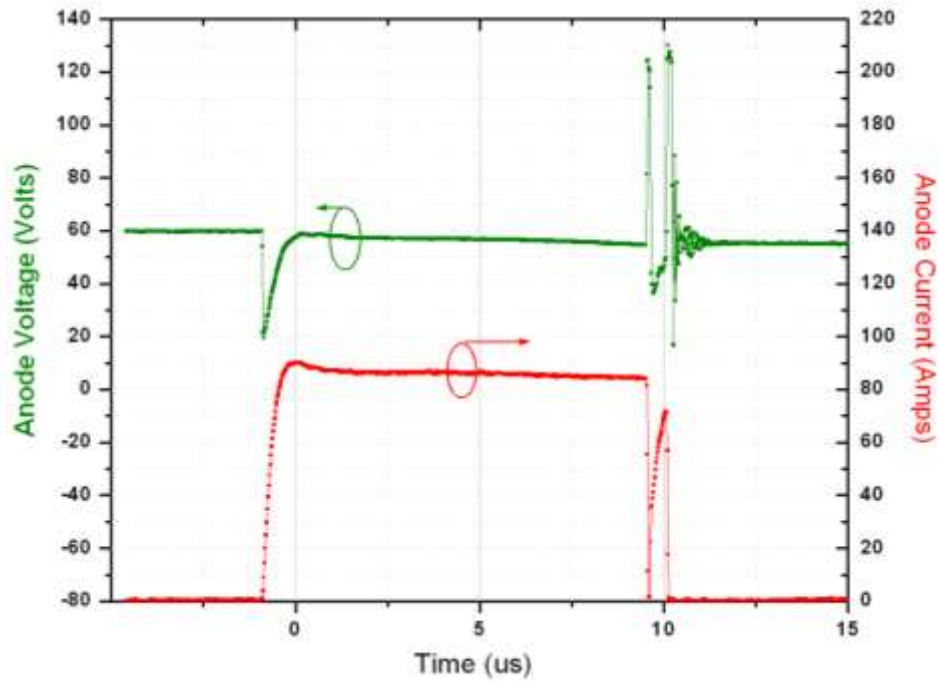
Figure 5-32: Measured short Circuit Performance of GaN devices at Rg=22Ω, T=250C and Vg=5V, VDC=60V
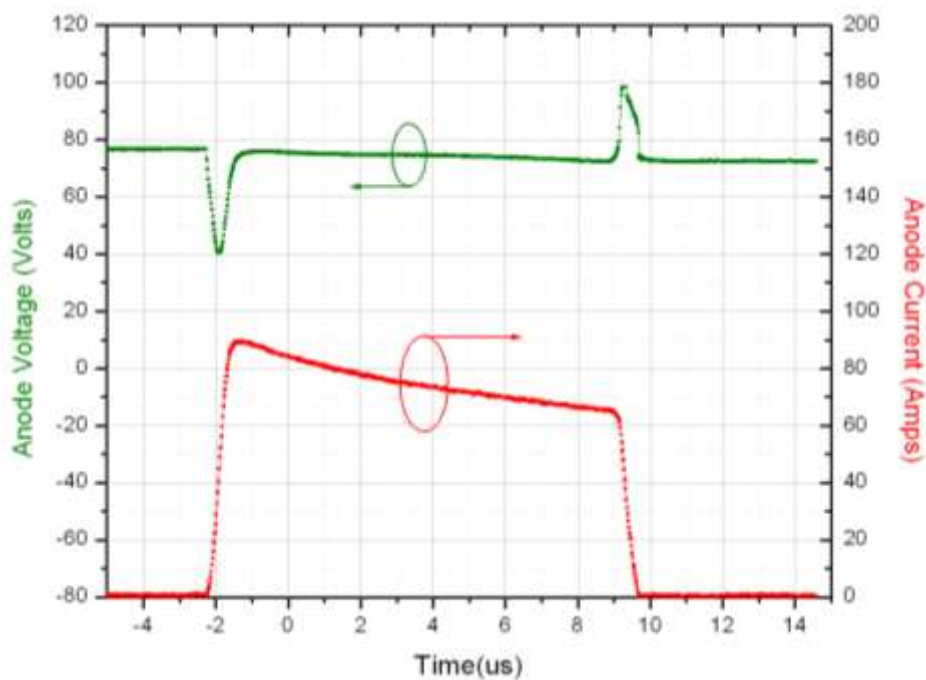
Figure 5-33: Short Circuit Performance of Silicon devices at Rg=22Ω, T=250C and Vg=15V, VDC=75V

As seen in Figure 5-32, the GaN devices show a false turn-on during the end of the short circuit period. This is due to the stray inductance associated with the gate end of the device. Therefore, the layout of the gate driver plays a very important role in determining the performance of the GaN device and these needs to be taken into account during the design of the power converter.

5.7.   CONCLUSION

The results presented in this chapter indicate that GaN based devices can, where appropriate ratings exist, provide a far superior performance as compared to Silicon devices for a similar power conversion application. The total estimated losses in the seven-Level GaN power converter show a power loss reduction by as much as 92% and 86% as compared to the two-level silicon converter and 31-Level silicon converter of the same rating.

5.8. REFERENCES

[5.1]   H.Ohashi, "Recent Power Devices Trend," *J.IEEJ,* vol. 122, pp. 168-171, 2002 2002.

[5.2]   R. P. Zingg, "On the specific on-resistance of high-voltage and power devices," *Electron Devices, IEEE Transactions on,* vol. 51, pp. 492-499, 2004.

[5.3]   J. W. Kolar, U. Drofenik, J. Biela, M. L. Heldwein, H. Ertl, T. Friedli, *et al.,* "PWM Converter Power Density Barriers," in *Power Conversion Conference - Nagoya, 2007. PCC '07,* 2007, pp. P-9-P-29.

[5.4]   B. Drury, *Control Techniques and Drives Hand book*, 2nd Edition ed.: Institution of Engineering and Technology 2009.

[5.5]   J.M.Park. (2004, Novel Power Devices for Smart Power Applications.

[5.6]   B. J. Baliga, "Trends in power semiconductor devices," *Electron Devices, IEEE Transactions on,* vol. 43, pp. 1717-1731, 1996.

[5.7]   B. J. Baliga, *Fundamental of Power Semiconductor Devices*: Springer, 2008.

[5.8]   G. Miller, "New semiconductor technologies challenge package and system setups," in *Integrated Power Electronics Systems (CIPS), 2010 6th International Conference on,* 2010, pp. 1-6.

[5.9]   H. Haimeng and C. Xingbi, "Optimization of Specific On-Resistance of Balanced Symmetric Superjunction MOSFETs Based on a Better Approximation of Ionization Integral," *Electron Devices, IEEE Transactions on,* vol. 59, pp. 2742-2747, 2012.

[5.10]   V. Khanna, *Novel IGBT Design Concepts, Structural Innovations, and Emerging Technologies* 2003.

[5.11]   S. Iwamoto, K. Takahashi, H. Kuribayashi, S. Wakimoto, K. Mochizuki, and H. Nakazawa, "Above 500V class Superjunction MOSFETs fabricated by deep trench etching and epitaxial growth," in *Power Semiconductor Devices and ICs, 2005. Proceedings. ISPSD '05. The 17th International Symposium on,* 2005, pp. 31-34.

[5.12]   J. Shuo, C. Yong, W. Deliang, Z. Baoshun, L. Kei May, and K. J. Chen, "Enhancement-mode AlGaN/GaN HEMTs on silicon substrate," *Electron Devices, IEEE Transactions on,* vol. 53, pp. 1474-1477, 2006.

[5.13]   C. H. Chen, C. W. Yang, H. C. Chiu, and J. S. Fu, "Characteristic comparison of AlGaN/GaN enhancement-mode HEMTs with CHF$_3$ and CF$_4$ surface treatment," *Journal of Vacuum Science & Technology B: Microelectronics and Nanometer Structures,* vol. 30, pp. 021201-021201-6, 2012.

[5.14]   W. B. Lanford, T. Tanaka, Y. Otoki, and I. Adesida, "Recessed-gate enhancement-mode GaN HEMT with high threshold voltage," *Electronics Letters,* vol. 41, pp. 449-450, 2005.

[5.15]   Y. Uemoto, M. Hikita, H. Ueno, H. Matsuo, H. Ishida, M. Yanagihara, *et al.,* "Gate Injection Transistor (GIT)—A Normally-Off AlGaN/GaN Power Transistor Using Conductivity Modulation," *Electron Devices, IEEE Transactions on,* vol. 54, pp. 3393-3399, 2007.

[5.16]   X. Hu, G. Simin, J. Yang, M. A. Khan, R. Gaska, and M. S. Shur, "Enhancement mode AlGaN/GaN HFET with selectively grown pn junction gate," *Electronics Letters,* vol. 36, pp. 753-754, 2000.

[5.17]   S. L. C. a. R. A.Beach. (2011, Fundamentals of Gallium Nitride Power Transistors. *(1).*

[5.18]   N.Zhang, "High Voltage GaN HEMTs with Low On-Resistance for Switching Application," PhD, University of California, Santa Barbara, 2002.

[5.19]   A. Nakajima, M. H. Dhyani, E. M. S. Narayanan, Y. Sumida, and H. Kawai, "GaN based Super HFETs over 700V using the polarization junction concept," in *Power Semiconductor Devices and ICs (ISPSD), 2011 IEEE 23rd International Symposium on,* 2011, pp. 280-283.

[5.20] T. Santini, M. Sebastien, M. Florent, L. V. Phung, and B. Allard, "Gate oxide reliability assessment of a SiC MOSFET for high temperature aeronautic applications," in *ECCE Asia Downunder (ECCE Asia), 2013 IEEE*, 2013, pp. 385-391.

[5.21] K. Sumi, M. Das, B. Hull, R. Sei-Hyung, J. Scofield, A. Agarwal, *et al.*, "Gate oxide reliability of 4H-SiC MOS devices," in *Reliability Physics Symposium, 2005. Proceedings. 43rd Annual. 2005 IEEE International*, 2005, pp. 592-593.

[5.22] S. E. Madathil, "GaN Power Device Technologies," presented at the NMI, 2014.

[5.23] M. Schweizer, I. Lizama, T. Friedli, and J. W. Kolar, "Comparison of the chip area usage of 2-level and 3-level voltage source converter topologies," in *IECON 2010 - 36th Annual Conference on IEEE Industrial Electronics Society*, 2010, pp. 391-396.

[5.24] R. Teichmann and S. Bernet, "A comparison of three-level converters versus two-level converters for low-voltage drives, traction, and utility applications," *Industry Applications, IEEE Transactions on,* vol. 41, pp. 855-865, 2005.

[5.25] R. H. B. a. L.H.Bannister, "Electric Power Converter," U.S. Patent, 1975.

[5.26] C. R. a. R. R. R. Diorge Alex Bao Zambra, "Comparison among three topologies of multilevel inverters," *9th Brazillan Power Electronics Conference,* pp. 528-533.

[5.27] N. Mittal, B. Singh, S. P. Singh, R. Dixit, and D. Kumar, "Multilevel inverters: A literature survey on topologies and control strategies," in *Power, Control and Embedded Systems (ICPCES), 2012 2nd International Conference on*, 2012, pp. 1-11.

[5.28] J. Rodriguez, L. Jih-Sheng, and P. Fang Zheng, "Multilevel inverters: a survey of topologies, controls, and applications," *Industrial Electronics, IEEE Transactions on,* vol. 49, pp. 724-738, 2002.

[5.29] L. Jih-Sheng and P. Fang Zheng, "Multilevel converters-a new breed of power converters," in *Industry Applications Conference, 1995. Thirtieth IAS Annual Meeting, IAS '95., Conference Record of the 1995 IEEE*, 1995, pp. 2348-2356 vol.3.

[5.30] A. Yoo, M. Chang, O. Trescases, W. Hao, and J. C. W. Ng, "FOM (Figure of Merit) Analysis for Low Voltage Power MOSFETs in DC-DC Converter," in *Electron Devices and Solid-State Circuits, 2007. EDSSC 2007. IEEE Conference on*, 2007, pp. 1039-1042.

[5.31] Z. J. Shen, X. Yali, C. Xu, F. Yue, and P. Kumar, "Power MOSFET Switching Loss Analysis: A New Insight," in *Industry Applications Conference, 2006. 41st IAS Annual Meeting. Conference Record of the 2006 IEEE*, 2006, pp. 1438-1442.

[5.32] J. C. P. a. Y. M. P. E.A. Alana Nakata, "Assembling EPC GaN Transistors," E. Corporation, Ed., ed, 2011.

CHAPTER SIX

ANALYTICAL AND EXPERIMENTAL EVALUATION OF GaN BASED DEVICES IN A MULTILEVEL CONVERTER

6.1.   INTRODUCTION

In the previous chapter it was shown that low voltage Silicon devices and GaN power devices can be used in a multilevel converter application due to their low conduction and switching losses when compared to an appropriate higher voltage Silicon device. In this chapter, Silicon and GaN devices are evaluated analytically in the context of a full converter in order to validate the findings of chapter 5. The impact of using ultra low-loss power devices on other elements of the converters such as the heat sink and passives components, are discussed. The chapter concludes by experimentally validating the loss predictions of commercially available GaN devices.

6.2.   CONVERTER LOSS ANALYSIS

In order to establish the losses of the devices in a converter application, a circuit and an associated loss model was developed in MATLAB-Simulink (using the simPowerSystem toolbox). The model was developed to predict the device losses in a converter more accurately as the voltage and current waveforms are time, temperature and load dependent. The general block diagram of the loss model is shown in Figure 6-1. The different functional blocks associated with the loss estimation model are described in this section.

Various methods have been discussed in literature for estimating losses of switching devices in a converter [6.1] [6.2] [6.3] [6.4] [6.5]. Among all these methods, two distinct methods have been used extensively to predict losses, viz. analytical loss modelling techniques and behavioural loss modelling techniques. The analytical loss modelling technique is very useful for determining the on-state conduction losses of the device. However, they tend to have

limited accuracy in determining the switching losses. The analytical method also suffers from greater computational time as compared to the behavioural method. In addition, the analytical method also requires a greater understanding of the physics of operation of the devices and since the selected devices are of different technologies and voltages, a comparison using this method would be very difficult and time consuming.

Behavioural modelling, on the other hand, is known to offer a reasonable accurate estimation of the switching and conduction losses (typically within 10% although this is dependent on device type and operating condition) without requiring excessive simulation time of the converter as described in [6.6] [6.4]. The basic principle involves the extraction of the device specific parameters from datasheets, device simulation or experimental measurements, and then using this information to estimate the losses of the devices in a converter application using relatively straightforward expressions.
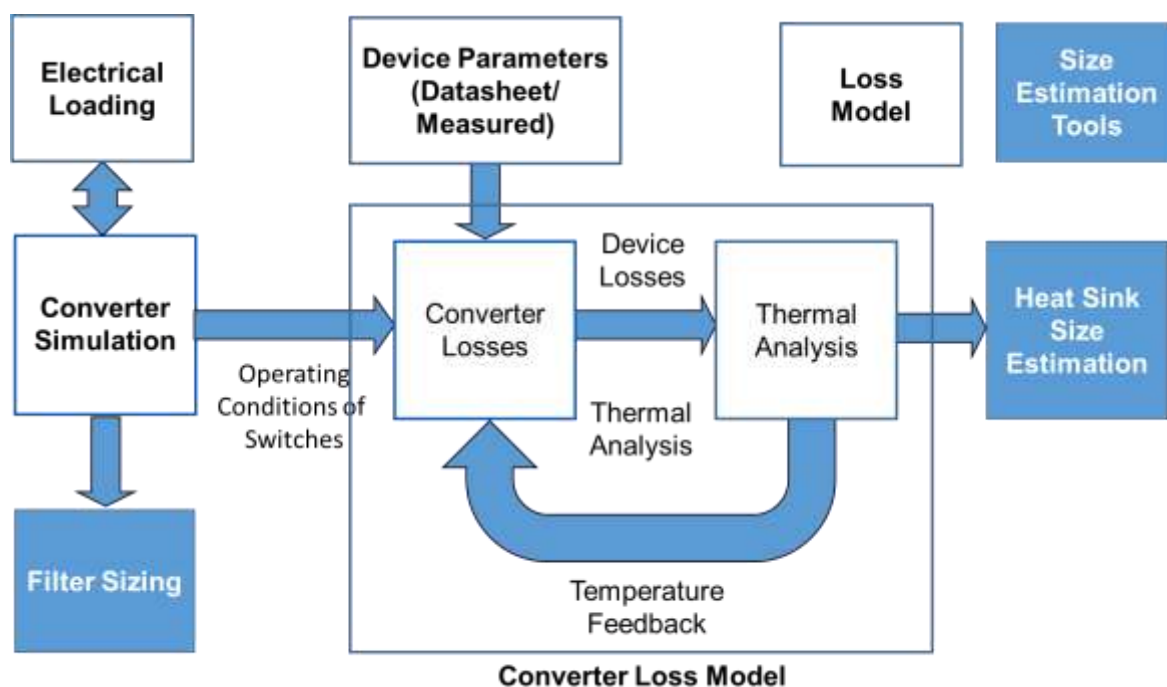
Figure 6-1: Block diagram of the loss estimation model

This method also allows the temperature and gate drive dependency to be evaluated as they can be included in the measurements or simulations results. This approach further allows the simulation of various converter topologies and device technologies to be considered within a reasonable simulation time, i.e. much shorter than analytical loss modelling techniques. Against this background, behavioural models were preferred for estimating device losses in a converter application. The loss model presented in this chapter comprises of the following key blocks.

- Electrical Loading Block

  o This block contains the electrical load that is connected to the power converters in order to estimate the losses in a converter. A purely resistive load was used to estimate the losses of the devices and to understand the relative performance benefits of the various devices selected.

- Converter Simulation Block

  o This block contains the basic elements of the power converter. For the purposes of calculating current and voltage waveforms, the switching devices are simulated as ideal switches. These waveforms then form the input for the converter loss estimation model.

  o The modulation strategy of the power converters and the reference gate signals are also derived in this block. A phase shifted PWM modulation scheme is used to exercise control over the current and voltage waveforms applied to the load. An open loop control is currently considered within the simulation. The modulation scheme, which is described in [6.7] [6.8] [6.9], is commonly used in cascaded H-bridge converters. The modulation strategy is based around the application of modulation signal to one half of a single H-Bridge and the phase shifted version of the signal (phase shift=180^0) to the other half bridge. These signals are then compared with the

triangular carriers to obtain the gate reference signals for the switching devices. The carrier and reference signals applied to a two level converter for a carrier frequency of 10 kHz is shown in Figure 6-2. A similar method has been used to previously measure converter losses [6.10].
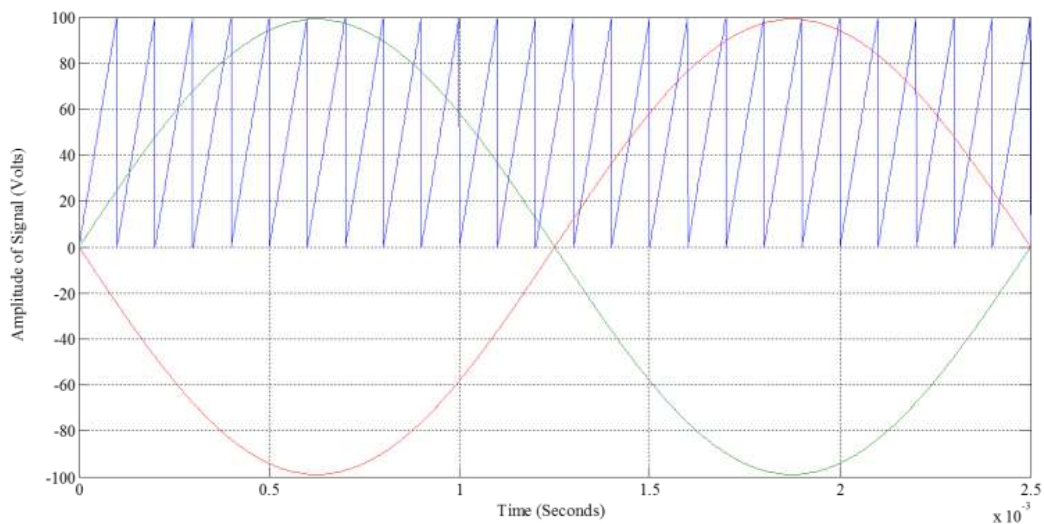
Figure 6-2: Carrier and reference signals for 2 level converter using phase shifted PWM
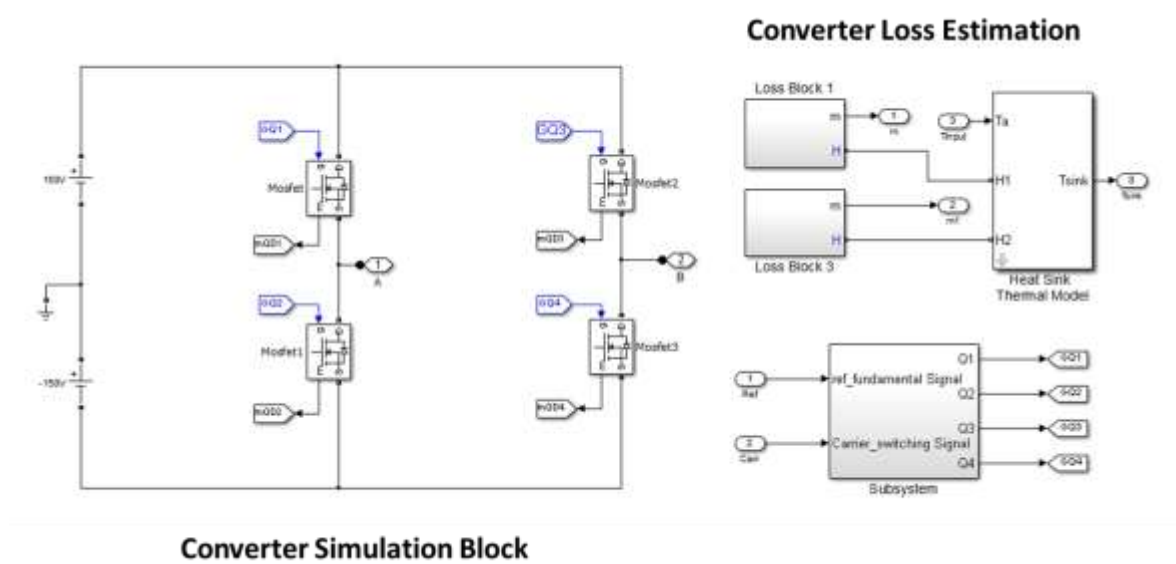
Figure 6-3: Simulink model for single phase 2-level converter along with loss estimation block

o This block can be adapted to accommodate different devices and the number of levels required.

- o The Simulink model of the 2-level converter is shown in Figure 6-3. As will be apparent, voltage and current measurements are used in the loss estimation block.

- Converter Loss Estimation Block.

  - o The Simulink model of the loss estimation block is shown in Figure 6-4. The model is divided into three distinct parts, viz. the device loss model, the diode loss model and the thermal loss model.

  - o This block receives voltage and current measurements from each individual switching device in the converter switching model.

  - o The device specific parameters and coefficients can be obtained from measured, simulated or from datasheets. These are used in the loss estimation model using an initialising script which is then used to calculate losses of the devices.
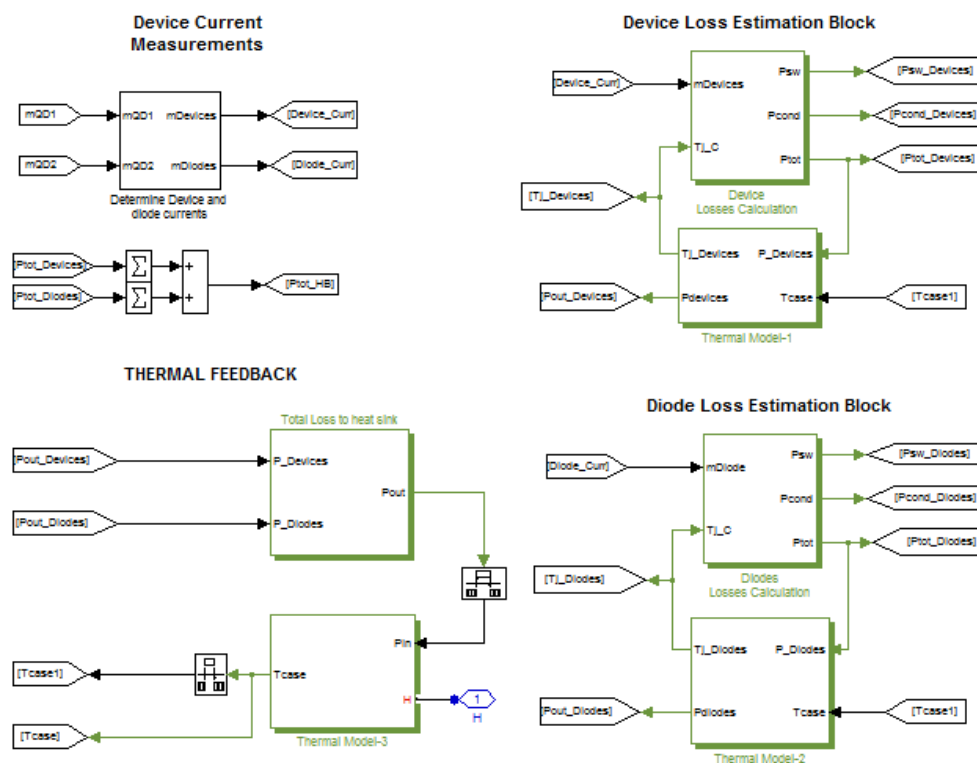
Figure 6-4: Simulink Model for the loss estimation block

o The thermal model for the converter is used to calculate the instantaneous junction temperature of the devices which is then fed back into the loss estimation model to determine the change in conduction and switching losses. A constant coolant temperature of 40^0C is assumed for all simulations and the thermal resistance of the cold plate is kept at the same value of 0.006^0C/W in order to provide a consistent comparison.

o The values of thermal resistance provided by device manufacturers are used to calculate the junction temperature of the device.

o The Simulink models for the device and diode loss estimation blocks are shown in Figure 6-5 and Figure 6-6 respectively. As seen in Figure 6-5 and Figure 6-6 the devices currents and temperatures are used to estimate the losses using a look up table. The overall loss of the converter is established from a summation of losses in all the switching devices of the power converter.
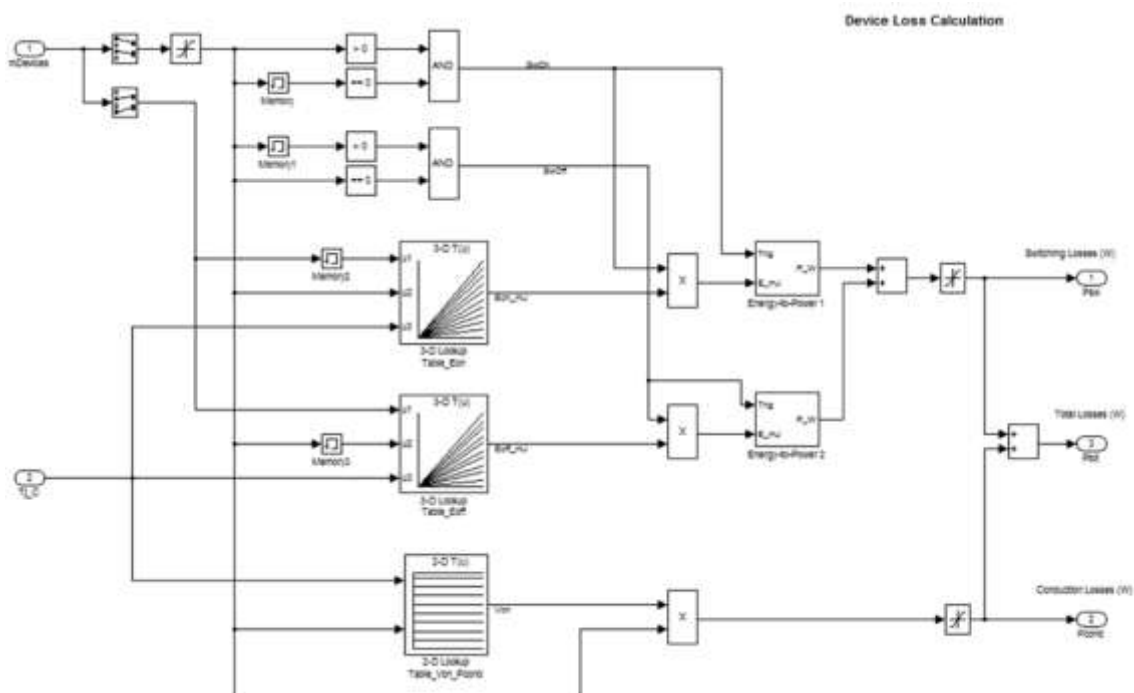
Figure 6-5: Simulink model for the device loss estimation block
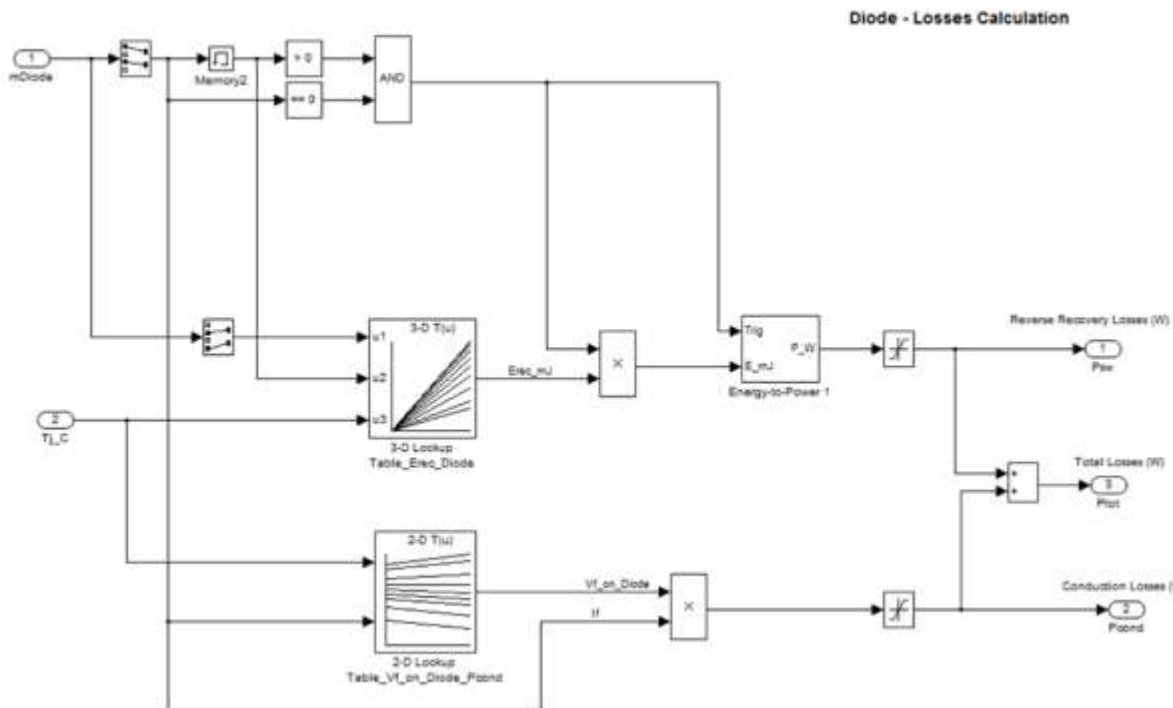
Figure 6-6: Simulink model for the diode loss estimation block

6.2.1. DEVICE PARAMETER ESTIMATION FOR LOOK UP TABLE

A simple chopper circuit was used to measure the turn-on/turn-off losses of the EPC1010, EPC1011 & the IRL3215PbF Silicon devices, as shown in section 5.6 of the previous chapter. The turn-on and turn-off losses can also be determined by using models provided by device manufacturers and these have been used to predict the turn-on and turn-off losses for most Silicon devices. The turn-on and turn-off losses for the 600V silicon device (Datasheet: 64N60P) estimated at different current and temperature ratings are shown in Figure 6-7, Figure 6-8 respectively. These values are then used to estimate the switching losses of the device in a converter.
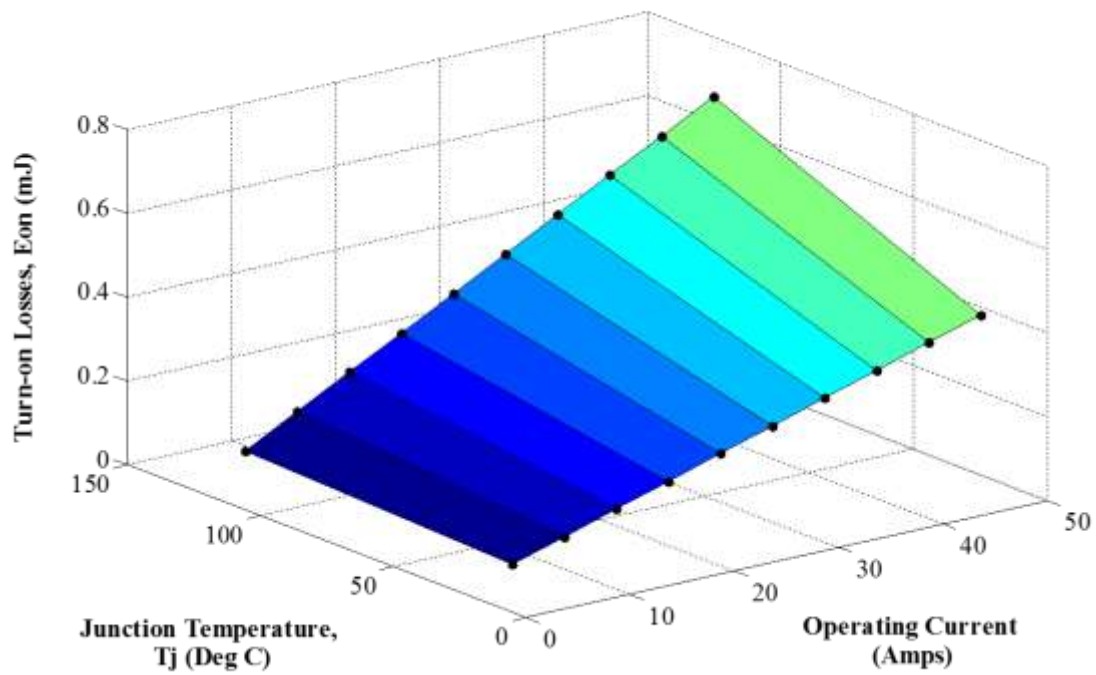
Figure 6-7: Data used to estimate the turn-on losses of the converter at 2-Level Silicon based converter at different current and temperature of operation
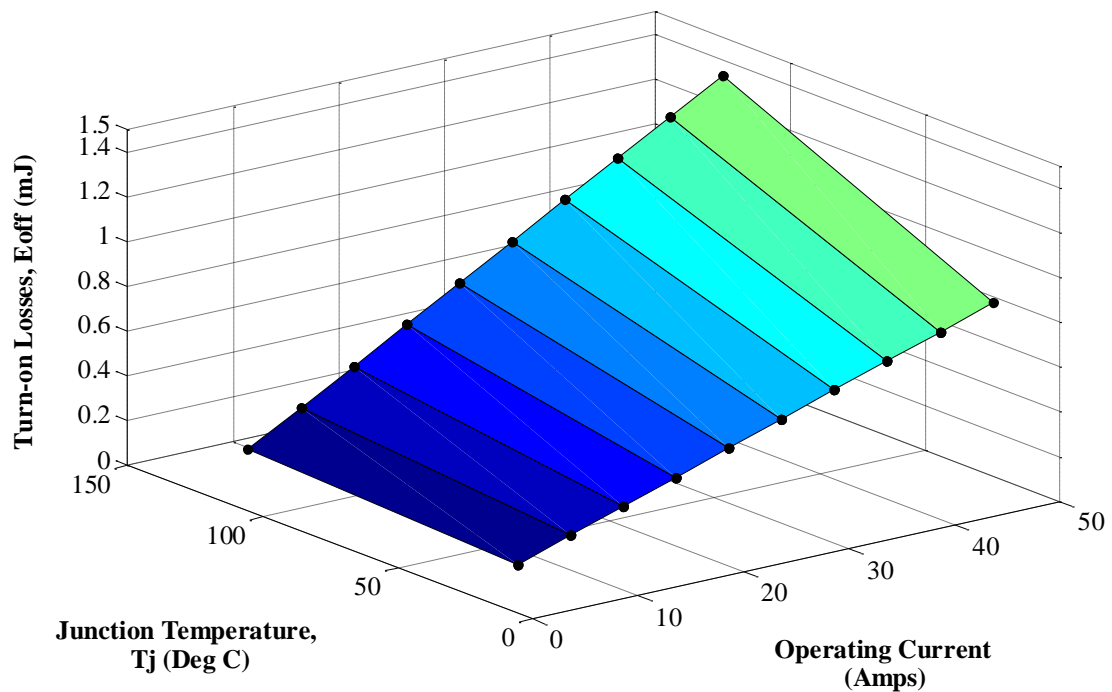
Figure 6-8: Data used to estimate the turn-off losses of the converter at 2-Level Silicon based converter at different current and temperature of operation

The on-state values of all the devices are estimated using the information provided in the device datasheets. The on-state values used for the estimation of the conduction losses for the 2-level converter are shown in Figure 6-9.
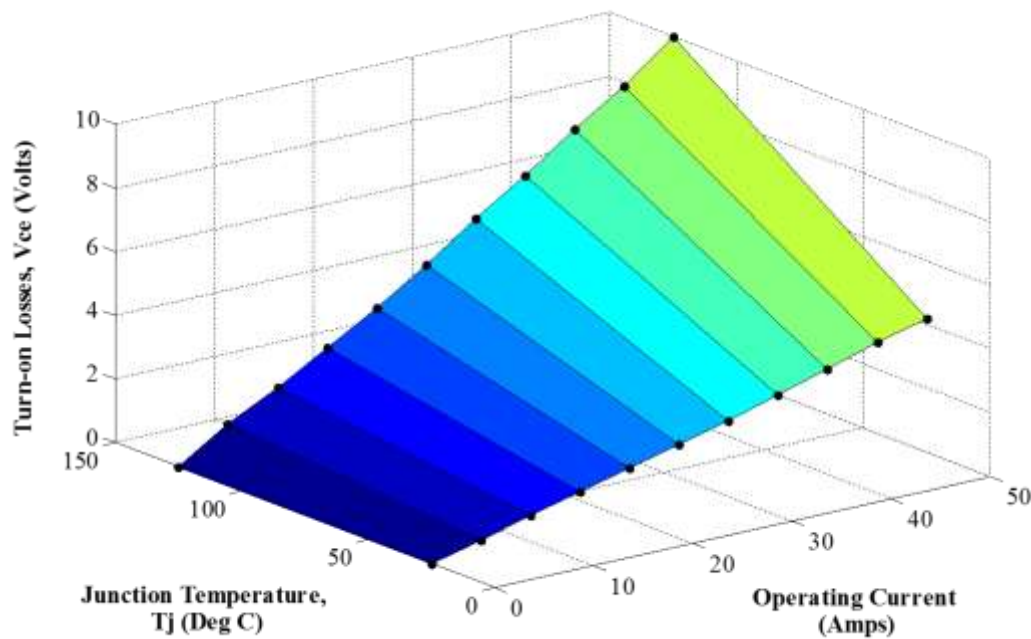
Figure 6-9: Data used to measure the conduction losses of the 2-Level Silicon based converter at different temperature and operating currents

Similar look up tables are created for all the devices in order to estimate the losses of the devices in a converter more accurately. Similar models are used to estimate the losses of devices in various other converter arrangements.

6.2.2. SIMULATION RESULTS

This section describes the results obtained using the models described in section 6.2. The output waveform for the 2-level converter using standard silicon devices (i.e. devices rated at 600V) and using a 6Ω resistive load, is shown in Figure 6-10. The load resistance of the converter was set to deliver output voltage and current of 300V/50A$_{peak}$ at a fundamental frequency of 400Hz no filtering was considered as a part of this study.
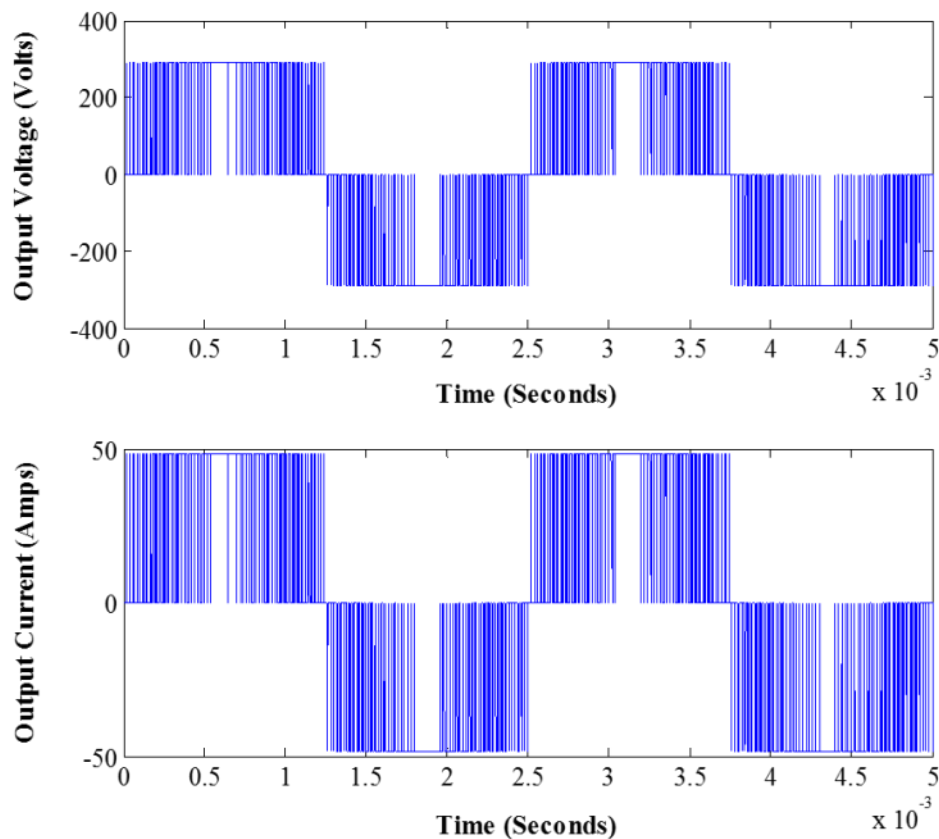
Figure 6-10: Output current and voltage waveforms of the two level converter fundamental frequency =400Hz, Carrier frequency=10 kHz

The estimated loss for the top device in one half of the H-Bridge configuration is shown in Figure 6-11. The loss estimations are all obtained after the converter reaches a steady state operating condition, i.e. after the temperature reaches near steady state and the temperature dependant coefficients in the model reach their steady-state values. The junction temperature variation of the devices in one half of the H-Bridge circuit is shown in Figure 6-12. It can be clearly seen that the junction temperature of the top and bottom device does not vary in a similar manner during converter operation, which is indicative of a significant difference in losses of the two devices.
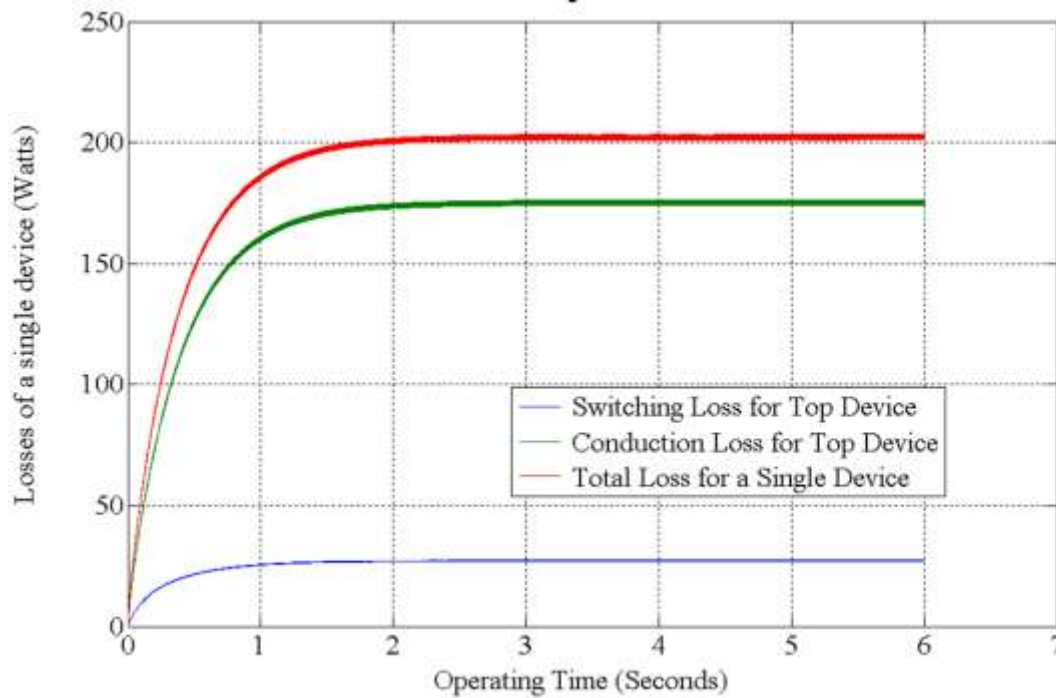
Figure 6-11: Estimated losses for the top device in one half of the H-Bridge configuration

The variation of the switching losses in a converter as a function of the number of levels and

the carrier frequency, is shown in Figure 6-13
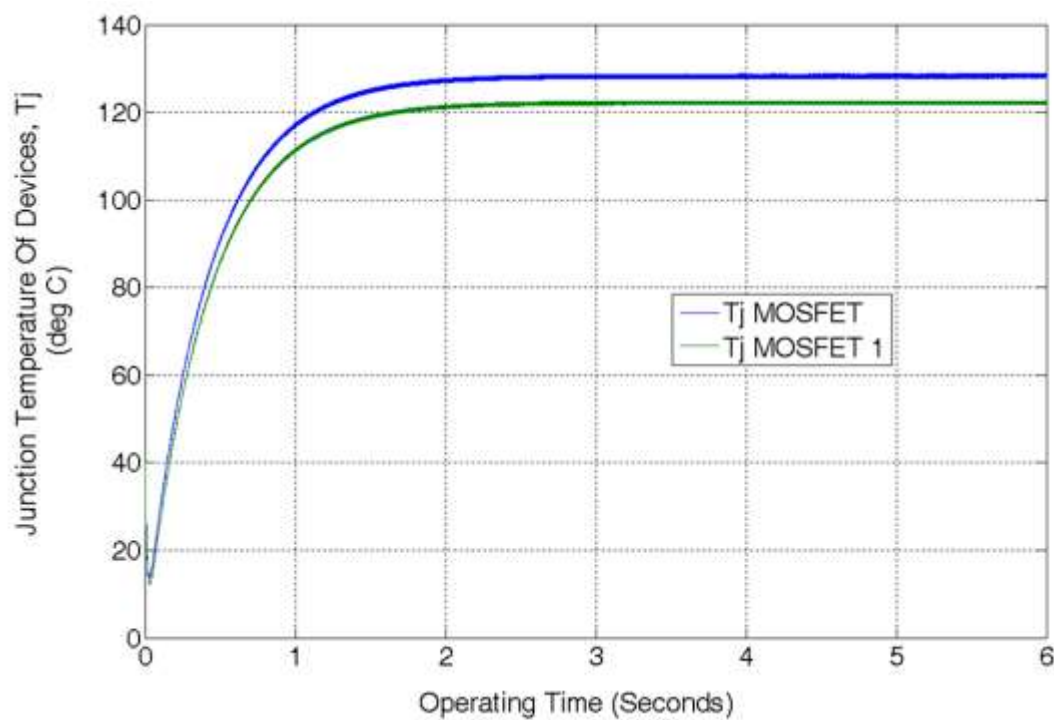
Figure 6-12: Variation of junction temperature with converter operation

.The switching losses show a similar trend to the losses estimated in section 5.4.2 of chapter 5. This further validates the fact that a low voltage silicon device might provide lower switching losses as compared to high voltage silicon devices.

The variation of conduction losses of the converter with the number of levels is shown in Figure 6-14. The conductions losses also show a similar trend as compared to results presented in chapter 5. However, the conduction losses are much higher than those indicated in chapter 5, and this is attributed to the self-heating effect on the on-state performance of the device. As the junction temperature of the device increases, the resistance of the device also increases leading to more losses and therefore impacting the converter performance. It is observed that this effect is more pronounced in high voltage devices than in low voltage devices. This can be attributed to the temperature co-efficient of on-state resistance for the two device ratings, i.e. (600V-2.38, 20V-1.38)
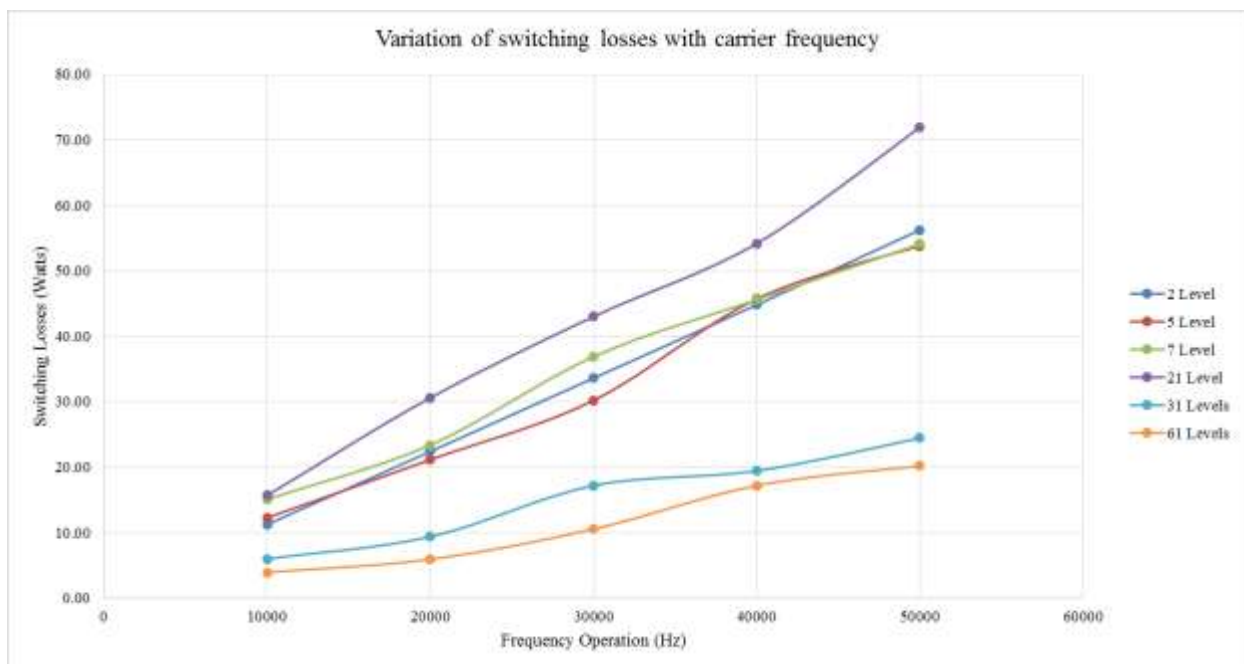
Figure 6-13: Variation of switching losses with carrier frequency
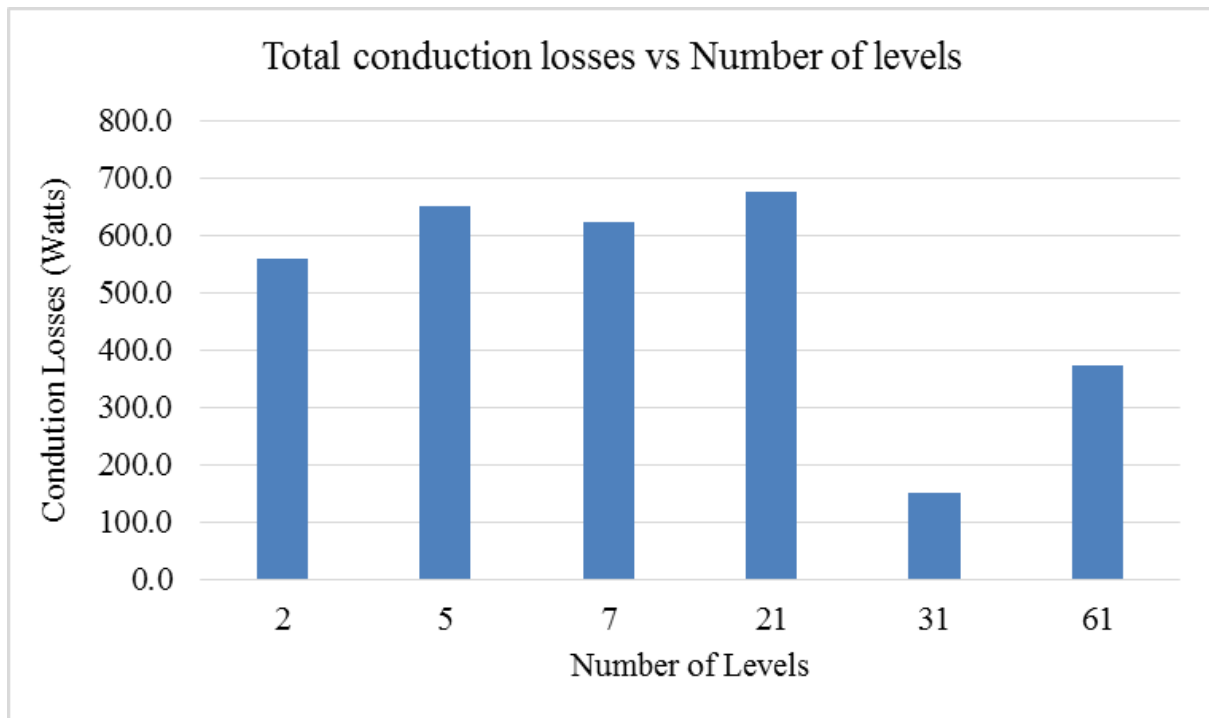
Figure 6-14: Total conduction loss of converter with number of levels
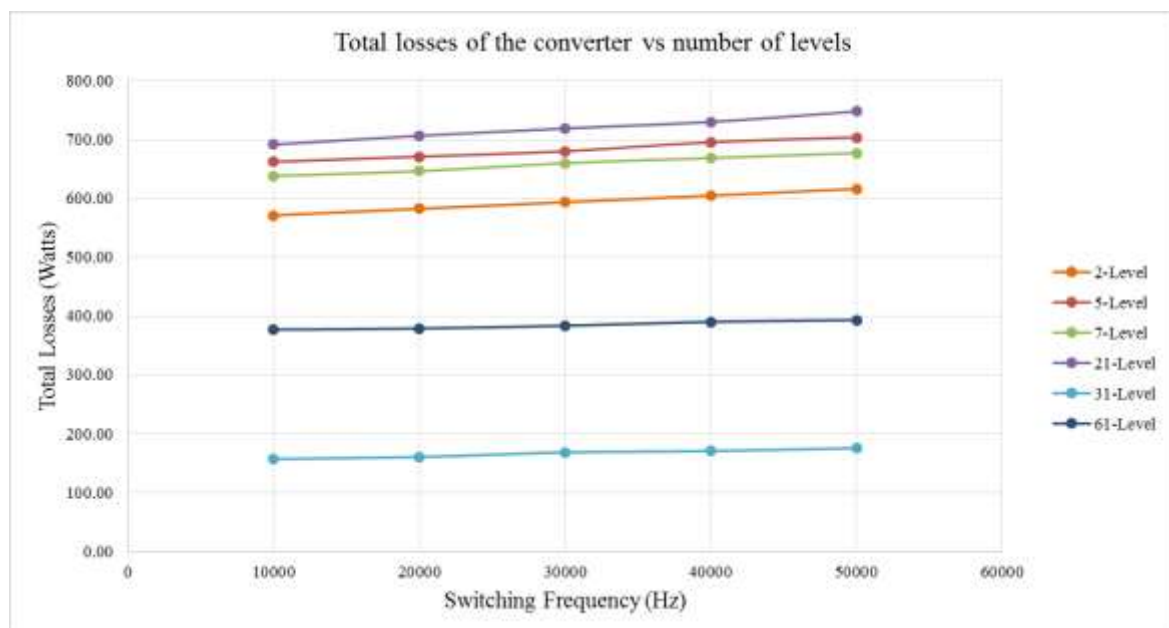
Figure 6-15: Total Losses of the converter with number of levels

Figure 6-15 shows the total losses of the various converter arrangements with a variation of the carrier frequency.It can be clearly seen that low voltage devices silicon devices can offer superior performance as compared to high voltage silicon devices. The trend shown in Figure

6-15 is similar to the results shown in chapter 5, further reinforcing the results presented previously in section 5.4.3.

6.2.2.1. LOSS COMPARISON OF SILICON AND GaN BASED CONVERTERS

Figure 6-16 shows a loss comparison between GaN and Silicon devices for an operating condition of 50A, 300V. The GaN devices show an 86% reduction in losses as compared to a 2-level silicon converter and a 51% reduction in losses as compared to a 31 level converter, for this particular operating point. This decrease in loss in attained without increasing the complexity of the power conversion stages and while maintaining the junction temperature of the devices within the operating margin.
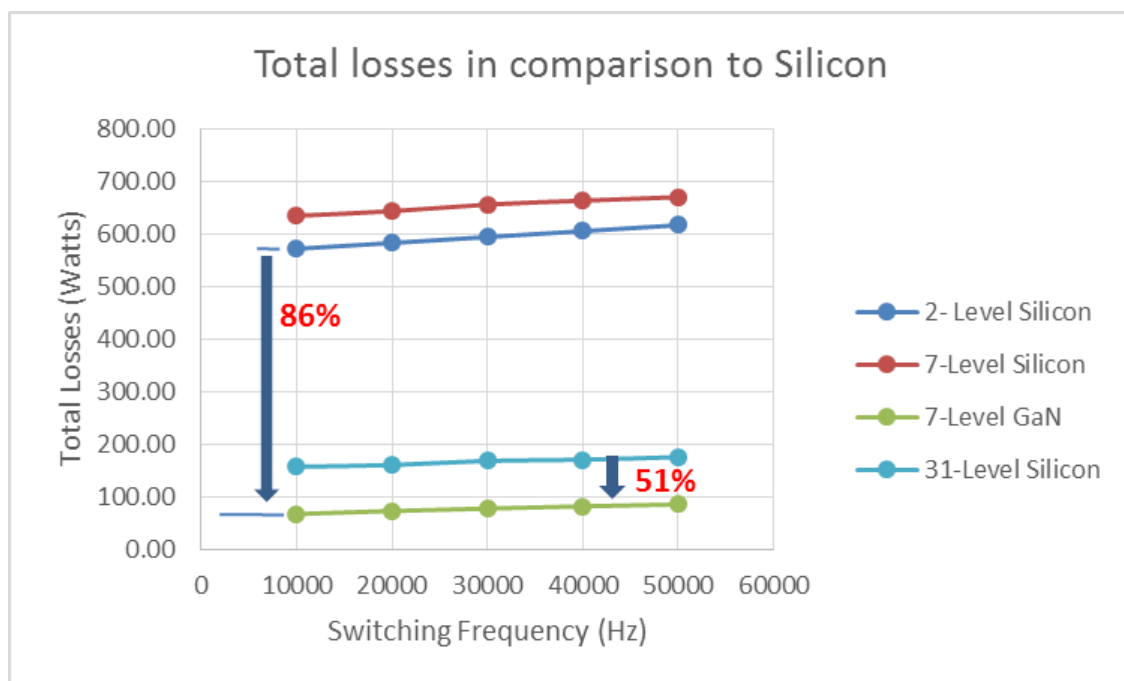
Figure 6-16: Total losses of converter GaN vs Silicon comparison (300V, 50A)

In most application the converter is expected to drive an inductive load as compared to a resistive load. Hence, in order to make a fair comparison an RL load was also considered as a part of this study.
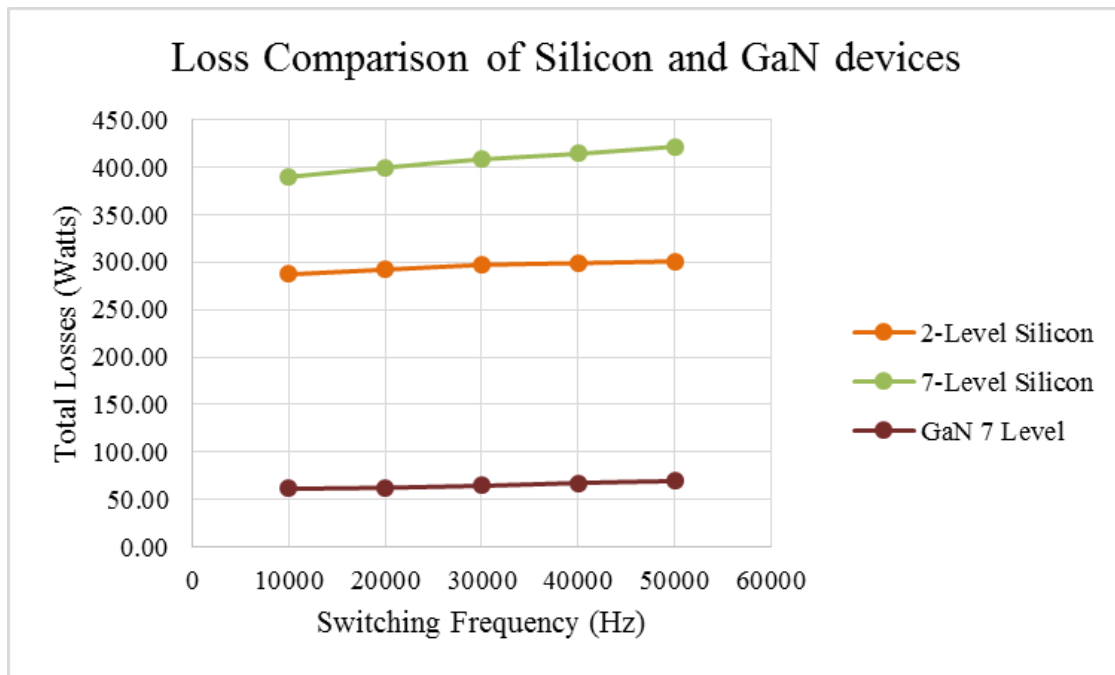
Figure 6-17: Loss comparison of Silicon and GaN devices for under an RL load
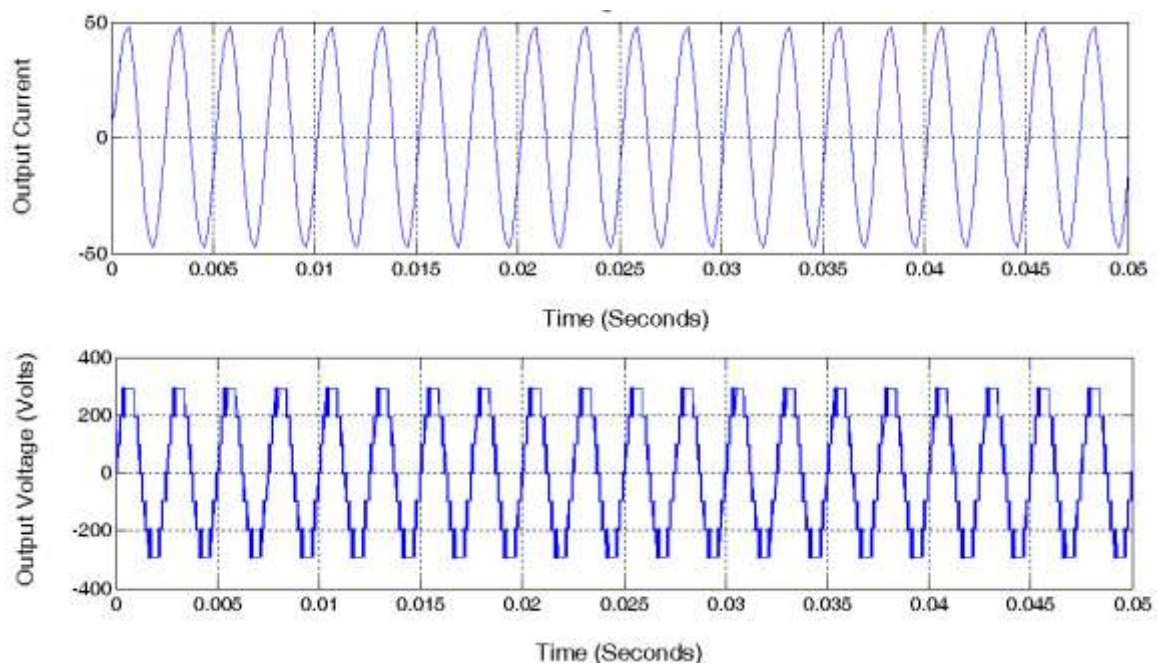
Figure 6-18: Output current and voltage waveforms of the 7-level converter, Fsw=10 kHz

The selection of the inductive component was made on the basis of the power factor of the loads and the ability to minimize the AC current ripple at the output of the converter. In most aerospace applications it has been suggested that the system shall operate to specification

when the power factor is between 0.95 leading and 0.85 lagging [6.11] [6.12]. The inductor value selected using this assumption is 1.2mH. Figure 6-17 shows the total losses of the converter operating under an RL loading. The results clearly show that the GaN based multilevel converter still outperforms the Silicon converter. The output waveforms of the 7-level Silicon converter under the RL load is shown in Figure 6-18. It can also be seen that the total losses of the converter have reduced this is because the on-state voltages and switching currents are load dependent.

6.2.3. IMPACT ON PASSIVE FILTER

Figure 6-19 shows the output voltage waveforms of the 2-Level, 7-level and the 31-level converter at a carrier frequency of 10 kHz.
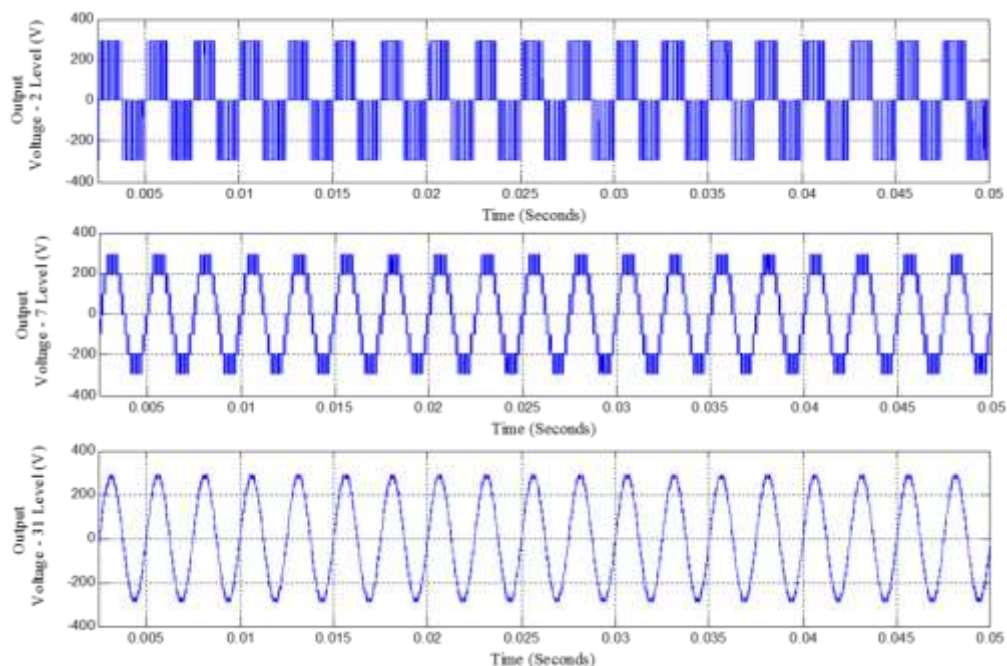
Figure 6-19: Output voltage of a 2-level, 7-level and 31-Level converter at a switching frequency of 10 kHz and 300V/50Amps

It can be clearly seen that as the number of levels are increased, the output voltage of the converter has markedly fewer harmonics when all converters are switched at the same

frequency. Hence, the extent of filtering required for a higher level converter would be much lower in weight and volume as compared to a two level converter although it is also worth noting that the increased number of levels could be exploited to reduce the switching frequency and losses for the same level of harmonic distortion. In practice, some trade-off between these two positions is adopted.

6.2.3.1. HARMONIC ANALYSIS OF THE OUTPUT VOLTAGE

In many power conversion applications, especially those concerning aerospace, it is highly desirable that the output waveform has low harmonic distortion in order to avoid signal interference with other electrical equipment and also to comply with appropriate standards. Many applications specify a THD content of less than 5% [6.11] in order allow compliance with network requirements, although in practice standards are rather more complex in setting different constrains in different frequency ranges. Equation 5.1 describes the basic formula used to define the output voltage of the converter. Using Fourier analysis method it is possible to determine the total harmonic distortion of the power converter based on the number of levels.

$$V_m(\theta) = \sum_{n=1,3,5}^{\infty} \frac{4}{n\pi}(V_1 \cos(n\theta_1) \pm V_2 \cos(n\theta_2)$$

$$\pm V_3 \cos(n\theta_3) \pm \cdots \pm V_s \cos(n\theta_s)) \sin(n\omega t) \dots (6.1)$$

Where total harmonic distortion (THD) can be defined the root mean square (RMS) value of the total harmonics of the signal, divided by the RMS value of this fundamental signal. Figure 6-20 shows a comparison of a total harmonic distortion with a number of levels, for a 300V/50A power conversion application. It can be seen that a 31-level converter eliminates

the need for a passive filter, at least in principle, to meet a 5% THD limit therefore enabling an improvement in converter power density.
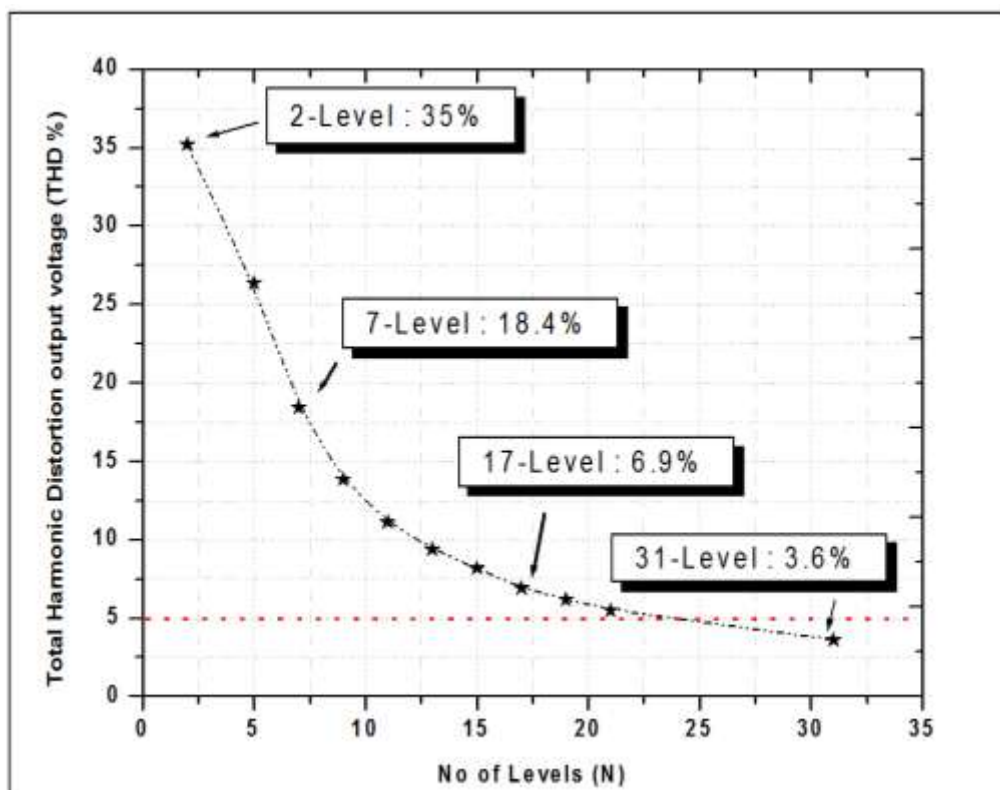
Figure 6-20: Total harmonic distortion vs number of levels

6.3. HARDWARE PROTOTYPE DEVELOPMENT

In order to validate the loss model experimentally, GaN devices were selected as they offered a far superior performance compared to Silicon devices. A number of prototype boards were developed to test and evaluate the device performance, both individually and then in a low power converter.

6.3.1. DEVELOPMENT OF PLUG-IN-MODULES

Section 4.6 shows the layout diagram of the plugin modules designed and developed in order to evaluate the device performance. Once the PCBs were fabricated, the power devices were mounted by depositing a thin layer of solder over the pads followed by the alignment of

devices on the solder pads and a reflow process. Figure 6-21 shows the deposition of solder on the PCB and Figure 6-22 shows the device after the reflow process. The temperature profile for the reflow process is defined in [6.5].
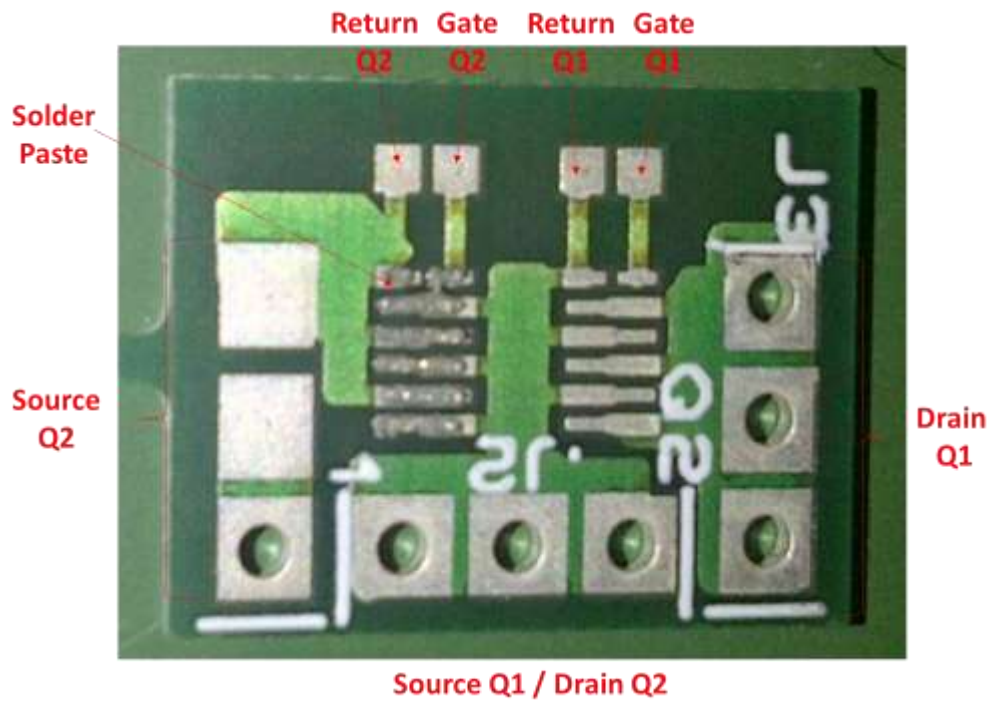
Figure 6-21: Deposition of solder on the PCB boards
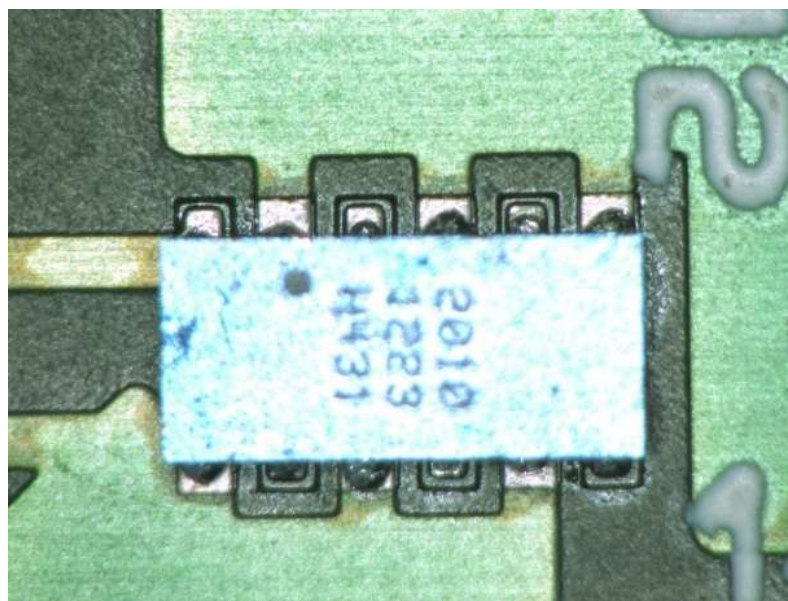
Figure 6-22: Picture of device post assembly

Figure 6-23 shows the failure of the plug-in modules using the process described above. These failures were due to the spacing between the source and drain pads and the thickness of the solder pads. In the latest generation of the device, EPC has optimised the distance between the solder pads in their generation two devices and the solder thickness is controlled using a stencil. The layout of the stencil to allow ease in prototype development is shown in Appendix D.

Short between
Source and drain pads
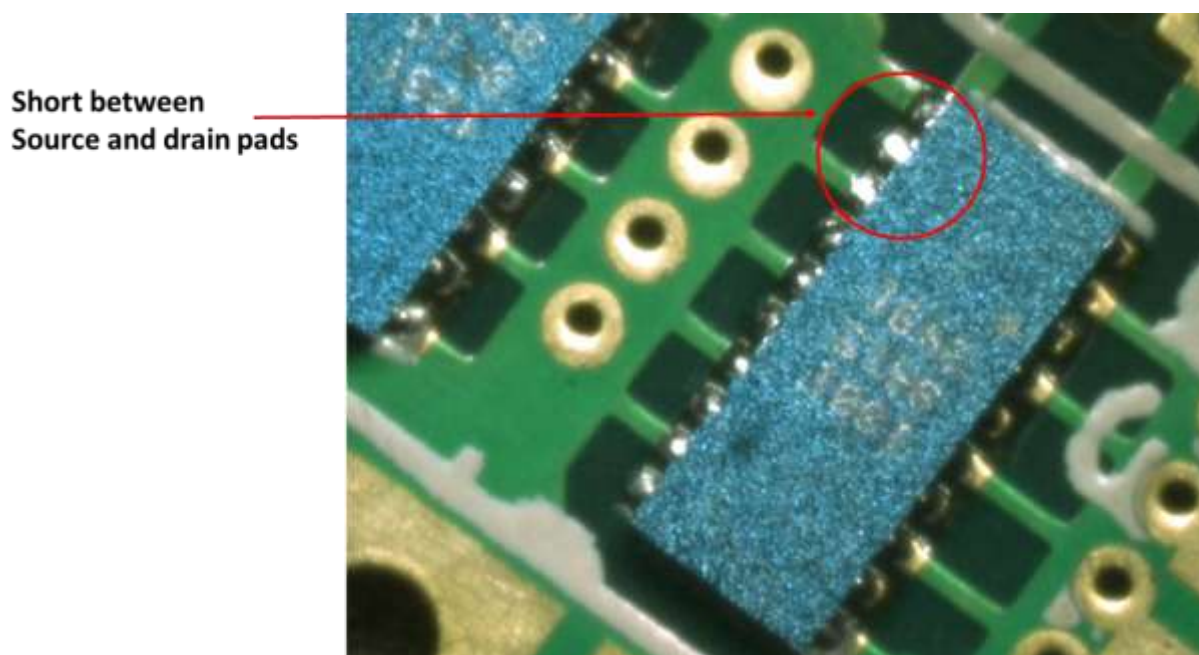
Figure 6-23: Failure of Plug-in Modules due to short between source and drain pads

An alternative layout arrangement of the cells can be used to allow better connectivity with the external circuit. The alternative layout arrangement for a GaN device so as to allow better interconnects is described in [6.13].

6.3.2. DEVELOPMENT OF THE H-BRIDGE CIRCUIT

The block diagram of the H-Bridge circuit using the plug-in modules described above is shown in Figure 6-24. Each H-bridge has an identical hardware setup and uses a common FPGA platform to provide the gate drive control signal. The main elements of the H-bridge

circuit are: Switching devices: Manufacturer part number EPC 1010 (Generation 1 devices) and EPC 1011 (Generation 1 devices). These GaN devices are rated at 200V-12A and 150-12A, respectively. A series of H-bridge circuits will be required to provide the 300V output. However in order to determine the losses, a single device or H-bridge arrangement would suffice.
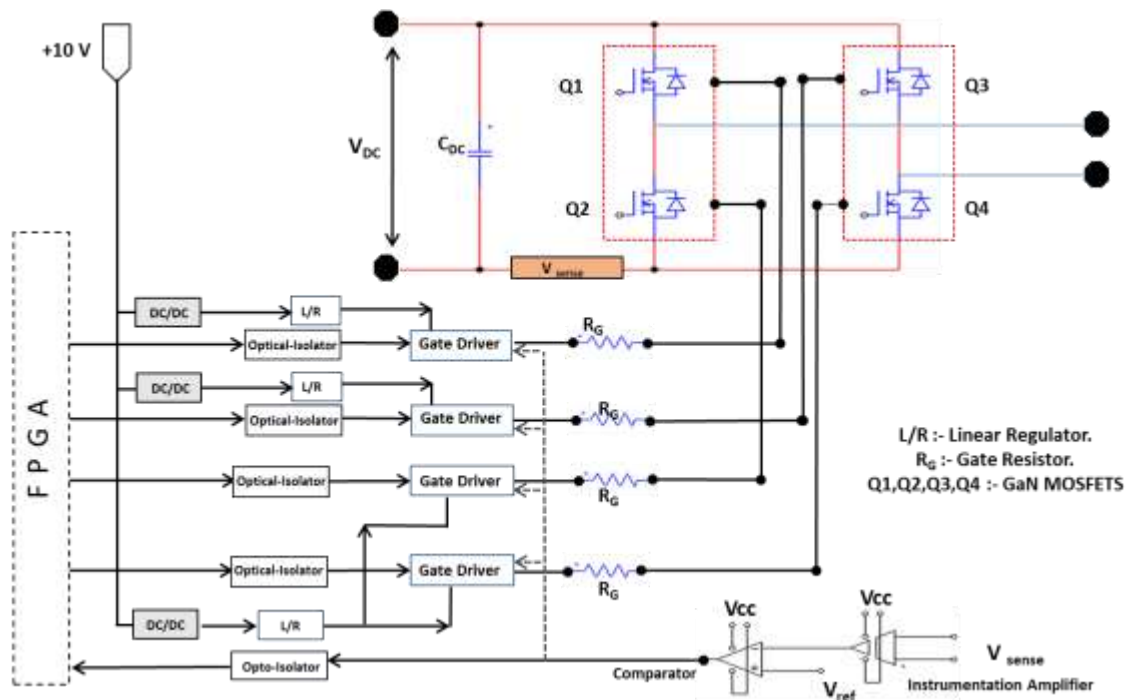
Figure 6-24: Block diagram of the H-Bridge Circuit

- Gate Drivers: The EL7158 Gate driver IC is used to generate the high and low side-gate drive signals independently. The dead time is configured in the FPGA code and sufficient dead time is provided in order to avoid shoot through of the devices, typically <10ns as recommended by the device manufacturer.

- Optical Isolator: An optical isolator is used to isolate the logic signals from the power stage (HCPL0600).

- Voltage Regulator: A MIC5377 voltage regulator is used to ensure the gate drive supply signals do not exceed 0-5V in order to operate the devices within their operating margin.

- DC-DC Converter: A LME120 DC-DC converter is used to provide isolated power stages for the gate driver and other ancillary components.

The drive circuitry for a single device is shown in Figure 6-25 and the layout diagram for the individual H-Bridges is shown in Appendix D (D-11) The high voltage/power stage is separated from the low stage or logic stage as shown in the figure.
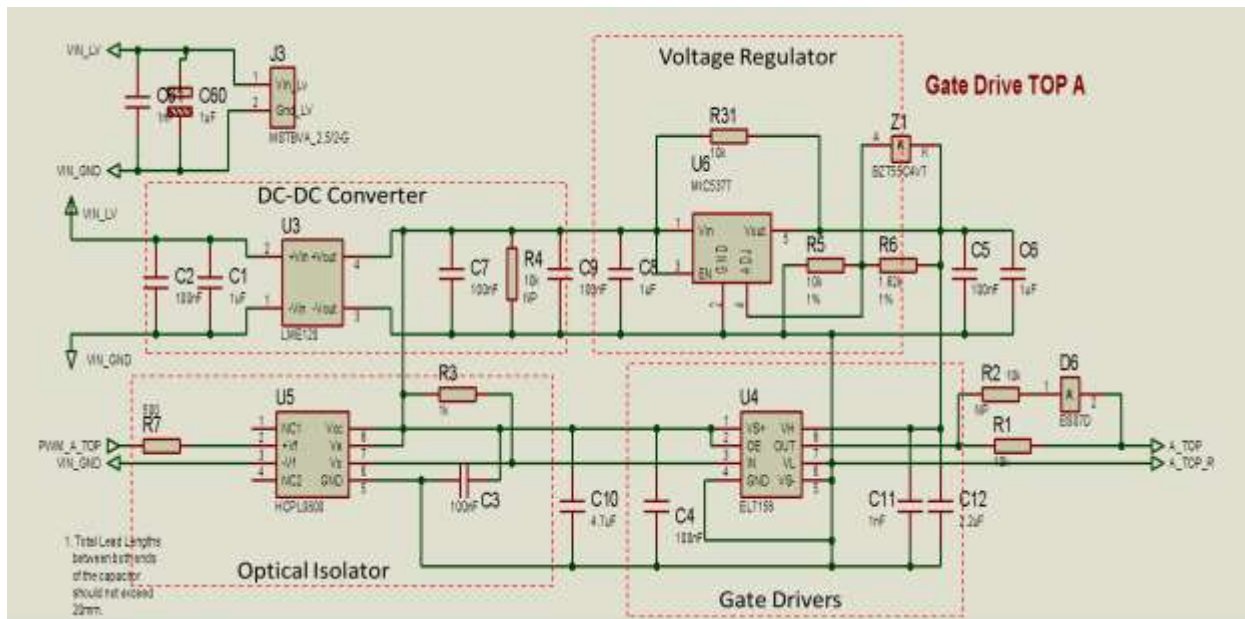
Figure 6-25: Drive circuit for the top device in one half of the H-bridge

The completed H-bridge circuit in a 5-level multilevel converter arrangement is shown in Figure 6-26. Each isolated H-bridge circuit is powered using an isolated DC-Power supply, which acts as the DC-Link for the H-bridge circuit.

6.3.3. DEVELOPMENT OF THE 5-LEVEL CONVERTER CIRCUIT

Figure 6-26 shows the completed H-Bridge circuit modules in a 5-level converter arrangement. The SPARTAN 3E-500 FG320 FPGA board is used to provide control signals for the gate drivers based on the modulation strategy. The specification of this demonstration board is described in [6.12].
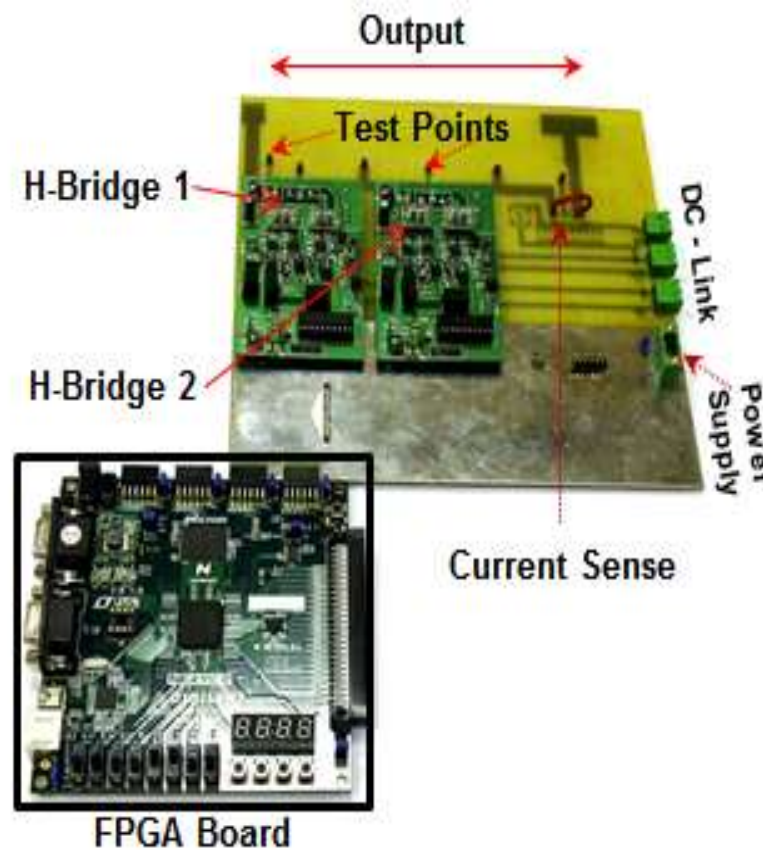
Figure 6-26: Completed H-Bridge Circuit in a 5-phase converter arrangement

The key features of the demonstration board are:

1. 16MB of Micron PSDRAN and 16 MB of Intel Strata Flash ROM.

2. 50MHz Oscillator plus socket for second oscillator.

3. 50 FPGA I/O routed to expansion connectors (one high speed Hirose FX2 connector and four 6-pin headers).

4. 8 LEDs, 4-digit 7-Seg display, 4 buttons, 8 slide switches.

5. 12-Pin PMOD connectors allow addition of features like motor control, A/D and D/A Conversion.

6. Can be powered by bench top power supplies via a PMOD connectors.

6.4. TEST SETUP

This section describes the test setup used for die level, the assembled device level and the converter level measurements.

6.4.1. TEST SETUP FOR STATIC DEVICE CHARACTERISTICS

The initial test setup for the die level measurement prior to assembly is shown in Figure 6-27, and the test setup post assembly is shown in Figure 6-28. The test setup prior to assembly consists of 4-test probes connected to the 2-Drain pads, the Gate pad and 1-Source pad such that the leakage characteristics can be measured. The pad layout for the EPC1010 GaN devices is shown in Figure 6-29. The test probes were interfaced to the Tektronix 371-B curve tracer in order to measure the leakage characteristics of the device.
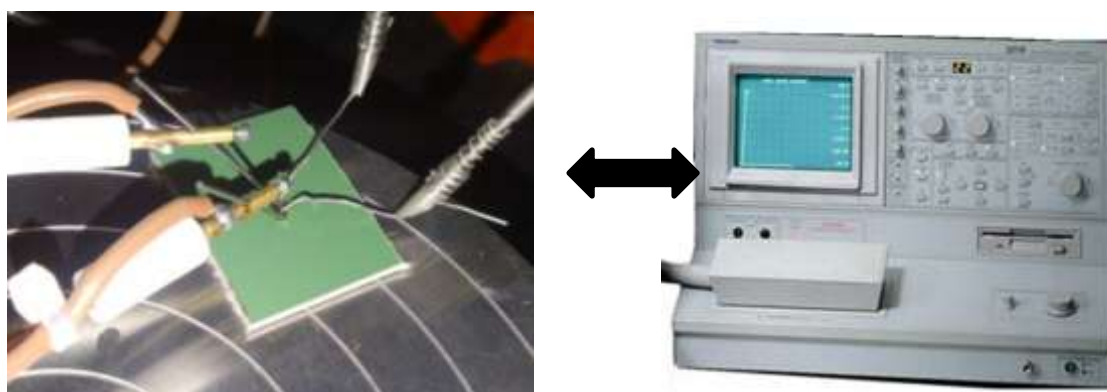
Figure 6-27: Probe measurement setup for the EPC1010 die using the Textronix-371B
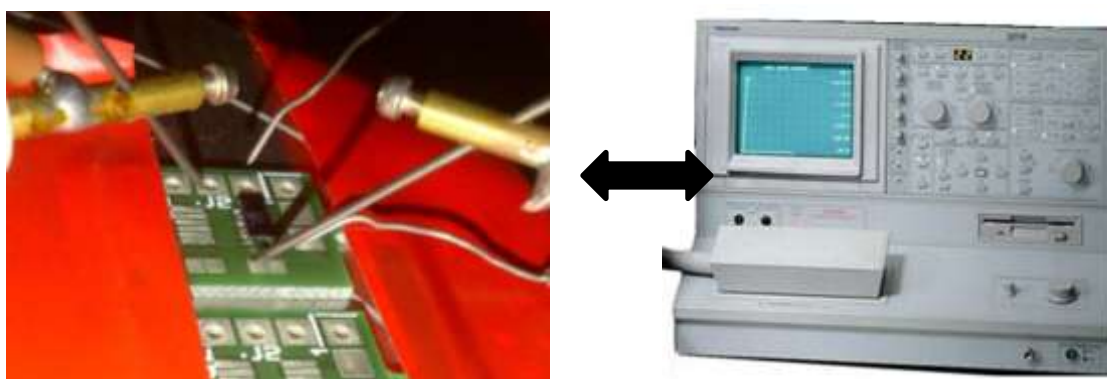
Figure 6-28: Test setup for assembled device post assembly
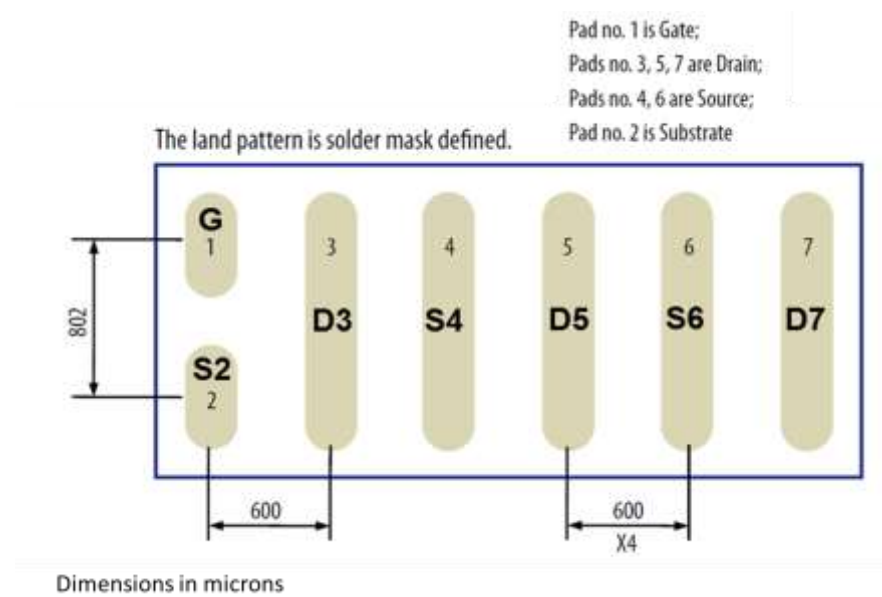
Figure 6-29: Pad Layout for EPC 1010 GaN Transistor (200V/12A) [6.14]

The on-state measurements were not taken at this stage to avoid excessive currents being drawn from a single pad or a series of cells which could result in damage to the device. The leakage current measurement results are shown and discussed in section 6.5.1. The test setup post assembly consists of probes connected to the Gate, to all of the Drain and to Source pads. The test probes were again connected to the curve tracer to measure the static characteristics of the device. The measured static characteristics for the EPC1010 devices are shown in section 6.5.1.

6.4.2. TEST SETUP FOR SWITCHING LOSS MEASUREMENTS

The switching loss measurements were done by assembling the plug-in modules into a standard chopper circuit arrangement. The circuit used to drive the GaN devices in this chopper arrangement is shown in Figure 6-30 and the layout of the PCB board developed is shown in Figure 6-31.
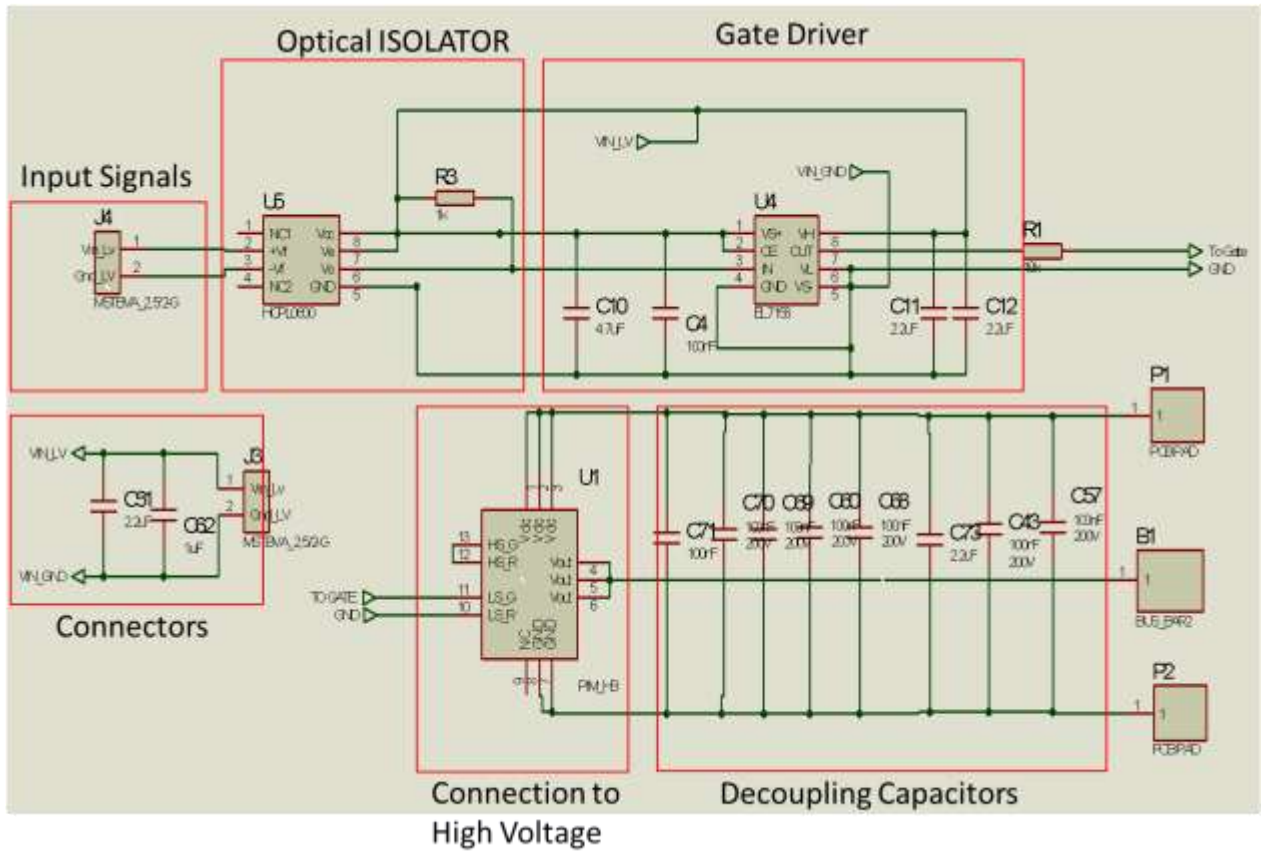
Figure 6-30: Circuit used to drive the GaN devices in a chopper circuit
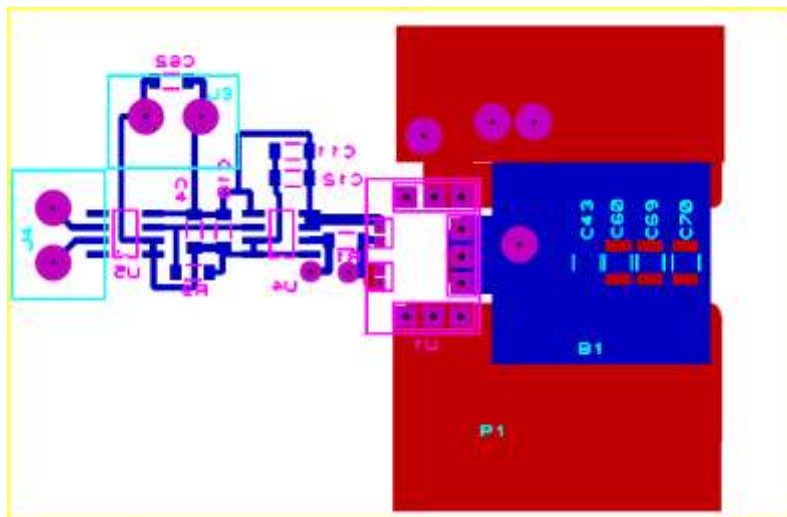
Figure 6-31: Layout circuit for the switching test setup, Top Copper (Silk), Bottom Copper (Blue), Yellow (Board Edge)

This gate drive arrangement is similar to the circuit used in the H-Bridge arrangement. The DC-DC converter and the voltage regulator are excluded from this setup as the gate driver and the optical isolator are powered via isolated supplies. Figure 6-32 shows the experimental prototype used to measure the turn-off, turn-on and short-circuit performance of the GaN devices. The FPGA board is programmed to produce the gate pulse in order to perform switching and short-circuit measurements on the device. The pulse duration at the input of the gate is controlled via the use of the switches provided on the FPGA demonstration board.
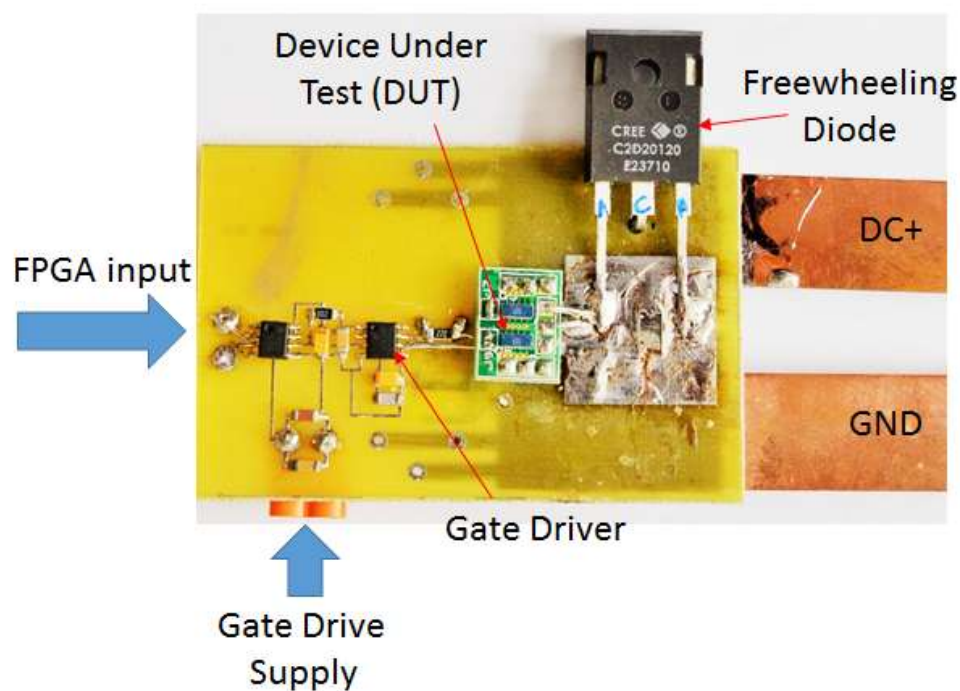
Figure 6-32: Test setup used to measure device switching and short-circuit performance

During the short-circuit measurement, the load inductor and the free-wheeling diode are removed in order to replicate the short-circuit condition across the device when the device is turned-on. The results obtained from these measurements are used in the loss estimation model to predict the overall losses. These results are also used to understand the impact of stray parameters on the device performance and their impact on the H-Bridge circuit design.

6.4.3. TEST SETUP FOR CONVERTER LOSS MEASUREMENTS

The test setup used to measure the losses of a 5-level converter arrangement is shown in Figure 6-33. This test setup consists of the following components:

- Two isolated power supplies to provide power to the isolated H-Bridges.

- Thermocouples which are mounted on the top of the devices in order to monitor case temperatures.

- The resistive load back used load the converter. The measured resistance and of the load banks is provided in Table 6-1. The load bank consists of 7 resistors in parallel. The switches located on top of the load banks are used to select the channels used for testing.

Table 6-1: Measured resistance of the Load Bank

	Measured Resistance (Ω)	Measured Stray inductance
Resistor 1	859	120 µH
Resistor 2	455.7	31.5 µH
Resistor 3	203.4	24.1 µH
Resistor 4	124.4	12.7 µH
Resistor 5	62.5	11.1 µH
Resistor 6	34.4	10.8 µH
Resistor 7	14.4	3.3 µH

- Oscilloscope which is used monitor the gate voltages and input/output voltages and currents.

- A low voltage power supply which is used to power the gate drivers and other components.

As the devices have a very small foot print and are very fragile, it was very difficult to mount a heat sink without damaging the device. The circuit considered within this chapter is operated at very low power levels in order to keep the case temperature within the

operating margin. An optimised layout could be developed to force air-cooling of the devices, thus facilitating higher power operation.
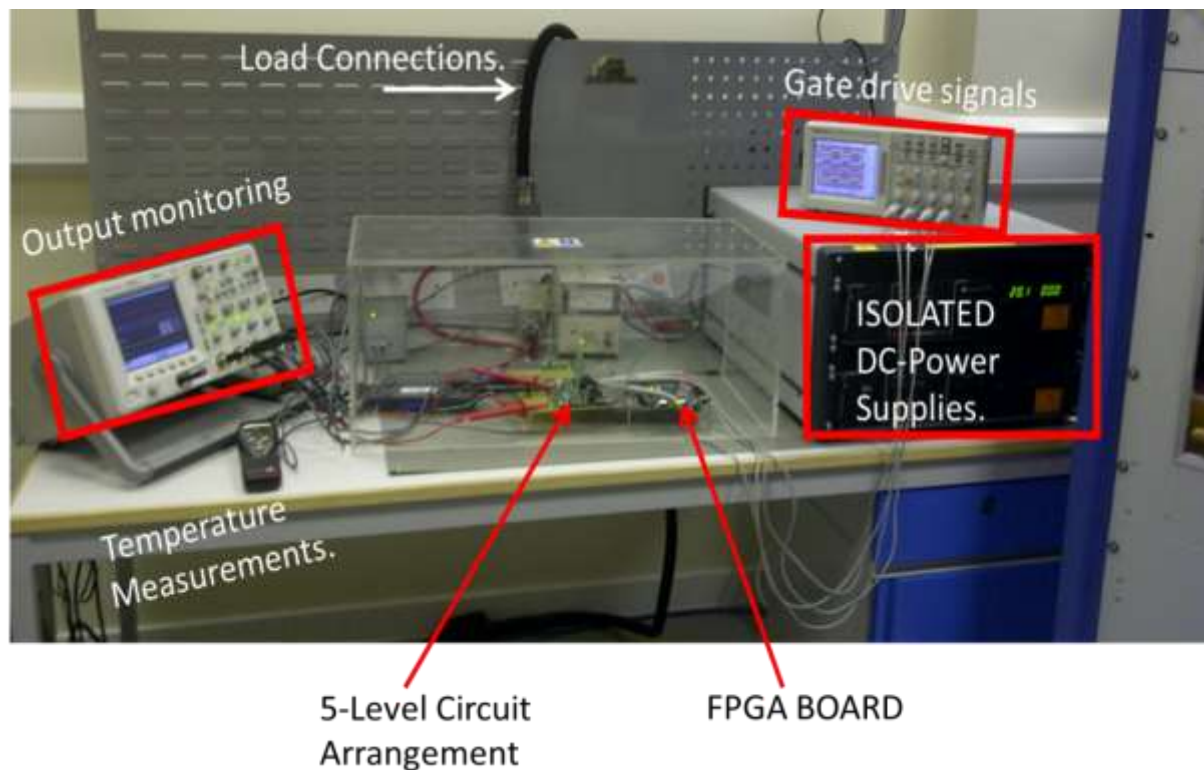
Figure 6-33: Test setup for the 5-Level converter

6.5. EXPERIMENTAL RESULTS

6.5.1. FORWARD BREAKDOWN VOLTAGE MEASUREMENTS

In order to understand whether the dies are able to withstand the breakdown voltages, the drain pads were subjected to a series of high voltages (i.e. between 0V and less than the breakdown voltage of the device) with the source and gate pads grounded. Due to limitations on the number probe points available, alternate source and drain pads of the device were used during the measurements. Figure 6-34 shows the breakdown characteristics of the devices as a function of anode voltage. It can be clearly seen that the GaN devices have a significantly higher leakage current as compared to Silicon devices. This, in turn, will result in the GaN devices having higher blocking losses compared to Silicon devices. However, as the leakage

current is very low (in the order of 10μA at the maximum), the losses during this phase of operation as a contribution to the overall losses, are of little significance.
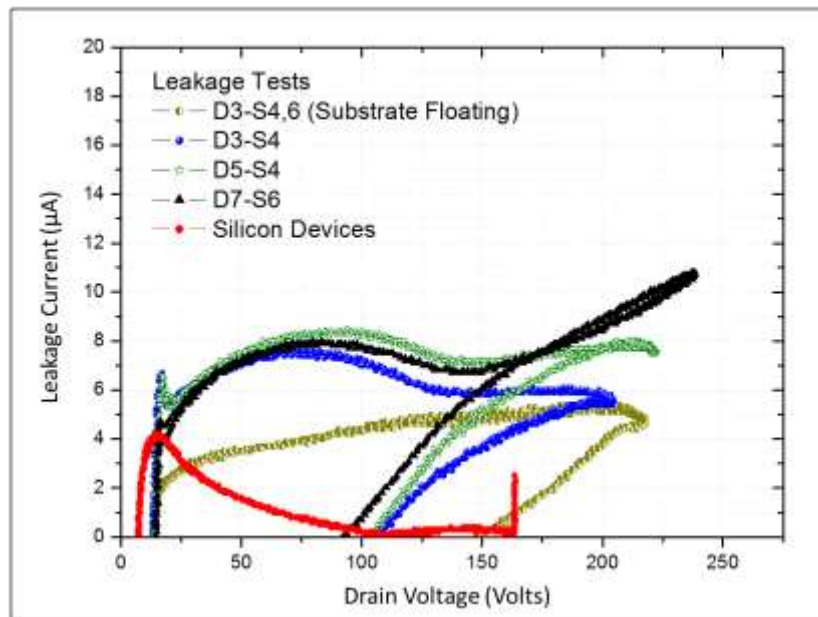
Figure 6-34: Measured Leakage current of the EPC1010 device as a function of anode voltage for various drain -source terminals (compared against 200V/12A Silicon Device)

Figure 6-35 shows the leakage characteristics of the device post assembly. The leakage current in this case is the summation of the leakage current of all the drain and source pads.
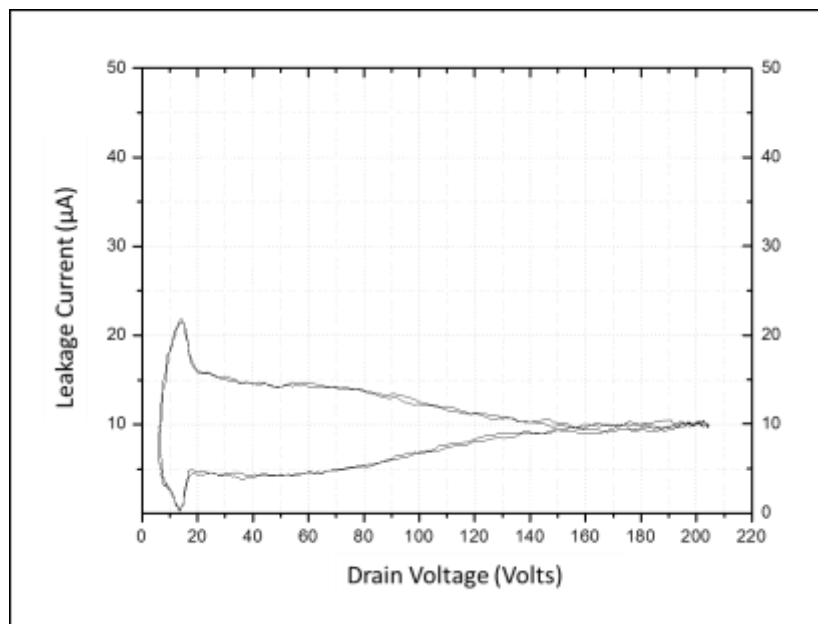
Figure 6-35: Leakage characteristics of the device post device assembly

This essentially highlights that the drain and source pads might not be connected internally and hence require a good interface to the PCB boards to ensure good use of device active area. It is also observed that the performance of the device under reverse blocking condition is within the bounds defined by the manufacturer datasheet. The equipment setup used to measure the leakage properties of the device was described previously in 6.4.1.

The hysteresis observed in Figure 6-34 and Figure 6-35 is due to the loop compensation of the curve tracer. The loop compensation is used to compensate for the stray capacitance which might occur within 371B as given in [6.15]. It is also observed that these GaN devices do not have avalanche capability.

6.5.2. STATIC MEASUREMENTS

The measured static characterises of the EPC1011 (150V-12A) GaN devices is shown in section 5.6.1. The measured static characteristics for single EPC 1010 devices and 2 devices connected in parallel are shown in Figure 6-36. As seen in the figure, the on-state voltage for 2-devices connected in parallel is higher than the single device. The on-state voltage of the EPC1010 device with 2-devices connected in parallel is ~0.1 V higher compared to the single device, a factor that will impact the conduction losses of the converter. The performance of body diodes with variation of anode voltage is shown in Figure 6-37. It can be clearly seen that GaN devices have a significantly lower performance as compared to Silicon devices in terms of their body diode. The on-state resistance (R_{on}) of the body diodes is some 5 times higher than that in the Silicon devices, a difference which arises from the fact that the intrinsic properties of the GaN device are very different to those of Silicon devices.
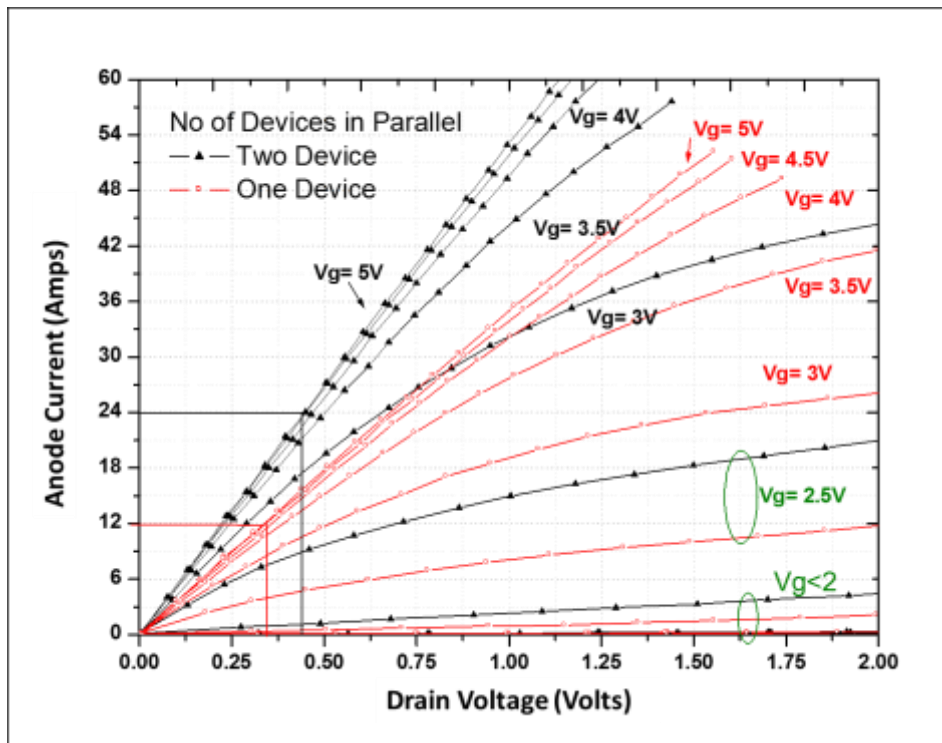
Figure 6-36: Typical I-V characteristics of EPC1010 GaN Devices
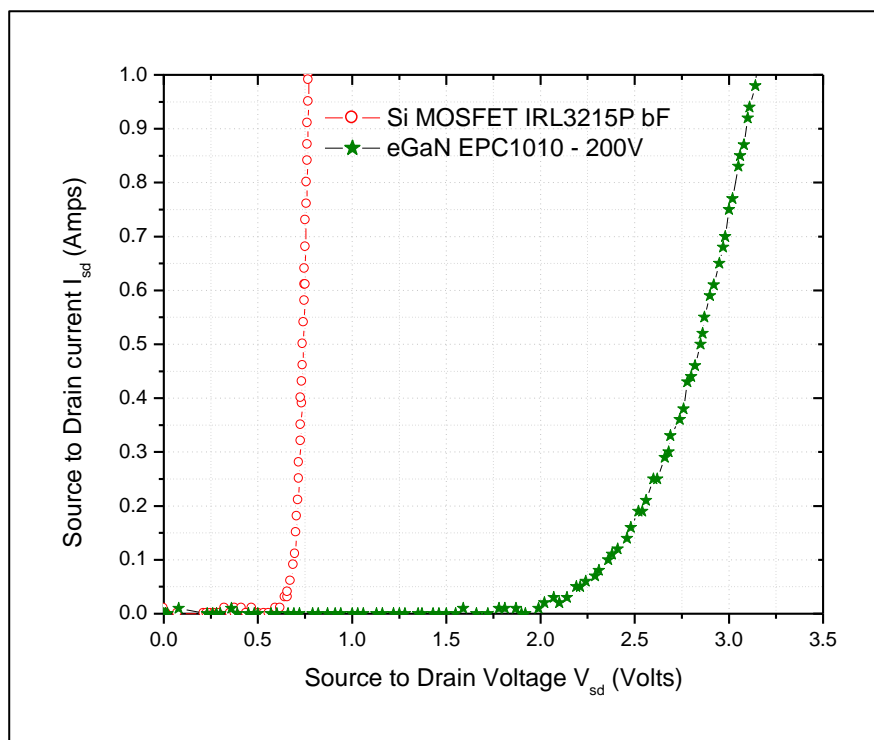
Figure 6-37: Typical forward characteristics of the body diode with drain-source current

While the Silicon devices have an intrinsic p-n junction formed by the P region connecting the source and the N-region connected to the drain, as seen in Figure 6-38, the GaN devices still rely on the 2-DEG electron gas for reserve conduction. The operating of the GaN device in reserve conduction mode is explained in [6.16] and the EPC devices operate in the reverse mode by injecting electrons under the gate region. Once the gate region reaches its threshold with respect to the drain, the channel starts to conduct. As the threshold voltage for this is higher in GaN, these devices exhibit a higher on-state voltage than their Silicon counterparts.
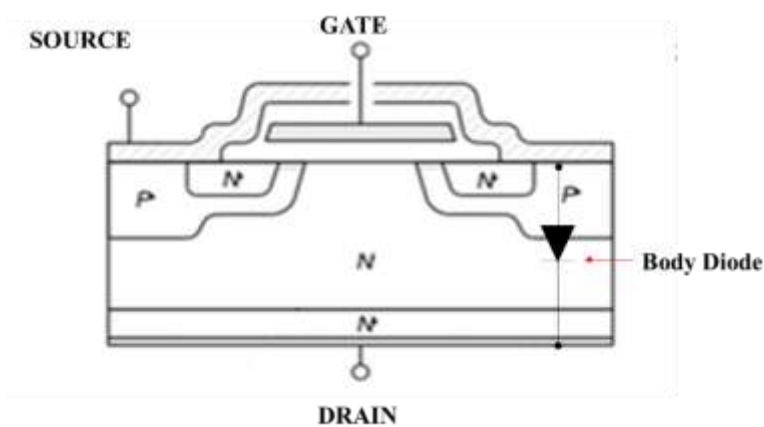
Figure 6-38: Structure of MOSFET showing body diode.

It is proposed that a silicon antiparallel diode should be incorporated such that the losses can be reduced in the reverse conduction mode.

6.5.3. SWITCHING LOSS MEASUREMENTS

Switching loss measurements were conducted on both EPC1010 and EPC1011 devices. However, the EPC1010 devices failed during the dynamic testing and due to unavailability of further samples of EPC1010 devices, subsequent evaluation was done only using EPC1011 devices. The switching waveform for the EPC1010 device is shown in section 5.6.2 of the previous chapter. Figure 6-39 shows the measured turn-off characteristics of the EPC 1011 GaN devices and Figure 6-40 shows the measured switching losses with variation of load

current. Figure 6-41 shows the Turn-off losses of the EPC 1010 GaN devices as a function of gate resistance.
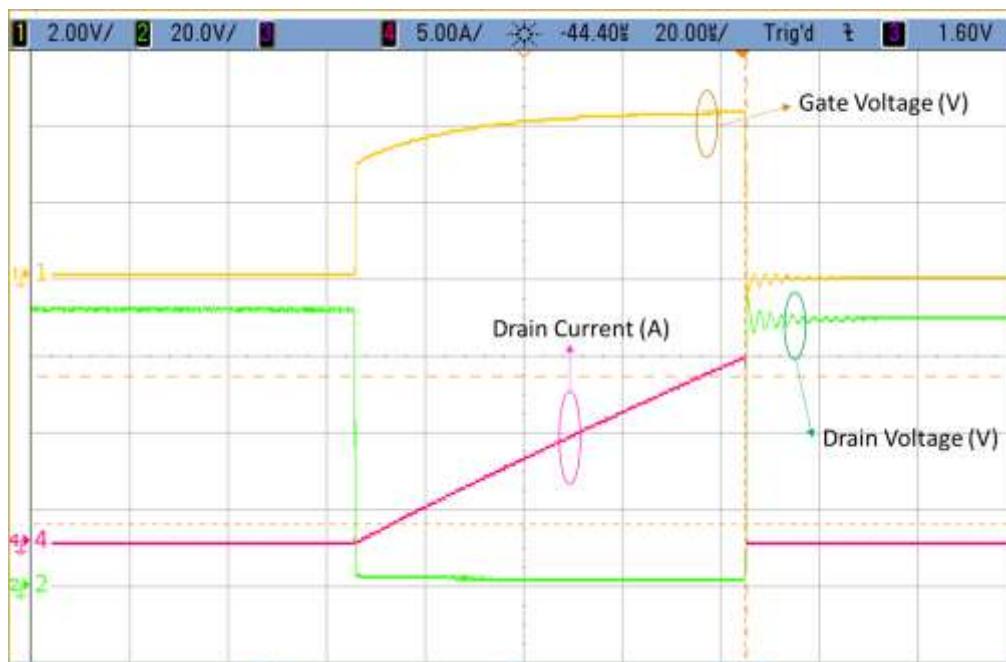
Figure 6-39: Measured turn-off performance of the EPC1011 GaN devices
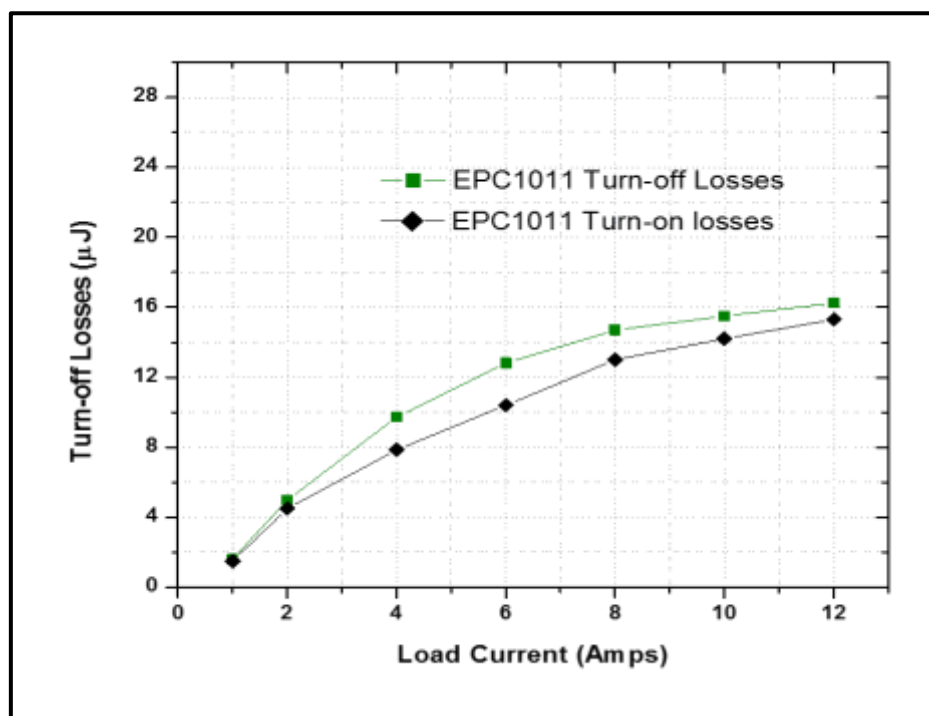
Figure 6-40: Measured turn-on and turn-off losses of EPC1011 GaN devices with load current
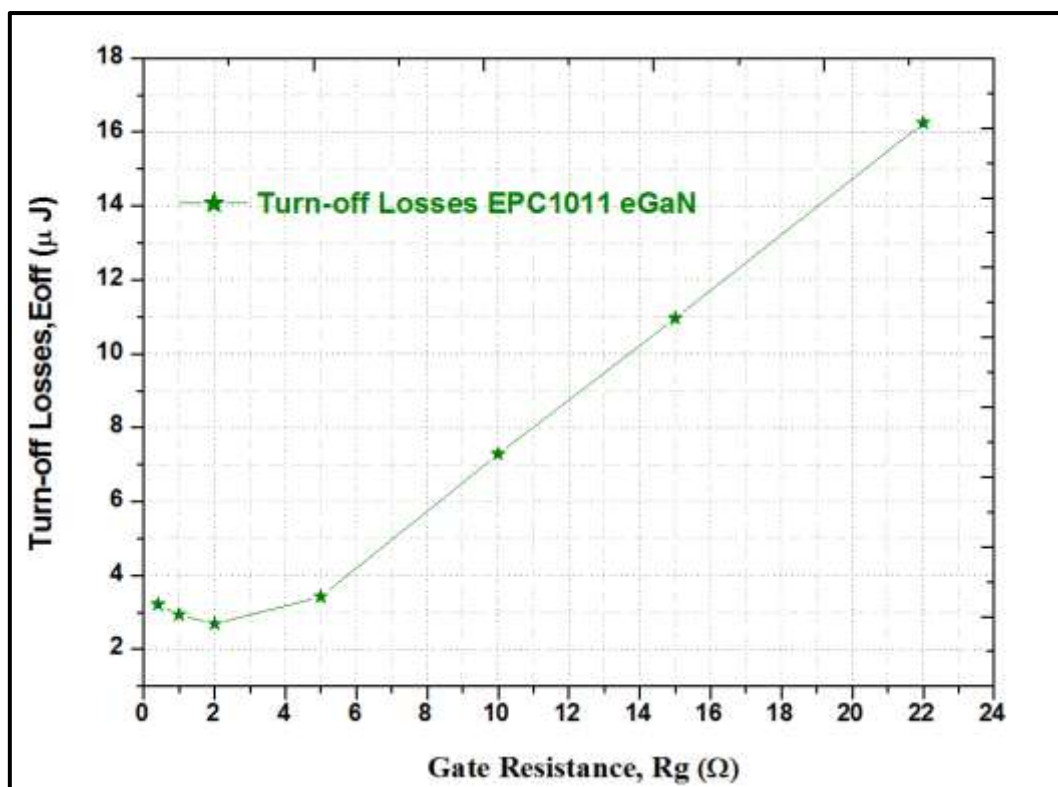
Figure 6-41: Measured variation in turn-off losses with Gate resistance

The turn-off losses of the GaN devices first decreases as a function of gate resistance as a result of behaviour associated with reduced device ringing. This in turn decreases the turn-off losses. The turn-off losses then increase due to the effective slowing down of the devices caused by switching transients.

6.5.4. CONVERTER LOSS MEASUREMENTS

Figure 6-42 shows the measured output waveform of the EPC1011 GaN devices in a single H-Bridge arrangement. The dead time in this circuit arrangement was reduced to less than 10 nanoseconds in order to reduce the impact of the body diode on the overall losses. Figure 6-43 shows the measured efficiency of the H-bridge in the converter when operating at 75V and 1Amp. The case temperature of the half bridge with variation of the switching frequency is shown in Figure 6-44. This clearly shows that the devices are operating well within their operating margin. Several devices failed when the load current was increased close to the

rated current and since generation 1 samples were no longer available, it was not possible to measure any further losses.
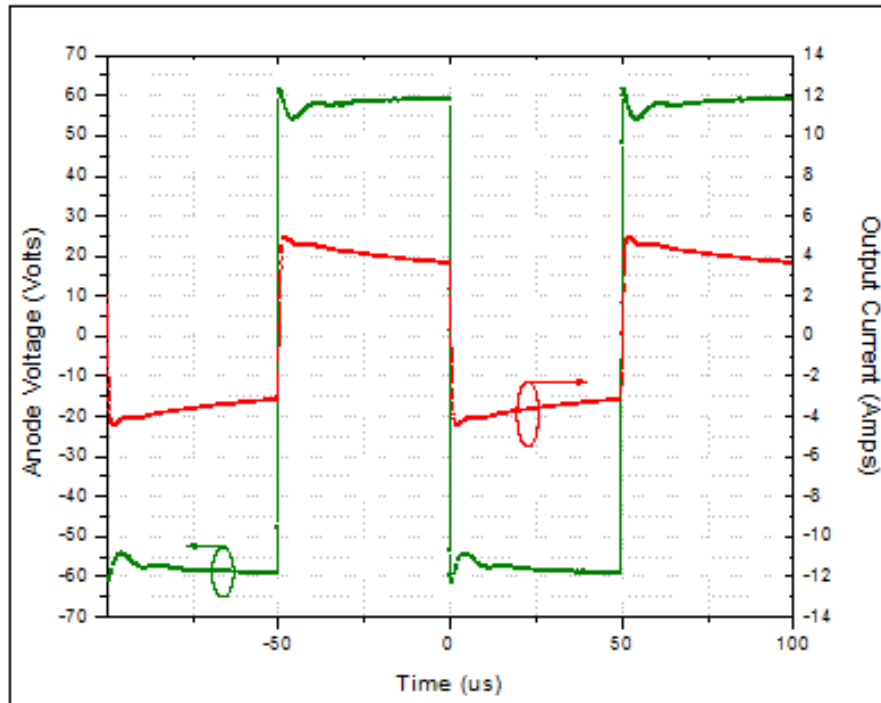
Figure 6-42: Measured output voltage and current waveforms of a single H-Bridge using EPC1011 devices (Switching frequency=10 kHz, DC link 60V)
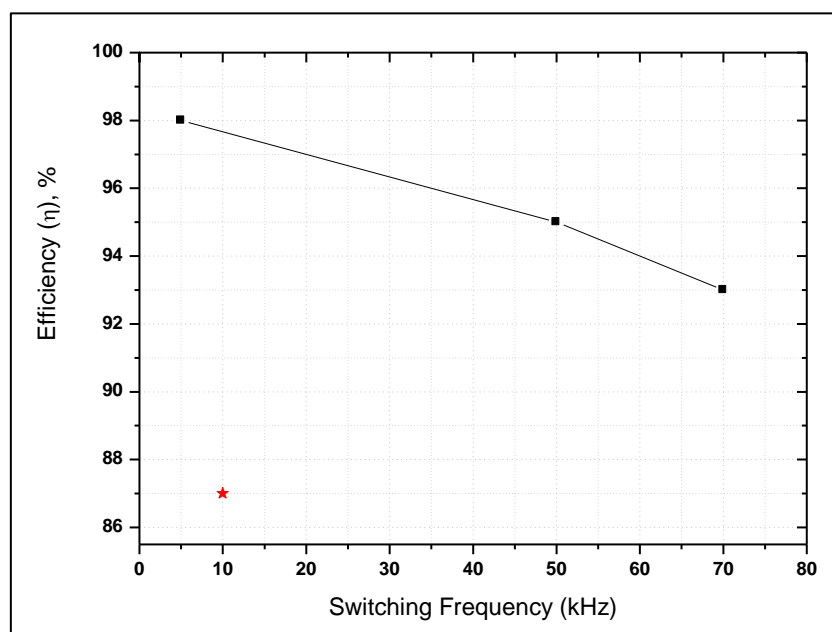
Figure 6-43: Measured efficiency of the H-Bridge circuit using EPC1011 devices (Vout=60V, Iout=1A)

The generation 2 devices had a long lead time which made the assembly and test non-feasible within the timescale of the thesis. The estimated losses for a single H-Bridge using the data measured in section 6.5.3 is shown in Figure 6-45, from which it can be observed that the losses of the single H-Bridge are not high in the context of their power rating.
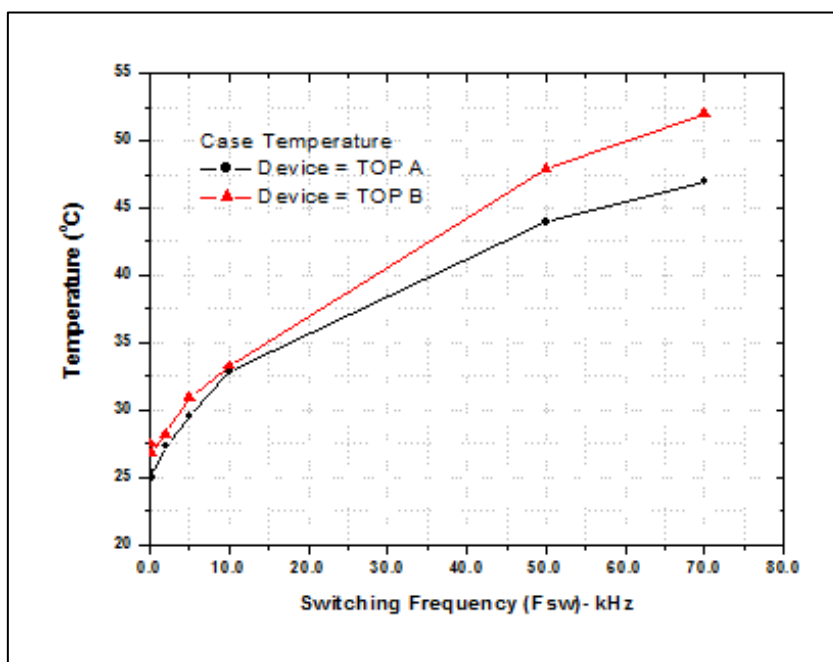
Figure 6-44: Measured case temperature of the device with switching frequency of 10 kHz, Operating voltage=60V and 1Amp

Figure 6-46 shows the variation in time, of the temperature of the device in the half bridge circuit. From this, it can be seen that the temperature of the device exceeds the maximum allowable temperature (i.e. 110°C based on a junction temperature de-rating factor of approximately 10%) for a steady state operation of the H-Bridges at their rated currents. This behaviour can, in large part, be attributed to the high thermal resistance of the GaN devices and package (i.e. 40K/W in still air).
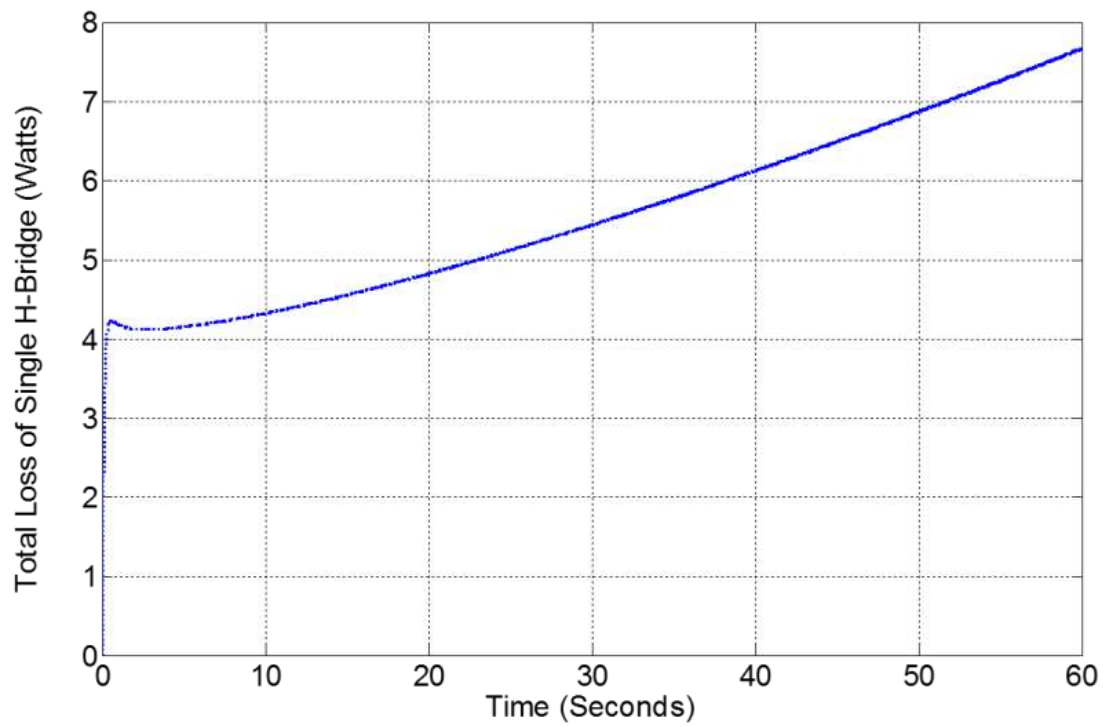
Figure 6-45 Total losses in a H-Bridge arrangment., Fsw=10kz, output current -12Amps, Vout=75V
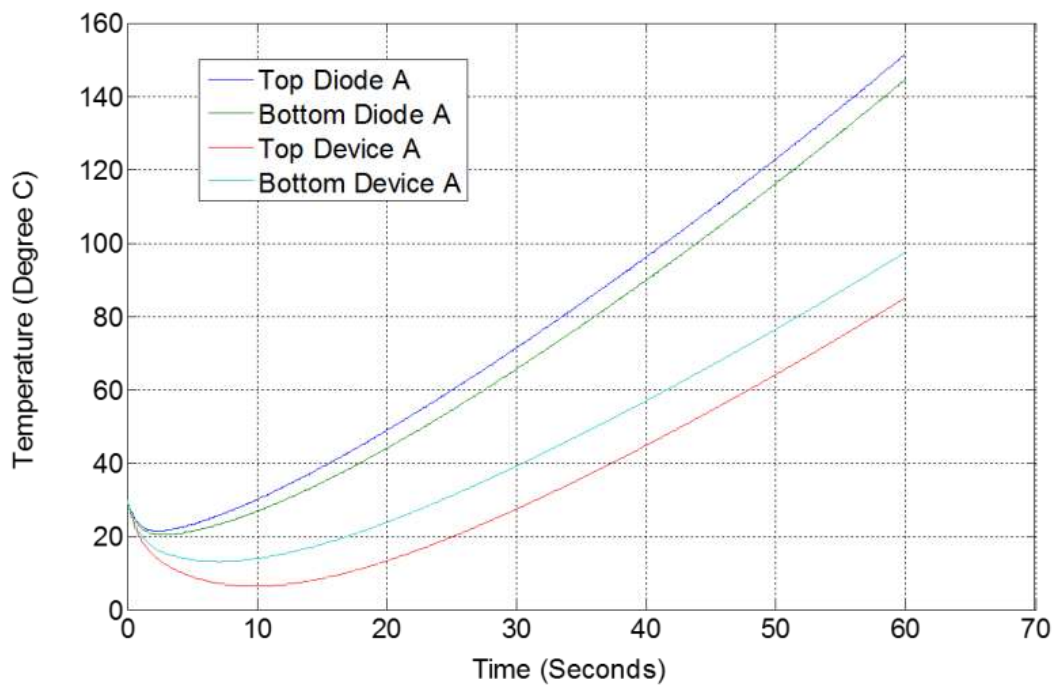
Figure 6-46: Case temperature of the device in the H-Bridge arrangment., Fsw=10kz, output current -12Amps, Vout=75V

6.6. CONCLUSION

In order to verify the results presented in chapter 5 a simulation bench was created to estimate the losses of the converter. The switching losses and on-state performance of the EPC1011 and EPC1010 devices were experimental obtained at different currents and temperatures. These were then fed into the model to estimate the losses in the converter application.

The results presented here clearly support the results presented in chapter 5. The simulation results clearly show that the 7-level GaN multilevel converter can offer up to 86% reduction in losses as compared to an equivalent 2-level converter in Silicon. Figure 6-16 also shows that the 31-level converter provides much lower losses as compared to the 2-level converter this is due to the use of low loss low voltage devices. However, the reduction in losses is offset by the reliability and complexity of the converter due to increased number of levels making the 31-level solution less feasible.

As the GaN devices offered a far more superior performance as compared to Silicon devices, particularly in terms of conduction and switching losses, work was undertaken to evaluate these devices first individually, then in an H-bridge arrangement and then subsequently build a 7-level converter to provide a proof of concept. Various challenges were encountered during these stages. These included availability of devices, assembly of the devices, reduction of stray inductance in the circuit, paralleling of devices, and assembly of devices on a heat sink to provide sufficient cooling. It was noted that although these devices offer a far superior performance they cannot be treated as like for like replacement of silicon devices. As the packaging solution provided makes them inherently fragile to use. In addition to this the thermal conductivity of the GaN devices is lower when compared to Silicon. Therefore the surface area of the PCB used to mount the devices also had to be optimised to provide adequate cooling. Without the use of adequate thermal management solution the GaN devices

could not be operated at their full rated power. This meant that the losses could not be validated at full power and was only validated at low current levels.

6.7. REFERENCES

[6.1] A. R. Hefner, "Device Models, Circuit Simulation, And Computer-controlled Measurements For The IGBT," in *Computers in Power Electronics, 1990 IEEE Workshop on*, 1990, pp. 233-243.

[6.2] A. R. Hefner and D. L. Blackburn, "A Performance Trade-Off for the Insulated Gate Bipolar Transistor: Buffer Layer Versus Base Lifetime Reduction," *Power Electronics, IEEE Transactions on,* vol. PE-2, pp. 194-207, 1987.

[6.3] A. R. Hefner and D. M. Diebolt, "An experimentally verified IGBT model implemented in the Saber circuit simulator," *Power Electronics, IEEE Transactions on,* vol. 9, pp. 532-542, 1994.

[6.4] M. Zygmanowski, B. Grzesik, M. Fulczyk, and R. Nalepa, "Analytical and numerical power loss analysis in Modular Multilevel Converter," in *Industrial Electronics Society, IECON 2013 - 39th Annual Conference of the IEEE*, 2013, pp. 465-470.

[6.5] K. Takao and H. Ohashi, "Accurate Power Circuit Loss Estimation Method for Power Converters With Si-IGBT and SiC-Diode Hybrid Pair," *Electron Devices, IEEE Transactions on,* vol. 60, pp. 606-612, 2013.

[6.6] S. Munk-Nielsen, L. N. Tutelea, and U. Jaeger, "Simulation with ideal switch models combined with measured loss data provides a good estimate of power loss," in *Industry Applications Conference, 2000. Conference Record of the 2000 IEEE*, 2000, pp. 2915-2922 vol.5.

[6.7] B. P. McGrath and D. G. Holmes, "Multicarrier PWM strategies for multilevel inverters," *Industrial Electronics, IEEE Transactions on,* vol. 49, pp. 858-867, 2002.

[6.8] B. P. McGrath and D. G. Holmes, "A comparison of multicarrier PWM strategies for cascaded and neutral point clamped multilevel inverters," in *Power Electronics Specialists Conference, 2000. PESC 00. 2000 IEEE 31st Annual*, 2000, pp. 674-679 vol.2.

[6.9] P. Omer, J. Kumar, and B. S. Surjan, "Comparison of multicarrier PWM techniques for cascaded H-bridge inverter," in *Electrical, Electronics and Computer Science (SCEECS), 2014 IEEE Students' Conference on*, 2014, pp. 1-6.

[6.10] G. S. Pierre Giroux, Olivier Tremblay, "Loss Calculation in a 3-Phase 3-Level Inverter using simPowerSystems and Simscape," Hydro-Quebec Research Institute (IREQ)30/08/2013.

[6.11] RTCA, "DO-160F Environmental Conditions and Test Procedures for Airborne Equipment," ed, 2007.

[6.12] I. O. f. Standardization, "ISO 1540:2006 Aerospace -- Characteristics of aircraft electrical systems," ed: ISO, 2006, p. 56.

[6.13] D. Songquan, M. Hong, T. Wu, X. Shangyang, and I. Batarseh, "Power losses estimation platform for power converters," in *Applied Power Electronics Conference and Exposition, 2004. APEC '04. Nineteenth Annual IEEE*, 2004, pp. 1784-1789 Vol.3.

[6.14] D. Zhong, L. M. Tolbert, and J. N. Chiasson, "Active harmonic elimination for multilevel converters," *Power Electronics, IEEE Transactions on,* vol. 21, pp. 459-469, 2006.

[6.15] Sony-Textronix, "371B-Programmable High Power Curve Tracer User Manual," Sony/Tektronix Corporation., JAPAN.

[6.16] S. L. C. a. R. A. Beach. (2009, Fundamental of GaN Power Transistor.

CHAPTER SEVEN

CONCLUSION AND FUTURE WORK

7.1. CONCLUSION

In the research reported in this thesis, numerous design aspects that might affect device and converter performance were investigated, discussed and evaluated in detail. The various methods of optimising the device losses and the converter loss performance have been discussed and experimentally evaluated starting with Silicon in chapters 2, 3, 4 and later on using the newer GaN technologies in chapter 5 and 6.

The results presented in Chapter 2 demonstrate that a variation in the substrate resistivity (at least within reasonable bounds expected within a controlled production environment) will not impact the device performance to any meaningful degree in terms of their on-state voltage and switching losses. However, a significant variation in substrate resistivity can lead to changes in the device properties across a wafer. It was identified that this variation can subsequently impact the reliability of the power modules and the converter if the devices were not selected and matched appropriately.

The results presented in Chapter 3 show that the device performance can be optimised via the use of a transparent anode structure. The simulation and experimental results demonstrate that the use of transparent anode in CIGBT can reduce turn-off losses of the devices by more 50% when compared to diffused anode technology. The experimental short-circuit evaluation also shows that the CIGBT can withstand a short circuit time in excess of 10μs even at 125°C, and has a maximum short circuit withstand capability of greater than 100μs, a value which is much higher that any MOS controlled bipolar device reported. The optimisation of

the N-well concentration and the cathode geometry was also discussed in this chapter and the results clearly show the variation of the on-state voltage and saturation current density based on the N-well doping concentration.

Chapter 4 was concerned with the optimisation of the TCIGBT structure using a segmented P-base concept. The various implementations of the TCIGBT structures were explored and experimentally evaluated for the first time. The experimental results clearly show that the segmented p-base with deep NMOS and PMOS gates can assist in improving the Vce-Eoff trade off without compromising device short-circuit capability. It was further shown how the PMOS cells can be optimised to enhance performance during the conduction and switching states of the device.

Chapter 5 and 6 evaluate the usage of low voltage Silicon devices and GaN devices in a multilevel converter arrangement. The key objective of this work was to use a bottom up approach on the converter design with an aim to reducing overall converter losses. The estimated losses clearly show the dominance of low voltage silicon devices and GaN devices over the high voltage silicon device using an established loss modelling technique. The results also show the various issues with the initial batch of GaN sample devices. However as these devices become more mature they will inevitably become more competitive in terms of viable commercial solutions, and will in turn displace Silicon based converters in some applications.

Having discussed both Silicon and GaN technologies in detail in this thesis, the author would like to conclude from his results that Silicon devices can still be engineered to push the limits further. Depending on the end application, the advantage of using these technologies would be more prominent. Although GaN is an excellent material for use in power applications, the maturity of the technology is still at a very early stage. There is a lot of research that needs to

be done in order to overcome the disadvantages discussed in chapters 5 and 6 especially around the thermal management and packaging of these devices. Silicon on the other hand, being a very mature technology can provide improved performance via the different methods discussed earlier and this can be chosen depending on the application.

FUTURE WORK

1. **Monolithic Integration of Silicon Devices**: High power applications have considered the use of modular multilevel converters. This topology has now been incorporated into a number of products in the market [7.1] [7.2]. The aim of such research would be to consider the use of low voltage lateral Silicon devices in a monolithic integrated form with the capacitors such that they form the building blocks for the modular multilevel converter. This converter would not require the use of isolated power stages and can be powered via a single DC-Link, hence reducing the complexity to producing the isolated power stages.

2. **Bespoke packaging of GaN Devices**: Commercially available GaN devices have a very small footprint and are very fragile. This, therefore, imposes a number of complexities in the circuit design as well as in the thermal management of these designs. Hence it becomes essential that a packaging solution be explored for GaN, such that the stray inductance is kept to a minimum while maximising the thermal performance of the device in a converter.

3. **Normally-ON GaN based converters:** Most GaN devices are available in a depletion mode configuration, i.e. They conduct with no gate voltage applied. Methods highlighted in available literature to attain an enhancement mode HEMT structure result in the modification of the band structure, such that the on-state performance of the device is compromised. Therefore, it is essential to explore the

use of a normally-on converter and understand the various methods for providing a

fail safe operation.

7.2. REFERENCES

[7.1]   K. Friedrich, "Modern HVDC PLUS application of VSC in Modular Multilevel Converter topology," in *Industrial Electronics (ISIE), 2010 IEEE International Symposium on*, 2010, pp. 3807-3810.

[7.2]   C. D. Barker and N. M. Kirby, "Reactive power loading of components within a modular multi-level HVDC VSC converter," in *Electrical Power and Energy Conference (EPEC), 2011 IEEE*, 2011, pp. 86-90.

APPENDIX A

APPENDIX A1 - SIMULATION FILES FOR CHAPTER 2

IGBT ½-CELL STRUCTURE GENERATION

```
;------------------------------------------------------------------
;Structure definition
;------------------------------------------------------------------
(sdegeo:set-default-boolean "BAB")
(sdegeo:create-polygon (list
(position 0.75 0.0 0)
(position 0.80 3.0 0)
(position 1.75 3.0 0)
(position 1.75 0.0 0)
(position 0.75 0.0 0))
"PolySi" "R.PolyGate")
(sdegeo:fillet-2d (find-vertex-id (position 0.80 3.0 0)) 0.2)

(sdegeo:create-polygon (list
(position 0.65 0.0 0)
(position 0.70 3.1 0)
(position 1.75 3.1 0)
(position 1.75 0.0 0)
(position 0.65 0.0 0))
"Oxide" "R.Gox")
(sdegeo:fillet-2d (find-vertex-id (position 0.70 3.1 0)) 0.2)

(sdegeo:create-rectangle   (position 0.75  0.0 0.0 )  (position 1.75 -0.3 0.0 ) "PolySi"  "R.PolyCont" )
(sdegeo:create-rectangle   (position 0.5 0.0 0.0 )  (position 0.75  -0.3 0.0 ) "Oxide"  "R.Spacer" )
(sdegeo:create-rectangle   (position 0.0  0.0 0.0 )  (position 1.75 120.0 0.0 ) "Silicon"  "R.Si" )
(sdegeo:define-contact-set "Emitter"   4 (color:rgb 0 1 0 ) "##" )
(sdegeo:define-contact-set "Collector" 4 (color:rgb 0 1  0) "##" )
(sdegeo:define-contact-set "Gate"      4  (color:rgb  0  1 0 ) "##" )
(sdegeo:define-2d-contact (find-edge-id (position 1.75 -0.3 0.0)) "Gate")
(sdegeo:define-2d-contact (find-edge-id (position 0.25  0.0 0.0)) "Emitter")
(sdegeo:define-2d-contact (find-edge-id (position 1.175 120.0 0.0)) "Collector")

;------------------------------------------------------------------
; Profiles
;------------------------------------------------------------------

(sdedr:define-constant-profile "Const.Substrate"  "PhosphorusActiveConcentration" @Drift@ )
(sdedr:define-constant-profile-material "PlaceCD.Substrate"  "Const.Substrate" "Silicon" )
(sdedr:define-refinement-window "BaseLine.pbody" "Rectangle"
(position 0.0 0.0 0.0)
(position 0.25 0.3 0.0))
(sdedr:define-constant-profile "Impl.pbodyprof"  "BoronActiveConcentration"  1e+20 )
(sdedr:define-constant-profile-placement "Impl.pbody"  "Impl.pbodyprof" "BaseLine.pbody")

(sdedr:define-refinement-window "BaseLine.pbase" "Line"
(position 0.0 0.3 0.0)
(position 1.75 0.3 0.0))
```

(sdedr:define-gaussian-profile "Impl.pbaseprof" "BoronActiveConcentration" "PeakPos" 0.0 "PeakVal" 1.7e+17
"ValueAtDepth" @Drift@ "Depth" 2.2 "Erf" "Length" 0.1)
(sdedr:define-analytical-profile-placement "Impl.pbase" "Impl.pbaseprof" "BaseLine.pbase" "Positive" "NoReplace" "Eval")

(sdedr:define-constant-profile "Const.PloyGate" "PhosphorusActiveConcentration" 1e+20)
(sdedr:define-constant-profile-material "PlaceCD.PloyGate" "Const.PloyGate" "PolySi")

(sdedr:define-refinement-window "BaseLine.nplus" "Rectangle"
(position 0.25 0.0 0.0)
(position 0.75 0.3 0.0))
(sdedr:define-constant-profile "Impl.nplusprof" "ArsenicActiveConcentration" 1e+19)
(sdedr:define-constant-profile-placement "Impl.nplus" "Impl.nplusprof" "BaseLine.nplus")

(sdedr:define-refinement-window "BaseLine.fieldstop" "Line"
(position 0.0 120.0 0.0)
(position 1.75 120.0 0.0))
(sdedr:define-gaussian-profile "Impl.fieldstopprof" "ArsenicActiveConcentration" "PeakPos" 0.0 "PeakVal" 1e+16
"ValueAtDepth" @Drift@ "Depth" 6 "Erf" "Length" 0.1)
(sdedr:define-analytical-profile-placement "Impl.fieldstop" "Impl.fieldstopprof" "BaseLine.fieldstop" "Negative" "NoReplace" "Eval")

(sdedr:define-refinement-window "BaseLine.collector" "Line"
(position 0.0 120.0 0.0)
(position 1.75 120.0 0.0))
(sdedr:define-gaussian-profile "Impl.collectorprof" "BoronActiveConcentration" "PeakPos" 0.0 "PeakVal" 1e+17
"ValueAtDepth" 1e+16 "Depth" 1 "Erf" "Length" 0.1)
(sdedr:define-analytical-profile-placement "Impl.collector" "Impl.collectorprof" "BaseLine.collector"
        "Negative" "NoReplace" "Eval")

;--
; Meshing AAT
;--

(sdedr:define-refinement-window "RW.SiTop" "Rectangle"
(position 0.0 0.0 0.0)
(position 1.75 6.0 0.0))
(sdedr:define-refinement-size "Ref.SiTop"
 0.301 0.3751
 0.05 0.05)
(sdedr:define-refinement-function "Ref.SiTop" "DopingConcentration" "MaxTransDiff" 1)
(sdedr:define-refinement-placement "RefPlace.SiTop" "Ref.SiTop" "RW.SiTop")

(sdedr:define-refinement-window "RW.SiMid" "Rectangle"
 (position 0.0 6.0 0.0)
 (position 1.75 50.0 0.0))
(sdedr:define-refinement-size "Ref.SiMid"
 0.601   0.751
 0.05   0.05)
(sdedr:define-refinement-function "Ref.SiMid" "DopingConcentration" "MaxTransDiff" 1)
(sdedr:define-refinement-placement "RefPlace.SiMid" "Ref.SiMid" "RW.SiMid")

(sdedr:define-refinement-window "RW.SiBot" "Rectangle"
 (position 0.0 50.0 0.0)

```
 (position 1.75 120.0 0.0 ))
(sdedr:define-refinement-size "Ref.SiBot"
 0.601 0.751
 0.05  0.05 )
(sdedr:define-refinement-function "Ref.SiBot"  "DopingConcentration" "MaxTransDiff" 1)
(sdedr:define-refinement-placement "RefPlace.SiBot"  "Ref.SiBot" "RW.SiBot" )


;-----------------------------------------------------------------
; Meshing Offseting
;-----------------------------------------------------------------

(sdenoffset:create-global
 "usebox" 2
 "maxangle" 200
 "maxconnect" 10000000
 "background" ""
 "options" ""
 "triangulate" 0
 "recoverholes" 1
 "hglobal" 5
 "hlocal" 0
 "factor" 1.3
 "subdivide" 0
 "terminateline" 3
 "maxedgelength" 5
 "maxlevel" 10)

(sdenoffset:create-noffset-block "region" "R.Si"  "maxedgelength" 5 "maxlevel" 12)
(sdenoffset:create-noffset-block "region" "R.PolyGate"  "maxedgelength" 0.25 "maxlevel" 8)
(sdenoffset:create-noffset-interface "region" "R.Si" "R.Gox"  "hlocal" 0.001 "factor" 1.5)
(sdenoffset:create-noffset-interface "region" "R.PolyGate" "R.Gox"  "hlocal" 0.002 "factor" 1.5)


;-----------------------------------------------------------------

; Saving BND file
(sdeio:save-tdr-bnd (get-body-list) "@tdrboundary/o@")

; Saving CMD file
(sdedr:write-cmd-file "@commands/o@")
```

APPENDIX A2 - SIMULATION FILES FOR CHAPTER 3

3.3kV CIGBT STRUCTURE FILE

$source str_c9.inp

```
assign name=pwdose n.val=4e13
assign name=nwdose n.val=6.5e13
assign name=pbdose n.val=7e13
assign name=nsdose n.val=1e15
assign name=pboost n.val=2e14
assign name=nadose n.val=5e15
assign name=padose n.val=1e16
assign name=thick n.val=500
assign name=drres n.val=2e13
assign name=pwmask n.val=16.5
assign name=nwmask n.val=18
assign name=nwpbext n.val=2
assign name=pbspace n.val=12
assign name=nwpb n.val=@nwpbext+@pbspace/2
assign name=chlength n.val=3
assign name=nlength n.val=1
assign name=plength n.val=6
assign name=cw n.val=4
assign name=grid n.val=1
assign name=pb1 n.val=@nwmask+@nwpb
assign name=cell n.val=2*@chlength+2*@nlength+@plength
assign name=cathcell n.val=2*@nlength+@plength
assign name=cell1 n.val=@pb1+@chlength+@nlength+@plength/2
assign name=pb2 n.val=@pb1+@cell+@pbspace
assign name=cell2 n.val=@pb2+@chlength+@nlength+@plength/2
assign name=full n.val=@pb2+@cell+@pbspace/2

$$$$$$$$$$$$$$$$$$$$$$$$$$$$$$$$$$$$$$$$$$$$$$$$$$$$$$$$$$$$$$$$$$$$$$$$$$
option dev=x

$ 1. Mesh

line x location=0.0 spacing=0.5 tag=left
line x location=@full spacing=0.5 tag=right
line y location=0 spacing=0.2 tag=top
line y location=0.9 spacing=0.05
line y location=1.2 spacing=0.05
line y location=1.6 spacing=0.1
line y location=6 spacing=0.7
line y location=16 spacing=1
line y location=20 spacing=2.5
line y location=50 spacing=20
```

line y location=100 spacing=25
line y location=@thick/2 spacing=25
line y location=@thick-12 spacing=1
line y location=@thick-2 spacing=0.2
line y location=@thick spacing=0.1 tag=sub

eliminate columns x.max=@pb1+@chlength-@grid
eliminate columns +
x.min=@cell1+@plength/2+@nlength+@grid x.max=@pb2+@chlength-@grid
eliminate columns x.min=@cell2+@plength/2+@nlength+@grid
eliminate columns +
y.min=6 x.min=@pb1+@chlength-@grid x.max=@cell1+@plength/2+@nlength+@grid
eliminate columns +
y.min=6 x.min=@pb2+@chlength-@grid x.max=@cell2+@plength/2+@nlength+@grid
eliminate columns y.min=9
eliminate columns y.min=16

$ 2. Structure
method pd.fermi err.fac=1 compress ox.adapt grid.oxide=0.01
region silicon xlo=left xhi=right ylo=top yhi=sub
boundary exposed xlo=left xhi=right ylo=top yhi=top
boundary reflecti xlo=left xhi=left ylo=top yhi=sub
boundary reflecti xlo=right xhi=right ylo=top yhi=sub

initialize <100> phosphorus=5e12

$source coef_new

boron silicon dip.e=3.53468
boron silicon/oxide seg.e=1.073842
phos silicon dix.e=3.69744
phos silicon/oxide seg.0=0.201926

$ 3. Deep P+

diffuse temp=906 time=20 f.n2=9.5 f.o2=0.5
diffuse temp=906 time=10 f.n2=5.5 f.o2=0.5
diffuse temp=906 time=10 f.n2=5.5 f.o2=0.5
diffuse temp=906 time=10 f.o2=3.3 f.hcl=0.165
diffuse temp=906 time=14.75 f.o2=3.3 f.hcl=0.165 f.h2=6
diffuse temp=906 time=5 f.o2=3.3
diffuse temp=906 time=20 f.n2=5
print layers

$implant boron dose=@dpdose energy=100 tilt=7
$source /emterc/users/intel/sim_files/smf_process/dp_drive.inp
print layers
etch oxide all

$savefile out.f=dp.sav

$savefile out.f=dp_med medici

$ 4. P-well

$source /emterc/users/intel/sim_files/smf_process/implant_ox.inp
diffuse temp=906 time=20 f.n2=9.5 f.o2=0.5
diffuse temp=906 time=10 f.n2=5.5 f.o2=0.5
diffuse temp=906 time=10 f.n2=5.5 f.o2=0.5
diffuse temp=906 time=10 f.o2=3.3 f.hcl=0.165
diffuse temp=906 time=14.75 f.o2=3.3 f.hcl=0.165 f.h2=6
diffuse temp=906 time=5 f.o2=3.3
diffuse temp=906 time=20 f.n2=5
print layers
deposit photoresist thickness=1.7
etch photoresit right p1.x=@pwmask
implant boron dose=@pwdose energy=80 tilt=7
etch photoresist all

$source /emterc/users/intel/sim_files/smf_process/pwell_drive.inp

diffuse temp=900 time=20 f.n2=9.5 f.o2=0.5
diffuse temp=900 t.final=1150 time=25 f.n2=8
diffuse temp=1150 time=1000 f.n2=8
diffuse temp=1150 time=65 t.final=900 f.n2=8
diffuse temp=900 time=20 f.n2=8
etch oxide all
savefile out.f=pw.sav
savefile out.f=pw_med medici

$ 5. N-well implant

boron silicon dip.e=3.44768
boron silicon/oxide seg.e=1.238842

$source /emterc/users/intel/sim_files/smf_process/implant_ox.inp
diffuse temp=906 time=20 f.n2=9.5 f.o2=0.5
diffuse temp=906 time=10 f.n2=5.5 f.o2=0.5
diffuse temp=906 time=10 f.n2=5.5 f.o2=0.5
diffuse temp=906 time=10 f.o2=3.3 f.hcl=0.165
diffuse temp=906 time=14.75 f.o2=3.3 f.hcl=0.165 f.h2=6
diffuse temp=906 time=5 f.o2=3.3
diffuse temp=906 time=20 f.n2=5

print layers
deposit photoresist thickness=1.7
etch photoresit right p1.x=@nwmask
implant phos dose=@nwdose energy=60 tilt=7
etch photoresist all

$source /emterc/users/intel/sim_files/smf_process/nwell_drive.inp
diffuse temp=900 time=20 f.n2=9.5 f.o2=0.5
diffuse temp=900 t.final=1150 time=25 f.n2=5.5
diffuse temp=1150 time=1180 f.n2=5
diffuse temp=1150 time=65 t.final=900 f.n2=5
diffuse temp=900 time=20 f.n2=5
etch oxide all
savefile out.f=nw.sav
savefile out.f=nw_med medici

$base oxide
$source /emterc/users/intel/sim_files/smf_process/implant_ox.inp
diffuse temp=906 time=20 f.n2=9.5 f.o2=0.5
diffuse temp=906 time=10 f.n2=5.5 f.o2=0.5
diffuse temp=906 time=10 f.n2=5.5 f.o2=0.5
diffuse temp=906 time=10 f.o2=3.3 f.hcl=0.165
diffuse temp=906 time=14.75 f.o2=3.3 f.hcl=0.165 f.h2=6
diffuse temp=906 time=5 f.o2=3.3
diffuse temp=906 time=20 f.n2=5
deposit nitride thickness=0.12 space=5

$ Field oxide
diffuse temp=900 time=20 f.n2=9.5 f.o2=0.5
diffuse temp=900 t.final=1000 time=10 f.n2=8
diffuse temp=1000 time=5 f.n2=8
diffuse temp=1000 time=5 f.o2=3.3
diffuse temp=1000 time=100 f.o2=3.3 f.h2=6
diffuse temp=1000 time=2 f.o2=3.3
diffuse temp=1000 time=15 f.n2=8
diffuse temp=1000 t.final=900 time=25 f.n2=8
diffuse temp=900 time=20 f.n2=8
etch oxide all
etch nitride all
etch oxide all

$ 6. P base
$source /emterc/users/intel/sim_files/smf_process/implant_ox.inp
diffuse temp=906 time=20 f.n2=9.5 f.o2=0.5
diffuse temp=906 time=10 f.n2=5.5 f.o2=0.5
diffuse temp=906 time=10 f.n2=5.5 f.o2=0.5
diffuse temp=906 time=10 f.o2=3.3 f.hcl=0.165
diffuse temp=906 time=14.75 f.o2=3.3 f.hcl=0.165 f.h2=6
diffuse temp=906 time=5 f.o2=3.3
diffuse temp=906 time=20 f.n2=5

print layers
deposit photoresist thickness=1.7
etch photoresist start x=@pb1 y=-3
etch photoresist continue x=@pb1 y=3
etch photoresist continue x=@pb1+@cell y=3

```
etch photoresist done x=@pb1+@cell y=-3
etch photoresist start x=@pb2 y=-3
etch photoresist continue x=@pb2 y=3
etch photoresist continue x=@pb2+@cell y=3
etch photoresist done x=@pb2+@cell y=-3
implant boron dose=@pbdose energy=50 tilt=7


etch photoresist all


$source /emterc/users/intel/sim_files/smf_process/pbase_drive_c3.inp
diffuse temp=900 time=20 f.n2=9.5 f.o2=0.5
diffuse temp=900 t.final=1150 time=25 f.n2=8
diffuse temp=1150 time=290 f.n2=8
diffuse temp=1150 t.final=900 time=65 f.n2=8
diffuse temp=900 time=20 f.n2=8


print layers
etch oxide all


savefile out.f=pb.sav
savefile out.f=pb_med medici


$ 8. Gate formation


boron silicon /oxid trans.0=0
phos silicon /oxid trans.0=0
$source /emterc/users/intel/sim_files/smf_process/gate_ox.inp
diffuse temp=945 time=20 f.n2=9.5 f.o2=0.5
diffuse temp=945 time=10 f.n2=5.5 f.o2=0.5
diffuse temp=945 time=10 f.n2=5.5 f.o2=0.5
diffuse temp=945 time=10 f.o2=3.3 f.hcl=0.165
diffuse temp=945 time=17.5 f.o2=3.3 f.hcl=0.165 f.h2=6
diffuse temp=945 time=5 f.o2=3.3
diffuse temp=945 time=10  f.n2=5
diffuse temp=945 time=20  f.n2=5


deposit poly thickness=1 space=1
method pd.fermi err.fac=3 compress ox.adapt grid.oxide=0.2


$source /emterc/users/intel/sim_files/smf_process/poly_dope.inp
diffuse temp=805 time=25 f.n2=5 f.o2=0.15
diffuse temp=805 t.final=1000 time=30 f.n2=5 f.o2=0.15
diffuse temp=1000 time=10 f.n2=5 f.o2=0.15
diffuse temp=1000 time=17 f.n2=5 f.o2=0.15 p=4.5e24
diffuse temp=1000 time=2 f.n2=5 f.o2=1.2
diffuse temp=1000 t.final=805 time=50 f.n2=5
diffuse temp=805 time=10 f.n2=5
diffuse temp=805 time=25 f.n2=5


electrical x=0.5 resistan
```

```
print layers
etch oxide all
savefile out.f=poly.sav
savefile out.f=poly_med medici
deposit photoresist thickness=1.7

etch photoresist start x=@pb1+@chlength y=-3
etch photoresist continue x=@pb1+@chlength y=3
etch photoresist continue x=@pb1+@cell-@chlength y=3
etch photoresist done x=@pb1+@cell-@chlength y=-3
etch photoresist start x=@pb2+@chlength y=-3
etch photoresist continue x=@pb2+@chlength y=3
etch photoresist continue x=@pb2+@cell-@chlength y=3
etch photoresist done x=@pb2+@cell-@chlength y=-3
etch poly thickness=1
etch photoresist all

savefile out.file=p1.sav

savefile out.f=p1_med medici
 $9. Cathode formation
phos silicon dix.e=3.45
implant phos dose=@nsdose energy=120 tilt=0
implant boron dose=@pboost energy=150 tilt=0
deposit oxide thickness=@nlength spaces=5
etch oxide thickness=@nlength+0.2
etch silicon thickness=0.1

electrical x=0.5 resistan
implant arsenic dose=@nadose energy=50 tilt=0
etch silicon thickness=0.5
etch poly thickness=0.5
implant boron dose=@padose energy=60 tilt=0
savefile out.f=pa.sav
savefile out.f=pa_med medici

$ 11. LTO deposition

$source /emterc/users/intel/sim_files/smf_process/sd_ox.inp
diffuse temp=900 time=20 f.o2=3.3
diffuse temp=900 time=10 f.o2=3.3
diffuse temp=900 time=10 f.o2=3.3 f.hcl=0.165
diffuse temp=900 time=32 f.o2=3.3 f.hcl=0.165 f.h2=6
diffuse temp=900 time=2  f.o2=3.3
diffuse temp=900 time=5  f.n2=5
diffuse temp=900 time=20  f.n2=5

electrical x=0.5 resistan
deposit oxide thickness=1 spaces=1
diffuse temp=905 time=70 f.n2=6
```

```
$source /emterc/users/intel/sim_files/smf_process/reflow.inp
diffuse temp=950 time=20 f.o2=3.3
diffuse temp=950 time=10 f.o2=3.3
diffuse temp=950 time=5 f.o2=3.3
diffuse temp=950 time=18 f.o2=3.3 f.h2=6
diffuse temp=950 time=5  f.o2=3.3
diffuse temp=950 time=20 f.n2=5

deposit photoresist thickness=1.7
etch photoresist start x=@pb1+@chlength+@nlength/2 y=-3
etch photoresist continue x=@pb1+@chlength+@nlength/2 y=3
etch photoresist continue x=@pb1+@cell-@chlength-@nlength/2 y=3
etch photoresist done x=@pb1+@cell-@chlength-@nlength/2 y=-3

etch photoresist start x=@pb2+@chlength+@nlength/2 y=-3
etch photoresist continue x=@pb2+@chlength+@nlength/2 y=3
etch photoresist continue x=@pb2+@cell-@chlength/2-@nlength/2 y=3
etch photoresist done x=@pb2+@cell-@chlength-@nlength/2 y=-3

etch oxide start x=@pb1+@chlength+@nlength/2 y=-3
etch oxide continue x=@pb1+@chlength+@nlength/2 y=3
etch oxide continue x=@pb1+@cell-@chlength-@nlength/2 y=3
etch oxide done x=@pb1+@cell-@chlength-@nlength y=-3

etch oxide start x=@pb2+@chlength+@nlength/2 y=-3
etch oxide continue x=@pb2+@chlength+@nlength/2 y=3
etch oxide continue x=@pb2+@cell-@chlength-@nlength/2 y=3
etch oxide done x=@pb2+@cell-@chlength-@nlength/2 y=-3

etch photoresist all
savefile out.f=cw.sav
savefile out.f=cw_med medici

$ 12. Metal

deposit al thickness=4 spaces=10
etch aluminum left p1.x=@pb1+@chlength+@nlength/2
etch aluminum start x=@pb1+@cell-@chlength-@nlength/2 y=-6
etch aluminum continue x=@pb1+@cell-@chlength-@nlength/2 y=3
etch aluminum continue x=@pb2+@chlength+@nlength/2 y=3
etch aluminum done x=@pb2+@chlength+@nlength/2  y=-6
etch aluminum start x=@pb2+@cell-@chlength-@nlength/2 y=-6
etch aluminum continue x=@pb2+@cell-@chlength-@nlength/2 y=3
etch aluminum continue x=@full y=3
etch aluminum done x=@full y=-6

electrical x=0.5 resistan
electrod bottom name=anode
electrod x=@cell1 name=source
electrod x=@cell2 name=source
```

electrod x=@pb1 name=gate1
electrod x=@pb2-@pbspace/2 name=gate2
electrod x=@full name=gate3
savefile out.file=cigbt33_kv.sav
savefile out.file=cigbt33_kv medici poly.ele elec.bot

APPENDIX A3 - SIMULATION FILES FOR CHAPTER 4

1.2kV SEGMENTED P-BASE TCIGBT STRUCTURE GENERATION

```
$ Defining Structure
assign name=xmin n.val=0.0
assign name=ymin n.val=0.0
assign name=xmax n.val=43
assign name=ymax n.val=120
assign name=towidth n.val=2
assign name=todepth n.val=3.0
assign name=tgwidth n.val=1.8
assign name=tgdepth n.val=2.9
assign name=cath  n.val=-1.0
assign name=cathmax  n.val=0.2
assign name=tgdepth1 n.val=4.9
assign name=todepth1 n.val=5.0
assign name=pbaseL n.val=43
assign name=pbst n.val=19.1
assign name=pbaseD  n.val=2.8
assign name=pplusL n.val=2
assign name=pplusD n.val=0.4
assign name=nplusL n.val=1
assign name=nplusD n.val=0.3
assign name=chlen n.val=4.5
assign name=gatest n.val=8.0
assign name=goxth n.val=-0.1
assign name=pwells n.val=5.0
assign name=nwells n.val=13.5
assign name=pbmax n.val=0.0
assign name=colD n.val=1
assign name=fsD n.val=6
assign name=pwellJ n.val=7
assign name=pwmax n.val=0
assign name=nwellJ n.val=3.0
assign name=driftC n.val=8e13
assign name=bufferC n.val=1e16
assign name=colC n.val=2e18
assign name=pplusC n.val=1e19
assign name=nplusC n.val=1e20
assign name=pbaseC  n.val=3e17
assign name=pwellC n.val=8e16
assign name=nwellC n.val=9e16
assign name=pbpeak  n.val=0.0
assign name=pwpeak n.val=0.0
assign name=nwpeak n.val=0.3

$ Meshing
```

mesh smooth.k=1.0 ^diag.fli adjust

```
x.mesh x.min=0          x.max=11.8   h1=0.2        h2=0.2
x.mesh x.min=11.8   x.max=12.2   h1=0.1        h2=0.1
x.mesh x.min=12.2   x.max=15.8   h1=0.2               h2=0.2
x.mesh x.min=15.8   x.max=16.2   h1=0.1   h2=0.1
x.mesh x.min=16.2   x.max=17.8   h1=0.2   h2=0.2
x.mesh x.min=17.8   x.max=18.2   h1=0.1   h2=0.1
x.mesh        x.min=18.2   x.max=19.8   h1=0.2        h2=0.2
x.mesh        x.min=19.8   x.max=21.2   h1=0.1        h2=0.1
x.mesh        x.min=21.2   x.max=22.8   h1=0.2        h2=0.2
x.mesh x.min=22.8   x.max=23.2   h1=0.1   h2=0.1
x.mesh x.min=23.2   x.max=24.8   h1=0.2   h2=0.2
x.mesh x.min=24.8   x.max=25.2   h1=0.1   h2=0.1

x.mesh        x.min=25.2   x.max=34.8   h1=0.2               h2=0.2
x.mesh x.min=34.8   x.max=35.2   h1=0.1   h2=0.1
x.mesh x.min=35.2   x.max=36.8   h1=0.2   h2=0.2
x.mesh x.min=36.8   x.max=37.2   h1=0.1   h2=0.1
x.mesh x.min=37.2   x.max=38.8   h1=0.2   h2=0.2
x.mesh x.min=38.8   x.max=39.2   h1=0.1   h2=0.1
x.mesh x.min=39.2   x.max=39.8   h1=0.2   h2=0.2
x.mesh x.min=39.8   x.max=40.2   h1=0.1   h2=0.1
x.mesh x.min=40.2   x.max=41.8   h1=0.2   h2=0.2
x.mesh x.min=41.8   x.max=42.2   h1=0.1   h2=0.1
x.mesh x.min=42.2   x.max=43    h1=0.2   h2=0.2

y.mesh  loc=@cath      spacing=0.5
y.mesh        location=-0.2  spacing=0.1
y.mesh        location=0     spacing=0.1
y.mesh        location=3     spacing=0.1
y.mesh        location=5     spacing=0.2
y.mesh        location=12    spacing=1
y.mesh        location=25    spacing=10
y.mesh        location=55    spacing=20
y.mesh        location=115   spacing=1
y.mesh  loc=@ymax-3.5  spacing=0.5
y.mesh        location=@ymax     spacing=0.5

eliminate columns y.min=17
eliminate columns y.min=19
eliminate columns y.min=50

region num=1 Oxide   x.min=@xmin   x.max=@xmax       y.max=@ymin
region num=2 Silicon    x.min=@xmin   x.max=@xmax     y.min=@ymin  y.max=@ymax
region num=3 Oxide   x.min=@xmin   x.max=12    y.min=@ymin   y.max=@todepth
region num=4 Oxide   x.min=16    x.max=18    y.min=@ymin   y.max=@todepth1
region num=5 Oxide   x.min=23    x.max=25    y.min=@ymin   y.max=@todepth1
region num=6 Oxide   x.min=35    x.max=37    y.min=@ymin   y.max=@todepth1
region num=7 Oxide   x.min=42    x.max=43    y.min=@ymin   y.max=@todepth1
```

region num=8 Oxide   x.min=20   x.max=21   y.min=@ymin y.max=@todepth1
region num=9 Oxide   x.min=39   x.max=40   y.min=@ymin y.max=@todepth1

$$$$ Electrodes

$elec name=Gate   x.min=@xmin   x.max=18   y.min=-1.0 y.max=@goxth void
elec name=Gate   x.min=16.1   x.max=17.9   y.min=-1.0 y.max=@tgdepth1
           void
elec name=Gate   x.min=23.1   x.max=24.9   y.min=-1.0 y.max=@tgdepth1
           void
elec name=Gate   x.min=35.1   x.max=36.9   y.min=-1.0 y.max=@tgdepth1
           void
elec name=Gate   x.min=42.1   x.max=43   y.min=-1.0 y.max=@tgdepth1
           void
elec name=Gate   x.min=@xmin   x.max=11.9   y.min=-1.0 y.max=@tgdepth
           void
elec name=Gate   x.min=20.1   x.max=20.9   y.min=-0.2 y.max=@tgdepth1
           void
elec name=Gate   x.min=39.1   x.max=39.9   y.min=-0.2 y.max=@tgdepth1
           void

elec name=Cathode x.min=18.5 x.max=19.9   y.min=@cath y.max=0.0   void
elec name=Cathode x.min=21.1 x.max=22.5   y.min=@cath y.max=0.0   void
elec name=Cathode x.min=37.5 x.max=38.9   y.min=@cath y.max=0.0   void
elec name=Cathode x.min=40.1 x.max=41.5   y.min=@cath y.max=0.0   void

electrod y.min=@ymax name=Hsink_bot thermal
elec name=anode   bottom

$ DOPING DRIFT REGION
doping unif conc=@driftC n.type y.max=@ymax reg=2

$ DOPING COLLECTOR REGION
doping p.type conc=@colC   x.min=@xmin   x.max=@xmax peak=@ymax
junction=@ymax-@colD reg=2

$ DOPING BUFFER REGION
doping n.type conc=@bufferC x.min=@xmin x.max=@xmax peak=@ymax-@colD
junction=@ymax-(@colD+@fsD) reg=2

$doping pwell region
doping conc=@pwellC p.type reg=2   x.min=14.4   x.max=@pbaseL y.max=1.0 junc=14

$doping nwell region
doping conc=@nwellC n.type reg=2 x.min=14.44 x.max=@pbaseL y.max=1.0 junc=4.7

$ DOPING PBASE REGION

```
doping  p.type conc=@pbaseC x.min=21.7 x.max=22.5 junction=2.5  reg=2
doping  p.type conc=@pbaseC x.min=18.5 x.max=19.3 junction=2.5  reg=2
doping  p.type conc=@pbaseC x.min=37.5 x.max=38.3 junction=2.5  reg=2
doping  p.type conc=@pbaseC x.min=40.7 x.max=41.5 junction=2.5  reg=2

$ DOPING Cell1
doping unif reg=2 p.type conc=@pplusC x.min=19 x.max=22 y.min=@ymin y.max=0.3
doping unif reg=2 n.type conc=@nplusC x.min=18 x.max=19 y.min=@ymin y.max=0.3
doping unif reg=2 n.type conc=@nplusC x.min=22 x.max=23 y.min=@ymin
y.max=@nplusD

$ DOPING Cell2
doping unif reg=2 p.type n.peak=@pplusC x.min=38 x.max=41 y.min=@ymin
y.max=@pplusD
doping unif reg=2 n.type conc=@nplusC x.min=37 x.max=38 y.min=@ymin
y.max=@nplusD
doping unif reg=2 n.type conc=@nplusC x.min=41 x.max=42 y.min=@ymin
y.max=@nplusD

regrid doping abs log ratio=2
save out.f=puTCIGBT.med
plot.2d grid junction boundary fil x.min=22 x.max=27 y.max=10
plot.2d grid junction boundary fil x.min=23.8 x.max=28.2 y.max=10
plot.2d grid junction boundary fil x.min=22 x.max=27 y.min=1.8 y.max=2.2
plot.2d grid junction boundary fil x.min=13.5 x.max=15.5 y.min=1.0 y.max=3.2
plot.2d junction boundary fil y.max=20
plot.2d junction boundary fil y.min=100 y.max=120
plot.2d grid junction boundary fil
plot.2d bound fil
plot.3d doping x.min=20 x.max=55 y.max=5 z.log z.min=1e13
plot.1d doping x.st=24.5 x.end=24.5 y.st=0 y.end=30 log title="Doping along the vertical
cutline at x=24.5um"
plot.1d doping x.st=26 x.end=26 y.st=0 y.end=30 log title="Doping along the vertical cutline
at x=26um"
plot.1d doping x.st=7 x.end=7 y.st=90 y.end=120 log title="Doping along the vertical cutline
at x=9um"
```

APPENDIX B

DEVICE CHARACTERICATION SIMULATION FILES

APPENDIX B1 – BREAKDOWN VOLTAGE MEASUREMENT

```
assign name=runf  c.val=yes
assign name=vgate    n.val=0
assign name=taun  n.val=20e-6
assign name=taup  n.val=20e-6
assign name=models c.val="arora prpmob consrh auger fldmob incomple impact.i
temp=300"

assign name=icharge  n.val=1e11
assign name=name  c.val="puTCIGBT"

if cond=(@runf="yes")
                mesh inf=puTCIGBT.med
        option save.sol
        contact name=Gate n.poly
        interface qf=@icharge
        models  @models
        symb carriers=0
        solve init
        symb newton carriers=2
        method cont.stk
        solve
                solve v(gate)=0  v(anode)=0
                log out.file="bv_"@name".log"
                solve elect=anode  vstep=1 nstep=10
                save out.f="BV@10va" solution
                solve elec=anode vstep=10 nstep=9
                save out.f="BV@100va" solution
                solve elec=anode vstep=10 nstep=20
                save out.f="BV@300va" solution
                solve elec=anode vstep=10 nstep=30
                save out.f="BV@800Va" solution
                solve elec=anode vstep=10 nstep=40
                save out.f="BV@1200Va" solution
                solve elec=anode vstep=10 nstep=10
                save out.f="BV@1300Va" solution
                solve elec=anode vstep=10 nstep=70
                save out.f="BV@2000Va" solution

if.end
extract expr=@i(anode) name=ia units=Acm^-2
plot.1d inf=bv_puTCIGBT.log   x.ax=v(anode) y.ax=ia log top=1  print
out.file=PMOS_NMOS_bv.dat
```

```
mesh inf=.puTCIGBT.med
load inf=BV@10Va
plot.2d bou junc fill depl y.max=10 title="Depletion at 10V"

mesh inf=puTCIGBT.med
load inf=BV@100Va
plot.2d bou junc fill depl y.max=20 title="Depletion at 100V"

mesh inf=puTCIGBT.med
load inf=BV@300Va
plot.2d bou junc fill depl y.max=20 title="Depletion at 300V"
plot.2d bou junc fill depl y.max=120 title="Depletion at 300V"

mesh inf=puTCIGBT.med
load inf=BV@800Va
plot.2d bou junc fill depl y.max=120 title="Depletion at 800V"
plot.2d bou junc fill depl y.max=120 title="Depletion at 800V"

mesh inf=puTCIGBT.med
load inf=BV@1200Va
plot.2d bou junc fill depl y.max=120 title="Depletion at 1200V"
plot.2d bou junc fill depl y.max=20 title="Depletion at 1200V"

mesh inf=puTCIGBT.med
load inf=BV@1300Va
plot.2d bou junc fill depl y.max=120 title="Depletion at 1300V"
plot.2d bou junc fill depl y.max=20 title="Depletion at 1300V"

mesh inf=puTCIGBT.med
load inf=BV@2000va
plot.2d bou junc fill depl y.max=20 title="Depletion at 2000V"
plot.2d bou junc fill depl y.max=120 title="Depletion at 2000V"
```

APPENDIX B2 – IV CHARACTERISATION

```
assign name=doiv c.val=yes

assign name=vg n.val=15
assign name=ivtn n.val=20e-6
assign name=ivtp n.val=20e-6
assign name=models c.val="analytic prpmob consrh auger bgn fldmob impact.i temp=300"
assign name=icharge n.val=1e11
assign name=name    c.val="puTCIGBT"



if cond=(@doiv="yes")
        mesh  in.file=puTCIGBT.med
        option save.sol
        contact name=Gate n.poly
        interface qf=@icharge
        material silicon taun0=@ivtn taup0=@ivtp
        models @models

        symb carriers=0
        solve init
        symb newton carriers=2
        method cont.stk
        solve
                solve v(gate)=0 v(anode)=0
                log out.file="iv_"@name".log"
                solve elect=(gate) vstep=0.5 nstep=30

                solve elect=(anode)  vstep=0.1 nstep=10
                save out.f="iv@1.0va" solution
                solve elect=(anode)  vstep=0.1 nstep=10
                save out.f="iv@2.0va" solution
                solve elect=(anode)  vstep=0.1 nstep=10
                save out.f="iv@3.0va" solution
                solve elect=(anode)  vstep=1 nstep=2
                save out.f="iv@5va" solution
                solve elect=(anode)  vstep=1 nstep=5
                save out.f="iv@10va" solution
                solve elect=(anode)  vstep=1 nstep=5
                save out.f="iv@15va" solution
                solve elect=(anode)  vstep=1 nstep=5
                save out.f="iv@20va" solution
                solve elect=(anode)  vstep=1 nstep=10
                save out.f="iv@30va" solution

                solve elect=(anode)  vstep=1 nstep=10
```

```
save out.f="iv@40va" solution

solve elect=(anode)  vstep=1 nstep=10
save out.f="iv@50va" solution

solve elect=(anode)  vstep=1 nstep=10
save out.f="iv@60va" solution

solve elect=(anode)  vstep=10 nstep=14
save out.f="iv@200va" solution

solve elect=(anode)  vstep=10 nstep=30
save out.f="iv@500va" solution

solve elect=(anode)  vstep=10 nstep=50
save out.f="iv@1000va" solution

solve elect=(anode)  vstep=10 nstep=20
save out.f="iv@1200va" solution

extract expr=@i(anode)/38e-8 name=ia units=Acm^-2
plot.1d inf=iv_puTCIGBT.log  top=200 right=4 x.ax=v(anode) y.ax=ia print
out.file=vce_200.dat



mesh inf=puTCIGBT.med
load inf=iv@1.0va
plot.2d bou junc fill depl y.max=10 title="Depletion at 15V"
plot.2d bou junc fill depl y.max=10 title="current flow at 15v"
contour flowlines ncont=101
plot.1d potential a.x=19 b.x=19 a.y=0 b.y=20 print out.file=clamping3.dat

mesh inf=puTCIGBT.med
load inf=iv@5va
plot.2d bou junc fill depl y.max=10 title="Depletion at 15V"
plot.2d bou junc fill depl y.max=10 title="current flow at 15v"
contour flowlines ncont=101
plot.1d potential a.x=19 b.x=19 a.y=0 b.y=20 print out.file=clamping5.dat

mesh inf=puTCIGBT.med
load inf=iv@10va
plot.2d bou junc fill depl y.max=10 title="Depletion at 15V"
plot.2d bou junc fill depl y.max=10 title="current flow at 15v"
contour flowlines ncont=101
plot.1d potential a.x=19 b.x=19 a.y=0 b.y=20 print out.file=clamping10.dat


mesh inf=puTCIGBT.med
load inf=iv@15va
plot.2d bou junc fill depl y.max=10 title="Depletion at 15V"
```

```
plot.2d bou junc fill depl y.max=10 title="current flow at 15v"
contour flowlines ncont=101
plot.1d potential a.x=19 b.x=19 a.y=0 b.y=20 print out.file=clamping15.dat

mesh inf=puTCIGBT.med
load inf=iv@50va
plot.2d bou junc fill depl y.max=10 title="Depletion at 50V"
plot.2d bou junc fill depl y.max=10 title="current flow at 50v"
contour flowlines ncont=101
plot.1d potential a.x=19 b.x=19 a.y=0 b.y=20 print out.file=clamping50.dat

mesh inf=puTCIGBT.med
load inf=iv@60va
plot.2d bou junc fill depl y.max=10 title="Depletion at 60V"
plot.2d bou junc fill depl y.max=10 title="current flow at 60v"
contour flowlines ncont=101
plot.1d potential a.x=19 b.x=19 a.y=0 b.y=20 print out.file=clamping60.dat


extract expr=@i(anode)/38e-8 name=ia units=Acm^-2
plot.1d inf=iv_puTCIGBT.log   x.ax=v(anode)  y.ax=ia print out.file=iv.dat
mesh inf=puTCIGBT.med
load inf=iv@200va
plot.2d bou junc fill depl y.max=10 title="Depletion at 200V"
plot.2d bou junc fill depl y.max=10 title="current flow at 200v"
contour flowlines ncont=101
plot.1d holes a.x=18.5 b.x=18.5 a.y=0 b.y=120 log title="Hole Concentration
@ 18.5" print out.file=hole.dat
plot.1d elec a.x=18.5 b.x=18.5 a.y=0 b.y=120 log title="Electron
Concentration @ 18.5" print out.file=elec.dat
plot.1d holes a.x=18.5 b.x=18.5 a.y=0 b.y=20 log title="Hole Concentration
@ 18.5"
plot.1d elec a.x=18.5 b.x=18.5 a.y=0 b.y=20 log title="Electron Concentration
@ 18.5"

plot.1d net.carrier a.x=18.5 b.x=18.5 a.y=0 b.y=120 log title="NCARR @
Pwell=18.5" print out.file=netcarr.dat


if.end
```

APPENDIX B3 – THRESHOLD VOLTAGE MEASUREMENT

```
assign name=doth c.val=yes
assign name=doiv c.val=no
assign name=dobv c.val=no
assign name=vg n.val=15
assign name=ivtn n.val=20e-6
assign name=ivtp n.val=20e-6
assign name=models c.val="analytic prpmob consrh auger bgn fldmob impact.i temp=300"


assign name=icharge n.val=1e11
assign name=name    c.val="puTCIGBT"

if cond=(@doth="yes")
        mesh  in.file=puTCIGBT.med
        option save.sol
        contact name=Gate n.poly
        interface qf=@icharge
        material silicon taun0=@ivtn taup0=@ivtp
        models @models
        symb carriers=0
        solve init
        symb  newton carriers=2
        method cont.stk
        solve
        solve v(Gate)=0  v(anode)=0
        log out.file="th_"@name".log"
        solve elect=(anode) vstep=0.1 nstep=100
        solve elect=(anode) vstep=0.1 nstep=40
                save out.f="cigbt_anode14" solution
        solve elect=(Gate) vstep=0.10 nstep=100
                save out.f="cigbt_gate_ramp" solution

if.end

        extract expr=@i(anode)/38e-8 name=ia units=Aum^-1
        plot.1d inf=th_puTCIGBT.log x.ax=v(gate) y.ax=ia top=0.10

        mesh in.file=puTCIGBT.med
        load inf=cigbt_anode14
        plot.2d bou junc fill depl y.max=50 title="TCIGBT Anode"
        contour flowlines ncont=101

        mesh in.file=puTCIGBT.med
        load inf=cigbt_gate_ramp
        plot.2d bou junc fill depl y.max=50 title="TCIGBT Gate Ramp"
        contour flowlines ncont=101
```

APPENDIX B4- UIS SWITCHING PERFORMANCE

```
$ switching parameters

assign name=vrail n.val=600
assign name=ia n.val=100
assign name=J n.val=100
assign name=L n.val=38

$set to correct truncate value s10=mesh1 s2_0=mesh2
assign name=W n.val=@ia/(@L*1e-8*@J)
assign name=msh c.val="puTCIGBT12kV"

mesh inf=puTCIGBT.med

options save.sol

contact name=gate n.poly

interface=1e11
material silicon taun0=20e-6 taup0=20e-6

models analytic prpmob consrh auger bgn fldmob impact.i temp=300
symb newton carriers=0
solve
symb newton carriers=2
solve
save out.f=DUT mesh w.models
end

start circuit
VBUS   1 0   0
Ls     1 2   150n
Rl     2 3   @vrail/@ia
Ll     3 4   125e-3
Rg     10 11   22
VG     11 0   pulse 15 -15 10n 10n 10n 15u 45e-6
PDUT   4=anode 10=gate file=DUT width=@W
d1     4 2   modela
$C1    10 0   220e-9
.model modela d
.ic v(11)=15 v(10)=15

finish circuit

save structure=pdut out.f=Tcigbt.str20us mesh

symb newton carriers=0
solve
```

```
solve
symb newton carriers=2
method stack=30
solve

solve element=VBUS v.elem=0 vstep=0.2 nstep=5
solve element=VBUS v.elem=1 vstep=0.5 nstep=8
solve element=VBUS v.elem=5 vstep=1 nstep=5
solve element=VBUS v.elem=10 vstep=5 nstep=8
solve element=VBUS v.elem=50 vstep=10 nstep=(@vrail-50)/10

log out.file="sw_"@msh"_20us_100A.log"
save structure=pdut sol out.f="sw_"@msh"20us_t0"

solve dt=1e-9 tstop=1e-6

save structure=pdut out.f="sw_"@msh"_t1us"

solve dt=1e-9 tstop=2e-6
save structure=pdut out.f="sw_"@msh"_t2us"

solve dt=1e-9 tstop=3e-6
save structure=pdut out.f="sw_"@msh"_t3us"

solve dt=1e-9 tstop=5e-6
save structure=pdut out.f="sw_"@msh"_t5us"

solve dt=1e-9 tstop=10e-6
save structure=pdut out.f="sw_"@msh"_t10us"
end

plot.1d inf=sw_puTCIGBT12kV_20us_100A.log x.ax=time y.ax=i(pdut.anode) print
out.file=i.dat
plot.1d inf=sw_puTCIGBT12kV_20us_100A.log x.ax=time y.ax=v(pdut.anode) print
out.file=v.dat

plot.1d inf=sw_puTCIGBT12kV_20us_100A.log x.ax=time y.ax=v(pdut.gate)  print
out.file=vg.dat


mesh inf=puTCIGBT.med
load in.file=sw_puTCIGBT12kV_t1us
plot.2d bou junc fill depl y.max=30
plot.2d bou junc fill depl y.max=30 title="@1us"
contour flowlines ncont=50

mesh inf=puTCIGBT.med
load in.file=sw_puTCIGBT12kV_t2us
plot.2d bou junc fill depl y.max=40
plot.2d bou junc fill depl y.max=40 title="@2us
```

```
contour flowlines ncont=31

mesh inf=puTCIGBT.med
load in.file=sw_puTCIGBT12kV_t3us
plot.2d bou junc fill depl y.max=40
plot.2d bou junc fill depl y.max=40 title="@3us
contour flowlines ncont=31

mesh inf=puTCIGBT.med
load in.file=sw_puTCIGBT12kV_t5us
plot.2d bou junc fill depl y.max=40
plot.2d bou junc fill depl y.max=40 title="@5us
contour flowlines ncont=31

mesh inf=puTCIGBT.med
load in.file=sw_puTCIGBT12kV_t10us
plot.2d bou junc fill depl y.max=40
plot.2d bou junc fill depl y.max=40 title="@10us
contour flowlines ncont=31
```

APPENDIX B5- SHORT CIRCUIT PERFORMANCE

$ switching parameters

assign name=vrail n.val=600
assign name=ia n.val=100
assign name=J n.val=100
assign name=L n.val=43

$set to correct truncate value s10=mesh1 s2_0=mesh2
assign name=W n.val=@ia/(@L*1e-8*@J)

assign name=msh c.val="Igbt33kV"

mesh inf=puTCIGBT.med

options save.sol

contact name=gate n.poly
contact name=Hsink_bot R.THERM=2e5
interface=1e11
material silicon taun0=20e-6 taup0=20e-6

models analytic prpmob consrh auger bgn fldmob impact.i temp=300
symb newton carriers=0
solve
symb newton carriers=2
solve
save out.f=DUT mesh w.models
end

start circuit
VBUS   3 0   0
VG   10 0   pulse 0 15 100n 100n 100n 15u 45e-6
PDUT   3=anode 10=gate file=DUT width=@W
.ic v(10)=0

finish circuit

save structure=pdut out.f=cigbt.str20us mesh
symb carriers=0
solve init
symb newton carriers=2 lat.temp coup.lat
method cont.stk

solve element=VBUS v.elem=0 vstep=0.2 nstep=5

```
solve element=VBUS v.elem=1 vstep=0.5 nstep=8
solve element=VBUS v.elem=5 vstep=1 nstep=5
solve element=VBUS v.elem=10 vstep=5 nstep=8
solve element=VBUS v.elem=50 vstep=10 nstep=(@vrail-50)/10

log out.file="sw_"@msh"_20us_100A.log"
save structure=pdut sol out.f="sw_"@msh"50us_t0"

solve dt=1e-9 tstop=1e-6

save structure=pdut out.f="sw_"@msh"_t1us"

solve dt=1e-9 tstop=2e-6
save structure=pdut out.f="sw_"@msh"_t2us"

solve dt=1e-9 tstop=3e-6
save structure=pdut out.f="sw_"@msh"_t3us"

solve dt=1e-9 tstop=5e-6
save structure=pdut out.f="sw_"@msh"_t5us"

solve dt=1e-9 tstop=10e-6
save structure=pdut out.f="sw_"@msh"_t10us"

solve dt=1e-9 tstop=20e-6
save structure=pdut out.f="sw_"@msh"_t10us"

solve dt=1e-9 tstop=30e-6
save structure=pdut out.f="sw_"@msh"_t10us"

end

plot.1d inf=sw_Igbt33kV_20us_100A.log x.ax=time y.ax=i(pdut.anode) print out.file=i.dat
plot.1d inf=sw_Igbt33kV_20us_100A.log x.ax=time y.ax=v(pdut.anode) print out.file=v.dat
plot.1d inf=sw_Igbt33kV_20us_100A.log x.ax=time y.ax=v(pdut.gate)  print out.file=vg.dat


mesh inf=puTCIGBT.med
load in.file=sw_Igbt33kV_t1us
plot.2d bou junc fill depl y.max=40
plot.2d bou junc fill depl y.max=40 title="@1us"
contour flowlines ncont=31

mesh inf=puTCIGBT.med
load in.file=sw_Igbt33kV_t2us
plot.2d bou junc fill depl y.max=40
plot.2d bou junc fill depl y.max=40 title="@2us
contour flowlines ncont=31

mesh inf=puTCIGBT.med
```

```
load in.file=sw_Igbt33kV_t3us
plot.2d bou junc fill depl y.max=40
plot.2d bou junc fill depl y.max=40 title="@3us
contour flowlines ncont=31


mesh inf=puTCIGBT.med
load in.file=sw_Igbt33kV_t5us
plot.2d bou junc fill depl y.max=40
plot.2d bou junc fill depl y.max=40 title="@5us
contour flowlines ncont=31


mesh inf=puTCIGBT.med
load in.file=sw_Igbt33kV_t10us
plot.2d bou junc fill depl y.max=40
plot.2d bou junc fill depl y.max=40 title="@10us
contour flowlines ncont=31
```

APPENDIX C

ELECTRICAL SIMULATION FILES (CHAPTER 5 & CHAPTER 6)
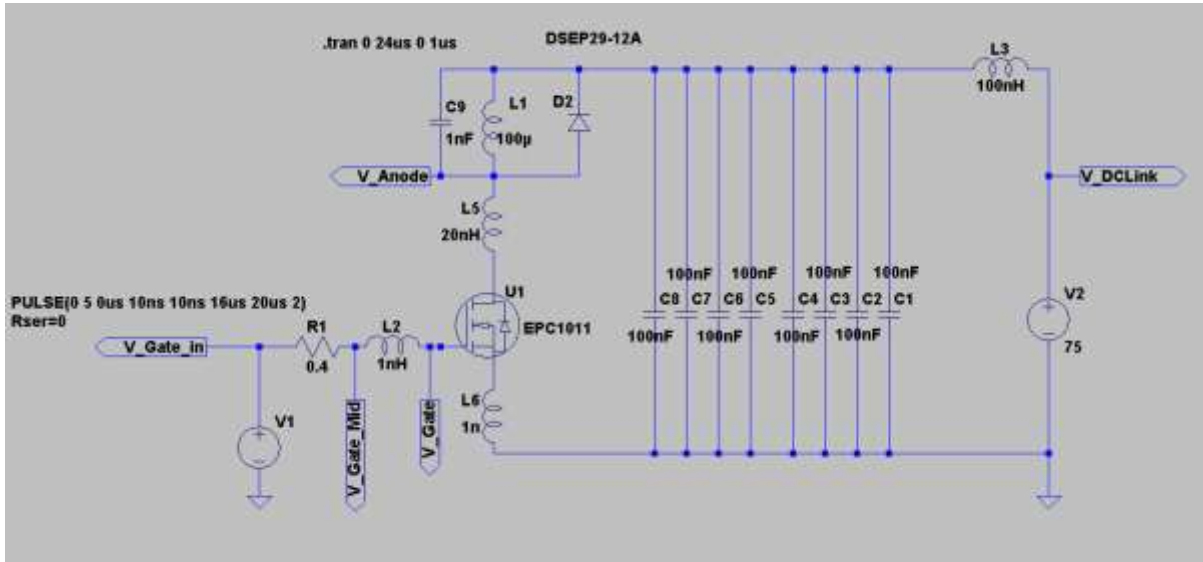
Figure C- 1: Simulation model to understand impact of stray inductance on the device
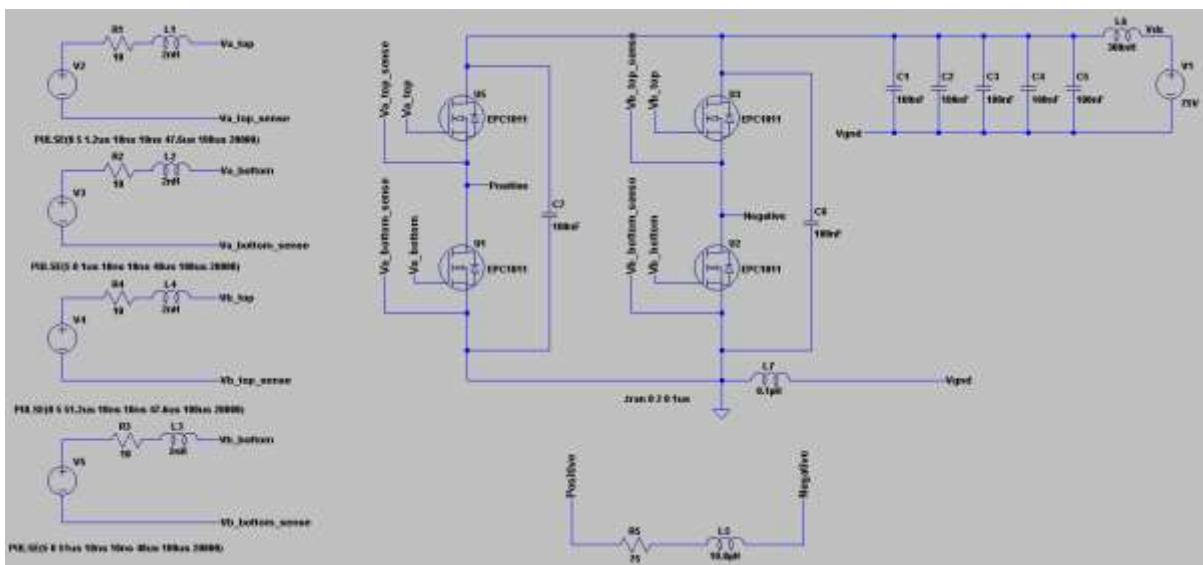
Figure C- 2: Simulation model to understand impact of stray components on H-Bridge design
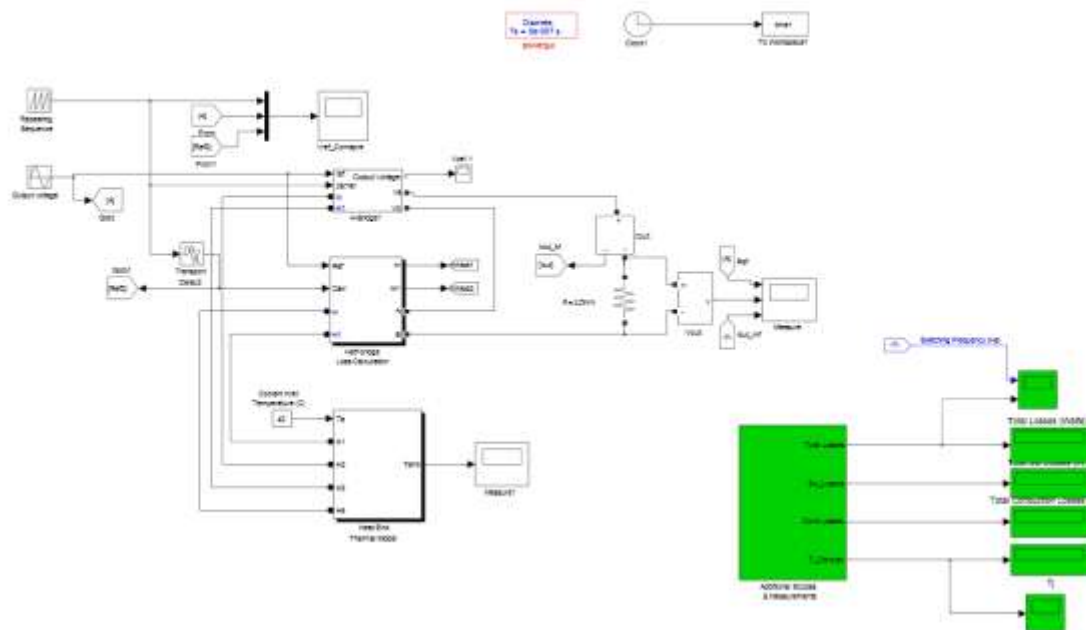
Figure C- 3: Loss Model 5-level converter
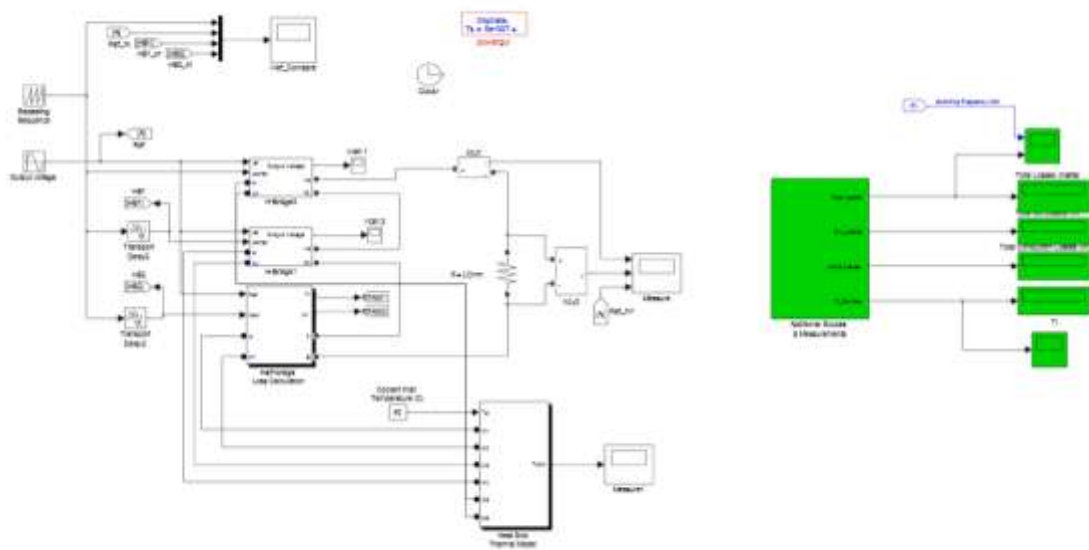
Figure C- 4: Loss model of a 7-level converter
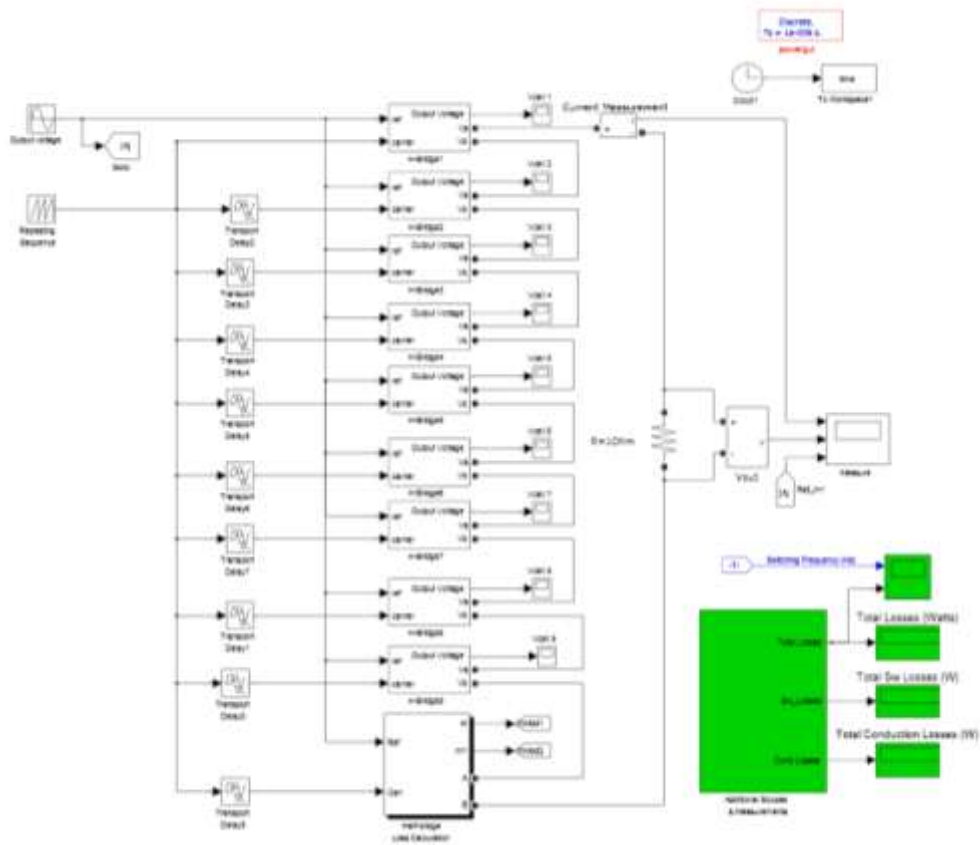
Figure C- 5: Loss model of 21-level converter
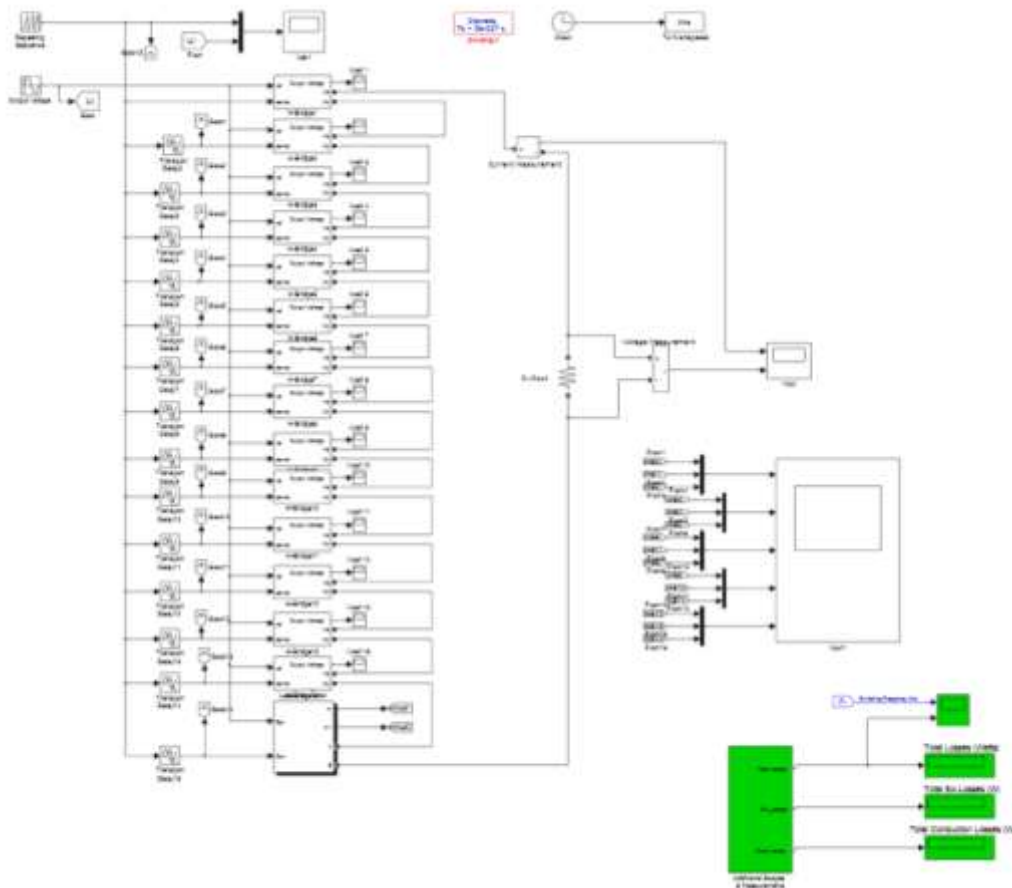
Figure C- 6: Loss model 31-level converter
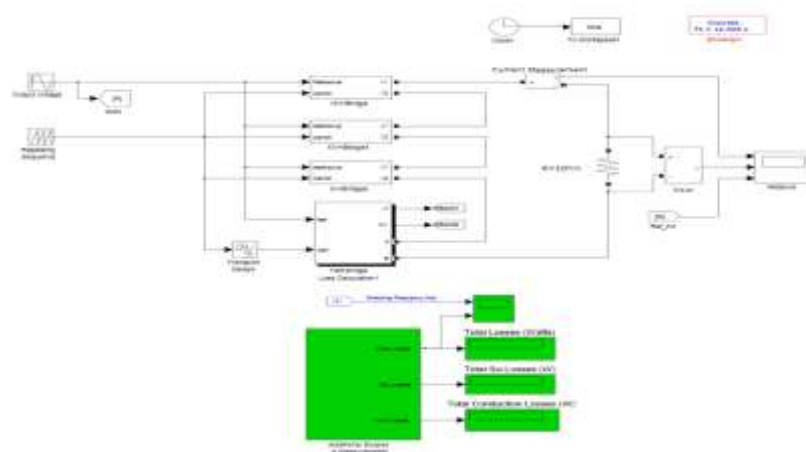
Figure C- 7: Loss model for a 61-level converter

APPENDIX D

CIRCUIT DESIGN AND LAYOUT FILES
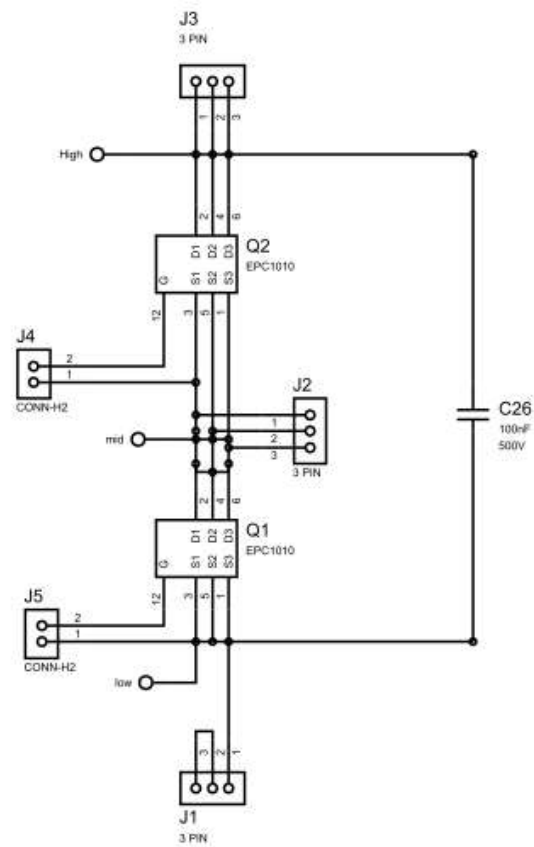
Figure D- 1: Circuit layout of plug-in modules
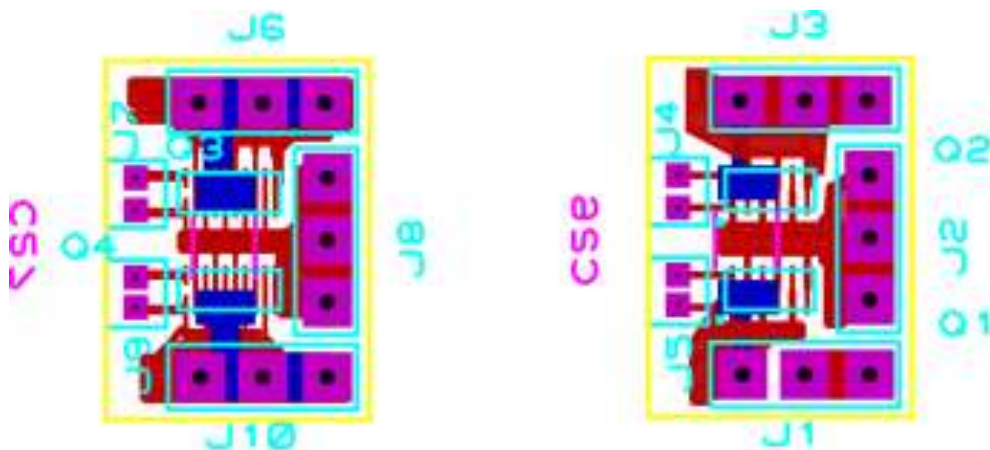
Figure D- 2: Layout of the Plug in modules left (EPC devices 1001/1005/1015) , right (EPC 1010/1011)
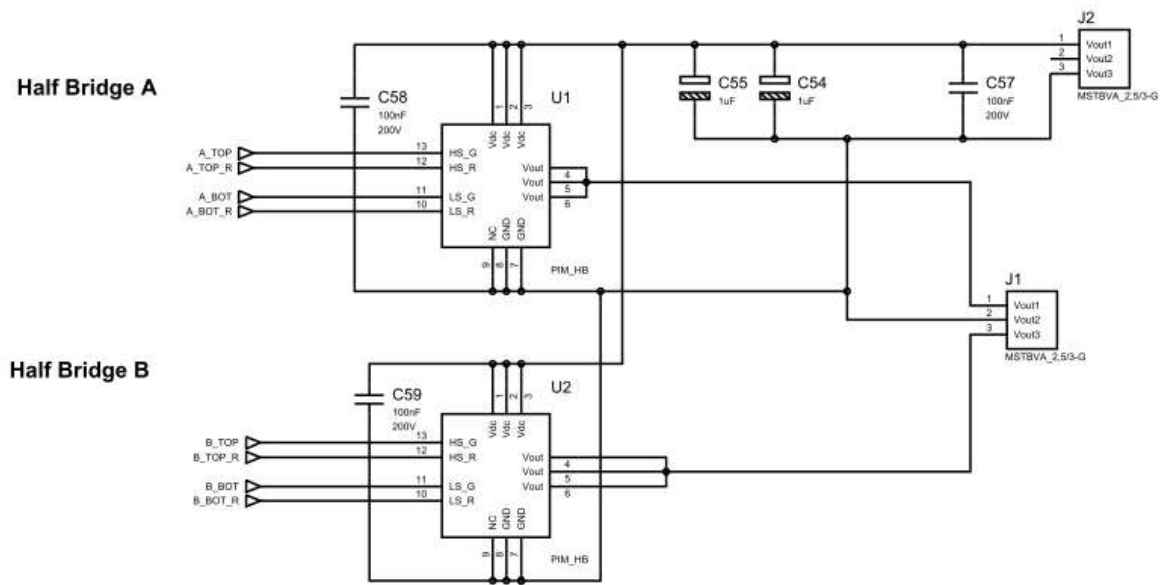
Figure D- 3: Implementation of the Plug-in-modules in an H-Bridge Circuit
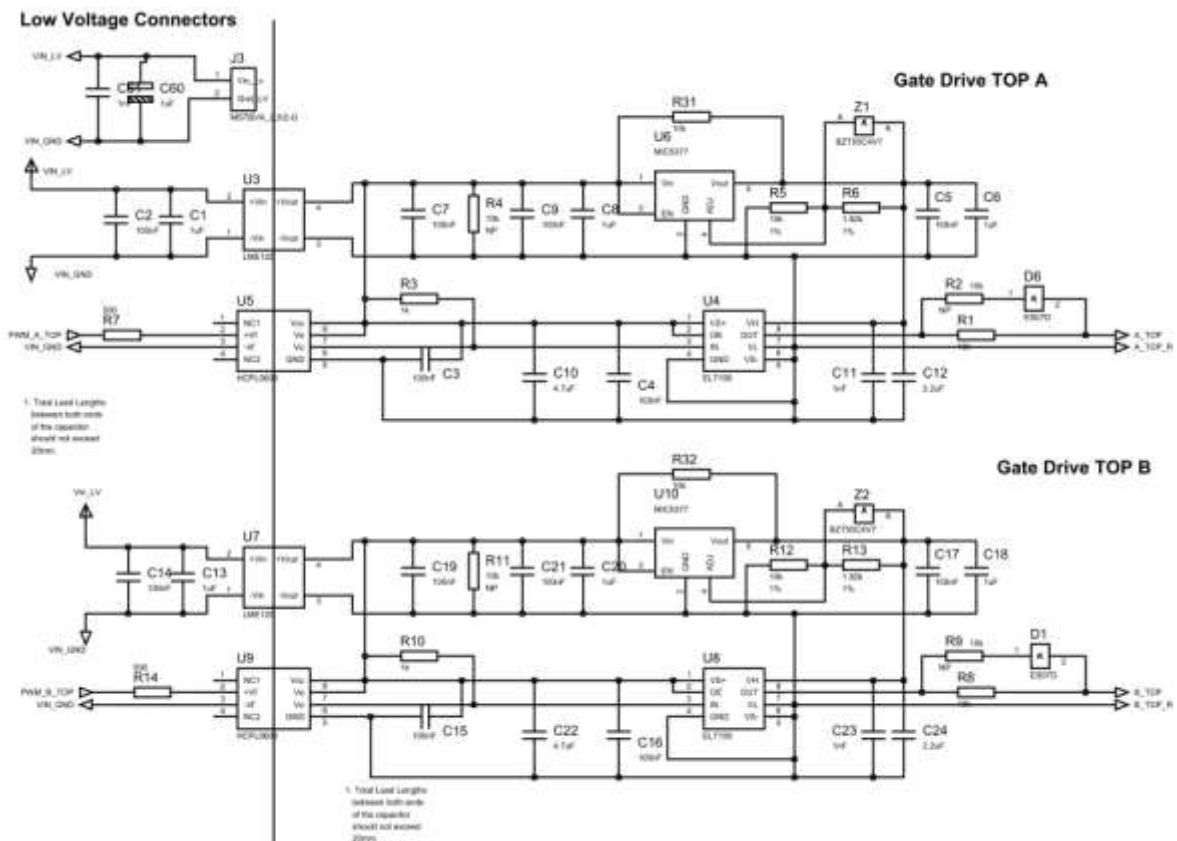
Figure D- 4: Circuit diagram for the high side devices
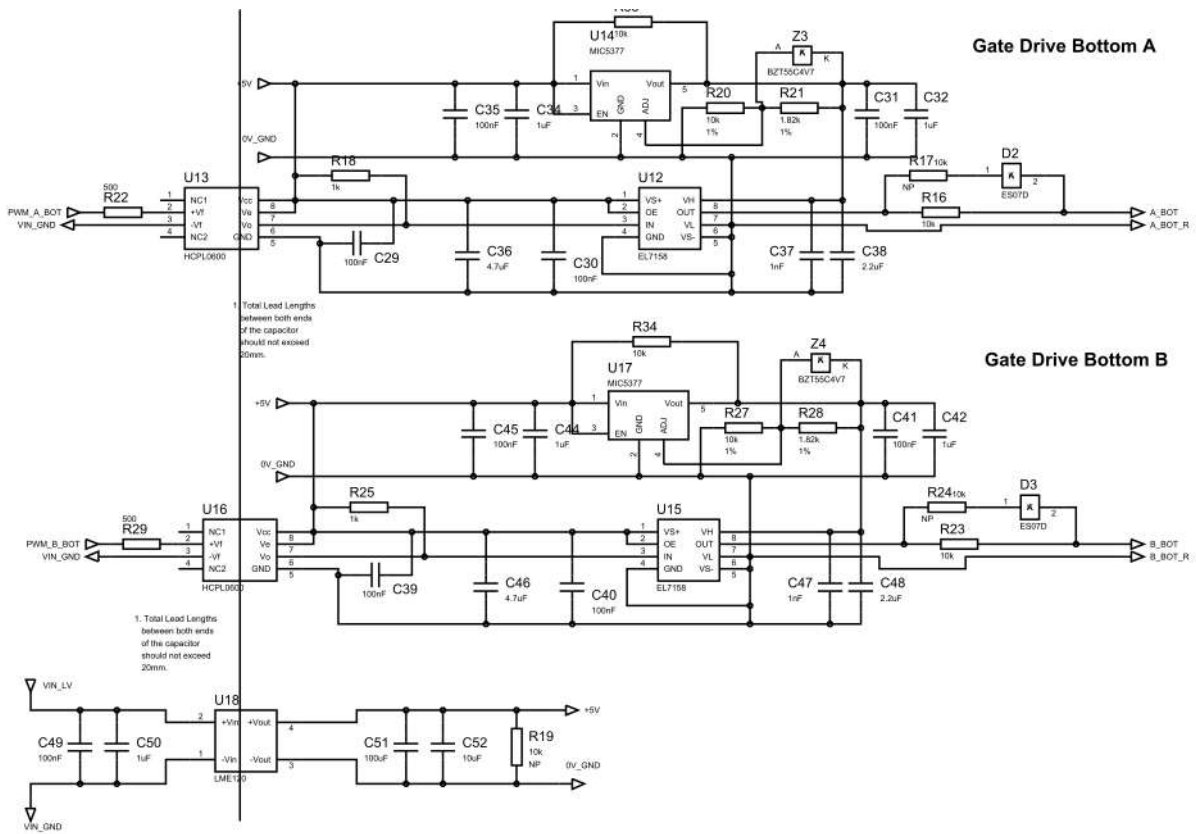
Figure D- 5: Circuit diagram for the Low side devices
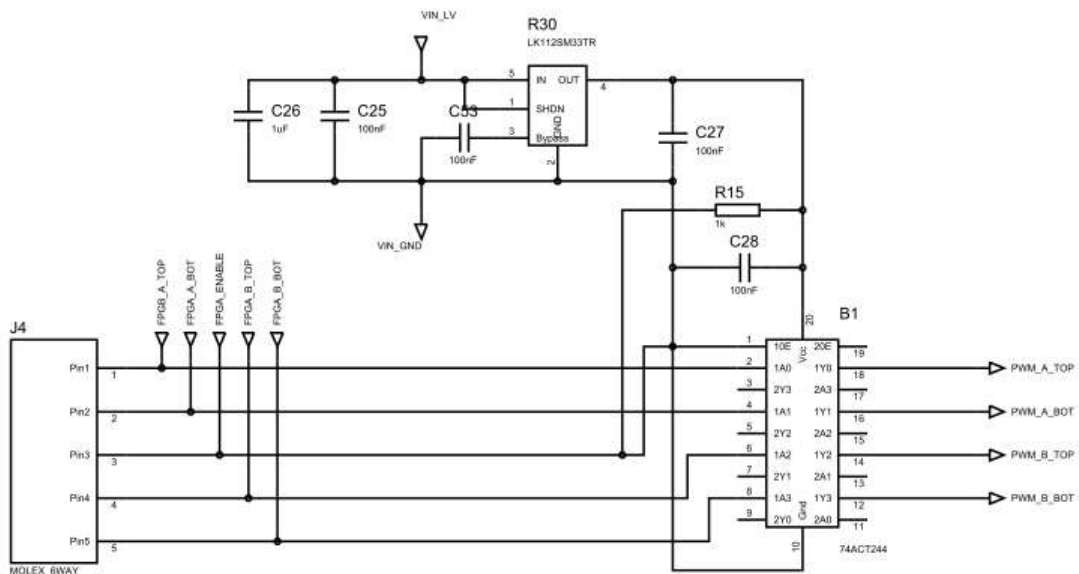
Figure D- 6: FPGA interface circuit diagram with H-Bridge Circuit
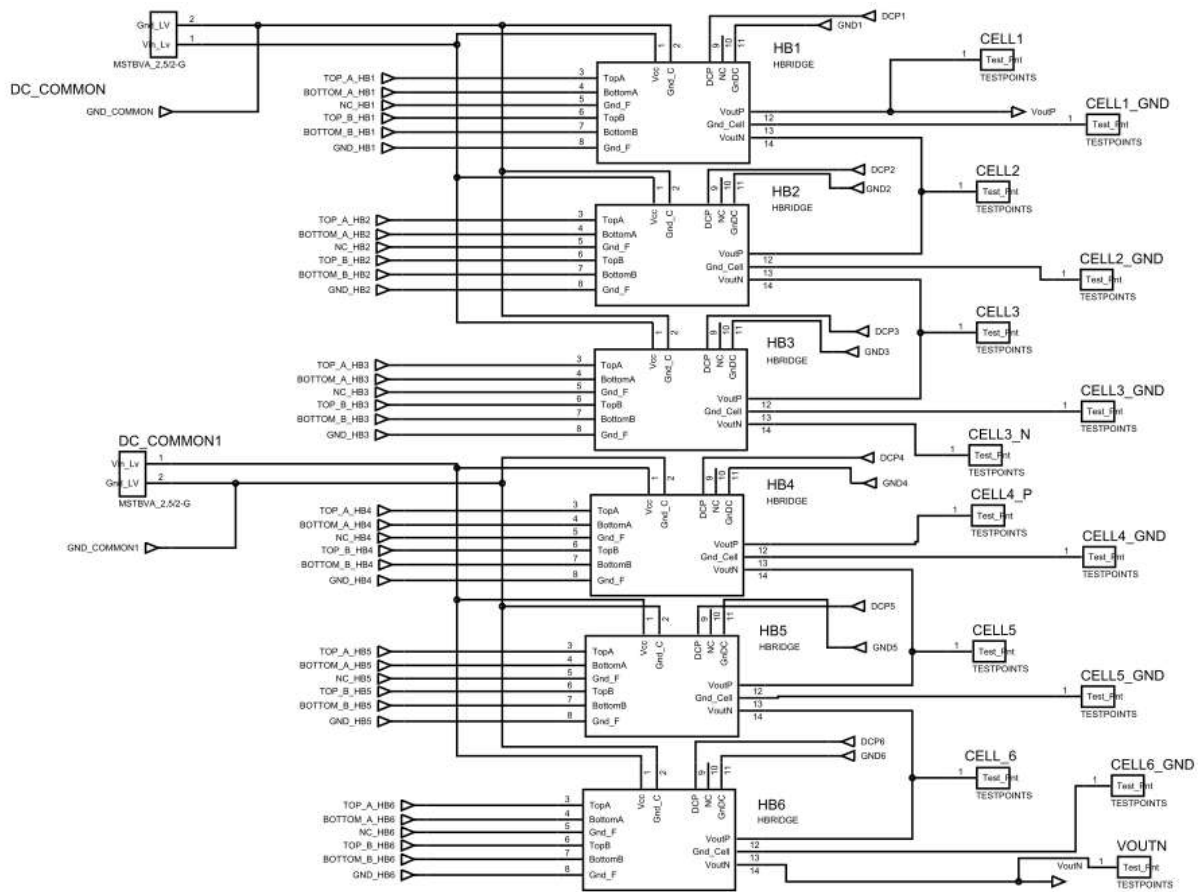
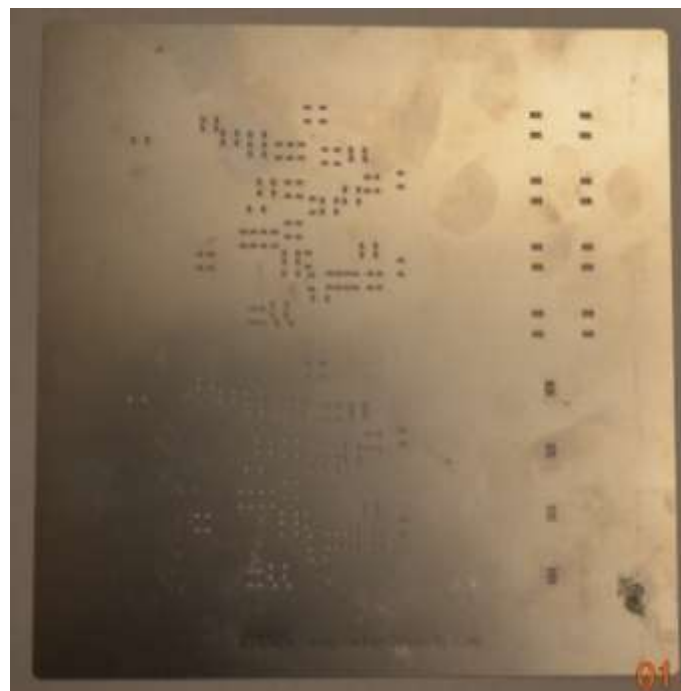**Figure D- 7: Circuit diagram to the external interface circuit**

Figure D- 8: Stencil used to allow uniform spread of solder
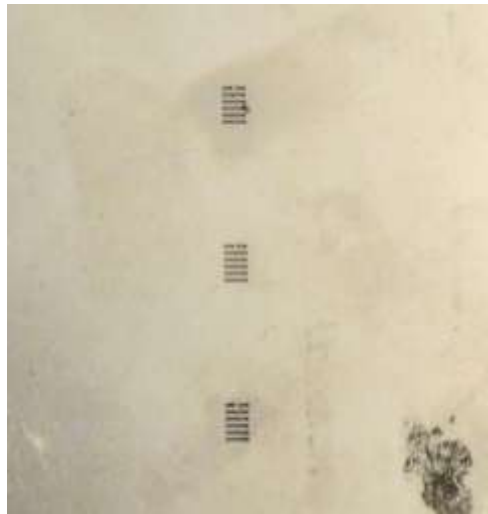
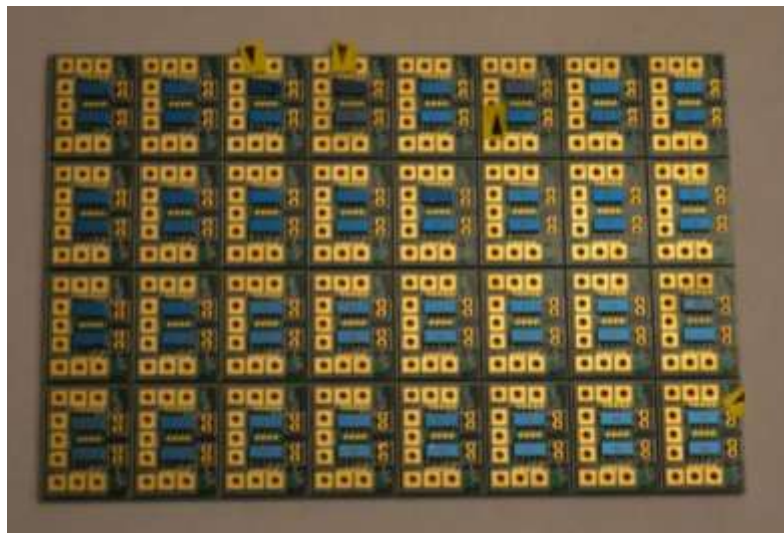**Figure D- 9: Zoomed in view of the stencil showing the device pads**

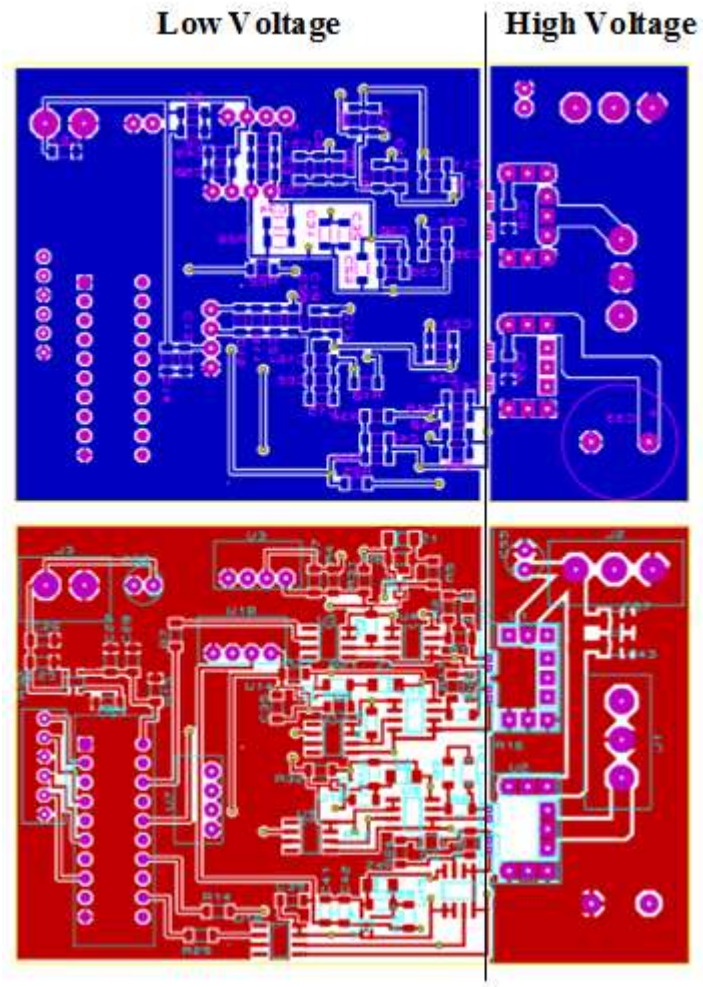**Figure D- 10: Zoomed in view of the stencil showing the device pads**

Figure D- 11: Layout diagram for the H-Bridge arrangment top side copper/silk (Bottom) and bottom copper/silk (Top)